National Library of Canada

Acquisitions and Bibliographic Services Branch

395 Wellington Street
Ottawa, Ontario
K1A 0N4

Bibliothèque nationale du Canada

Direction des acquisitions et des services bibliographiques

395, rue Wellington
Ottawa (Ontario)
K1A 0N4

*Your file Votre référence*

*Our file Notre référence*

## NOTICE

The quality of this microform is heavily dependent upon the quality of the original thesis submitted for microfilming. Every effort has been made to ensure the highest quality of reproduction possible.

If pages are missing, contact the university which granted the degree.

Some pages may have indistinct print especially if the original pages were typed with a poor typewriter ribbon or if the university sent us an inferior photocopy.



## AVIS

La qualité de cette microforme dépend grandement de la qualité de la thèse soumise au microfilmage. Nous avons tout fait pour assurer une qualité supérieure de reproduction.

S'il manque des pages, veuillez communiquer avec l'université qui a conféré le grade.

La qualité d'impression de certaines pages peut laisser à désirer, surtout si les pages originales ont été dactylographiées à l'aide d'un ruban usé ou si l'université nous a fait parvenir une photocopie de qualité inférieure.



Canada

ISBN 0-315-82502-2

UNIVERSITÉ D'OTTAWA
UNIVERSITY OF OTTAWA

To my parents who value education so much

## ABSTRACT

The first part of the thesis is concerned with the problem of temperature dependence of the Tafel slope for various electrochemical processes including the cathodic $H_2$ and anodic $O_2$ evolution reactions at Au, Pt and Ni in 0.2 N NaOH aqueous solutions at elevated temperatures up to 473 K by means of steady-state polarization experiments. It is found that the commonly assumed representation of the Tafel slope, $b$, as $b = RT/\beta F$ with $\beta$ a constant, often equal to 0.5, is not followed, i.e. $\beta$ is dependent on T. Several examples of this unconventional behaviour of $b$ on temperature are provided in this thesis.

The effect of temperature on the surface processes of oxide film formation and reduction in both acid and alkaline aqueous solutions is also examined by means of cyclic voltammetry experiments at temperatures as high as 529 K. In addition to the expected behaviour, such as the higher is the temperature the larger is the rate of reaction, the processes also become more reversible. Experimental examples are provided in this thesis.

The second part of the thesis is about the anodic $O_2$ evolution reaction at the two "allotropic" forms of lead dioxide, $\alpha$- and $\beta$-$PbO_2$ in 1 N $HClO_4$ aqueous solutions. The existence of these two forms of $PbO_2$ provides a rare opportunity of examining the structural effect in electrocatalysis and kinetics of the $O_2$ evolution process. Significant differences between the dimorphs are observed both in the kinetics and the adsorption behaviour of the O and OH intermediates of the reaction.

Both potential-relaxation transients, following prior current interruption, and a.c. frequency-response spectroscopy are used in deriving the adsorption behaviour of the reaction intermediates, both H and O/OH species.

## ACKNOWLEDGEMENTS

The author wishes to express the most sincere gratitude to his research supervisor, Professor B.E. Conway, for his continuous interest and guidance throughout the course of this work. His teaching will always be treasured in the author's memory. Professor Conway is also thanked for his assistance with the preparation of this thesis.

Grateful acknowledgement is made to Ms. R. Simpraga and Dr. G. Tremillosi Filho for their initial interest and later contributions to the lead dioxide complementary-project,the details of which constitute a sizable part of this thesis.

Special thanks is also due to Dr. G. Tremillosi Filho and Mr. S.Y. Qian in our laboratory and Mr. E. Kristoff, the Master glassblower of the Chemistry Department, for constructive discussions on various aspects of the development of the experimental techniques and for fabricating some of the highly specialized glass apparatus utilized in this work.

Finally, the author is thankful to those who have offered their support and encouragement during the difficult times. Many thanks.

TABLE OF CONTENTS


| | Page |
|---|---|
| ABSTRACT | iii |
| ACKNOWLEDGEMENTS | iv |
| TABLE OF CONTENTS | v |
| LIST OF FIGURES | x |
| LIST OF TABLES | xvii |
| I. GENERAL INTRODUCTION | 1 |
| I.A.1 Temperature Effects in Electrode Kinetics | 2 |
| I.A.2 Problems Requiring Clarification | 10 |
| I.A.3 Previous Experimental Studies of *b* as a Function of Temperature | 14 |
| I.B.1 Monolayer Thick Oxide Formation and Reduction on Noble Metals | 18 |
| I.C.1 Brief Review on the Hydrogen and Oxygen Evolution Reaction Kinetics ( HER and OER ) | 30 |
| I.C.1a Hydrogen Evolution Reaction ( HER ) | 30 |
| I.C.1b Oxygen Evolution Reaction ( OER ) | 33 |
| II. SCOPE AND AIMS OF THE WORK COVERED IN THE THESIS | 36 |
| III. EXPERIMENTAL | |
| III.A Experimental ( High Temperature and Pressure Conditions ) | 40 |
| III.A.1 Problems Arising in High Temperature and Pressure Work | 40 |
| III.A.1a High Temperature and Pressure Autoclave | 41 |
| III.A.1b Electrical Feed-throughs | 44 |
| III.A.1c Reference Electrodes for High Temperatures | 46 |
| III.A.2 Development of an Experimental System | 50 |
| III.A.2a High Pressure Bombs | 50 |
| III.A.2b Pressure Read-Out | 53 |
| III.A.2c Temperature Control System | 53 |
| III.A.3 Basis for Successful Experiments | 54 |
| III.A.4 Methods of Measurements | 58 |
| III.A.4.1 Cell Preparation | 58 |
| III.A.4.2 High Temperature Measurements | 58 |

Page

III.A.4.2.1 General 58

III.A.4.3 Cyclic Voltammetric Studies 59
III.A.4.4 Steady-State Tafel Experiments 61
III.A.4.5 Potential-Decay Transients 62
III.A.4.6 A.C. Impedance Measurements 63

III.A.5 Cells and Electrode Designs 63

III.A.5.1 Electrochemical Cells for Use in High-Temperature/High-Pressure Experiments 63

III.A.5.1a Three-Compartment Pyrex Glass Cell 64
III.A.5.1b One-Compartment Pyrex Glass Cell 64
III.A.5.1c Two-Compartment Teflon Cell 67

III.A.5.2 Electrodes for Use in High-Temperature/High-Pressure Experiments 67

III.A.5.2a Miniature Pyrex Electrodes 69
III.A.5.2b Standard Sized Pyrex Electrodes 69
III.A.5.2c Miniature Pyrex/Teflon Electrodes 71

III.A.6 Systems Studied 71

III.A.6.1 Reference Electrodes 71

III.A.6.1a Dynamic Hydrogen Electrode ( DHE ) 71
III.A.6.1b Dynamic Pd/PdH Electrode 72
III.A.6.1c Palladium Wire Reference Electrode 73
III.A.6.1d Platinum-Platinum Oxide Electrode 73

III.A.6.2 Working Electrodes 74

III.A.6.2a Gold Electrodes 74
III.A.6.2b Platinum Electrodes 74
III.A.6.2c Nickel Electrodes 75

III.A.6.3 Counter Electrodes 75

III.A.6.4 Solutions 76

III.A.6.4a Sulphuric Acid Solutions 76
III.A.6.4b Perchloric Acid Solutions 76

Page

III.A.6.4c Sodium Hydroxide Solutions 76

III.B Experimental ( OER at α- and β-Lead Dioxides ) 77

III.B.1 Methods 77

III.B.1.1 Constant Potential, Steady-State Anodic Polarization 77
III.B.1.2 Potential-Relaxation Transients 77
III.B.1.3 A.C. Impedance Measurements 78
III.B.1.4 'iR' drop Corrections 78

III.B.2 Cell 79

III.B.3 Electrodes 79

III.B.3.1 α- and β-$PbO_2$ Electrode Preparation 79
III.B.3.2 $PbO_2$ Electrode Characterizations 80
III.B.3.3 Reference Electrode 80
III.B.3.4 Counter Electrode 83

III.B.4 Solutions 83

III.B.5 Gases 83

IV. RESULTS AND DISCUSSION 84

IV.A Oxide Film Formation and Reduction 84

IV.A.1 Cyclic Voltammograms for Gold and Platinum at Room Temperature 85

IV.A.1.1 General 85
IV.A.1.2 Reversibility and Hysteresis Behaviour at Room Temperature 87

IV.A.1.2a Oxide Reduction Potential vs Anodic Potential Limits 87
IV.A.1.2b Anodic and Cathodic Peak Potential vs Sweep Rate 88

IV.A.2 Cyclic Voltammograms for Pt and Au at Elevated Temperatures 91

IV.A.2.1 General 91

Page

IV.A.2.2 Relationship between Temperature and Reversibility 98

IV.A.2.2.1 Cathodic Peak Potential vs Anodic Potential Limits 98

IV.A.2.2.1a Platinum 98
IV.A.2.2.1b Gold 99

IV.A.2.2.2 Anodic vs Cathodic Peak Potential Relations 101

IV.A.2.2.2a Gold 101
IV.A.2.2.2b Platinum 103

IV.A.2.2.3 Anodic and Cathodic Peak Potentials vs Sweep Rate 103

IV.A.2.2.3a Gold 103
IV.A.2.2.3b Platinum 105

IV.A.2.3 Metal Oxide Dissolution at Elevated Temperatures 105

IV.A.2.4 Conclusions on the Oxide Film Formation and Reduction at Au and Pt at Elevated Temperatures 110

IV.B Hydrogen Evolution Reaction 111

IV.B.1 Tafel Relations 112

IV.B.1.1 Tafel Relations for the HER at Gold 112
IV.B.1.2 Tafel Relations for the HER at Nickel 116
IV.B.1.3 Tafel Relations for the HER at Platinum 118

IV.B.2 Potential-Decay Transients and Analysis of Pseudocapacitance Behaviour 120

IV.B.2.1 Potential-Decay Transients for the HER at Gold 124
IV.B.2.2 Potential-Decay Transients for the HER at Nickel 130

Page

IV.B.2.3 Potential-Decay Transients for the HER at Platinum 136

IV.B.3 A.C. Impedance Behaviour 142

IV.B.3.1 A.C. Impedance Behaviour of the HER at Gold 144

IV.B.3.2 A.C. Impedance Behaviour of the HER at Nickel 152

IV.B.3.3 A.C. Impedance Behaviour of the HER at Platinum 159

IV.B.4 Conclusions on the HER Behaviour at Au, Ni and Pt at Elevated Temperatures 162

IV.C Oxygen Evolution Reaction 163

IV.C.1 Oxygen Evolution Reaction at Platinum 163

IV.C.1.1 Tafel Relations for the OER at Pt 165

IV.C.1.2 A.C. Impedance Behaviour of the OER at Pt 168

IV.C.2 Conclusions on the OER Behaviour at Pt at Elevated Temperatures 170

IV.D Electrocatalysis and Adsorption in the Anodic Oxygen Evolution Reaction at Lead Dioxide in its Dimorphic States, $\alpha$ and $\beta$-$PbO_2$ 171

IV.D.1 Review of Relevant Previous Work 172

IV.D.2 Choice of Experimental Approaches 177

IV.D.3 The Primary Current vs Potential Relations at Several Temperatures 178

IV.D.4 Potential-Relaxation Transients and Analysis of Adsorption Pseudocapacitance Behaviour 183

IV.D.5 A.C. Impedance Behaviour at Room Temperature. 189

IV.D.6 Simulation of the Frequency Response Behaviour 194

IV.D.7 Conclusions on the OER Behaviour at $\alpha$ and $\beta$-$PbO_2$ Surfaces 196

V. CLAIMS TO ORIGINAL RESEARCH 198

VI. LIST OF REFERENCES 201

## LIST OF FIGURES


| | | Page |
|---|---|---|
| Fig.1 | The effects of applied potential on potential energy of activation. | 5 |
| Fig.2 | A schematic representation of the effect of potential on the energy of activation. | 6 |
| Fig.3 | Relationship between coverage, $\Theta$, and adsorption pseudocapacitance, $C_\phi$, pro...es with respect to potential for a simple "single-state" surface process, below a monolayer, being deposited or ionized. | 22 |
| Fig.4 | Theoretical form of the cyclic voltammogram for the oxidation and reduction of an adsorbed species A on an electrode surface where adsorption follows a Langmuir isotherm. | 23 |
| Fig.5 | Electrochemical deposition and desorption of H and OH/O species at Pt in 0.5 M $H_2SO_4$ | 24 |
| Fig.6 | Cyclic voltammogram of a polycrystalline gold electrode at (a) 348 K and (b) 262 K in 5 M $H_2SO_4$. | 29 |
| Fig.7 | Schematic diagram of the steel bomb's Pyrex liner. | 43 |
| Fig.8 | Schematic diagram of the commercial, multi-lead feed-through system. | 45 |
| Fig.9 | Schematic diagram of the home-made feed-through system. | 47 |
| Fig.10 | Schematic diagram of the commercial Conax type commercial feed-through seal. | 48 |
| Fig.11 | Schematic diagram of the high-temperature/high-pressure apparatus. | 51 |
| Fig.12 | Schematic diagram of the temperature-control system. | 55 |
| Fig.13 | Circuit utilized in the cyclic voltammetry experiments. | 60 |
| Fig.14 | Three-compartment miniature Pyrex glass cell. | 65 |
| Fig.15 | One-compartment, standard size Pyrex glass cell. | 66 |
| Fig.16 | Detailed illustration of the 2-compartment Teflon cell with the membrane holder. | 68 |

| | | Page |
|---|---|---|
| **Fig.17** | Schematic diagram of the miniature Pyrex electrode. | 70 |
| **Fig.18** | Schematic diagram of the standard-size Pyrex electrode. | 70 |
| **Fig.19** | Schematic diagram of the miniature Pyrex/Teflon electrode. | 70 |
| **Fig.20** | Cyclic voltammograms for oxide film formation and reduction processes at gold in 1 N $H_2SO_4$ solutions at three temperatures: a) 297 K, b) 377 K and c) 450 K. | 93 |
| **Fig.21** | Cyclic voltammograms for the oxide film formation and reduction processes at gold in 1 N $HClO_4$ solutions at three temperatures: a) 296 K, b) 398 K and c) 473 K. | 94 |
| **Fig.22** | Cyclic voltammograms for the oxide film formation and reduction processes at platinum in 1 N $H_2SO_4$ solutions at four temperatures; a) 295 K, b) 373 K c) 478 and d) 529 K. | 95,96 |
| **Fig.23** | Plot of the hydrogen adsorption/desorption peak potentials vs temperature for Pt in 1 N $H_2SO_4$. | 97 |
| **Fig.23a** | Plot of anodic/cathodic peak potential difference, $V_a$-$V_c$, vs temperature for platinum in 1 N $H_2SO_4$. | 97 |
| **Fig.24** | Plot of cathodic peak potential vs anodic potential limits for the oxide formation and reduction processes at platinum in 1 N $H_2SO_4$ at 4 temperatures: 295 K, 373 K, 429 K and 478 K. | 100 |
| **Fig.25** | Plot of cathodic peak potential vs anodic potential limits for the oxide formation and reduction processes at gold in 1 N $H_2SO_4$ at 8 Temperatures: 297 K, 321 K, 350 K, 377 K, 402 K, 425 K, 450 K, and 476 K. | 100 |
| **Fig.26** | Plot of oxide formation/reduction peak potentials vs temperature for gold in 1 N $H_2SO_4$. | 102 |
| **Fig.27** | Plot of anodic/cathodic peak potential difference, $V_a$-$V_c$, vs temperature for gold in 1 N $HClO_4$. | 102 |
| **Fig.28** | Plots of anodic peak potential vs sweep-rate for gold in 1 N $HClO_4$ solutions at 8 temperatures: 296 K, 323 K, 348 K, 373 K, 398 K, 423 K, 448 K, and 473 K. | 106 |

Page


| | | |
|---|---|---|
| **Fig.29** | Charge balance, $Q_c/Q_a$, vs sweep-rate plots for gold in 1 N $HClO_4$ solutions at 8 temperatures: 296 K, 323 K, 348 K, 373 K, 398 K, 423 K, 448 K, and 473 K. | 106 |
| **Fig.29a** | Charge balance, $Q_c/Q_a$, vs sweep-rate plots for platinum in 1 N $H_2SO_4$ solutions at 4 temperatures: 296 K, 373 K, 438 K, 480 K. | 106a |
| **Fig.30** | Cyclic voltammograms for oxide film formation and reduction processes at gold in 0.2 N NaOH for 3 temperatures: a) 298, b) 425 and c) 473 K at a sweep rate = 0.02 V/s. | 108 |
| **Fig.30d** | Cyclic voltammogram for the oxide film formation and reduction processes at gold in 0.2 N NaOH at 425 K and at a sweep rate = 1.0 V/s. | 109 |
| **Fig.31** | Anodic and cathodic peak potentials vs sweep-rate plots for platinum at 296 K in 1 N $H_2SO_4$; $A_1$, $A_2$, $A_3$, and $C_1$ correspond to the 3 oxide formation states and 1 oxide reduction state observed in Fig.22a. | 115 |
| **Fig.32** | Tafel relations for the HER at gold in 0.2 N NaOH solutions at 8 temperatures: 1) 450 K, 2) 432 K, 3) 405 K, 4) 382 K, 5) 361 K, 6) 343 K, 7) 318 K, 8) 293 K. | 113 |
| **Fig.33** | *b*/T vs T plot for the upper and lower linear segments of the Tafel relations in Fig.32 for the HER at gold. | 115 |
| **Fig.34** | Tafel relations for the HER at 6 temperatures: 1) 450 K, 2) 432 K, 3) 408 K, 4) 384 K, 5) 360 K, 6) 347 K at nickel in 0.2 N NaOH solutions. | 117 |
| **Fig.35** | Tafel relations for the HER at platinum in 0.2 N NaOH solutions at 8 temperatures: 1) 294 K, 2) 320 K, 3) 347 K, 4) 371 K, 5) 398 K, 6) 423 K, 7) 449 K, 8) 473 K. | 119 |
| **Fig.36a** | Potential-relaxation transients taken from -0.5 V (vs Pd/PdH) initial overpotential and corresponding prior steady-state current densities of the HER at gold in 0.2 N NaOH solutions at 7 temperatures: 1) 450 K, 2) 432 K, 3) 382 K, 4) 361 K, 5) 343 K, 6) 318 K, 7) 293 K. | 125 |
| **Fig.36b** | Plots of log[-dV/dt] vs overpotential for the HER at gold in 0.2 N NaOH solutions at 7 temperatures: 1) 450 K, 2) 432 K, 3) 382 K, 4) 361 K, 5) 343 K, 6) 318 K, 7) 293 K in 0.2 N NaOH solutions. | 126 |

Page


| | | |
|---|---|---|
| **Fig.36c** | Interfacial capacitance vs potential plots derived from analysis of the potential-relaxation transients (with the respective Tafel relations in Fig.32) at gold in 0.2 N NaOH at 7 temperatures: 1) 450 K, 2) 432 K, 3) 382 K, 4) 361 K, 5) 343 K, 6) 318 K, 7) 293 K. | 127 |
| **Fig.37** | Potential-relaxation transients, as in Fig.36a, but for 3 initial overpotentials and corresponding prior steady-state current densities of the HER at gold at (a) 361 K and (b) 450 K. | 128 |
| **Fig.38a,b** | Potential-relaxation transients for 3 initial overpotentials and corresponding prior steady-state current-densities of the HER at nickel in 0.2 N NaOH at 2 temperatures: (a) 360 K and (b) 450 K. | 131 |
| **Fig.38c,d** | Interfacial capacitance vs potential plots derived from analysis of the potential-relaxation transients (with the respective Tafel relations in Fig.34) at nickel in 0.2 N NaOH at the same 2 temperatures as in Fig.38a,b, (c)360 K and (d) 450 K. | 134 |
| **Fig.39a** | Potential-relaxation transients from various initial overpotentials and corresponding prior steady-state current densities of the HER at platinum in 0.2 N NaOH solutions at 8 temperatures: 1) 294 K, 2) 320 K, 3) 347 K, 4) 371 K, 5) 398 K, 6) 423 K, 7) 449 K, 8) 473 K. | 137 |
| **Fig.39b** | Plots of log[-dV/dt] vs overpotential in the HER at platinum in 0.2 N NaOH solutions at 8 temperatures: 1) 294 K, 2) 320 K, 3) 347 K, 4) 371 K, 5) 398 K, 6) 423 K, 7) 449 K, 8) 473 K in 0.2 N NaOH solutions as in Fig.39b. | 138 |
| **Fig.39c** | Interfacial capacitance vs potential plots derived from analysis of the potential-relaxation transients (with the respective Tafel relations in Fig.35) at platinum in 0.2 N NaOH at the same 3 temperatures: (i) 294 K, (ii) 371 K, and (iii) 473 K. | 141 |
| **Fig.40a** | Complex-plane plots for the frequency response of imedance of the HER at gold in 0.2 N NaOH solutions for an overpotential of -0.5 V vs PdH at 8 temperatures: 1) 450 K, 2) 432 K, 3) 405 K, 4) 382 K, 5) 361 K, 6) 343 K, 7) 318 K, 8) 293 K. | 145 |
| **Fig.40b** | Phase-angle Bode-type plots as a function of log $\omega$ for an HER overpotential of -0.5 V vs PdH at the same 8 temperatures as for Fig.40a at gold. | 146 |

Page


| | | |
|---|---|---|
| **Fig.40c** | Log \| Z \| vs log $\omega$ plots for the same HER overpotential and temperatures as for Fig.40a for gold. | 146 |
| **Fig.41** | Simplest equivalent circuits for electrochemical surface reactions: (a) simple charge-transfer across the double-layer capacitance involving a potential-dependent Faradaic resistance $R_1$; (b) charge-transfer reaction across the double layer capacitance leading to potential dependence of coverage by a chemisorbed intermediate characterized by an adsorption capacitance, $C_\phi$ or $C_p$. $R_s$ represents the solution resistance between the working and the reference electrode. | 143 |
| **Fig.42** | 3-dimensional Bode-type plots for the HER at gold: (a) phase-angle vs log $\omega$ corresponding to the 2-dimensional plots in Fig.40b, and (b) Log \| Z \| vs log $\omega$ corresponding to the 2-D plots in Fig.40c. | 147 |
| **Fig.43** | Simulated phase-angle plots using an equivalent circuit of the type illustrated in Fig.41a for $C_{dl} = 10^{-2}$ F, $R_s = 1\ \Omega$, and four $R_1$'s 1) $10^1\ \Omega$, $10^2\ \Omega$, $10^3\ \Omega$, and $10^4\ \Omega$. Note the characteristic width at the peaks' half-height. | 150 |
| **Fig.44** | 3-dimensional Bode-type phase-angle plots for a series of overpotentials in the HER at gold at 450 K. | 150 |
| **Fig.45** | A.c.impedance plots for gold as in Fig.40a-c but at -0.1 V vs PdH: (a) complex-plane plots; (b) phase-angle vs log $\omega$ plots; and (c) log \| Z \| vs log $\omega$ plots. | 151 |
| **Fig.46a** | Complex-plane plots for the frequency response of impedance of the HER at nickel at 360 K for 5 HER overpotentials of 1) -0.5 V, 2) -0.4 V, 3) -0.3 V, 4) -0.2 V and 5) -0.12 V vs PdH. | 154 |
| **Fig.46b** | Phase-angle Bode-type plots as a function of log $\omega$ for the same series of HER overpotentials and temperature as in Fig.46a for nickel. | 155 |
| **Fig.46c** | Log \| Z \| vs log $\omega$ plots for the same HER overpotentials and temperature as in Fig.46a for nickel. | 155 |
| **Fig.47a** | Complex-plane plots for the frequency response of impedance of the HER at nickel at 450 K for 5 HER overpotentials of: 1) -0.5 V, 2) -0.4 V, 3) -0.3 V, 4) -0.2 V, and 5) -0.12 V vs PdH. | 156 |

Page


| | | |
|---|---|---|
| **Fig.47b** | Phase-angle Bode-type plots as a function of log $\omega$ for the same series of HER overpotentials and temperature as in Fig.47a for nickel. | 157 |
| **Fig.47c** | Log $\lvert Z \rvert$ vs log $\omega$ plots for the same HER overpotentials and temperature as in Fig.47a for nickel. | 157 |
| **Fig.48a** | Complex-plane plots for the frequency response of impedance of the HER at platinum at 294 K for 5 HER overpotentials of: 1) -0.5 V, 2) -0.4 V, 3) -0.3 V, 4) -0.2 V, and 5) -0.10 V vs PdH. | 160 |
| **Fig.48b** | Phase-angle Bode-type plots as a function of log $\omega$ for the same series of HER overpotentials and temperature as in Fig.48a for platinum. | 161 |
| **Fig.48c** | Log $\lvert Z \rvert$ vs log $\omega$ plots for the same HER overpotentials and temperature as in Fig.48a for platinum. | 161 |
| **Fig.49** | Tafel relations for the OER at platinum in 0.2 N NaOH solutions at 8 temperatures: 1) 476 K, 2) 449 K, 3) 423 K, 4) 399 K, 5) 370 K, 6) 349 K, 7) 325 K and 8) 301 K. | 166 |
| **Fig.50** | Phase-angle Bode-type plots as a function of log $\omega$ for a series of low and high overpotentials in the OER at 3 temperatures: (a) 476 K, (b) 399 K, and (c) 301 K for platinum in 0.2 N NaOH. | 169 |
| **Fig.51** | Tafel relations for the OER at (a) $\alpha$-$PbO_2$ and (b) $\beta$-$PbO_2$ at 5 temperatures: 1) 299 K, 2) 309 K, 3) 319 K, 4) 329 K, 5) 339 K. | 179 |
| **Fig.52** | Scanning electron micrographs of (a) $\alpha$-$PbO_2$ prior to polarization measurements, (b) after such experiments, and (c) and (d) corresponding photos for $\beta$-$PbO_2$. Note differences of morphologies. | 181,182 |
| **Fig.53** | Potential-relaxation transients for 3 initial overpotentials and corresponding prior steady-state current-densities of the OER at (a) $\alpha$-$PbO_2$ and (b) $\beta$-$PbO_2$ at 299 K. | 184 |
| **Fig.54** | Potential-relaxation transients, as in Fig.53, but at 3 temperatures: (1) 299, (2) 319 and (3) 339 K for (a) $\alpha$-$PbO_2$ and (b) $\beta$-$PbO_2$. | 185 |
| **Fig.55** | Plots of Log[-dV/dt] vs overpotential in the OER at (a) $\alpha$-$PbO_2$ and (b) $\beta$-$PbO_2$ at (1) 299, (2) 319 and (3) 339 K. | 186 |

Page


| | | |
|---|---|---|
| **Fig.56** | Interfacial capacitance vs potential plots derived from analysis of the potential-relaxation transients (with the respective Tafel relations) at (a) $\alpha$-$PbO_2$ and (b) $\beta$-$PbO_2$ at (1) 299, (2) 319 and (3) 339 K. | 188 |
| **Fig.57** | Complex-plane plots for the frequency response of impedance of the OER at (a),(c) $\alpha$-$PbO_2$ and (b),(d) $\beta$-$PbO_2$ at 299 K for OER potentials of 1.80 and 2.20 V, respectively ( vs RHE ). | 190 |
| **Fig.58** | Phase-angle Bode-type plots as a function of log $\omega$ for a series of overpotentials in the OER: (a) for $\alpha$-$PbO_2$; (b) for $\beta$-$PbO_2$, both at 299 K. | 192 |
| **Fig.59** | Evaluation of the pseudocapacitance arising in the OER at $\alpha$-$PbO_2$ (299 K) for the impedance analysis as a function of overpotential in the OER. | 195 |
| **Fig.60** | Evaluation of the charge-transfer resistance, $R_{ct}$, arising in the OER at $\alpha$-$PbO_2$ (299 K) as a function of overpotential, derived from the analysis of the impedance behaviour. (Note equivalence of the $R_{ct}^{-1}$ plot to Tafel polarization behaviour, as expected.) | 195 |
| **Fig.61a** | Powder X-ray diffraction pattern of $\alpha$-$PbO_2$ deposit after it had been stripped from the Pt wire substrate. | 81 |
| **Fig.61b** | Powder X-ray diffraction pattern of $\beta$-$PbO_2$ deposit after it had been stripped from the Pt wire substrate as in Fig.61a for the $\alpha$ deposit. | 82 |
| **Fig.62** | Illustration of how the structural differences between (a) $\alpha$- and (b) $\beta$-$PbO_2$ arise principally from the different arrangements of "$PbO_2$" hexa-coordinate units. | 173a,b |

## LIST OF TABLES


| | | Page |
|---|---|---|
| Table I. | Tafel slopes and exchange current densities recorded for various temperatures between 293 and 450 K for the HER at gold in 0.2 N NaOH solutions | 114 |
| Table II | Tafel slopes and exchange current densities recorded for various temperatures between 346 and 450 K for the HER at nickel in 0.2 N NaOH solutions | 118 |
| Table III | Estimated values of the double-layer and pseudocapacitance derived from the potential-decay experiments for gold in 0.2 N NaOH solutions between 293 and 450 K | 130 |
| Table IV | Estimated values of the double-layer capacitance and pseudocapacitance derived from the potential-decay experiments for Ni in 0.2 N NaOH solutions between 346 and 450 K | 135 |
| Table V | Estimated values of the double-layer and pseudocapacitance derived from the potential-decay experiments for Pt in 0.2 N NaOH solutions between 294 and 473 K | 140 |
| Table VI | Comparison between estimated values of the $C_{dl}$ for the HER at gold in 0.2 N NaOH derived from impedance spectroscopy and the potential-decay method for several temperatures | 149 |
| Table VII | Estimated $C_{dl}$ for nickel in 0.2 N NaOH solutions between 294 and 450 K | 158 |
| Table VIII | Comparison of the estimated $C_{dl}$ values obtained by the a.c. impedance and the potential-decay experiments | 162 |
| Table XI | Tafel slopes observed for the OER at Pt in 0.2 N NaOH at several temperatures | 168 |

## I. GENERAL INTRODUCTION

In recent years, there has been increasing interest in investigations on the chemical thermodynamics and kinetics of electrochemical processes at temperatures well displaced from room temperature. Such experiments provide important information and a better understanding of the mechanisms of the processes involved, especially: a) how Tafel slopes, $b$, and the corresponding barrier symmetry factor ($\beta$) depend on temperature and b) how the highly irreversible processes of surface oxidation of noble and semi-noble metals can be made to become substantially more reversible at high temperatures.

In the opposite direction of low temperatures, work has been carried out in order to try to identify the role of proton tunneling in electrochemical proton transfer in the cathodic $H_2$ evolution mechanism [40-44] and also how $b$ depends on temperature well below 273 K.

Thus, there have been a number of significant investigations [1-7] of electrochemical processes at the lower end of the temperature scale from room temperature down to as low as 183 K by Conway and Salomon [3,4] and Conway, MacKinnon and Tilak [2],and even lower in frozen $HClO_4.5H_2O$ electrolyte in works by Stimming [8]. However, due to technical difficulties relating to the conduct of experiments at temperatures well *above* room temperature and the normal boiling point of water, much less work has been done at such elevated temperatures at which most aqueous electrolytes will boil at atmospheric pressure. It is therefore important to extend the upper temperature limit in order to get a broader view of the processes being examined and how they may depend on the structure of the electrolyte fluid, including where possible up to and through

the critical point [9,10].

Also, there is considerable interest in the field of high-temperature electrochemistry with many practical applications closely related to operation of power generation plants, the chemical process industries as well as de-salination plants where knowledge of the mechanisms of aqueous corrosion of steel and other metals at elevated temperatures is important.

## I.A.1 Temperature Effects in Electrode Kinetics

The rates of chemical reactions depend on various factors such as concentration, pressure and temperature. However, the rates of electrode reactions, in addition to the above factors, are also *potential dependent* when a charge-transfer step in the process is rate-determining.

Conventionally, the rate of electrode reactions is represented by the empirical Tafel relation:

$$\eta = a + b \ln i \qquad (1)$$

where $a$ and $b$ are constants, $\eta$ is the overpotential defined as the difference between the applied potential and the reversible potential of the reaction involved. The net current I in A or the corresponding current-density $i$ in A $cm^{-2}$ can be conveniently represented by the difference of the current-densities of the forward and backward reactions at a given electrode potential:

$$i = \vec{i} - \overleftarrow{i} \qquad (2)$$

As the net current is equal to zero at the reversible potential ($\eta = 0$), a rather

important parameter in electrode kinetics is obtained: the exchange current density, $i_o$, *viz*,

$$i_o = \vec{i} = \overleftarrow{i} \qquad (3)$$

Therefore, Eq.(1) can be rewritten in terms of $i_o$ in an exponential form as

$$i = i_o \exp ( \eta / b ) \qquad (4)$$

where the parameter $b$ is the so-called " Tafel slope" $d\eta$ / d ln $i$ and is represented empirically by the factor RT/F or a multiple or fraction of it. The effect of temperature on electrode kinetics is therefore usually assumed to arise through the decrease of ln $i$ with $T^{-1}$, as in the kinetics of regular chemical processes involving an enthalpy or energy of activation, as in the Arrhenius equation. Correspondingly, $\eta$ decreases linearly with T for a given constant ln $i$ value on account of the "$b$" term in eqn. (4).

The first general theoretical treatment of the rate of an electrochemical reaction involving a single electron transfer process was given, independently, by Volmer [11] and by Butler [12] in terms of the forward and backward components ( Eq.(2) ) of the net current density, *viz*.

$$i = i_o \left\{ \exp (\alpha\eta F/RT) - \exp [-(1-\alpha)\eta F/RT] \right\} \qquad (5)$$

The above equation, at appreciable net current $i$, becomes simplified into a form of Tafel equation with the Tafel slope $b = RT/\alpha F$ where $\alpha$ is termed the charge-transfer coefficient. Shortly after Volmer and Butler published their papers, Glasstone, Laidler and Eyring [13] applied their transition-state rate theory (TST) to a treatment of the rates of electrode reactions. For a chemical reaction, according to the TST, the rate constant k can be represented by the following equation:

$$k = (\kappa\, kT/h) \exp ( - \Delta G^{o\ddagger}/RT ) \qquad (6)$$

where $\kappa$ is a constant related to the percentage of activated complexes which pass over the barrier and is usually taken as unity. $\Delta G^{o\ddagger}$ is the chemical standard Gibb's energy of activation and all other symbols have their usual meanings. For electrode reactions, an electrochemical Gibb's energy of activation, $\Delta\overline{G}^{o\ddagger}$ is used. The relation between $\Delta\overline{G}^{o\ddagger}$ and its chemical counterpart is as follows:

$$\Delta\overline{G}^{o\ddagger} = \Delta G^{o\ddagger} \pm \beta\eta F \qquad (7)$$

where $\eta$ is the overpotential, F the Faraday constant and $\beta$, a barrier symmetry factor, is analogous to a Brønsted coefficient and identical with the charge transfer coefficient $\alpha$ (Eq.5) for simple one-electron transfer reactions; formally it can have a value between 0 and 1, but usually it is near 0.5, i.e., when the energy barrier is approximately symmetrical. It has been found that for a number of simple electron-transfer processes, e.g. as in the hydrogen evolution reaction (HER) on Hg, $\beta$ is approximately equal to 0.5 at room temperature over a wide range of potentials.

The effect of potential on $\Delta\overline{G}^{o\ddagger}$ can be represented in a well-known way in Figure 1 in terms of an energy barrier diagram.

In this Figure, it is assumed that the effect of potential is entirely on the work function, $\Phi$, of the metal, i.e., on the energy state of electrons involved in the process:

$$\Phi_{(\eta)} = \Phi_{(\eta=0)} \pm e\eta \qquad (8)$$

Therefore the effect of potential on the potential energy profile of the reactants and products (Fig.1) would be a vertical shift without any change in their shapes, corresponding to $\beta$ being a constant. If the potential energy curves cross symmetrically

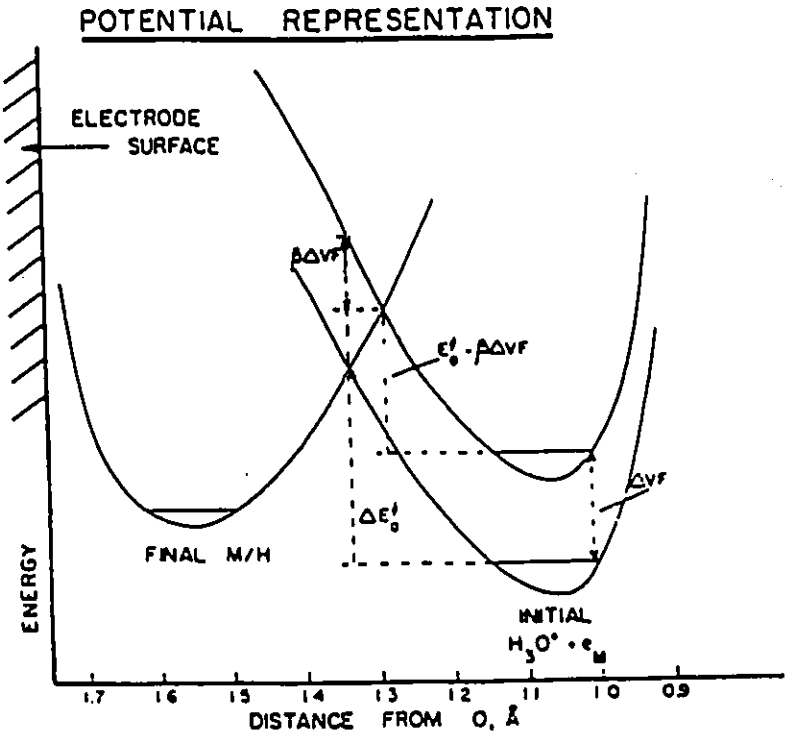


**Fig.1** The effects of applied potential on potential energy of activation. ( From Ref. 41 )

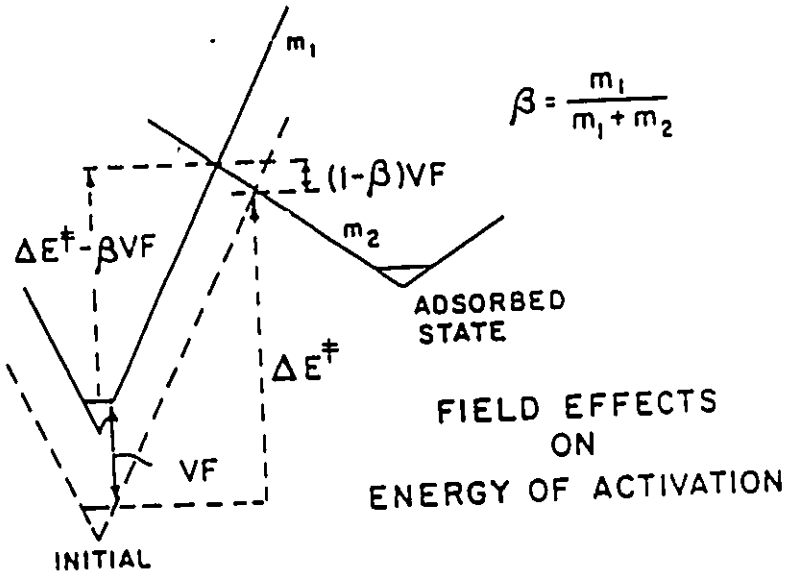


**Fig.2** A schematic representation of the effect of potential on the energy of activation. Note that when the potential energy curves cross symmetrically, i.e. $m_1 = m_2$, then $\beta = 0.5$. ( From Ref. 41 )

( Fig.(2) ), then $\beta = 1/2$.

Substituting Eq.(7) into Eq.(6), one obtains

$$k = (\kappa\, kT/h) \exp [-(\Delta G^{o\ddagger} - \beta\eta F)/RT ] \qquad (9)$$

In electrode reactions, the rate of reaction per $cm^2$ of electrode surface can be expressed directly in terms of equivalent current-density $i$ if the current efficiency for the given process is at or near 100 %. If there are zF coulombs required per mole of products formed on 1 $cm^2$ of electrode surface and the electrochemical rate is $v$ moles $cm^{-2}$, then $i = zFv$. When the surface concentration c of reactant ions at the interphase[1] and the coverage $\theta$ of intermediates of products on the surface is taken into account, Eq.(9) can be rewritten as

$$i = (\kappa\, kT/h) \exp (-\Delta G^{o\ddagger}/RT) \exp (-\beta\eta F/RT ) zF\, c\, (1-\theta) \qquad (10)$$

Again, Eq.(10) takes the form of a Tafel relation with

$$i_o = (\kappa\, kT/h) \exp ( -\Delta G^{o\ddagger}/RT ) zF\, c\, (1-\theta) \qquad (11)$$

giving a Tafel slope, $b = RT/\beta F$. It is to be noted that according to this treatment, $b$ is also a linear function of temperature, as commonly assumed.

In all the rate equations presented above, there is one term that is common; the exponential term involving 1/T. According to Arrhenius, for ordinary chemical reactions, the majority of collisions between the reactant molecules are not energetic enough to produce products. However, there is a small fraction of the collisions for which, according to the Boltzmann distribution principle, energy is in excess of a particular value

---

[1]In a fuller treatment, the local concentration of reactant ions in the interphase has to be expressed in terms of its double-layer structure and potential-profile across the double-layer. Correspondingly, the $\eta$ factor has to take into account the latter factor.

$E^{\ddagger}$, i.e. with a probability $\exp(-E^{\ddagger}/RT)$ . This fraction becomes larger as temperature increases. The rate of reaction, either chemical and electrochemical, should therefore be exponentially related to reciprocal temperature.

The rates of electrode reactions could, in principle, be predicted at temperatures beyond the accessible ranges if the apparent thermodynamic parameters such as $\Delta\overline{H}_a^{\ddagger}$, $\Delta\overline{S}_a^{\ddagger}$, $\Delta\overline{G}_a^{\ddagger}$ etc. could be evaluated. In fact, electrochemistry provides one of the most accurate procedures for the evaluation of these parameters (for electrochemical reactions) as voltage can be measured and controlled to better than a millivolt with high precision and currents can also be measured, now digitally, with great accuracy and down to very low values, $\mu$A and nA.

From general electrochemical thermodynamics, one can write

$$\Delta\overline{S} = zF( \partial V/\partial T )_p \qquad (12)$$

and $$\Delta\overline{H} = zF[ V - T( \partial V/\partial T )_p ] \qquad (13)$$

for a z-electron process associated with a potential V.

However in practice there are some formal difficulties associated with the use of above parameters. The reason is that in electrochemistry, potential must be measured with reference to some reversible electrode in the system. As temperature is varied, the metal-solution potential difference at the reversible reference electrode also varies. In the case of the standard hydrogen electrode (SHE), its potential is arbitrarily set to be "zero" at all temperatures. Hence, electrode potentials may be compared formally over a wide range of temperatures. This does <u>not</u> mean, however, that the SHE (or other electrode potentials) has no real finite temperature coefficient. In fact, it can be estimated fairly

reliably from single-ion entropies [59], as noted below.

Theoretically, the temperature coefficient of the metal-solution potential difference at the hydrogen reference electrode may be calculated from the standard entropy of the half-cell reaction:

$$H_2O + e \rightharpoonup \tfrac{1}{2} H_2 + OH^- \quad \text{in alkaline solution} \qquad (14)$$

or $$H_3O^+ + e \rightharpoonup \tfrac{1}{2} H_2 + H_2O \quad \text{in acid media} \qquad (15)$$

provided that data on the temperature dependence of the surface potential $\Delta\chi$ at the $Pt/H_2$ - water interphase is known or could be estimated.

The thermodynamic parameters for activation, obtained experimentally, are therefore "apparent" and cannot be used in treating rates of electrode reactions in the same way as may be done for most other chemical reactions.

Although the thermodynamic parameters obtained experimentally cannot be easily related to the mechanism of the reaction, meaningful comparison of some electrode-kinetic parameters such as the Tafel slope $b$ and the corresponding $\beta$ over a range of temperatures for a given reaction conducted at different metals is very informative; correspondingly, *differences* of the apparent thermodynamic parameters, $\Delta H_a^{\ddagger}$ and $\Delta S_a^{\ddagger}$, for a given reaction at various metals can provide meaningful information on electrocatalysis of the process involved. Note that the slopes of Tafel lines are independent of any changes of scale of potentials resulting from a change in the reference electrode potential as temperature is varied.

## I.A.2 Problems Requiring Clarification

With the exception of the HER at Hg from acid solutions at room temperature, most experimental electrode-kinetic information has shown that the classical relationship representing the Tafel slope $b$ as $b = 2.3RT/\beta F$ is not actually followed. This unconventional temperature dependence of $b$ has been empirically represented as a temperature dependence of the barrier symmetry factor $\beta$ which is interpreted as arising from a potential dependence of $\Delta\overline{S}_a^{\ddagger}$ as was first suggested by Agar [14]. In this approach, not only the $\Delta\overline{H}_a^{\ddagger}$ of activation but the $\Delta\overline{S}_a^{\ddagger}$ of activation are assumed to be a linear function of potential. The basis of the assumption is that the rate of the electrochemical process, e.g. as in Eq. (15), is given logarithmically as

$$\ln i = \kappa - \Delta\overline{G}_a^{\ddagger}/RT \tag{16}$$

where $\kappa$ includes various constants and concentration and $\Delta\overline{G}_a^{\ddagger}$ represents the electrochemical Gibbs energy of activation including the effect of electrode-solution potential difference V, or $\eta$ in terms of overpotential.

The inverse Tafel slope $b^{-1}$ is formally given by

$$d\eta / d\ln i = d(-\Delta\overline{G}_a^{\ddagger})/ F.d\eta \tag{17}$$

$$= d(-\Delta H_a^{\ddagger})/F.d\eta + T\, d(\Delta S_a^{\ddagger})/F.d\eta \tag{18}$$

Conventionally, it is the variation of $\Delta\overline{H}_a^{\ddagger}$ with $\eta$ F that provides the definition of $\beta$, expressed integrally as

$$\Delta H_{a,\eta}^{\ddagger} = \Delta H_{a,\eta=0}^{\ddagger} \pm \beta\eta F \tag{19}$$

or in terms of $\Delta G_a^{\ddagger}$ (conventionally)

$$\Delta G_{a,\eta}^{\ddagger} = \Delta G_{a,\eta=0}^{\ddagger} \pm \beta\eta F \tag{20}$$

neglecting the possibility of $\Delta S_a^{\ddagger}$ being $f(\eta)$.

Eq. (18) represents the possibility, formally required, that $\Delta G_a^{\ddagger}$ can vary with the $\eta$ not only because of a dependence of $\Delta H_a^{\ddagger}$ on $\eta$ through the Fermi level change (see Eq. (8) ), but *also* because the $\Delta S_a^{\ddagger}$ in $\Delta G_a^{\ddagger}$ could be $f(\eta)$. Thus

$$\Delta \overline{G}_a^{\ddagger} = \Delta \overline{H}_a^{\ddagger} - T\Delta \overline{S}_a^{\ddagger} \tag{21}$$

$$\Delta \overline{S}_a^{\ddagger} = \Delta S_a^{\ddagger} \pm \beta_S \eta F \tag{22}$$

and

$$\Delta \overline{H}_a^{\ddagger} = \Delta H_a^{\ddagger} \pm \beta_H \eta F \tag{23}$$

serve to define entropic ($\beta_S$) and enthalpic ($\beta_H$) components of $\beta$,

i.e.

$$\Delta \overline{G}_a^{\ddagger} = \Delta G_a^{\ddagger} \pm (\beta_H - T\beta_S)F \tag{24}$$

It follows from Eq.(9) that the Tafel slope is then represented in a more general way by the relation

$$b = RT/(\beta_H - T\beta_S)F \tag{25}$$

rather than by $b = RT/\beta F$ with $\beta$ a constant.

Theoretically, all experimentally observed "anomalous" temperature dependences of the Tafel slope could formally be accounted for in terms of this revised representation of $b$.

The effect of potential on the entropy of activation of the reaction is believed to arise from the effects of potential on reagents ( ions, molecules etc. ) outside the metal, in the double-layer region of the metal/solution interphase. Conway *et al.* [15] suggested

that this effect of potential on $\Delta S_a^{\ddagger}$ could originate from the change of states of solvent molecules oriented in the Helmholtz inner region of the double-layer; i.e. the potential might influence the orientation of the dipoles of the solvent molecules and therefore their entropy. This, in turn, could influence the entropy of reacting solvated ions in the environment of the oriented solvent dipoles in the reaction interphase in the double-layer and thus also affect the entropy of the transition state in ion discharge.

In some extreme abnormal cases, such as the anodic bromine evolution reaction at the mercury electrode, the Tafel slopes are seemingly independent of temperature as is also the case for the reduction of oxygen in $H_3PO_4$ [7]. In order to account for this type of experimental observation, one must formally assume that the effect of potential is entirely on $\Delta S_a^{\ddagger}$, i.e. that $\beta_H$ is close to zero. As potential will almost always have an effect on $\Delta H_a^{\ddagger}$ through the effect of potential on the work function of the metal ( Eq.(8) ), this is one aspect of the approach that is rather difficult to explain. In a recent paper by Gileadi [16], the physical significance of the parameter $\beta_S$ is questioned. The author suggested that the potential dependence of the entropy of activation be re-defined as follows:

$$\Delta\overline{S}_a^{\ddagger} = \Delta S_a^{\ddagger} - (\beta_S'/T)\eta F \qquad (26)$$

so that $$b = RT/(\beta_H - \beta_S')F \qquad (27)$$

This assumption that it is only $\beta_S/T$ that varies reciprocally with temperature however, does not explain many of the experimentally observed dependences of $b$ on temperature. Thus, the representation given by Gileadi gives $b$ always a simple and direct linear function of T (the classical or conventional behaviour) (contrast Eq. (25) ) that is, in fact, commonly not observed.

The question whether the Tafel slope is a direct first-power or a more complex function of temperature is a central point in the understanding of the effect of electrode potential on reaction rates at charged metal or semiconductor interfaces. In so far as a temperature dependence of $\beta$ and thus a non-conventional temperature dependence of $b$ can be formally associated [15] with a potential dependence of the entropy of activation, a major departure from the usual representation of the origin of the Tafel equation is involved; that is that changes of electrode potential, i.e. of the Fermi level, influence not only the energy of activation but also the entropy of activation. In certain but rare cases, to be quoted below, it seems, at least formally, that the effect of potential can be almost wholly on the entropy of activation rather than the enthalpy when $b$ is independent of T.

In recent work that has been done on this question [22] care has been taken to focus attention on the kinetics of these processes the rates of which are determined only by a simple ion discharge step, preferably one not complicated by anion or other adsorption effects (that could introduce spurious temperature-dependent effects) involving significant chemisorption of an intermediate, nor any process that occurs at an oxide film, the properties of which are usually temperature dependent.

Surprisingly, the reduction of $NH_2OH$ at Hg, recently studied by Gileadi *et al.* [19], gives quite normal behaviour with $b$ having the conventional dependence on T with $b$ constant, near 0.5. The reaction, however, must be complex involving at least one intermediate, as 2 electrons and proton-transfer steps must be involved in generating the final product, $NH_3$:

$$NH_2OH + 2\,e + 2\,H^+ \rightarrow NH_3 + H_2O \qquad (28)$$

In acidic medium, the reactant is presumably $N^+H_3OH$. The first electron transfer may then be to the N producing $NH_3$ + the $OH\cdot$ radical. The mechanism of this reaction is not well understood.

Alternatively, a first electron transfer could form $N\cdot H_3OH$ which could dissociate to the radical $N\cdot H_2$ + $H_2O$. Further electron and proton transfer to $N\cdot H_2$ (adsorbed ?) would then lead again to the final product, $NH_3$. From the known chemistry of Hg, $N\cdot H_2$ would be expected to have an affinity for the Hg surface.

It must be mentioned that a detailed review of work and ideas on the temperature dependence of the Tafel slope and the corresponding symmetry factor $\beta$ has been given by Conway in an attempt to establish the real form of the Tafel equation [26].

## I.A.3 Previous Experimental Studies of *b* as a Function of Temperature

Weaver [17,18] has measured the temperature dependence of the Tafel slope of some outer sphere ionic redox couples and reported that the behaviour of $b$ as a function of temperature follows the conventional prediction. This is, in fact, one of the few examples of conventional behaviour of $b$ on temperature actually observed. However, several of the $\beta$ values for various aquo-Cr(III) complexes were near 0.8 rather than 0.5, an unexpected and unexplained result, especially as these redox reactions are essentially "symmetrical" , unlike the situation with proton discharge for which $\beta \approx 0.5$ but the process itself is "unsymmetrical".

One of the earliest reported cases of the *un*conventional temperature dependence of $b$ was for the discharge of azide ion on platinum by Stout [20]:

$$2\ N_3^{\cdot} \rightarrow 3\ N_2 + 2\ e \qquad (29)$$

The mechanism of this reaction has not yet been at all well characterized but it is known that the $N_3^{\cdot}$ discharge takes place on an oxidized surface of the Pt anode [45]. The interpretation of these data is therefore obscured by the possible temperature dependence of the oxide film growth and properties, etc. as in studies of temperature dependence of *b* for the oxygen evolution reaction (OER) in aq. $H_2SO_4$ at platinum [21].

Among the metals examined in studies of the temperature dependence of *b*, mercury has received the most attention as the mechanism of, say, the HER at mercury has been extensively studied and is usually devoid of complications from specific adsorption of ions such as $Cl^-$, $ClO_4^-$, $SO_4^{2-}$ in dilute acid solutions or from effects on adsorbed H coverage since that is very small ( < 0.1 % ) and the reaction rate is known to be determined only by the initial charge-transfer step involving $H^+$. Most importantly, the major advantage of studying mercury and the temperature dependence of its *b* values is that the potential dependence of coverage by the adsorbed intermediate H in the case of HER, is minimal. It would be rather difficult to interpret the effect of temperature on *b* if the Tafel slope were determined not only by the symmetry factor $\beta$ of the rate-determining charge transfer step but also by the potential dependence of coverage by the adsorbed intermediate, H, as in the case for the HER at transition metals [2].

From most experimental data on the HER at mercury, it was found that both above and well below *ca.* 280 K, the conventional temperature dependence of *b* is *not* followed and $\beta$ seems to be a function of temperature. It is evidently quite a coincidence that *b* = 0.116 V at room temperature (298 K) for the HER at Hg, for which value $\beta$ would be

equal to 0.5 when calculated directly from the classical representation of $b$ as $RT/\beta F$. However, it was found that the data could also be fitted [2] to the following empirical equation with a temperature independent term, K = *ca.* 40 mV:

$$b = RT/\beta F = RT/\beta' F + K \qquad (30)$$

In order to estimate the true "$\beta$" written as $\beta'$ in Eq.(30), it is necessary to take the derivative of $b$ with respect to temperature from a series of Tafel lines obtained at several different temperatures [26], i.e.

$db/dT = R/\beta' F$ with $\beta'$ being found to be *ca.* 0.4 at Hg.

It appears that $\beta'$ is quite constant over a wide range of temperatures down from 280 K to 173 K in methanolic and ethanolic HCl solutions [2-4].

Later, Conway *et al.* [15,22] proposed a different and more general way of treating the results as a function of temperature, on the basis of Eqs. (22), (23) and (24), giving the supposed enthalpic ($\beta_H$) and entropic ($T\beta_S$) components of the overall charge transfer symmetry factor $\beta$ for the HER at mercury. They applied this approach to analysis of results for various proton donors such as oxonium, ammonium and proton donors at Hg over a wide range of temperatures, using Eq. (25) as a basis for treatment of their results. Linear relations were obtained when $\beta_S$ was plotted against the logarithm of the electrochemical Arrhenius factor containing the entropy of activation and also between $\beta_H$ and determined $\Delta H_a^{\ddagger}$ values.

Another frequently studied metal is nickel as it is widely used in various applied electrochemistry technologies. Conway *et al.* [2] studied the HER at nickel in methanolic HCl over a wide range of temperature ( from room down to low temperatures, *ca.* 183 K).

Again the Tafel lines obtained did not follow the conventionally assumed temperature dependence of $b$ and showed, in fact, two linear regions. These two Tafel segments interestingly showed *opposite* dependences of their $b$ values on temperature. It was also found that the distinction between the two Tafel regions could be made to disappear when methanolic $HClO_4$ solutions, made up from $HClO_4$-70% aqueous acid instead of anhydrous HCl acid, was used, indicating that the unusual two Tafel regions observed from methanolic HCl might be due to $Cl^-$ adsorption.

Bockris *et al.* [23] reviewed the facts concerning the variation of $\beta$ with temperature and put a series of models forward to explain the phenomena by considering a) double-layer changes with temperature and b) electrode kinetic effects. For instance, in the case of aqueous electrolytes, as temperature increased, it was supposed that the concentration of H-bonded solvent aggregates (e.g. water dimers) decreases. Hence, the effective thickness of the double-layer would increase and this would affect the symmetry of the barrier and therefore the symmetry factor. Variation of temperature may also have an effect on the symmetry factor via the variation of the local reagent concentration in the double-layer and also an effect on the diffuse-layer potential, $\psi_1$.

A detailed investigation of the influence of the $\psi_1$-potential on the kinetics of the HER at a mercury electrode and its role on the temperature dependence of the Tafel slope $b$ was given by Tsionskii *et al.* [24]. According to these authors, the equation for the logarithm of the rate of a single-electron transfer process may be written as:

$$\ln i = \ln A + (1 - \alpha).\ln c - E_s^{\ddagger}/RT + \alpha F\eta/RT - (n - \alpha)F\psi_1/RT \qquad (31)$$

where $A$ is the pre-exponential factor, n and $\alpha$ are the charge and the charge transfer coefficient, respectively, c the concentration of electroactive species on the surface of the electrode, and $E_a^{o\ddagger}$ the activation energy at equilibrium, i.e. for $\eta = 0$; these quantities were assumed to be temperature and potential independent. Thus, by differentiating Eq. (31) with respect to overpotential, the reciprocal of the Tafel slope is obtained as follows:

$$( d \ln i /d\eta )_T = \{ [ 1 - ( d\psi_1/d\eta )_T.( n - \alpha )/\alpha ].\alpha \} F/RT \qquad (32)$$

where the term in parentheses is referred to as the apparent transfer coefficient, $\alpha_\eta$. The effect of temperature on the experimentally observed apparent charge transfer coefficient could be estimated if the dependence of $( d\psi_1/d\eta )_T$ on temperature is known; it can usually be calculated from diffuse double-layer theory [123,124].

## I.B.1 Monolayer Thick Oxide Formation and Reduction on Noble Metals

In recent years, there has been much interest in studies of surface processes on noble metals. Potentiodynamic sweep experiments or cyclic voltammetry has been shown to be one of the best techniques for obtaining detailed information on the thermodynamic states and kinetic behaviour of chemisorbed species at metal/solution interfaces. A detailed review on the electrochemical study of multiple-state adsorption in monolayers by cyclic voltammetry was given by Conway and Angerstein-Kozlowska [27]. This technique has been employed in high temperature experiments such as those described by Crooks and Bard [25] in their studies of the reductions of some aza-aromatic compounds at the critical condition of ammonia (423 K).

This technique was derived from early potential-sweep experiments by Sevcik [125]

in which electrode potential was modulated in a single or repetitive sweep, linearly in time ( dV/dt = constant). The resultant current is usually plotted as a function of potential in a form of i/V profiles or repetitively as cyclic voltammograms. The i/V profiles of electrochemical surface processes provide sensitive measurements of a) surface coverage as a function of potential; b) the adsorption pseudocapacitance of the ad-species associated with the potential dependence of their coverage; c) free energies of several species adsorbed in distinguishable surface states, with high precision; c) behaviour of multiple states of electrosorbed species below monolayer coverage; d) distinction between reversible and irreversible surface processes and so on.

In order to understand how cyclic voltammetry is used to provide information in electrochemical surface studies, it will be useful to consider the basis of the method with a simplest case of deposition or desorption of a species A on a metal M as an example:

$$\underset{1-\theta_A}{M} + \underset{C_A\pm}{A^{\pm}} \rightleftharpoons \underset{\theta_A}{M.A_{ad}} \mp e \qquad (33)$$

The electrode potential at time $t$, V during a sweep experiment is given by

$$V_t = V_i \pm s\,t$$

where $V_i$ is the initial potential and $s$ is the sweep-rate ( dV/dt ). The kinetic equations for the forward and backward reactions in the above equation can be written as

$$\vec{i}_t = q_1 k_1 C_{A\pm} (1 - \theta_A) \exp[\, \pm\beta\eta F/RT \,] \qquad (34)$$

$$\overleftarrow{i}_t = q_1 k_{-1} \theta_A \exp[\, \pm(1 - \beta)\eta F/RT \,] \qquad (35)$$

The net current $i$ passing at time $t$ per $cm^2$ of electrode material M is then written as

$$i = q_1.d\theta_A/dt = \overline{i}_i - \overline{i}_{-i} \qquad (36)$$

$$= i_i = q_1 k_i C_{A\pm} (1 - \theta_A)\exp[\pm\beta\eta F/RT] - q_1 k_{-1}\theta_A \exp[\pm(1 - \beta)\eta F/RT] \qquad (37)$$

where $q_1$ is the charge required for the formation or removal of a monolayer of A on M (i.e. $\theta = 1$). When the coverage $\theta_A$ is small, as the potential V is increased, the net current $i$ at first increases exponentially with potential until it peaks at or around $\theta_A \approx 0.5$ and then decreases exponentially as $\theta_A$ approaches 1. Because a surface process is limited by the surface area available, the current $i$ cannot be observed continuously in a steady-state experiment so that a non-steady state condition arises over the coverage range $\theta_A$ between 0 and 1.

The coverage $\theta_A$ can be expressed as a function of potential in the form of an electrosorption isotherm by equating the forward and backward currents from the rate equation above. That is

$$q_1 k_i C_{A\pm} (1 - \theta_A)\exp[\pm\beta\eta F/RT] = q_1 k_{-1}\theta_A \exp[\pm(1 - \beta)\eta F/RT]$$

$$\theta_A/1 - \theta_A = K\, C_{A\pm} \exp(-\eta F/RT) \qquad (38)$$

or $$\theta_A = K\, C_{A\pm} \exp(-\eta F/RT)/ [1 + K\, C_{A\pm} \exp(-\eta F/RT)] \qquad (39)$$

where $K = k_i / k_{-1}$.

When the above equation is differentiated with respect to V, one obtains:

$$d\theta_A/dV = F/RT.\ K\, C_{A\pm} \exp(-\eta F/RT)/ [1 + K\, C_{A\pm} \exp(-\eta F/RT)]^2 \qquad (40)$$

$$= C_\phi / q_1$$

and

$$C_\phi = q_1 F/RT.\ K\ C_{A\pm} \exp(-\eta F/RT)/ [1 + K\ C_{A\pm} \exp(-\eta F/RT)]^2 \qquad (41)$$

where $C_\phi$ has the essential quality of a capacitance and is referred to as the "pseudo-capacitance" to be distinguished from the electrostatic double-layer capacitance, $C_{dl}$ which arises at all electrode interfaces. Usually, $C_\phi$ is much larger than $C_{dl}$ for $0.1 < \theta_A < 0.9$. Figure 3 shows graphically the relationship between $\theta_A$ and $C_\phi$ with respect to electrode potential. Note that a single peak with its maximum at $\theta_A \approx 0.5$ arises when the adsorption process is under Langmuir conditions, i.e. when lateral interactions expressed in terms of a parameter g are absent ( $g = 0$ ). The height of the peaks decreases when $g > 0$ and becomes narrowed when $g < 0$ ( attractive interactions ). The parameter g measures any changes of energy of adsorption that may arise with coverage in $\Delta G_{ads}$. When $g = 0$, there are no repulsive nor attractive lateral interactions among adsorbate species. When lateral repulsive interactions are significant, $g > 0$; if attractive interactions are involved, $g < 0$.

For a reversible "single state" electron transfer reaction, a cyclic voltammogram similar to that shown in Figure 4 will be obtained.

One of the striking features of cyclic voltammetry is that it enables the sensitive observation of multiple states of adsorption and desorption of a species to be made below the level of monolayer coverage, e.g. for the case of underpotential deposition (UPD) and ionization ( or desorption ) of H on platinum as shown in Figure 5. It is to be emphasised that the adsorption and desorption peaks are almost mirror images of each other suggesting that the process is highly reversible.

The multiplicity of the adsorption and desorption processes is a result of multiple-

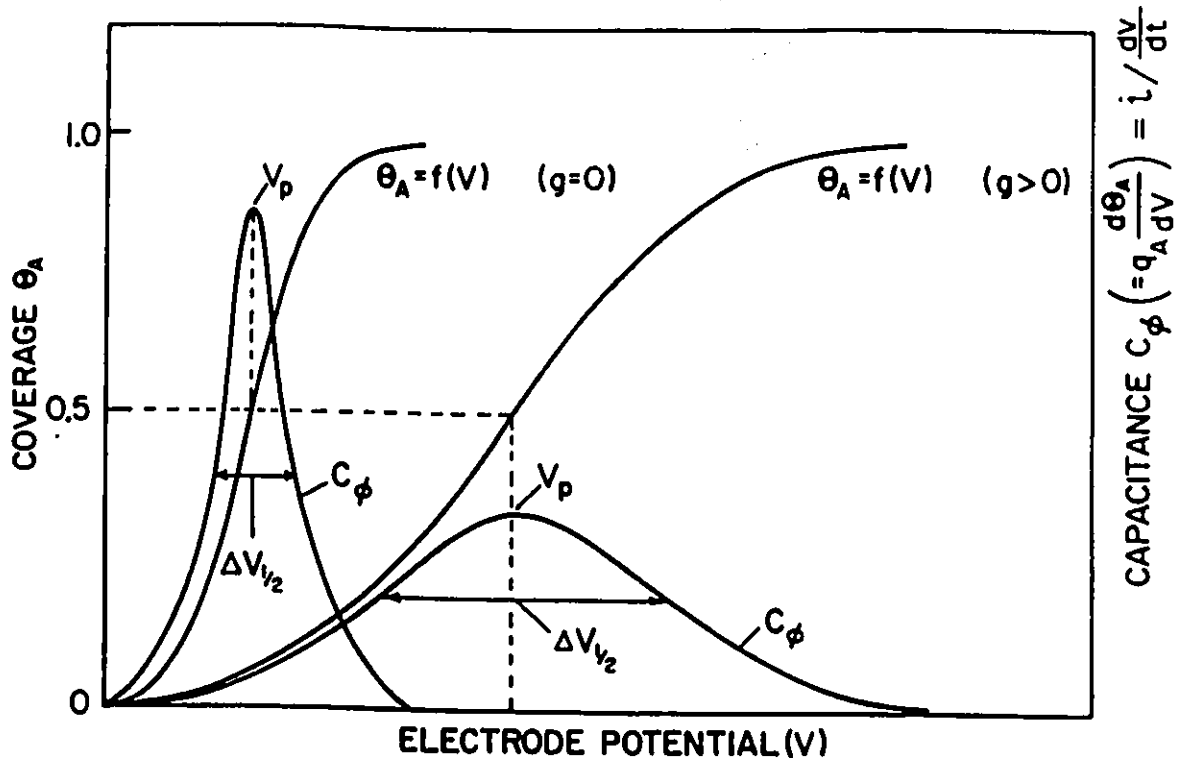


**Fig.3** Relationship between coverage, Θ, and adsorption pseudocapacitance, $C_\phi$, profiles with respect to potential for a simple "single-state" surface process below a monolayer is deposited or ionized. g measures any changes of energy of adsorption in $\Delta G_{ads}$ due to lateral interaction effect, with increasing Θ. $\Delta V_{1/2}$ is almost linear in g. ( From Ref. 27 )

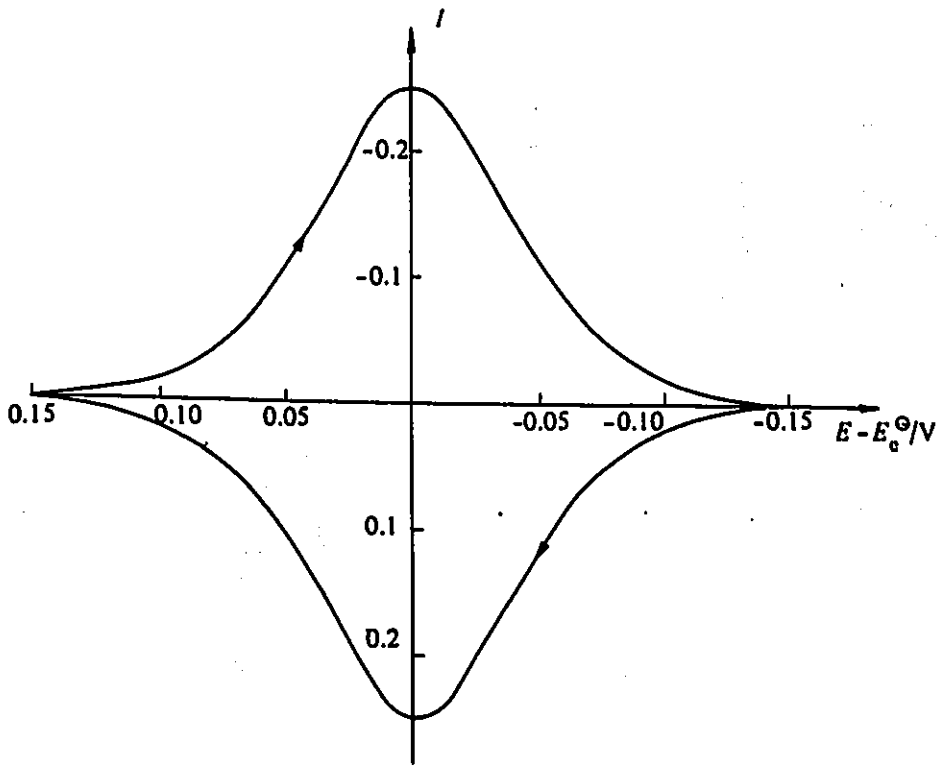


**Fig.4** Theoretical cyclic voltammogram for the oxidation and reduction of an adsorbed species A on electrode surface where adsorption follows a Langmuir isotherm. ( From Ref. 40 )

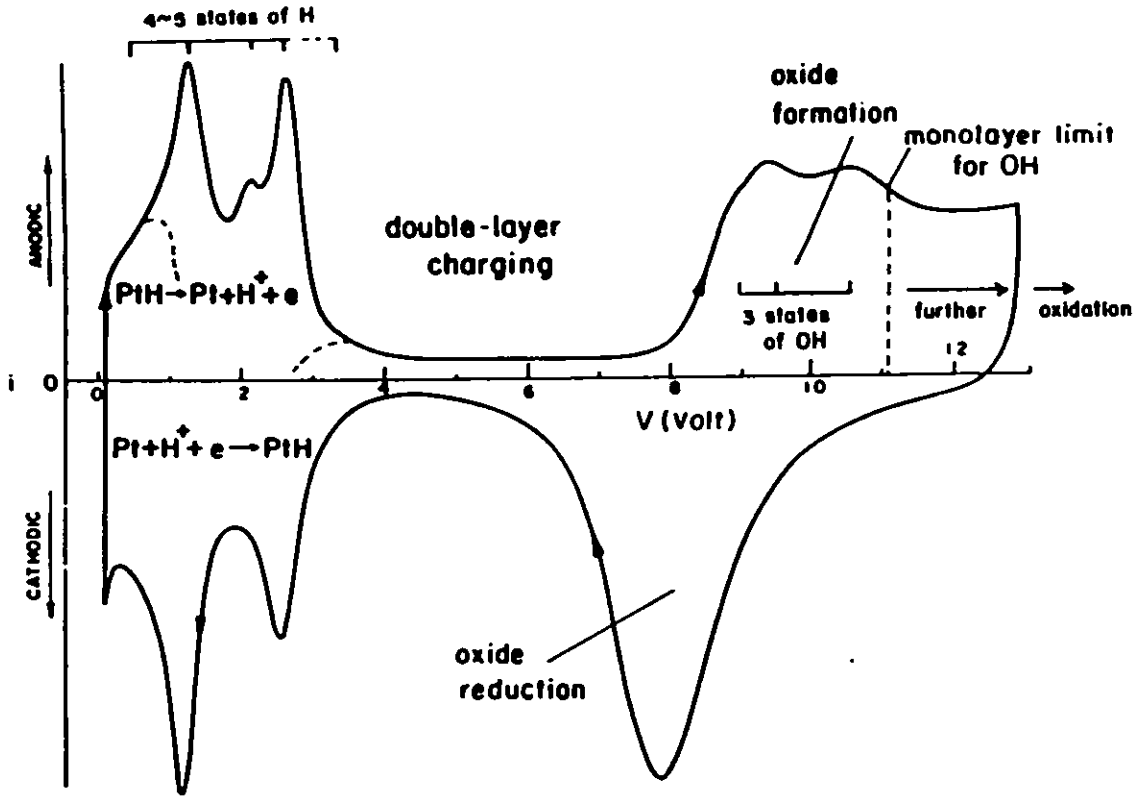


**Fig.5** Electrochemical deposition and desorption of H and OH/O species at Pt in 0.5 M $H_2SO_4$; sweep rate = 25 mV/s. ( From Ref. 27 )

state-adsorption or desorption ( in this case H ); this was once believed to be due to surface heterogeneity in the earlier works on polycrystalline metals e.g. Pt. However, later works on well-defined and characterized single-crystal metal surfaces revealed that multiple state adsorption and desorption peaks are *still* observed [28]. However, for H adsorption and desorption on platinum, the weakly bound H states are now known to be associated with the Pt(111) single-crystal surface while the strongly bound one is associated with the Pt(100) surface.

These interesting results therefore suggested that the multiple-state adsorption in UPD on polycrystalline metals is not simply due to the presence of different single crystal-planes. Since surface heterogeneity alone does not explain the origin of multiple-state adsorption, various other factors have been considered. For instance, as $\theta$ increases from 0 to 1, the electronic properties of the surface might be modified by the adatoms and also, there can be some long-range electronic and electrostatic interactions between adatoms already on the surface; a further interesting possibility is that there could be a reconstruction of the substrate/adsorbate layer as $\theta$ approaches 1.

As mentioned earlier, the UPD of base metals and H atoms on noble metals e.g. Pb on Au and H on Pt, are highly reversible processes as deduced from the fact that the adsorption and desorption peaks (cathodic and anodic profiles ) of their i/V profiles are almost mirror images of each other if the sweep rates are low enough. At sufficiently high sweep rates, however, the processes become kinetically irreversible simply because they cannot follow the rate of change of potential. Under kinetically irreversible conditions, the peak's potential shift from its reversible peak potential value is such that a plot of

$V_p$ *vs* log ( sweep rate, $s$ ) is linear, as for a Tafel relation [29]. The equation representing the shift of potential with log of $s$ when lateral interactions between adsorbates on the surface are insignificant ( g = 0 ) has been worked out by Angerstein-Kozlowska and Conway [29]:

$$V_{p,irrev} = V_{p,rev} + (RT/\beta F).\ln s_o - (RT/\beta F).\ln s \qquad (42)$$

or

$$V_{p,irrev} - V_{p,rev} = b \log s_o - b \log s$$

where $s_o$ is the limiting sweep-rate below which the process is kinectically reversible. $s_o$ is thus analogous to $i_o$ for a regular electrode process.

Thus the limiting sweep-rate, $s_o$, can be obtained from a plot of peak potentials *vs* log $s$ by extrapolating the line passing through a set of $V_{p,irrev}$ ,log $s$ points to the line of the reversible potential for which $V_p$ is independent of $s$. According to Angerstein-Kozlowska and Conway, $s_o$ is related to the exchange current density, $i_o$ in the following way:

$$s_o = i_o / C_{\phi,r} \qquad (43)$$

where $C_{\phi,r}$ is the observed pseudocapacitance at the peak when the process is reversible (compare Eq. (42) with the Tafel equation $\eta = b \log i_o - b \log i$).

It is to be emphasised that $s_o$ is a quantity which is intrinsic to the kinetics of a surface process as $i_o$ is for a regular continuous Faradaic reaction. However, the procedure has the advantage that the *real surface area* of the electrode is *not* required for evaluation of $s_o$ in contrast with that for $i_o$. It is therefore a convenient parameter to be used in characterizing a surface process as the general problem of distinguishing the factor

of surface area from that of catalytic effects at various electrode surfaces can be avoided.

Another piece of kinetic information that can be obtained from this kind of experiment is the Tafel slope $b$ for the surface process when $V_{p,irrev}$ - $V_{p,rev}$ is plotted against log $s$ for $s > s_o$ as shown by Eq. (42).

On most noble metals the process of the formation and reduction of a monolayer of oxide film on say Pt or Au always shows some kind of hysteresis, i.e. the anodic and cathodic profiles of the process are not mirror image peaks as they are for the H case, (see Fig.5 ) . The hysteresis arises no matter how slow is the sweep rate. When the oxide film is formed at higher potentials, the hysteresis increases. This is believed to be due to surface reconstruction of the initially deposited submonolayer of OH or O species via a place-exchange mechanism [46,47].

There have been only few studies on oxide formation and reduction process by cyclic voltammetry at elevated temperatures. Calandra *et. al.* [30] and De Tacconi *et. al.* [31] examined the behaviour of monolayer oxide formation and dissolution on polished Pt electrodes in molten sodium bisulphate-potassium bisulphate melts in the temperature range of 450 to 573 K. A $Pt/H_2/H^+$ reversible electrode was used as the reference electrode. The formation of the monolayer of oxide in the melts was assumed to be due to the presence of a water-formation equilibrium process:

$$2\ KHSO_4 \rightharpoonup H_2O + K_2S_2O_7 \qquad (44)$$

then

$$Pt + H_2O \rightharpoonup PtOH + H^+ + e \qquad (45)$$

followed by a second electron-transfer step:

$$PtOH \rightharpoonup PtO + H^+ + e \qquad (46)$$

as in aqueous media.

Their results obtained in the melts were similar to those in aqueous systems and coupled with the electron transfer reactions of oxide formation and reduction, are chemical processes such as ageing. Ageing, according to the authors, is a process involving a transformation of the surface species already formed at the early stage of the oxidation process into a more stable, reconstructed surface species. Similar observations in aqueous acid solutions were made by Conway and co-workers [32]. Such phenomena lead to the well-known hysteresis between the oxide formation and reduction peaks. At higher temperatures, they also observed some chemical dissolution of the anodically formed oxide film on open-circuit. The rate of this dissolution process increased significantly with temperature as might be expected. However, the time required for the transformation of surface species into a more stable one by the ageing process naturally becomes shorter at higher temperatures.

Similar kinds of experiments were carried out on Au electrodes in aqueous sulphuric acid in the 262 to 348 K temperature range by the cyclic voltammetric method by Ferro *et. al.* [38,39]. Typical cyclic voltammetric curves for the polycrystalline gold electrode at 348 K in 5 M $H_2SO_4$ and that at 262 K in 5 M $H_2SO_4$ are shown in Fig.6. As seen from these curves, the i/V profiles change with temperature. Again, both ageing and chemical dissolution of the oxide layer occur. Both the anodic formation and cathodic reduction peaks of the oxide become narrower and more symmetric, and also evidently more reversible, at higher temperature.

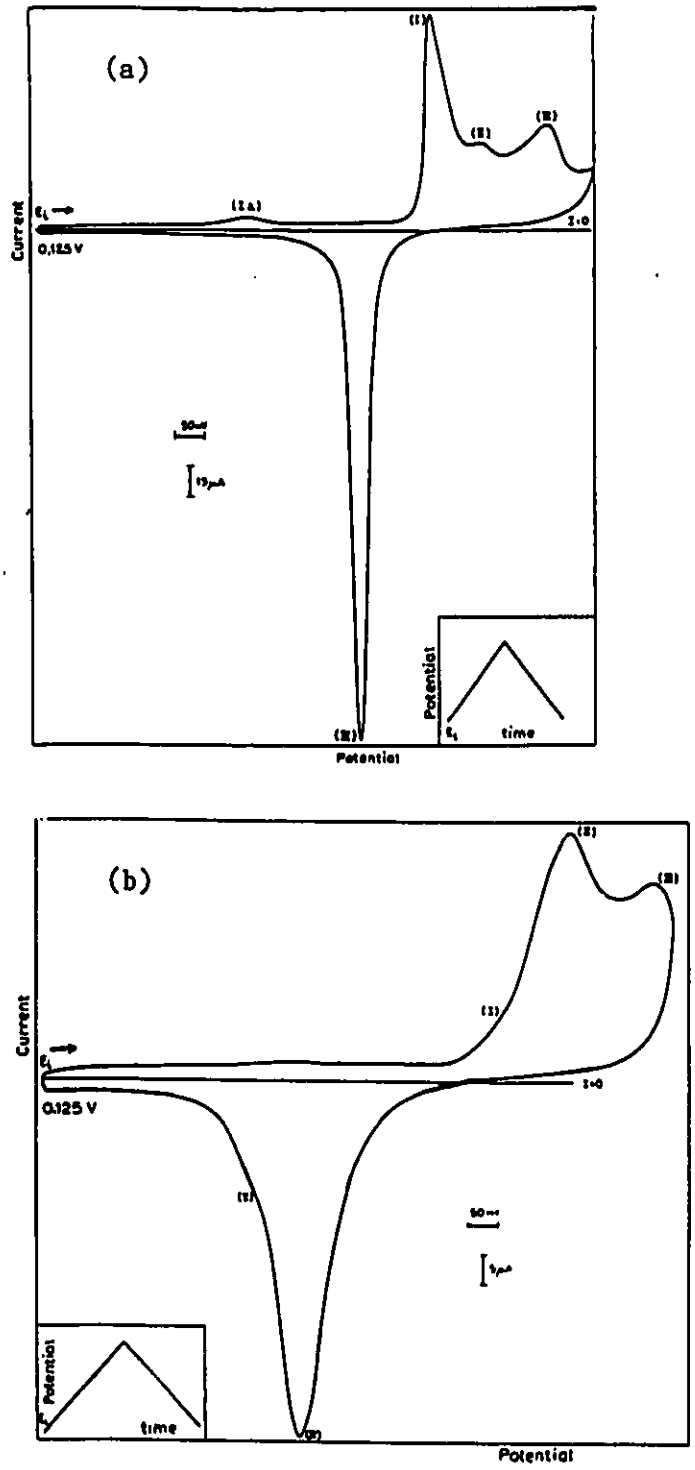


**Fig.6** Cyclic voltammogram of a polycrystalline gold electrode at (a)348 K and (b)262 K in 5 M $H_2SO_4$. ( From Ref. 38 )

## I.C.1 Brief Review on the Hydrogen and Oxygen Evolution Reactions ( HER and OER ) Kinetics

These two electrochemical reactions have been studied in the present work over a range of elevated temperatures. Therefore a brief review of the background on these processes will be given here.

### I.C.1a Hydrogen Evolution Reaction (HER)

Historically, in the studies of electrode kinetics, the HER is a very important one. Firstly, it has been the most widely studied reaction in this field and has contributed greatly to much of our understanding of electrode kinetics. Secondly, it has substantial industrial applications, e.g. the HER is the essential process in water electrolysis, producing hydrogen; a principal method of producing $D_2O$; a competing reaction in many metal deposition reactions, etc; a co-reaction in corrosion in the absence of $O_2$; and a principal by-product in electrolytic $Cl_2$ and $F_2$ production. Moreover, the fact that hydrogen can be evolved at various metals enables studies of its rate of reaction at a variety of such metals to be made, thereby providing information on the electrocatalysis of the process. Other reactions such as oxygen evolution can be complicated by metal dissolution or metal oxide formation reactions; thus it is difficult to learn about the most basic aspects of electrode kinetics from that kind of reaction.

The HER overall pathway is:

$$2H^+ + 2e \rightarrow H_2 \qquad \text{in acid solutions} \qquad (47)$$

and

$$2H_2O + 2e \rightarrow H_2 + 2\,OH^- \qquad \text{in alkaline media} \qquad (48)$$

In theory, the Tafel slopes of the HER or any other electrochemical reactions can be predicted if the mechanism or pathways of the reaction are known. Consider the mechanism of the HER in acid solutions as follows:

(I) $H_3O^+ + e + M \rightarrow MH_{ads} + H_2O$ discharge (49)

(II) $H_3O^+ + e + MH_{ads} \rightarrow H_2O + H_2 + M$ electrochemical desorption (50)

or alternatively to (50)

(III) $2\,MH_{ads} \rightarrow H_2 + 2\,M$ chemical recombination (51)

If step (I), the electrochemical discharge step, is rate determining, then the rate equation is (without introducing double-layer effects )

$$i_1 = 2Fk_1C_{H+}(1 - \theta_H)\exp[-\beta\eta F/RT] \quad (52)$$

Since it is assumed that I is here the rate-determining step, as e.g. at Hg, coverage by the H intermediate would be small, i.e. $1 - \theta_H$ is close to 1. Then it can be seen that the Tafel slope $d\eta/d \ln i$ is equal to $RT/\beta F$. If the symmetry factor, $\beta = 0.5$ and $T = 298$ K, then $b = 0.12$ V decade$^{-1}$ for the discharge control process, as found for Hg at this temperature. Note that when the discharge step is rate-determining, one cannot be sure of the overall mechanism. i.e. whether step (II) or (III) is the step following the initial discharge process.

If step (II), the electrochemical desorption process were rate-determining and is much faster than step (III), then the current would be given by

$$i_2 = 2Fk_2C_{H+}\theta_H \exp[-\beta\eta F/RT] \quad (53)$$

The coverage by hydrogen atoms, $\theta_H$ can be obtained as a function of potential using the quasi-equilibrium assumption for step (I), i.e. the rate of the forward reaction in that step

equals the rate of the backward reaction. This gives

$$k_1 C_{H+} (1 - \theta_H) \exp[ -\beta\eta F/RT ] = k_{-1} C_{H+} \theta_H \exp[ -(1 - \beta) \eta F/RT] \quad (54)$$

or

$$\theta_H = K.C_{H+} \exp[ -\eta F/RT ]/(1 + K.C_{H+} \exp[ -\eta F/RT ]) \quad (55)$$

Hence, Eq.(53) can be rewritten as

$$i_2 = 2Fk_2 C_{H+} \{K.C_{H+} \exp[ -\eta F/RT ]/(1 + K.C_{H+} \exp[-\eta F/RT]\} \exp[ -\beta\eta F/RT] \quad (56)$$

For $\theta_H$ less than 1 and a function of potential, $d\eta/d\ln i = RT/(1 + \beta)F$. At 298 K and $\beta = 0.5$, $b = 0.039$ V decade$^{-1}$. When $\theta_H$ approaches 1 and is therefore no longer a function of potential, $b = RT/\beta F = .0.12$ V decade$^{-1}$ at 298 K.

Finally, if step (III) is rate-determining, preceded by the initial discharge step (I), then the current is given by

$$i_3 = 2Fk_3( \theta_H )^2 \quad (57)$$

$$= 2Fk_3 \{ K.C_{H+} \exp[ -\eta F/RT ]/(1 + K.C_{H+} \exp[ -\eta F/RT ])\}^2 \quad (58)$$

Hence, for low coverage and when $\theta_H$ is a function of potential, $b = RT/2F = 0.03$ V decade$^{-1}$ at 298 K and as $\theta_H$ approaches 1, $d\eta/d \ln i = \infty$, i.e. a limiting current arises.

It can be seen in the kinetic treatment of the HER above that the coverage $\theta_H$ and particularly its dependence on potential plays an important role in determining the Tafel slope. Direct experimental information on $\theta_H$ is, however, surprisingly scarce until recently [33]. It is the purpose of part of the work reported in this thesis to evaluate coverage behaviour of H and OH/O species in the HER and OER through determination

of the pseudocapacitance, $C_\phi$.

From the above, it is clear that the dependence of $\theta_H$ or $d\theta_H/dV$ on temperature could have some significant effect on the experimentally observed temperature dependence of *b*.

I.C.1b Oxygen Evolution Reaction ( OER )

The oxygen evolution process is the counter reaction to the HER in water electrolysis as well as being involved in several other electrolytic processes such as metal extraction, metal plating, etc. It is also the principal reaction occurring at the positive plate of the lead acid battery when the latter is over-charged. The OER is a more complex electrode process than the HER, firstly simply because it requires 4 electrons in the overall process of oxygen production rather than two, as well as complications due to the fact that it always proceeds on an *oxide film covered* surface. On noble metals such as platinum and gold, the extent of formation of the oxide film can be as high as at least a monolayer before any $O_2$ evolution can be observed. On the other hand, oxide films on some transition metals such as nickel and iron can be up to 100 Å thick under conditions where $O_2$ is being evolved. Unlike the situation with the HER, many metals are not suitable for the study of the OER as their corresponding oxides are either not a good conductor of electricity. e.g. for Ti, Ta, W, V, Zr, and Al, or there is dissolution of the metal depending on pH. Exceptions are lead and manganese dioxide, nickel oxide and the noble metals mentioned above.

The overall reaction of the OER process is as follows:

$$4\ OH^- \rightarrow O_2 + 2\ H_2O + 4\ e \quad \text{alkaline pH} \tag{59}$$

or

$$2\ H_2O \rightarrow O_2 + 4\ H^+ + 4\ e \quad \text{acid pH} \tag{60}$$

The standard reduction potentials for the OER are 0.401 V and 1.229 V vs SHE in alkaline and acid solutions respectively. However, the equilibrium potential is not by any means as easily established experimentally as for the case of the HER since an extremely small exchange current density is involved ($i_o \sim 10^{-10}$ A $cm^{-2}$). Using the kinetic analysis approach as shown above for the HER, Bockris has worked out the Tafel slopes ( about twenty ) that can arise with the OER, based on various assumed rate-determining steps and mechanisms [34].

The most commonly assumed pathways for the OER in acid and alkaline solutions, without involvement of the complicated peroxide intermediate, but with O or OH species, can be written as follows:

In acid solutions,

(I) $$H_2O + M.Ox \rightarrow M.Ox.OH + H^+ + e \tag{61}$$

(II) $$2\ M.Ox.OH \rightarrow 2\ M.Ox.O + 2\ H^+ + 2\ e \tag{62}$$

(III) $$2\ M.Ox.O \rightarrow 2\ M.Ox + O_2 \tag{63}$$

or

(IV) $$M.Ox.OH \rightarrow M.Ox.O + 2\ H^+ + e \tag{64}$$

In alkaline solutions,

(V) $$M.Ox + OH^- \rightarrow M.Ox.OH + e \tag{65}$$

(VI) $M.Ox.OH + OH^{\cdot} \rightarrow M.Ox.O + H_2O + e$ (66)

(VII) $2\ M.Ox.OH \rightarrow M.Ox.O + M.Ox + H_2O$ (67)

(VIII) $2\ M.Ox.O \rightarrow 2\ M.Ox + O_2$ (68)

In the above reaction equations, M.Ox represents the oxidized surface of the metal M, on which the OER proceeds.

The kinetics of the OER are closely related to the properties of the oxide film, M.Ox, covering the electrode surface. Hence, reproducible experimental data can be obtained only if the surface oxide of the electrode is prepared in a controlled way with respect to the electrocatalytic properties of the exterior surface of that film, and measurements are taken under reproducible conditions. With such precautions in mind, reproducible Tafel slopes have been observed for the OER at Pt in $H_2SO_4$ solution having values of about 0.12 V decade$^{-1}$. The kinetics of the OER can also depend on the morphology of the oxide film as exemplified by the different electrochemical behaviour of the two dioxides of lead, $\alpha$- and $\beta$-$PbO_2$ studied in the present work; for example, Tafel slopes of 0.07 and 0.12 V decade$^{-1}$ in $H_2SO_4$, respectively, have been observed [35] for these two allomorphs.

## II. SCOPE AND AIMS OF THE WORK COVERED IN THE THESIS

The principal aim of the several directions of work described in this thesis was to examine a) the problem of temperature dependence of the Tafel slope for various processes, with provision of more experimental data especially at elevated temperatures in aqueous solution. b) Reversisbility of oxide film formation at noble metals at elevated temperatures and c) kinetic and adsorption behaviour in the HER and OER processes at elevated temperatures.

Tafel slopes measured at high temperatures for the same electrochemical reaction from different sources usually show some discrepancies. The reason may be one or some of the following: a) use of a single compartment electrolytic cell in the high temperature/pressure bomb instead of a three or two compartment cell; as a result, unwanted contaminants from the counter electrode might diffuse to and poison or otherwise interfere with the process at the working electrode; b) use of an external reference electrode system so that unknown junction and thermal gradient potentials are unavoidable; and c) autoclaves or cells are not clean due to corrosion of the materials in the high-temperature and high-pressure aqueous environment.

Thus, it is also an aim of this thesis to describe the development of the necessary experimental techniques and equipment for achieving a clean environment, free of contaminant, for the study of electrochemical processes under elevated temperature conditions.

Originally, plans were made to increase the working temperature up to and exceeding the critical condition of water which is 647 K and 22.1 x $10^6$ Pa. Due to

various substantial technical difficulties encountered during the course of the project, this idea of ultra-high temperature work had to be abandoned. Nevertheless, relatively high temperatures of about 473 K even sometimes up to 529 K were achieved with the help of highly specialized equipment, developed by the writer in the course of the work, as will be shown later in the Experimental section of this thesis.

In the process of developing the high-temperature/high-pressure set-up for the study of the temperature dependence on Tafel slopes and reaction kinetics, it was felt that, for the sake of simplicity and the reason mentioned earlier, an internal reference electrode should be employed in the same solution as that of the working and the counter electrodes. Several different types of reference electrodes including the Ag/AgCl, the dynamic hydrogen electrode, DHE [52], the dynamic Pd/PdH electrode, a special $Pt/H_2$ electrode and a Pt/Pt oxide electrode were tested for stability and reliability under the working conditions.

While testing the DHE in aqueous sulphuric and perchloric acid electrolytes over the experimental working temperature range, the method of cyclic voltammetry was employed and the i/V profiles of gold and platinum were monitored. The principle of the testing procedure was that if reproducible i/V profiles were obtained with respect to a particular reference electrode under test, then stability and reversibility of that particular reversible reference electrode under the test conditions could be assured.

Success in obtaining clean and reproducible cyclic voltammograms at high temperatures led to a more comprehensive study on oxide film formation and reduction processes on these two noble metals, up to quite high temperatures in aqueous solutions.

Although there were no problem in getting good and fairly reproducible i/V profiles with the use of the dynamic reference electrodes (both of the Pt and Pd type ), for some unknown reasons, such electrodes were not quite as stable when used in the studies on the HER. As a result, a search for a new reference electrode was initiated. It was found that a piece of Pd or Pt wire could be used as a stable reference if the autoclave which housed the whole electrolytic cell was pressurized with a certain amount of hydrogen gas. By using this reference electrode arrangement, it was found that the HER could be examined at Pt, Au and Ni metals wire electrodes in both acid and alkaline solutions. At about the same time, the Tafel line and Tafel slope experiments were carried out together with a series of potential-decay experiments in order to derive additional information about the potential dependence of the coverage of the H intermediate ( cf. Refs. [33,48] ). Also, a.c. impedance experiments were carried out on the same system under the same elevated temperature experimental conditions in order to provide data complementary to those derived from the potential-decay experiments.

During the studies of the OER, there was once again some problem with the reference electrode system which had proved satisfactory for the prior work involving both the cyclic voltammetry and the HER. Eventually, an oxide electrode of Pt [53], made chemically, was used as the reference in the subsequent OER experiments at Pt. Au did not, however, seem to be a candidate suitable for similar kinds of experiment at elevated temperature since preliminary investigations on that electrode in alkaline solution at high temperature resulted in a severe metal dissolution problem.

Other materials at which the OER was examined were the two well known forms,

$\alpha$ and $\beta$, of lead dioxide which provided the rare opportunity of studying electrocatalysis in the OER on two structurally different forms of the same chemical material. Unfortunately the electrolytic deposition of $PbO_2$ on a Pt metal wire substrate was not stable at temperatures higher than 353 K or so and the oxide deposit, in fact, fell off the Pt substrate. Presumably this was due to poor mechanical contact between the oxide deposit and the platinum metal wire, and to some swelling of the oxide material as well. Hence, there will be a section later in this thesis that will be devoted to the studies of the OER at the two different morphological forms of lead dioxide studied at several temperatures ranging from 299 K to 339 K and ambient pressure.

Much of the thesis deals with the experimental difficulties that were encountered in working at high temperature in an aqueous high pressure environment and how the problems were solved with the development of some highly specialized hardware, e.g. a special electrolytic cell, autoclave feed-throughs, and various kinds of special electrode holders and reference electrodes. Experimentally, these aspects of the work constitute a number of original contributions in the field of electrode process and electrosorption studies.

## III.A EXPERIMENTAL (HIGH TEMPERATURE AND PRESSURE CONDITIONS)

### III.A.1 Problems Arising in High Temperature and Pressure Work

Work at high temperatures with solutions introduces problems that are completely different from those at room temperature [49]. Basically, as mentioned in the Introduction section, the rates of both chemical and electrochemical reactions are much higher at elevated than ordinary temperature conditions, e.g. the rates of reactions are proportional exponentially to the $-E^{\ddagger}/kT$ term, including all those unwanted side reactions such as corrosion of the materials from which the cell and/or autoclave is made.

High temperature (i.e. well above 373 K) aqueous solution work also means that correspondingly high pressures are involved. This introduces problems of another type, mainly the requirement for use of an high-pressure vessel and the corresponding feed-through system for the electrical leads connecting the inside electrodes to the polarization and recording instruments outside the vessel. Leakages through the feed-through and the pressure vessel lid are of major concern.

Finally, the choice of reference electrode is of paramount importance, as referred to earlier, as all measurements and control of potentials are referred to this electrode. Hence, it must be at least stable and reproducible throughout the course of the experiment and the range of temperatures involved, and should be also rather simple and easy to implement. Preferably, it should enable the data obtained to be easily related to a thermodynamic scale such as that corresponding to the hydrogen reference electrode.

The problems described above can be classified into three general areas: a) those arising from the use of the high temperature and pressure autoclave; b) those from the

electrical feed-throughs and c) those associated with the reference electrode.

It was felt that it would be rather helpful, especially for subsequent work by others, to summarize the difficulties that were encountered during the preparation and use of the experimental set-up with special reference to the three main areas of concern listed above.

III.A.1.a High Temperature and Pressure Autoclave

Unlike many studies on temperature effects at the lower end of the temperature scale, where relatively low temperatures can be reached easily by utilizing the low freezing-point properties of some alcoholic acid solutions, e.g., measurements of Tafel relations for the cathodic HER on Ni, Hg, Fe, Co and Pt using alcoholic acid solutions down to 183 K have been reported [3,36] as well as on Pt cathodes down to as low as 126 K in a solid electrolyte, $HClO_4.5H_2O$ [8], studies on temperature effects in dilute aqueous solutions at the higher end of the temperature scale usually require the use of an high-temperature/high-pressure vessel or autoclave from which loss of solvent must be avoided. Actually, not all high temperature studies have been or need be conducted inside an autoclave. As we know, the boiling point of some concentrated acid or base solutions can be much higher than 373 K thereby providing the necessary high temperature condition with the use of ordinary cells and equipment, e.g., as for the anodic OER [37] where the source of O or OH was water. However, difficulties arise specially when concentrated acid solutions, say $H_2SO_4$ or $H_3PO_4$ are used for cathodic HER studies to provide the proton donor source which can then be the simple hydronium ion in $H_3O^+$, $CF_3SO_3^-$ or a more complicated undissociated sulphuric or phosphoric acid molecule itself.

Special attention must be paid to autoclaves being used for high temperature aqueous electrochemical measurements since corrosion of the autoclave material will certainly introduce contaminants into the electrolyte solutions. Suitable materials must be strong enough to withstand the extreme pressure and temperature condition yet be relatively resistant to corrosion. Only a few candidate materials meet these requirements such as stainless steels and some nickel or titanium alloys.

The first autoclave or bomb (as it is commonly called) that was purchased for some of the cyclic voltammetric work in the present project was made only of mild steel but it had a convenient size and geometry. However, as a result, severe corrosion problems were detected after only the first few high temperature test runs. Much effort was then directed towards keeping the corrosion products away from the electrolytes by the use of a specially constructed internal bomb liner consisting of a stainless-steel lid and a round-bottom Pyrex glass container. A schematic diagram of the liner is shown as Fig.7. Eventually, a second bomb, fabricated in stainless steel was employed in all the subsequent experiments.

Vapour leakage was frequently observed due to damaged pressure-gasket seals (Brunner rubber O-rings were used in the steel bomb and a metal alloy ring was used in the stainless steel one). Pressure leakage can also be developed as the temperature is varied from high to low values because the O-ring sometimes suffered from deformation under the high temperature and pressure conditions.

Initially, plans were made to study the electrochemical system in aqueous solutions at constant volume in a small volume bomb so that temperatures substantially higher than

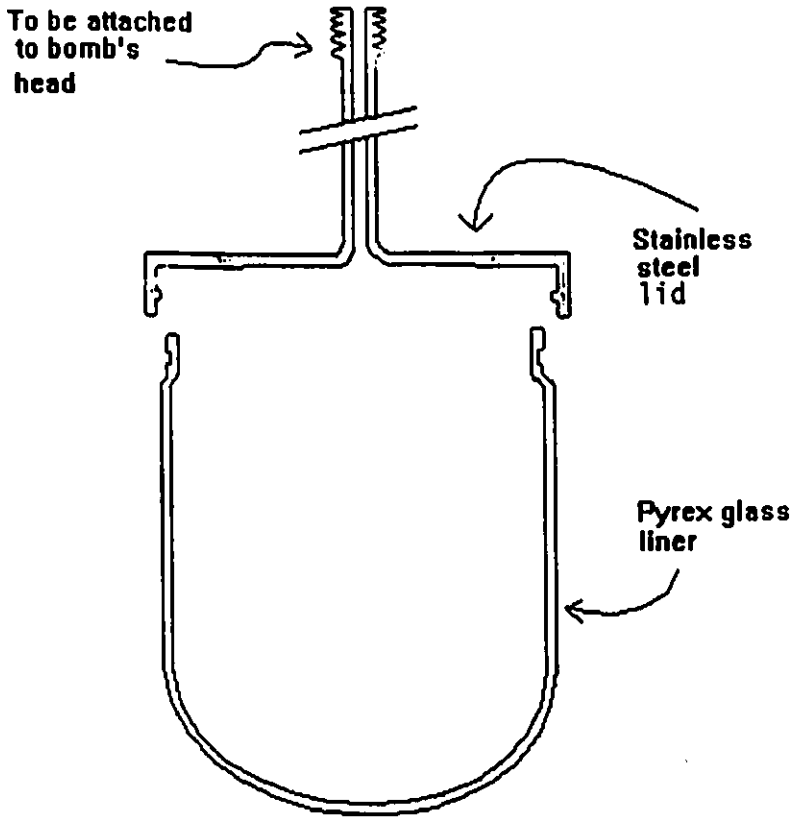


**Fig.7** Schematic diagram of the steel bomb's Pyrex liner.

373 K could be reached with the pressure of the system being the vapour pressure of water ( or of the solutions ) at all temperatures. Unfortunately, some changes of concentration due to loss of solvent did arise regardless of whether or not solvent was placed outside the electrolytic cell but inside the bomb. Eventually, positive high inert gas pressure was applied to prevent the electrolyte from boiling. This also helped solve the feed-through condensation problem to be described below.

III.A.1.b Electrical Feed-throughs

Dealing with the electrical feed-throughs was probably one of the most troublesome and painstaking parts of the work. The sole purpose of the electrical feed-through is to provide insulated electrical leads passing through the bomb from external instruments into the electrolytic cell inside, a seemingly simple matter. However, it must be certain that the leads are well insulated at all temperatures and pressures and that the electrical signals obtained via these leads reflect and relate directly to the electrochemical process inside the autoclave and not to some leakage processes in the feed-throughs. It was rather surprising to find out that the very first highly specialized, commercially-made feed-through that was used, failed to perform at all properly. Electrical shorts between the leads and the body of the bomb were commonly detected whenever there was excessive pressure and moisture build-up inside the system.

Fig.8 represents schematically the arrangement of the multi-lead feed-through system. The ceramic insulator was probably not sufficiently good in the presence of high-temperature steam as the chance of having a minute amount of water penetrating through

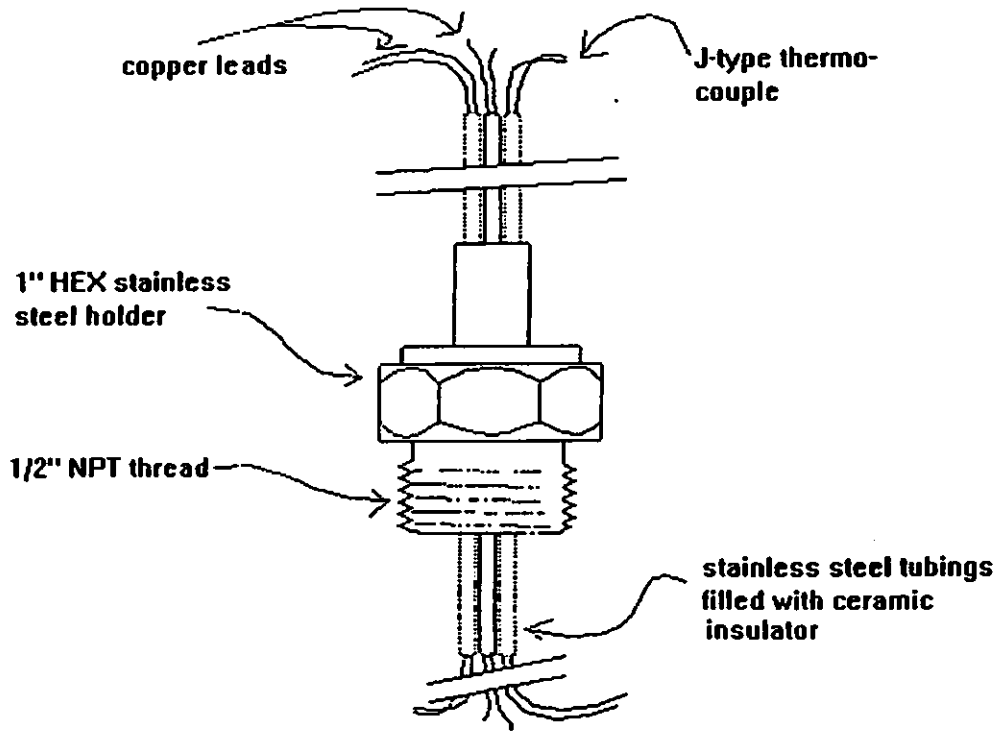


**Fig.8** Schematic diagram of the commercial, multi-lead feed-through system.

a millimetre or so of the insulator was evidently quite high so that the feed-through was rendered rather useless after a short period of use.

A home-made feed-through system composed of a stainless steel holder and four sparking plugs was then devised by the writer and employed rather successfully. Fig.9 shows a schematic diagram of this sparking-plug arrangement. Unfortunately and probably due to faulty design (moisture condensed at and round the metal-lead/sparking plug connection) and use of unsuitable sparking plugs ( i.e. not with the right pressure rating), some electrical short problems still persisted but could be made to disappear if the whole feed-through system was kept at about or above the same temperature as the rest of the bomb. However, some pressure leakages developed eventually through the metal-lead/ceramic contacts during prolonged experiments. Nevertheless, some high temperature cyclic voltammograms *were obtained* successfully using this home-made feed-through system. Finally, a much simpler and reliable Conax type [54] commercial feed-through seal provided with copper wires insulated individually with thick Teflon tubing was employed in conjuction with the stainless steel bomb. A schematic diagram of the seal is shown in Fig 10.

III.A.1.c Reference Electrodes for High Temperatures

The most commonly used primary reference electrode, hydrogen/Pt/$H^+$ for room temperature electrochemical studies is not easily implemented under a high-temperature/high-pressure environment. A continuous flow of pure hydrogen gas in and out of the autoclave requires complicated engineering design and expensive hardware.

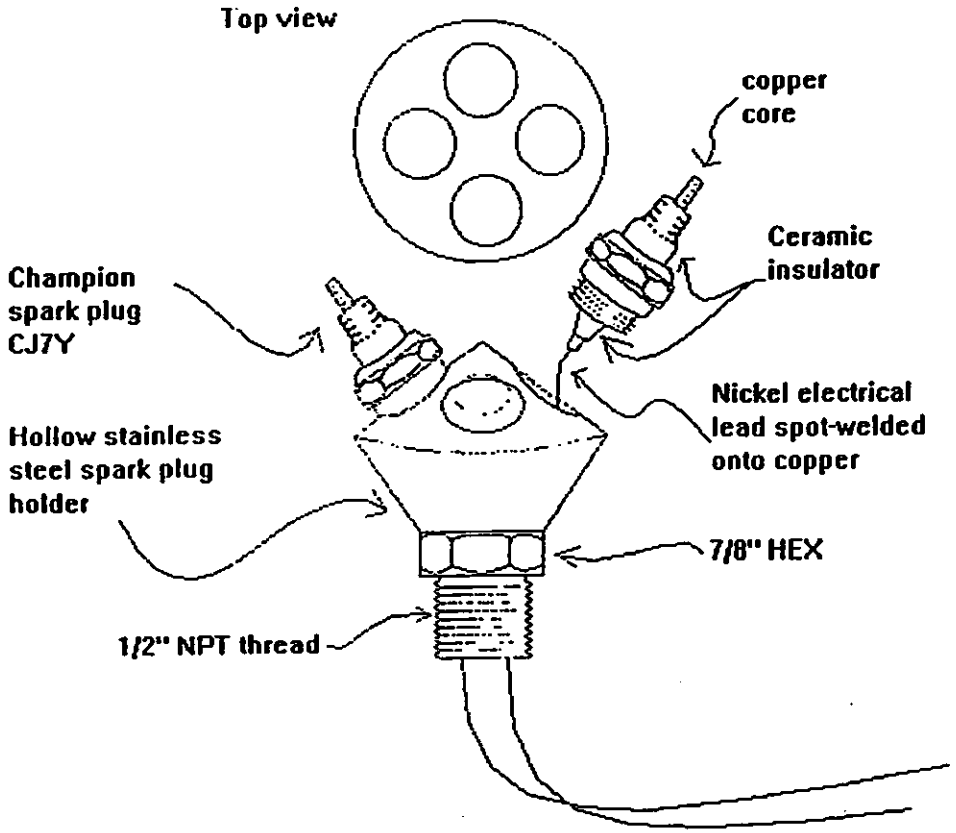


**Fig.9** Schematic diagram of the home-made feed-through system.

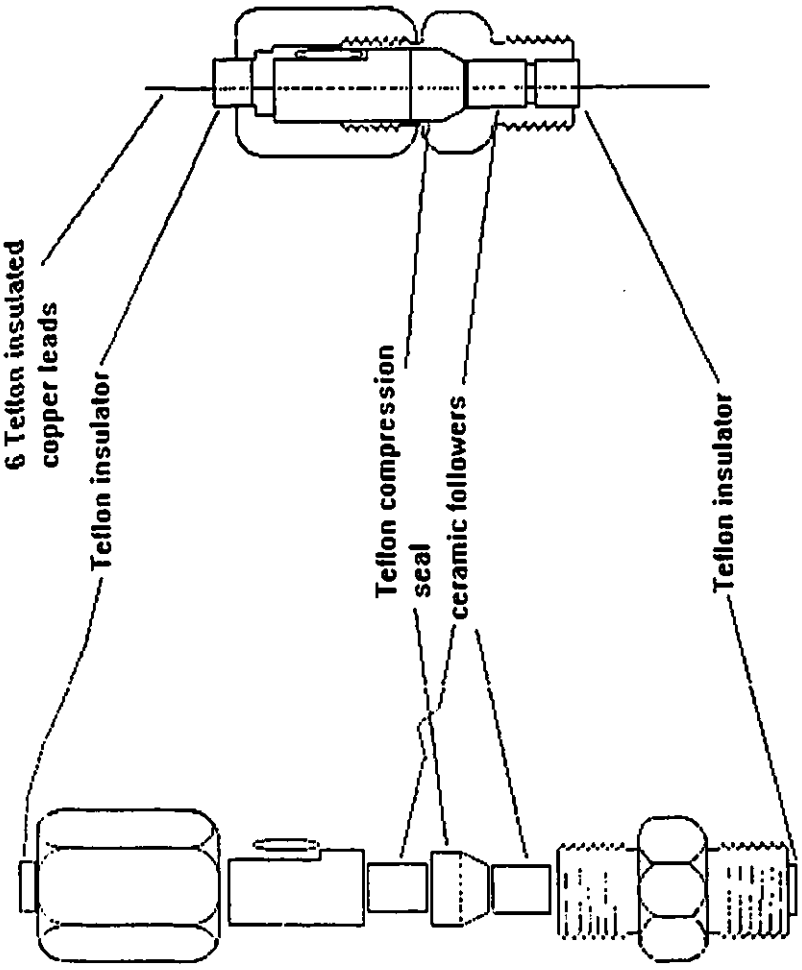


**Fig.10** Schematic diagram of the commercial Conax type commercial feed-through seal.

Secondary type reference electrodes such as silver/silver-compound electrodes seemed promising as the solubility of appropriate silver compounds is extremely low even at quite high temperatures. However, preliminary tests on the Ag/AgCl electrode showed that it was not suitable for the present work. First, a secondary ion, $Cl^-$, is needed in the electrolyte to established the required equilibrium at the reversible electrode. For most electrochemical studies such as the HER at Au or Pt, a small amount of chloride ion can seriously poison the electrode surface and modify its behaviour, as $Cl^-$ is capable of becoming chemisorbed on Pt surface and dissolving Au by forming a soluble $AuCl_6^{-3}$ complex [50]. Moreover, $Cl^-$, under high temperature and pressure conditions, also attacks soda-glass as well as Pyrex glass, but to a lesser extent. It also greatly facilitates corrosion of any metal parts. It is to be noted that soda glass is the only glass (it has the same linear expansion coefficient as platinum) that forms a tight metal/glass seal [51] over a range of temperatures. Finally, it is quite possible that small amounts of silver metal might become dissolved into electrolytes such as sulphuric acid under open-circuit, high temperature conditions. The mercury/mercury-compound electrodes were not tested as these electrodes would produce toxic vapour at high temperatures and will certainly suffer from a mercury dissolution problem. Therefore, the choice of reference electrodes had to be limited to the few which utilized noble metals, e.g. the dynamic hydrogen electrode (DHE) and the Pt oxide/Pt electrode. Also, the Pd/PdH electrode was examined but was not as reliable as the DHE over a wide temperature range.

## III.A.2 Development of an Experimental System

Apparatus for studying high temperature and pressure electrochemistry is not readily or normally available commercially. Usually, major modifications are necessary to any such apparatus to meet the special requirements of electrochemical research at high temperature and pressure. The system employed in the present work basically consisted of a high pressure vessel or bomb the head of which was machined to accept a feed-through which contained the necessary electrical connections. Heating was provided by a heating jacket mounted on the outside-wall of the pressure bomb to generate the necessary moderate to high temperatures inside. Precise temperature control was achieved by means of a temperature-controller coupled with a thermocouple. The high-temperature/high-pressure apparatus was enclosed in a specially constructed armoured trolley which provided some mobility as well as protection in the case of an explosion. A schematic diagram of the apparatus is shown in Fig.11.

### III.A.2.a High Pressure Bombs

Two different types of high pressure bomb were used in the present work, one being made of mild steel ( High Pressure Equipment Co. ) and the other of stainless steel ( High Pressure Equipment Co. ). The steel bomb was relatively small in size and its inside volume ( ca. 750 m*l* ) so that the pressure bomb could be heated up to the working temperatures relatively quickly with relatively little electrolyte being needed. The rating of the pressure bomb was 10,000 psi when tested at 298 K. This particular pressure bomb was not recommended to be used at temperatures higher than 393 K due to the fact that

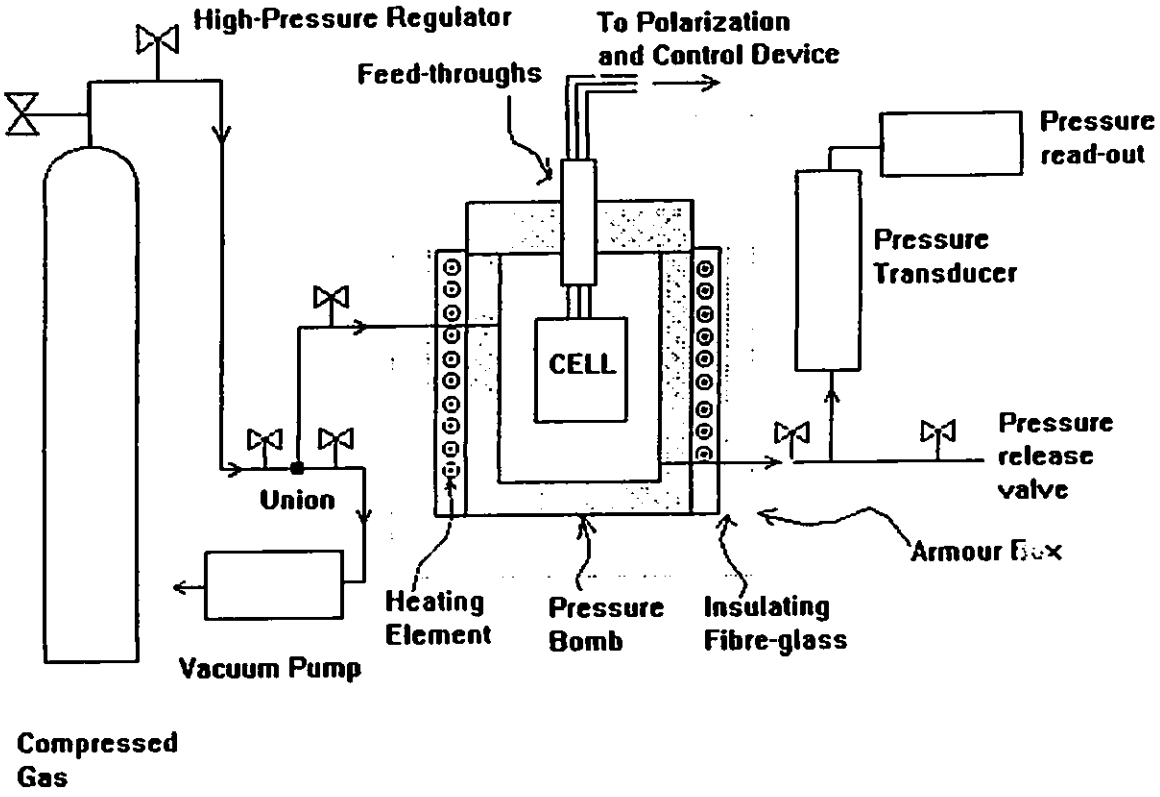


**Fig.11** Schematic diagram of the high-temperature/high-pressure apparatus.

a low-temperature rubber O-ring ( Brunner rubber ) was supposed to be used for the pressure seal. By simply replacing the Brunner rubber O-ring with one that was made of high-temperature Viton rubber, the upper working temperature limit of the pressure bomb could be extended to ca. 473 K. Viton rubber is relatively inert to both acid and alkaline attack yet would not produce unwanted gases or lose its elasticity until 473 K or higher.

Into the head of the pressure bomb was fitted the stainless steel home-made feed-through system which accommodated 4 sparking plugs ( Champion Sparking Plugs model CJ7Y ) as electrical connections, as explained earlier. Nickel wire insulated with heat shrinkable Teflon spaghetti tubing was spot-welded onto each sparking plug individually. A schematic diagram of the feed-through system is presented in Fig.9. In order to prevent moisture condensation, a flexible heating tape was wrapped around the part of the system which was exposed to the room-temperature environment.

The second high pressure bomb was made of stainless steel and was much larger in size and volume; hence it required a much longer time for its temperature to be changed from one value to another. The pressure rating of this bomb was also 10,000 psi at ambient temperature. A flat metal ( asbestos-aluminum ) gasket was used for making the high pressure seal.

Although the metal gasket alone was supposed to give the proper pressure seal if compression from the bomb's head was applied evenly and sufficiently via a set of eight heavy-duty steel screws, it was found to be particularly useful in preventing pressure leakage at all temperatures if the metal gasket was covered by a layer of Teflon sealing tape.

The feed-through system employed here was a commercial Conax-type seal and its schematic illustration is shown in Fig.10. The Conax-type feed-through consists of a 60 degree cone seal through which several Teflon insulated electrical copper leads pass. The seal is compressed by the two ceramic insulator followers onto the electrical leads, thereby making the seal tight. Teflon is the most suitable material to be used in this type of seal up to 10,000 psi at 323 K [49]. For higher temperatures, however, minor extrusion of the Teflon did occur.

III.A.2.b Pressure Read-Out

Pressure inside the apparatus was monitored through a high-pressure fitting on the side wall of the pressure bomb by means of an electronic pressure transducer ( Ametek Controls Division ) which utilizes a silicon piezoresistive sensing element consisting of four strain gauges forming a bridge circuit the resistance of which will vary when strained by pressure. The pressure transducer is used in conjunction with an electronic process indicator ( Viconics Electronics Inc. ) to provide a digital read-out.

III.A.2.c Temperature Control System

The required heating was provided externally by a heating element made of resistive wire wrapped around the outside wall of the bomb and is completely insulated by, and embedded in, high temperature cement. Heat lost to the surroundings was then minimized by covering the apparatus with several layers of thick glass fibre insulating cloth. The temperature was controlled by a solid-state temperature controller ( Nanmac

Corp. ) to within ± 1 K. The heater was switched on and off by a mercury relay ( H - B Instrument Corp. ) which enables relatively noise-free switching to be achieved. A J- or K- type thermocouple passing through the feed-through system, into the pressure bomb, located just above the electrolytic cell, was used for accurate temperature recording, e.g. as in the case of the Conax seal feed-through used in the stainless-steel pressure bomb.

A schematic diagram of the temperature control system is shown in Fig.12.

Due to difficulties in incorporating thermocouple wires into the home-made feed-through system with the steel bomb, temperature recording was made by placing the thermocouple probe outside of the bomb in a thermocouple well immediately next to the heating element. This arrangement provided temperature control without indicating the actual temperature inside the pressure bomb. The remedy was then to have the temperature scale re-calibrated. This was done by monitoring the vapour pressure of pure distilled water inside the vessel at each temperature. Reproducible vapour pressure readings were obtained at all temperatures in both ascending and descending order of temperature change, indicating good reliability of the calibration method. All vapour pressure data for water as a function of temperature were obtained from the Handbook of Chemistry and Physics.

### III.A.3. Basis for Successful Experiments

In order to get meaningful experimental results in high temperature and pressure experiments, in addition to what has already been discussed earlier such as choice of pressure-vessel material, reference electrode and design of feed-through, one must also

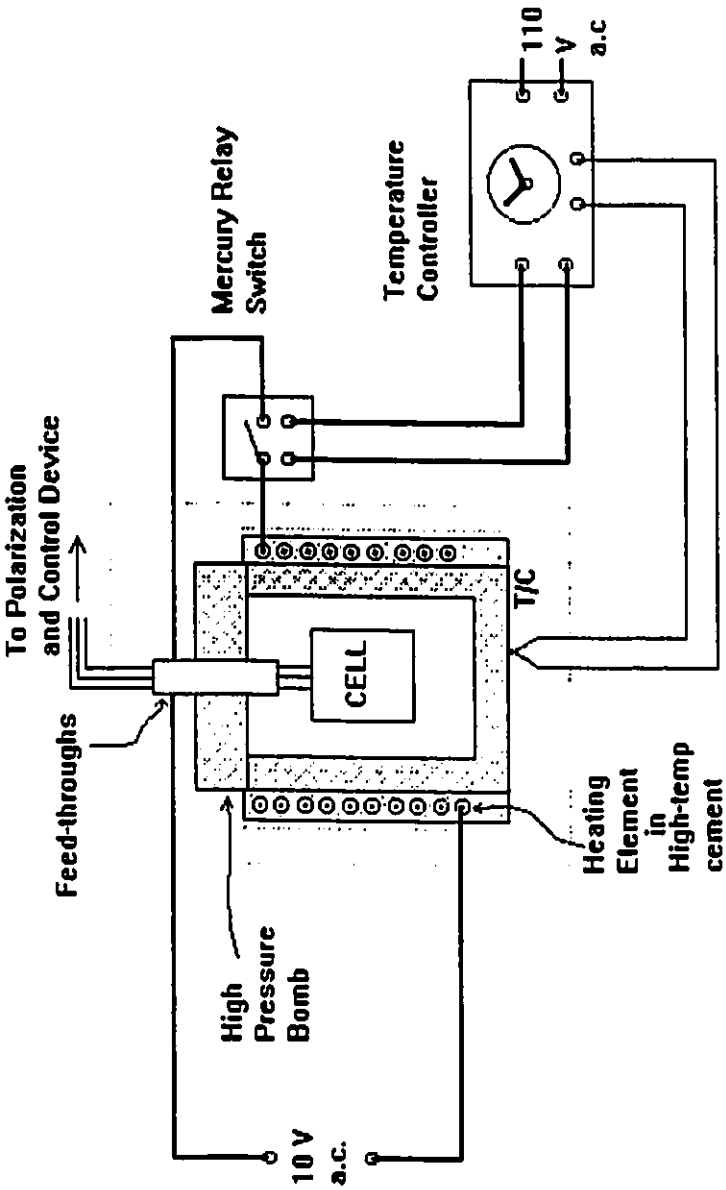


Fig.12 Schematic diagram of the temperature-control system.

take into consideration the design and choice of material of the electrolytic cells, electrodes, and some other matters listed below. First, glass is probably the most commonly used construction material for both the electrolytic cells and electrodes as it is one of the most inert substances available even at high temperatures. It is particularly useful when acid rather than alkaline solutions are used as electrolyte. For alkaline solutions, Teflon has been proven to be more appropriate. However, due to the hydrophobic nature of Teflon, small capillaries or tunnels must be avoided in the design of electrolytic cell since any gas bubble formed on such surfaces tends to stay there thus creating high ohmic-drop resistance say between the reference and working electrode in the Luggin capillary. Although a three-compartment cell is more effective in isolating electrodes from adverse diffusion of gases, a two-compartment cell is more realistic and practical for high temperature and pressure work as it is simpler and thus less likely to break down in the course of an experiment. It would be a troublesome problem if one had to terminate an experiment that had been in progress for a while at *high* temperature and pressure to reveal and deal with such problems. In other words, the design of electrolytic cells must be as simple as possible. Another important point to be kept in mind when designing cells to be used in a closed high-pressure vessel is that the usual procedure of continuous degassing of the compartment containing the working electrode with inert gas such as nitrogen is impractical, if it were at all possible. Hence, a good separator should be used between the working and counter electrode compartments in order to isolate any undesirable gas products generated from the counter electrode, e.g. oxygen in the case of HER experiments.

Tight glass-to-metal seals are a paramount requirement for all electrodes being used at both ambient and elevated temperatures. Leaky electrodes are often the source of some incomprehensible and unexpected results, especially with voltammograms. Unfortunately, the best known and frequently used metal-to-glass seal in electrochemistry, the platinum/soda-glass seal is virtually useless under high-temperature/high-pressure aqueous conditions even with relatively mild acid solutions. A specially designed electrode was then made in which a tungsten/uranium-doped Pyrex glass seal was used and found to be most resistive to the hostile environment. A detail description of this electrode will be given later.

Changes of electrolyte concentration during experiments can seriously complicate the interpretation of results, although one type of experiment might be more susceptible than another, e.g. UPD of H or O/OH might not be affected as much as some gas evolution reactions. One convenient way to avoid that would be applying a high positive pressure with an inert gas or a gas, the evolution reaction of which is of interest, e.g. as for hydrogen in the case of the HER. When hydrogen gas was used, it also served as part of the reference electrode system in which a piece of palladium or platinum wire satisfactorily acted as a stable and reversible reference electrode at all temperatures and pressures. The positive pressure also compensates any minor pressure leakage the apparatus might have ( a 100% pressure-tight seal at all temperatures is hard to get).

Finally, it must be emphasised that enough time should be given to the system for it to acquire thermal equilibrium before moving on to the next temperature of interest with measurements being taken. Often, two to three hours equilibration time between

temperatures is required, depending upon the size of the pressure vessel employed.

## III.A.4. Methods of Measurements

### III.A.4.1 Cell Preparation

All the electrolytic cells used for the high-temperature measurements, including those made of glass and Teflon, were cleaned in the following way. The cells was first washed in chromic acid for several hours, followed by thorough rinsing in distilled water. The cell was then filled with doubly-distilled water and allowed to soak overnight. Before the cell was used for an experiment, it was filled with the appropriate solution and allowed to soak for thirty minutes or so. It was then emptied and filled with the solution required for the experiment a second time immediately before it was introduced into the high-temperature/high-pressure bomb.

### III.A.4.2 High Temperature Measurements

#### III.A.4.2.1 General

After the cell had been prepared as described in section III.A.4.1 above, the leads of the cell were connected to those on the interior of the head of the high-temperature/high-pressure bomb. The electrical connections were made by means of metal-alloy screw connectors. Adequate slack was given to the copper leads to facilitate easy assembly of the cell. The electrical connections were checked and marked on the exterior of the bomb to match the electrical leads inside. The electrical leads on the outside were then connected to the appropriate polarization and recording devices.

III.A.4.3 Cyclic Voltammetric Studies

Cyclic voltammetry was carried out using a PAR 173 potentiostat and a PAR 175 universal programmer ( a function generator ). The potentiostat was equipped with a PAR 179 digital coulometer or PAR 376 logarithmic current converter which enabled conversion of current to voltage easily without the use of a resistance box. i/V profiles were monitored and recorded by means of a digital oscilloscope. The resulting data were stored on floppy disks and used in subsequent plotting and calculations.

After the appropriate cell was prepared and its electrical lead connections made, electrolyte was then placed outside of the cell in the bomb liner to minimize solvent loss during experiments. The bomb was then made pressure-tight and vacuum was applied to remove air. When the pressure inside the system had reached a minimum and steady value, purified nitrogen was introduced until the bomb was pressurized to about one atmosphere. The whole process of vacuuming and pressurizing was repeated as many times as necessary to remove all ambient and dissolved oxygen from the electrochemical system. The reference electrode system, DHE, was then activated by passing a small and continuous d.c. current through the circuit. Usually, at least 30 minutes was allowed for the reference electrode to establish a stable voltage before any measurements was made. The circuit utilized in the cyclic voltammetry experiments is shown in Fig.13. Cyclic voltammetry experiments were conducted at temperatures from 298 up to 538 K (265 C). Some attempts were made to reach the critical temperature of water but failed to technical and engineering difficulties with the seals.

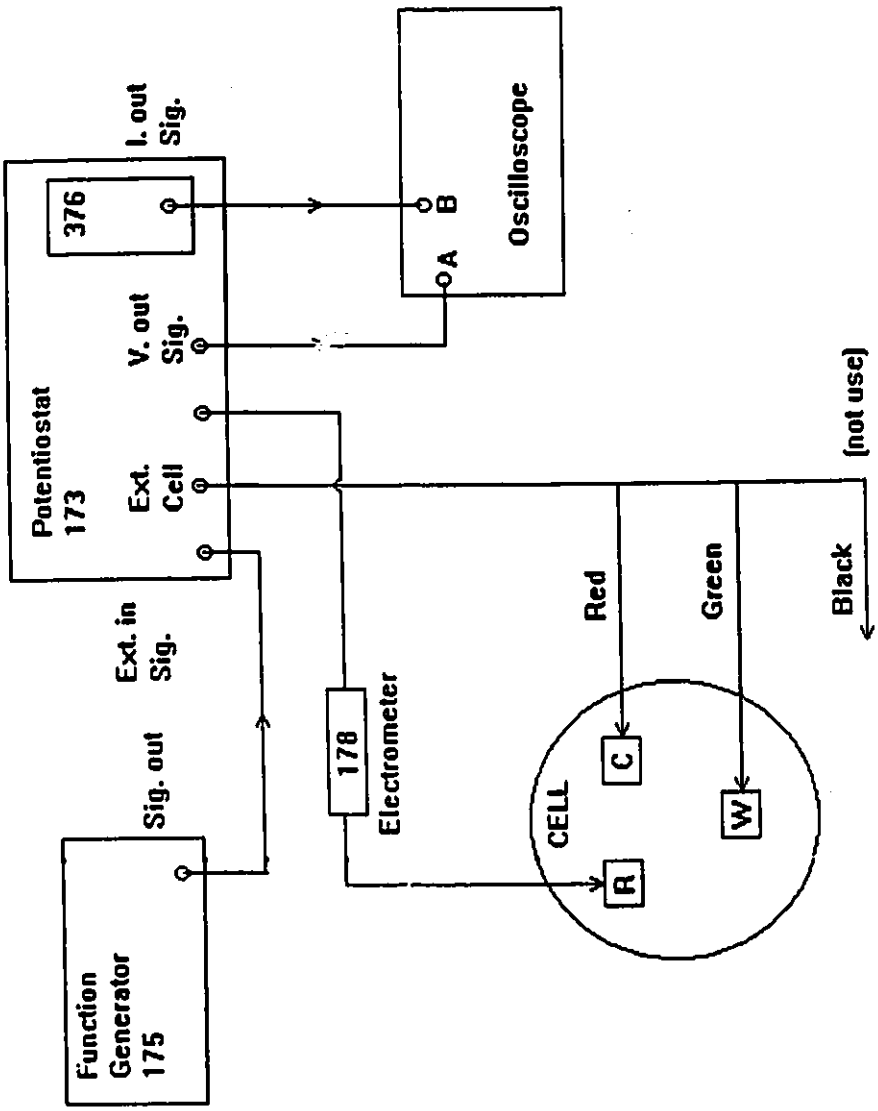


**Fig.13** Circuit utilized in the cyclic voltammetry experiments.

III.A.4.4 Steady-State Tafel Experiments

Tafel-polarization experiments were carried out using an automated system consisting of a PAR 173 potentiostat connected to an HP 86B computer, a Keithley 195A digital multimeter and a Kepco analogue-to-digital converter or a PAR 273 potentiostat communicating with an IBM computer. These computer-assisted potentiostats enabled the Tafel relations to be determined under exactly reproducible conditions of polarization potential and time; hence very reproducible Tafel lines could be obtained.

The degassing procedure utilized here was similar to that described above for the cyclic voltammetry experiments except at the end of the degassing steps, high positive pressure of either $H_2$ or $O_2$, about 100 psi, was applied. Tafel relations were determined in descending order of potential change and conducted at temperatures from 298 K up to 473 K.

Contrary to the conditions employed for the cyclic voltammetry experiments, the Tafel-relation experiments were carried out at the highest temperature first unless mentioned otherwise. This was to ensure that data at the highest possible temperature be obtained first before any problems arose due to prolonged experimentation at high temperature and high pressure. At the end of the Tafel-relation experiments, the potential-decay transients for the system ( see section III.A.4.5 ) under similar conditions of temperature and pressure were recorded, followed by a series of a.c. impedance measurements ( see section III.A.4.6 ).

III.A.4.5 Potential-Decay Transients

The potential-decay transients, V(t), were recorded digitally in time(t) on a Nicolet 206 digital oscilloscope upon interruption of various prior steady polarizing currents using a specially designed mercury contact switch. The procedure employed in recording the decay transients was as follows. The potential of the working electrode was first adjusted to the desired polarizing potential, V. The potential-decay transient was then initiated and recorded once the prior current-density had become stabilized and was the same as that from the Tafel relations obtained immediately before the decay experiments were started. Upon completion of the first decay transient, the polarization potential was readjusted to a new V less negative in value in the case of the HER or less positive in value in the case of the OER. Several transients were recorded by this procedure over a range of potentials and corresponding current densities. Data were collected using 2-3 different time-scales covering over 5-6 decades of time with a single oscilloscope. In order to avoid perturbation of the electrochemical system, potential decays over the shortest time-scales were performed first. The decay and the complementary Tafel polarization data were analyzed, as described in papers published earlier [21,48,65], on a Hewlett Packard 9000 computer using a computing programme developed in this laboratory by P.Gu and S.Y.Qian or on an IBM PC using a similar data-treatment programme written by the present author.

Potential decay experiments were conducted at temperatures ranging from 298 K to 473 K.

III.A.4.6 A.C. Impedance Measurements

The a.c. impedance behaviour was evaluated using a Solartron 1255 HF frequency response analyzer in conjunction with a computer-controlled PAR 273 potentiostat. With commercially available, electrochemical impedance software, Z-PLOT, this instrument is capable of measuring the total impedance of the electrode and recording its real (Z') and imaginary (Z") components separately, over a wide range of frequencies from $10^{-3}$ to $10^{5}$ Hz. Experiments were conducted at temperatures from 298 K to as high as 473 K at frequencies ranging from $10^{-3}$ to $10^{4}$ Hz and over a range of d.c. level potentials. The amplitude of the perturbing sinusoidal signal was 10 mV peak to peak. The a.c. data were analyzed by the Z-PLOT software when not appreciably "depressed"[2] complex-plane plots were obtained. When depression was significant, a "constant phase element" was introduced in the evaluation of the behaviour, and can provide a semi-empirical basis for it.

## III.A.5. Cells and Electrode Designs

### III.A.5.1 Electrochemical Cells for Use in High Temperature/High Pressure Experiments

The electrochemical cells were designed to meet the requirements for the high-temperature/high-pressure conditions involved in the experiments as described earlier, as

---

[2] Complex-plane semicircle plots are referred to as being "depressed" when their diameters are rotated below the Z' axis about the Z'= 0 point. This also corresponds to their centres being located below the Z' axis.

well as taking account of the space available in the high-pressure vessels. Three types of cells were designed and fabricated from either Pyrex glass or Teflon.

III.A.5.1a Three-Compartment Pyrex Glass Cell

The first cell made was a simple 3-compartment Pyrex glass cell consisting of a bottom and a top part joined together by means of a ground glass joint and a Teflon sleve. The top part contained the DHE reference electrode situated in a Luggin capillary adjacent to the working electrode, while the bottom part was made up of concentric working and counter electrode compartments separated by means of a wetted ground glass joint which could be opened slightly for passage of larger currents. The counter electrode was a cylinder of platinum gauze located concentrically in the counter electrode compartment with the working electrode located in the center of the cell in the working electrode compartment. This arrangement allowed current to be distributed evenly between the working and the counter electrodes thus meeting the requirements for electrode kinetic studies. This cell was used successfully in the cyclic voltammetry experiments on gold and platinum electrodes in acid solutions in the steel bomb. A schematic diagram of the cell is shown in Fig.14.

III.A.5.1b One-Compartment Pyrex Glass Cell

Another type of cell for the cyclic voltammetry work was a one-compartment Pyrex glass cell having the standard design used in this laboratory for room temperature experiments. It was simpler to use as it accepted standard size electrodes. Usually, a pair

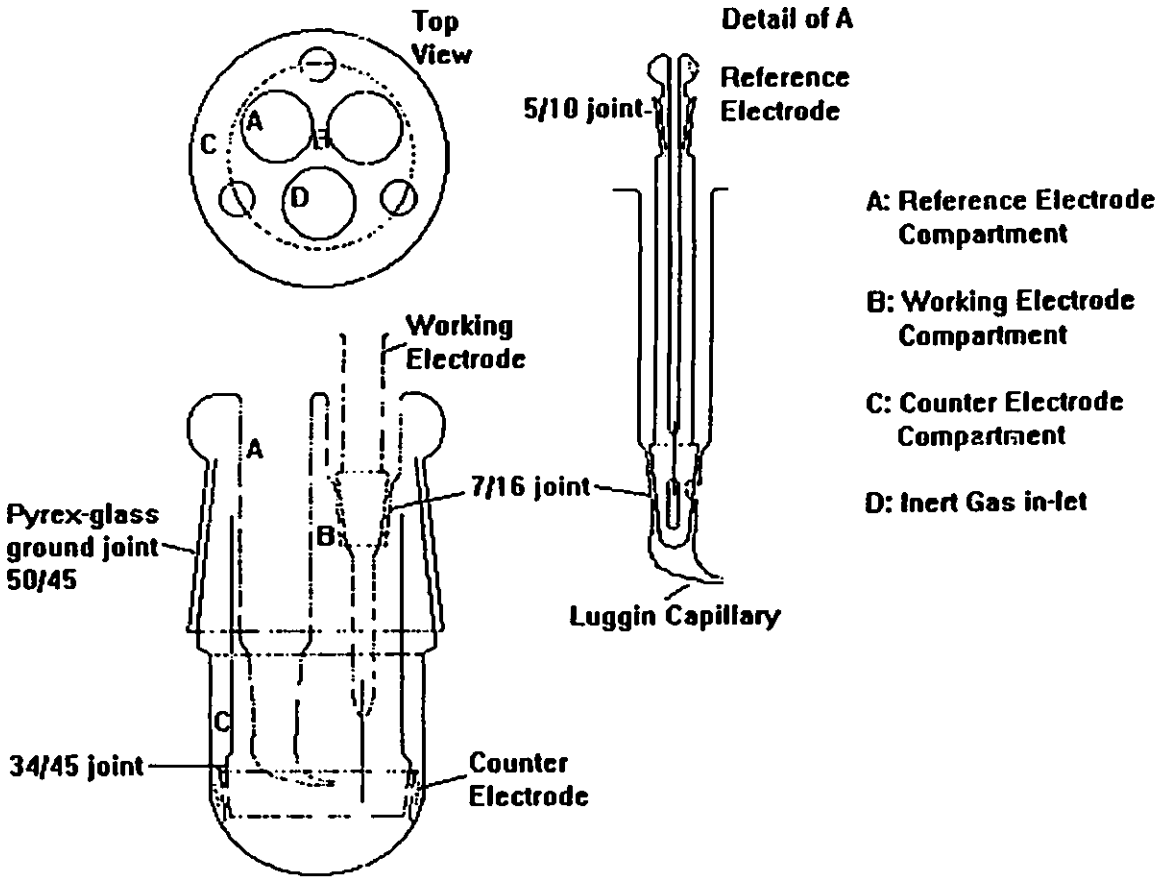


**Fig.14** Three-compartment miniature Pyrex glass cell.

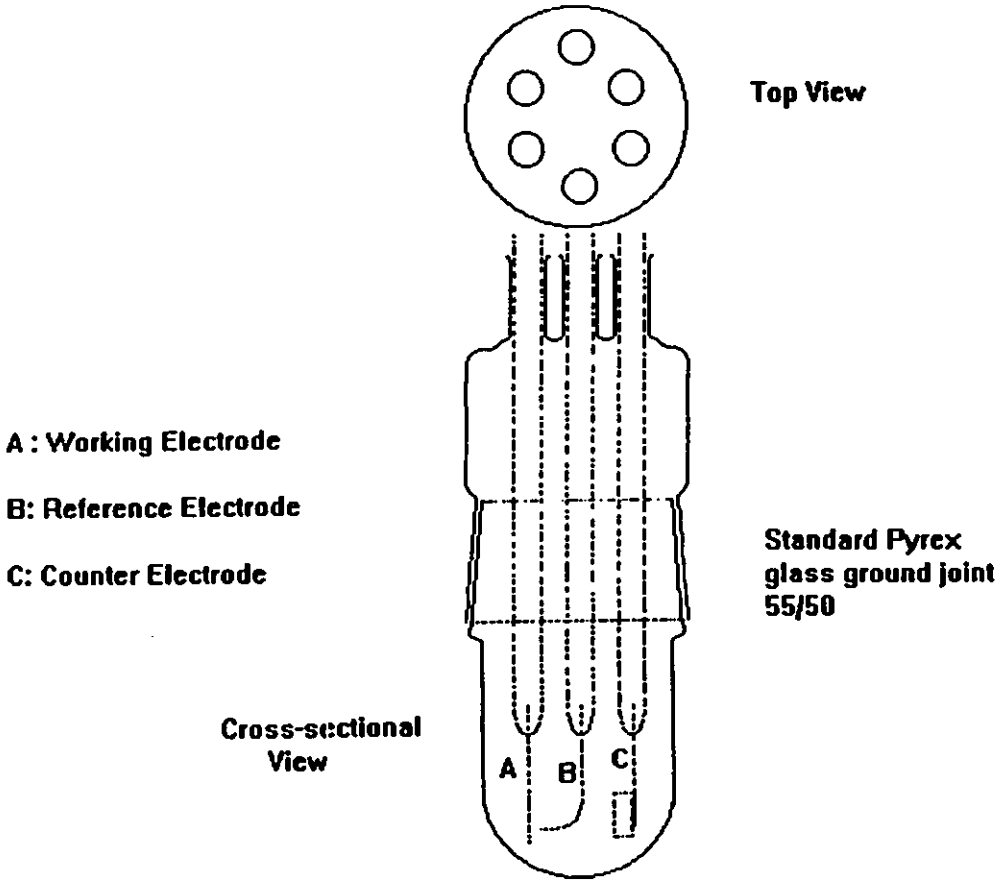


**Fig.15** One-compartment standard size Pyrex glass cell.

of palladium wires was used as the dynamic reference electrode. This cell is illustrated in Fig.15 and was used successfully in the stainless-steel bomb.

III.A.5.1c Two-Compartment Teflon Cell

This Teflon cell consisted of a standard 3-electrode arrangement with the reference electrode situated adjacent to the working electrode, without the use of a Luggin capillary. This was achieved by utilizing a piece of Pd wire or a Pt-oxide covered Pt wire as the reference electrode. In fact, the tips of these reference electrodes could be placed so close to the working electrode that any iR-drop could be ignored. The counter electrode, usually a platinum gauze, was located in a well separated counter electrode compartment. Between the counter electrode compartment and that housing the working and reference electrodes, was fitted a Nafion perfluorosulfonic acid membrane ( The Electrosynthesis Co., Inc., membrane type: 117 ) separator which provided a good electrolytic connection as well as a satisfactory barrier against diffusion of molecular gases. The membrane was mounted in a specially designed holder frabricated from Teflon. A detailed illustration of the cell and the membrane holder is shown in Fig.16.

III.A.5.2 Electrodes for Use in High Temperature/High Pressure Experiments

Three different types of electrode designs were utilized to match the three different kinds of cells described above. In general, they were highly resistive to the adverse experimental conditions and are relatively inexpensive.

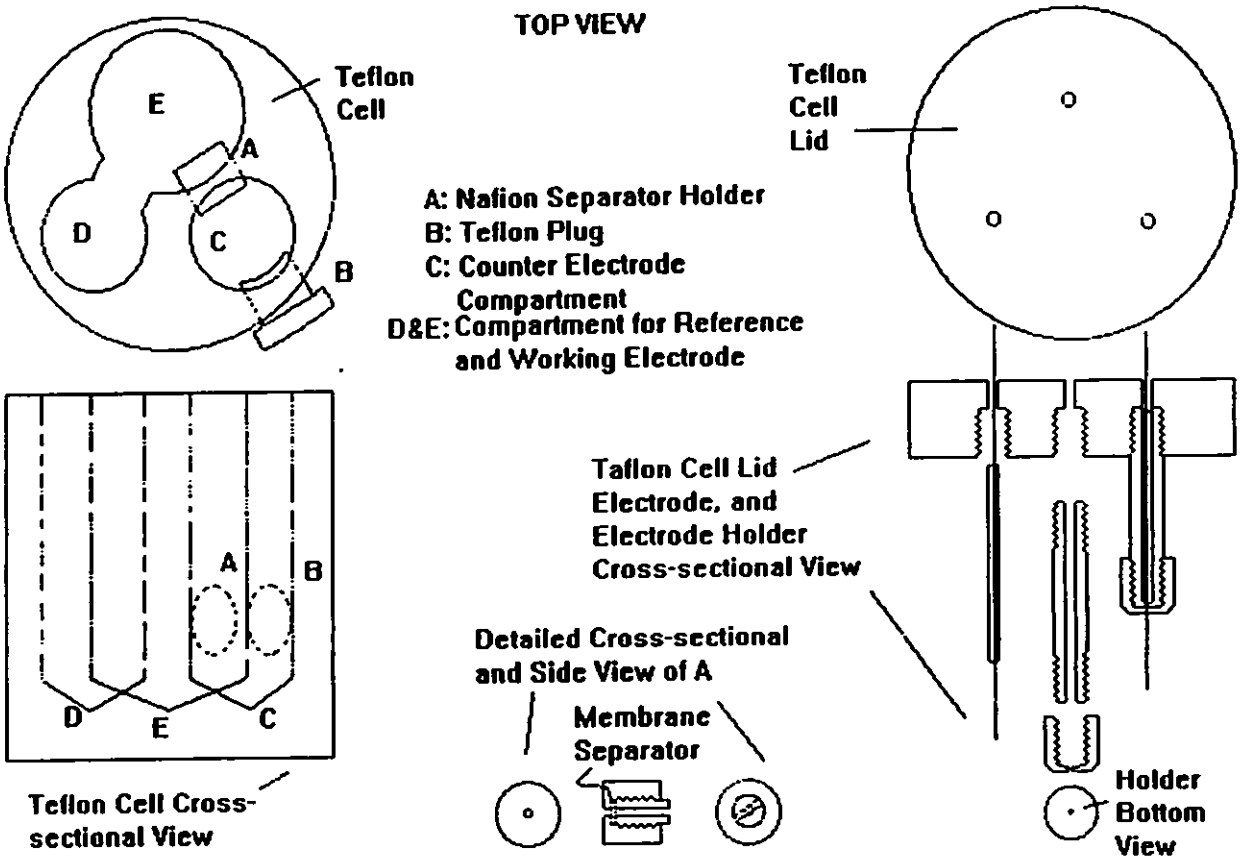


**Fig.16** Detailed illustration of the 2-compartment Teflon cell with the membrane holder.

III.A.5.2a Miniature Pyrex Electrodes

This type of electrode was designed to be used in the 3-compartment Pyrex glass cell ( III.A.5.1b ). Its main component was a male 7/16 Pyrex glass joint. The electrical lead was made of fine platinum wire ( about 0.05 mm in diameter ) hammered flat to facilitate a tight metal-to-glass seal. Fig.17 shows a schematic diagram of the electrode.

III.A.5.2b Standard Sized Pyrex Electrodes

This type of electrode was designed to be used in the one-compartment cell (III.A.5.1b ). It utilized the usual design and dimension of electrodes for use in cells for room-temperature experiments. The main feature of this kind of electrode is the special tungsten-to-uranium doped glass seal, developed by our glass blower, Mr. E. Kristoff, which was the result of much searching for the right metal-to-glass seal for use in the high-temperature/high-pressure aqueous environment. The electrode was prepared in the following way: a piece of clean platinum wire was first spot-welded to a piece of thin tungsten rod which was welded to a piece of nickel wire as the electrical lead and had been previously cleaned with potassium nitrate crystals in a flame, followed by thorough rinsing with distilled water; it was then air dried, and the tungsten/platinum joint was "beaded" ( precoated with glass ) with uranium-doped Pyrex glass, which allows the glass-to-glass seal to be made more easily. The whole assembly of Ni-tungsten-Pt was then sealed into a piece of Pyrex tubing of standard dimensions ( about 7 mm o.d. and 20 cm long ). Fig.18 shows a schematic diagram of the electrode.

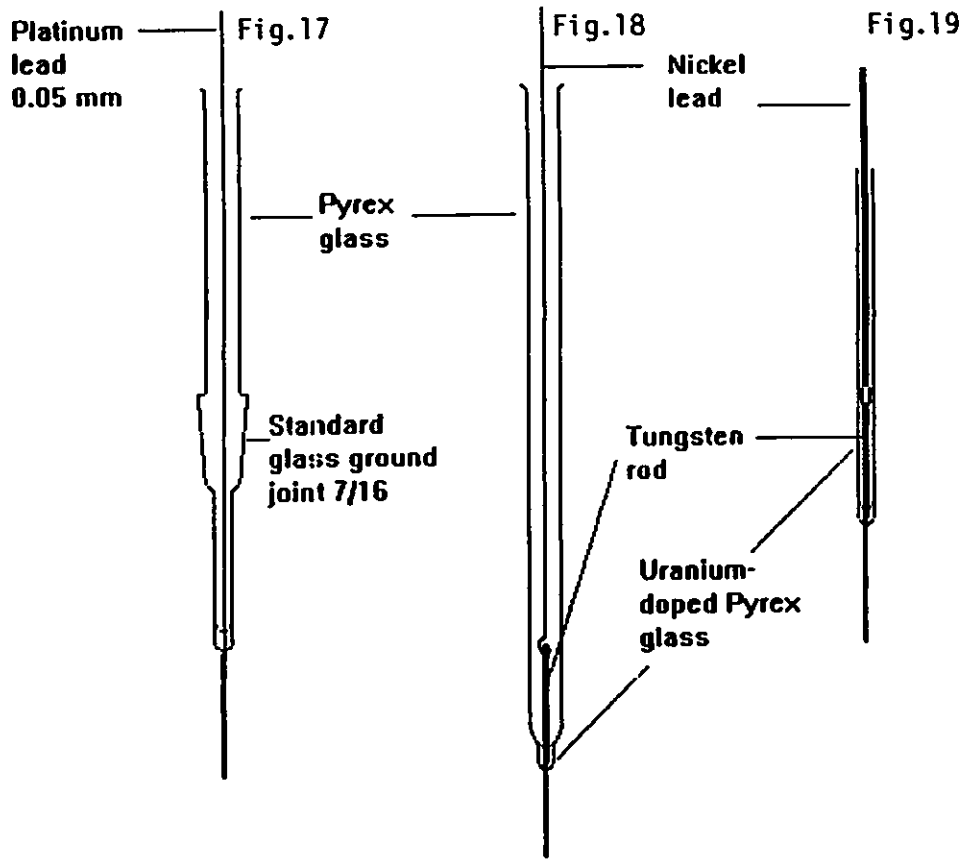


**Fig.17** Schematic diagram of the miniature Pyrex electrode.

**Fig.18** Schematic diagram of the standard-size Pyrex electrode.

**Fig.19** Schematic diagram of the miniature Pyrex/Teflon electrode.

III.A.5.2c Miniature Pyrex/Teflon Electrodes

This type of electrode was designed to be used in the 2-compartment Teflon cell ( III.A.5.1c ). The electrode consisted of a miniature Pyrex electrode of the same design as that described above (III.A.5.2b ) and a specially constructed Teflon sleeve which was meant to protect the Pyrex electrode from alkaline or acid corrosion. Before the Pyrex electrode was introduced into the Teflon sleeve, it was first covered with a thin layer of Teflon sealing tape. This was found to be essential as the Teflon sleeve did not provide complete isolation of the electrode from being in contact with the electrolyte. A schematic diagram of the electrode is shown in Fig 19.

## III.A.6 Systems Studied

### III.A.6.1 Reference Electrodes

#### III.A.6.1a Dynamic Hydrogen Electrode ( DHE )

The DHE consisted of two platinized-platinum gauze electrodes of about the same size ( about 1 $cm^2$ each ). The oxygen-generating electrode was located in the counter electrode compartment along with the cell's own counter electrode so that the hydrogen-generating electrode, which is situated inside the reference electrode compartment, would not be affected by the diffusion of oxygen. Stable potential readings were obtained so long as the reference electrode compartment was saturated with hydrogen gas generated during the cathodic electrolysis at the DHE.

The reference electrode was prepared in the following way. A platinum gauze electrode was first cleaned in warm aqua-regia solution, followed by thorough rinsing with

doubly-distilled water. The one which was to be used as the hydrogen electrode was protected cathodically in 1 N $H_2SO_4$ solution until ready to be platinized. The platinizing solution was a 2% chloroplatinic acid solution with no lead salt added. The platinizing process was carried out in a beaker filled with the above solution, the two electrodes being then connected to a d.c. current supply to be platinized. The current was adjusted to a value ( usually about 20 mA/cm$^2$ ) so that excessive gas evolution would be avoided. The polarity of the current was switched every minute or so until a fairly dark coating of Pt was observed on each electrode. The electrode was then rinsed in doubly-distilled water before use.

As long as the hydrogen electrode was cathodically polarized by a small d.c. current, the difference in potential between the DHE and the true reversible hydrogen electrode was small ( 10 to 20 mV at a current of 1 mA/cm$^2$ ) and could be made negligible when a smaller current of 50 to 100 $\mu$A/cm$^2$ was utilized as the polarizing current. The d.c. current supply consisted of a 9 V battery, a variable resistance box and a micro-ammeter.

III.A.6.1b Dynamic Pd/PdH Electrode

A pair of Pd wire electrodes of the same length ( about 2 cm ) was cleaned with aqua-regia solution for a short time and washed with doubly-distilled water. The Pd/PdH reference electrode was then prepared by cathodic constant current charging in the electrolytic cell. The reference electrode was oxidized for 1 minute, followed by a 90 second reduction at a current density of about 100 mA/cm$^2$. This cycling procedure was

continued for about 10 minutes with the reduction being the last step in the process. A constant and continuous cathodic current ( 50 - 100 $\mu A/cm^2$ ) was then used to polarize the electrode throughout the experiment. It was found that after the electrode had been polarized for some time, quite stable potentials could be obtained regardless of whether cathodic current was still passed or not.

III.A.6.1c Palladium Wire Reference Electrode

This type of reference electrode was prepared in the same manner as that described for the dynamic Pd/PdH electrode above, except that no constant current electrolysis was required. Instead, a high positive pressure of $H_2$ ( about 100 psi ) was used to establish the necessary Pd-PdH equilibrium. This type of reference electrode was used successfully in some of the HER experiments.

III.A.6.1d Platinum/Platinum-Oxide Electrode

An alternative type of reference electrode, the Pt/PtO system was used in some experiments. The Pt/PtO electrode was prepared chemically from a piece of Pt wire by heating in potassium nitrate to a high temperature. The Pt wire was first cleaned with aqua-regia, followed by repeated washing with doubly distilled water. Oxidation of Pt was then carried out by immersion of the previously cleaned Pt wire in a potassium nitrate melt at about 773 K for at least 1 hour. The platinum oxide-covered Pt wire was then rinsed with, and soaked in, distilled water for 30 minutes to dissolve any traces of nitrate. This "PtO"-covered wire was spot-welded to a tungsten rod ( 1 mm in diameter ) which

was then sealed into uranium-doped Pyrex glass as described earlier in section III.5.2b.

### III.A.6.2 Working Electrodes

#### III.A.6.2a Gold Electrodes

Gold electrodes were prepared from high purity Au wire about 0.5 mm in diameter in the following way. A length of gold wire was fused to a platinum bead which had previously been sealed into glass ( either Pyrex or uranium-doped, depending on the type of electrode and the experiment ). The electrode was cleaned in aqua-regia solution for 1 minute, followed by thorough washing with doubly-distilled water.

#### III.A.6.2b Platinum Electrodes

Platinum electrodes were prepared from high purity wire in the following way. A piece of platinum wire was cleaned in the usual way with aqua-regia, followed by washing with distilled water. The electrode was then spot-welded to a piece of thin W rod with Ni wire as electrical lead and was then sealed in uranium-doped glass as described in section III.A.5.2b or III.A.5.2c, depending on the type of electrode configuration required. The real surface area of the platinum electrodes was estimated from the charge required for deposition of a monolayer of adsorbed H on the electrode surface in a cyclic voltammetry experiment, assuming that 210 $\mu$C of charge is required for the formation of a full monolayer of adsorbed H on 1 $cm^2$ of Pt (111) surface.

III.A.6.2c Nickel Electrodes

Nickel electrodes were prepared from high purity Ni wire in the following manner. A piece of nickel wire about 2 cm long was first cleaned and degreased in 95% ethanol. The wire which may initially be covered with a layer of nickel oxide was then reduced in a Pyrex glass tube in the presence of a continuous flow of purified hydrogen gas at high temperature ( ca. 700 C ). The wire was heated carefully to red heat with the help of a glass blowing torch. Once the wire was free of oxide and had a bright metallic surface, the glass tubing containing the oxide-free nickel wire and an ample amount of hydrogen was then sealed off at both ends. The wire was kept in the glass capsule until ready for use.

Immediately before an experiment was started, the oxide-free nickel wire was spot-welded to a short piece of regular nickel wire which had previously been sealed into uranium-doped glass in the way described in section III.5.2c. Oxide formation was prevented by cathodic protection at all times when the electrode was not in use.

**III.A.6.3 Counter Electrodes**

The counter electrode was made of Pt-gauze and was in the form of cylinder. In the 3-compartment cell ( III.A.5.1a ), it was a large cylinder of about the same diameter of the concentric glass joint separating the working and the counter electrode compartments so that the counter electrode was securely located ( see Fig.14 ). A smaller Pt gauze cylinder was used in both the one- and two- compartment cells (III.A.5.1b and III.A.5.1c) in the usual way.

III.A.6.4 Solutions

Doubly-distilled water was used for preparation of all solutions. It was found that ultra-pure pyro-distilled water was not necessary for the type of work described in this thesis.

III.A.6.4a Sulphuric Acid Solutions

Aqueous $H_2SO_4$ solutions were utilized in one of the series of cyclic voltammetry experiments. The 1 N acid solutions were made up volumetrically from BDH Aristar-grade $H_2SO_4$ and doubly-distilled water. The purity of these solutions was found to be excellent as indicated by the resulting i/V profiles of a Pt electrode in a cyclic voltammetry experiment.

III.A.6.4b Perchloric Acid Solutions

1 N aq.$HClO_4$ solutions were used in several cyclic voltammetry experiments and were made up volumetrically from BDH Aristar grade 70% aqueous $HClO_4$ solution and the doubly-distilled water.

III.A.6.4c Sodium Hydroxide Solutions

0.2 N NaOH solutions were employed in most of the experiments involving either oxygen or hydrogen evolution. The alkaline solutions were made up volumetrically from BDH Aristar grade sodium pellets and the doubly-distilled water.

## III.B Experimental (OER at $\alpha$- and $\beta$- Lead Dioxides )

### III.B.1 Methods

#### III.B.1.1 Constant Potential, Steady-State Anodic Polarization

Potential against logarithm of current (V vs log i) Tafel relations were recorded by means of a computer-controlled PAR 173 potentiostat which enabled results to be obtained under very reproducible conditions of polarization potential and time; the latter, for each potential, was 10 s and the polarization potentials covered a range of 0.1 to 0.5 V positive to the open-circuit potential of the working electrode which was normally approximately about 1.60 V ( RHE ) for both $\alpha$- and $\beta$-$PbO_2$. The Tafel relations were determined in both ascending and descending directions of potential change but no significant differences were observed. Hence, only the *descending* Tafel relations are shown here and used in subsequent calculations in this thesis. The Tafel relations for freshly prepared lead dioxides were reproducible only after the first 30 minutes or so of polarization. Therefore, all the lead dioxide electrodes were pre-conditioned by polarizing at a high anodic potential ( ~ 2.00 V vs RHE ) for 30 minutes prior to taking measurements which were then quite reproducible. Such experiments were conducted at temperatures between 299 and 339 K.

#### III.B.1.2 Potential Relaxation Transients

The potential-decay transients, V(t), were recorded digitally in time (t) on a Nicolet 206 digital oscilloscope (cf.[48]) following interruption of various prior steady polarizing currents using a specially designed mercury contact switch. The procedure employed in

recording the decay transients was the same as for the high temperature experiments described in section III.A.4.5. Several transients were recorded over the potential range 2.00 to 2.15 V and 2.10 to 2.20 V, and corresponding current-densities of 5 to 20 mA $cm^{-2}$ and 4 to 12 mA $cm^{-2}$ for $\alpha$-$PbO_2$ and $\beta$-$PbO_2$, respectively.

These potential relaxation experiments were conducted at 299, 319, and 339 K.

III.B.1.3 A.C. Impedance Measurements

The a.c.impedance behaviour of the OER at the lead dioxides was recorded using a Solartron 1255 HF frequency response analyzer coupled with a computer-controlled PAR 273 potentiostat as described for the high temperature experiments in section III.A.3.4.6. Experiments were conducted at 298 K at frequencies from $10^{-3}$ to $10^{4}$ Hz over a range of d.c. potentials form 1.75 to 2.30 V (RHE). The impedance data were analyzed on a PC using a curve-fitting program (Complex Nonlinear Least Squares Immittance Fitting) provided by J.Ross Macdonald.

III.B.1.4 'iR' drop Corrections

'iR' drop values between the Luggin capillary of the reference electrode and the working electrode were measured by means of the a.c.impedance and the potential decay technique at various current-densities in the usual way. Values between 0 and 0.5 Ω were obtained from both methods with good agreement within experimental error; iR corrections were then made as necessary.

## III.B.2. Cell

A conventional 3-compartment glass cell provided with a Luggin capillary probe was used in the $PbO_2$ work. The solution in the compartment containing the $\alpha$- and $\beta$-$PbO_2$ working electrode was kept saturated with $O_2$ by bubbling. Temperature control was achieved by immersing the whole three-compartment cell, which was provided with glass-sleeved stopcocks, in a thermostatted water bath.

## III.B.3. Electrodes

### III.B.3.1 $\alpha$- and $\beta$-$PbO_2$ Electrode Preparation

Both $\alpha$- and $\beta$-$PbO_2$ electrodes were prepared by the procedure of Ruetschi *et al.* [35] involving constant-current electrodeposition from an appropriate electrolyte onto a platinum wire being sealed at both ends into Pyrex glass. The diameter of the platinum wire was 1.0 mm and the exposed surface area was in a range of 0.4 to 0.8 $cm^2$.

Since the objective of this work was to compare the electrochemical behaviour of $\alpha$- with that of $\beta$-$PbO_2$, reproducible electrode surfaces were essential. Three variables of the electrodeposition conditions were therefore strictly controlled in these experiments: a) electrolyte temperature; b) initial electrolyte concentration and c) deposition time. The electrodeposition of both types of $PbO_2$ electrodes was performed in a 50 ml one-compartment cell equipped with a concentric cylindrical Pt gauze counter electrode, a magnetic stirrer, a thermometer and a water-jacket held at 323 K. The deposition current used was 1 mA $cm^{-2}$ and lead dioxide was deposited onto a platinum wire for 19 h. to a thickness of approximately 0.1 mm. The electrolyte was renewed prior to each deposition.

At the end of deposition, the electrode was rinsed thoroughly with distilled water to remove any traces of $Pb^{++}$ ion and then air-dried and stored in a dry tube. In order to deposit adherent $PbO_2$ film, it was found that the Pt substrate must be roughened and degreased by brief immersion in a bath of chromic acid solution, followed by thorough washing with water prior to the electrodeposition. This pretreatment procedure provides a better support for the growth of the $PbO_2$ crystals. As a way to monitor the reproducibility of the lead dioxide deposits, a set of several electrodes of the same kind were prepared for each experiment. In spite of much effort to control the deposition conditions, some variations from one electrode to another still arose.

III.B.3.2 $PbO_2$ Electrode Characterizations

Scanning Electron Micrographs (SEM) of the surfaces of the electrodeposited $PbO_2$ electrode films were recorded using a Nanolab 7 Scanning Electron Microscope at magnifications corresponding to 0.1 to 10 $\mu$m per cm. The surfaces were examined before and after the electrochemical $O_2$-evolution experiments. Powder X-ray diffraction patterns of the lead dioxide deposits, after they had been stripped from the Pt wires, were recorded at the National Research Council of Canada in Ottawa and were compared with the respective standard pattern of $\alpha$- and $\beta$-$PbO_2$ (11-0549 and 22-0389) in Fig.61a,b. All attempts at recording diffraction patterns by the single-crystal X-ray diffraction method were, however, ineffective.

III.B.3.3 Reference Electrode

Potentials were measured against a reversible $H_2$ reference electrode (RHE) in the

**Fig.61a** Powder X-ray diffraction pattern of $\alpha$-$PbO_2$ deposit after it had been stripped from the Pt wire substrate. (Correction: the words "ID: GAMA PBO2 JIMMY HO" in the figure should read "ID: ALPHA PBO2 JIMMY HO").

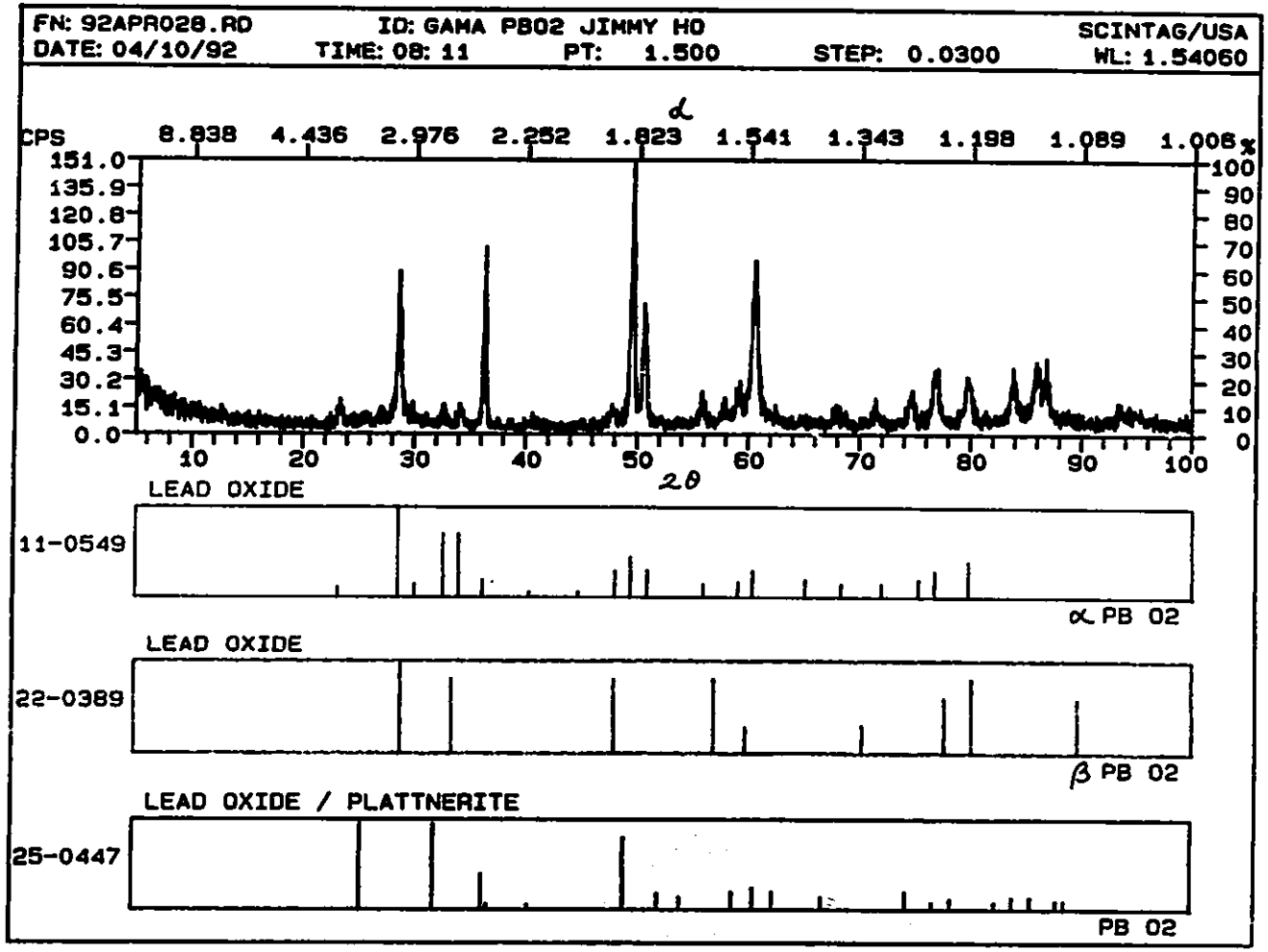

**Fig.61b** Powder X-ray diffraction pattern of $\beta$-$PbO_2$ deposit after it had been stripped from the Pt wire substrate as in Fig.61a for the $\alpha$ deposit.

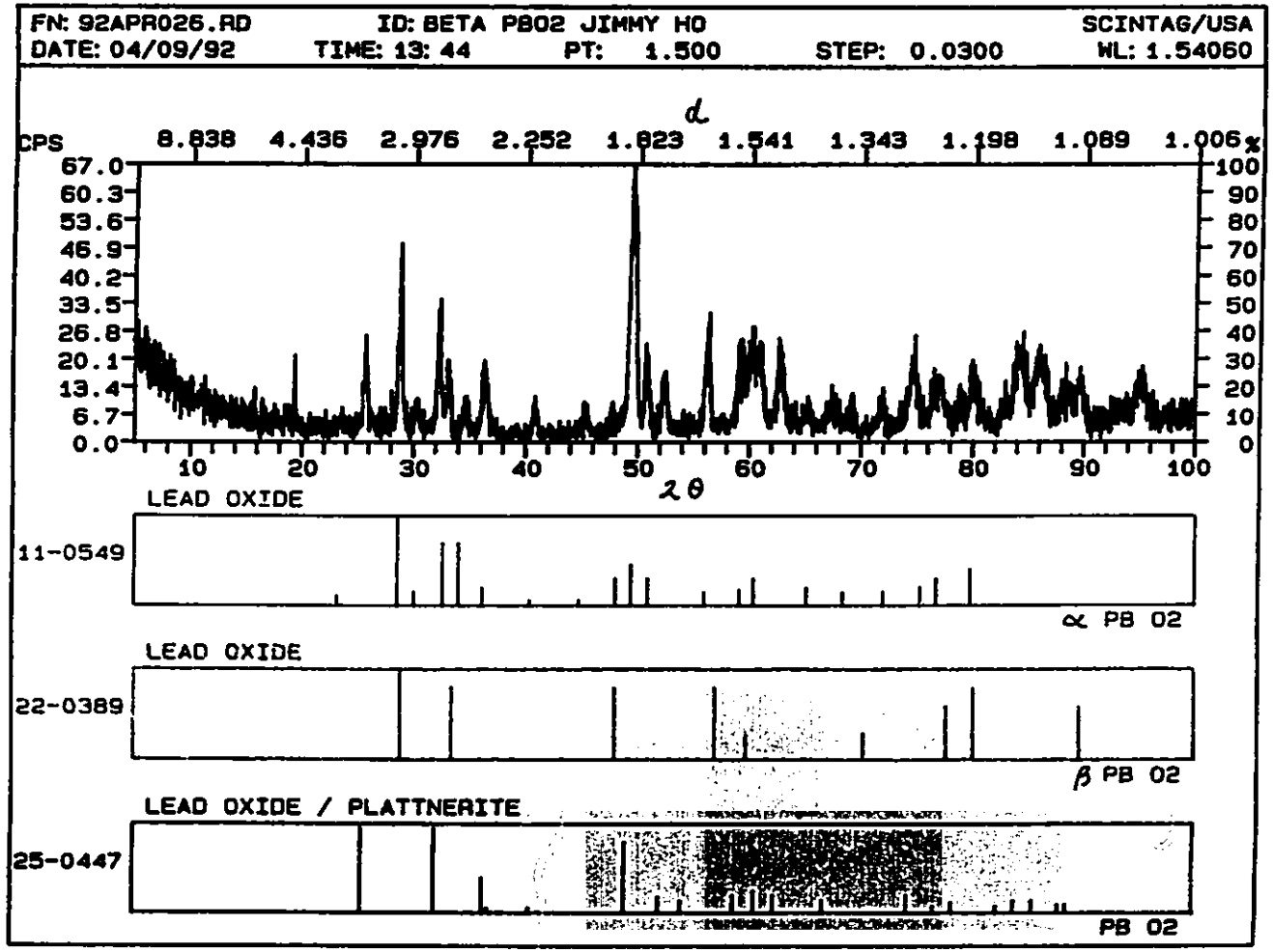

same solution and at the same temperature as that of the $PbO_2$ electrodes.

III.B.3.4 Counter Electrode

A piece of Pt gauze of about 1 $cm^2$, spot-welded onto a Pt wire sealed into soda glass, was used as the counter electrode.

## III.B.4. Solutions

1 M aq. perchloric acid solutions were prepared from BDH Aristar grade 60 % $HClO_4$ in high purity water. The electrolyte used for the electrodeposition of $\alpha$-$PbO_2$ was prepared by making a 1:1 dilution of a stock solution of lead plumbate with water. The stock solution was prepared by mixing 500 ml of saturated sodium acetate, 100 ml of saturated lead acetate, 1.0 *l* of carbonate-free saturated KOH and 500 ml of water. For the electrodeposition of $\beta$-$PbO_2$, the electrolyte used was an aqueous $Pb(NO_3)_2$ solution (240 g $dm^{-3}$). Water, doubly distilled from alkaline $KMnO_4$, was used throughout the work.

## III.B.5. Gases

Hydrogen gas, purified from a gas-line consisting of heated fine copper turnings in conjunction with a palladized-asbestos catalyst, activated charcoal(-193 C) and molecular sieves was used for the reversible $H_2$ reference electrode. High purity $O_2$ gas, used for bubbling over the $PbO_2$ anode surfaces, was as supplied by Air Products, without further purification.

## IV. RESULTS AND DISCUSSION

In this section on results and discussion the material is divided into four sections depending on the type of electrode process studied.

Since a considerable amount of work has been done on oxide formation and reduction processes at noble metals by the cyclic voltammetric technique, the first section (Section IV.A) will be devoted to results obtained for these processes at such noble metals, here platinum and gold, mainly in one alkaline and two acid solutions and at temperatures substantially above room temperature, up to 538 K. The second section (Section IV.B) is concerned with the cathodic hydrogen evolution reaction ( HER ) process in alkaline solutions at the two noble metals plus a baser transition metal, nickel, at temperatures up to 473 K. The third section (Section IV.C) is about the anodic oxygen evolution reaction ( OER ) process at platinum in alkaline solutions at temperatures up to 473 K. Finally, in relation to the third section, there will be a separate fourth section (Section IV.D) devoted entirely to the OER studied at two dimorphic forms of lead dioxide at several temperatures ranging from 298 to 339 K. In each of the last three sections (Sections IV.B, IV.C and IV.D), the results are presented and discussed in three sub-sections corresponding to results obtained by the three different experimental techniques employed here for the gas evolution reacitons, *viz.*, i) potential vs log(current) or Tafel relations; ii) potential-relaxation and iii) a.c. impedance.

### IV.A. Oxide Film Formation and Reduction

In an attempt to understand the effect of temperature, T, over a wide range of T,

on the oxide formation and reduction processes at noble metals, Au and Pt were studied in 1 N aq. $H_2SO_4$, 1 N aq. $HClO_4$ and 0.2 N aq. NaOH solutions over ranges of temperature from 293 to 473 K. In the following paragraphs, for the sake of simplicity, the concentrations of the individual acid or alkaline solution will not be further referred to.

The results are organized into two sections. First the behaviour of the noble metals recorded at room-temperature ( R.T.) will be presented and discussed, then followed by that at elevated temperatures. Comparison between results obtained at different temperatures will be made wherever appropriate.

## IV.A.1 Cyclic Voltammograms for Gold and Platinum at Room Temperatrue

### IV.A.1.1 General

The results obtained for gold and platinum at R.T. were similar to those reported by other workers [55,56,57] in the literature and are given only for reference. The main features for both noble metals between the potentials for the evolution of hydrogen and oxygen were the oxide film formation and reduction with hysteresis being exhibited between these processes. In the case of platinum, the extra features of hydrogen adsorption and desorption were also observed as is well known from previous works. The behaviours are demonstrated in Figs.22a and 21a which show the cyclic voltammograms or i/V profiles for Pt in $H_2SO_4$ and for Au in $HClO_4$ taken to various anodic potential limits. As can be seen from these examples, when the noble metal electrodes were anodized under the dynamic potential-sweep conditions, an oxide film is formed. The

potential range over which the oxide film is formed before evolution of oxygen commences significantly was about 0.8 to 1.5 V ( vs Pd/PdH ) and 1.3 to 1.6 ( vs DHE ) for Pt and Au, respectively. The oxide films formed in the anodic potential sweep are always completely reduced during the returning cathodic potential sweep. The anodic oxide formation i/V profiles recorded under these conditions usually exhibit a complex structure: thus, for the case of platinum, at least three distinguishable but overlapping anodic peaks are observed suggesting that a rather complex process is involved ( cf. refs. [27] ). The cathodic oxide reduction profiles, however, appear to be much simpler, with just one single peak being usually observable although for gold in $HClO_4$ a small shoulder is seen at more negative potentials. The nature of these oxide films and the mechanism of their formation has still not been fully resolved but the charges involved in the process of say platinum oxide formation indicate that the thickness of these films is on the order of one or two monolayers. Further, the charges required for the reduction of these oxide films, for a wide range of anodic potential limits, are practically the same as those for their formation as can be seen in the $Q_c/Q_a$ ratios[3] plotted in Fig.29a for Pt in $H_2SO_4$ and in Fig.29 for Au in $HClO_4$. Thus, it appears as though the oxide formation and reduction processes are, from a charge point of view, reversible but the hysteresis indicates that the overall electrode surface process is irreversible, except as found in earlier work [32] for the first 10 ~ 15 % of the monolayer.

---

3

$Q_c$ and $Q_a$ are the respective charges corresponding to the reduction and oxidation i/V profiles of an electrochemical process such as oxide film formation and reduction. The $Q_c/Q_a$ ratio can usually be used as a means to evaluate the charge balance of the system with respect to the oxidation and reduction processes involved.

The process of hydrogen adsorption and desorption at Pt, which arises in the potential range of 0.0 to 0.3 V ( vs Pd/PdH ), however, seems to be a much simpler and more reversible process, as illustrated in Fig.22a. Principally, both the anodic and cathodic i/V profiles exhibit two major narrow peaks and are almost mirror images of each other. These are examples of a totally reversible electrode surface process with a simple reaction mechanism as has been treated elsewhere [121]. In fact, the charge involved in the H adsorption process corresponds quantitatively to that of a monolayer of UPD H and can be used in estimating the real surface area of a Pt electrode when properly corrected for the double-layer charging contribution.

IV.A.1.2 Reversibility and Hysteresis Behaviour at R.T.

IV.A.1.2.a Oxide Reduction Potential vs Anodic Potential Limits

Contrary to the hydrogen adsorption/desorption processes, the oxide formation and reduction processes exhibit a high degree of hysteresis between the relatively broad oxide formation and reduction peaks ( i.e. they are not mirror images ). Moreover, as complex anodic i/V profiles are observed for these oxide formation processes and the fact that their corresponding cathodic oxide reduction peak potentials depend on the anodic potential limits, suggests that there are stepwise processes involving rearrangement of the surface film [46] as potential becomes more positive, giving rise to the formation of a more stable oxide film. This can be seen both for Pt in Fig.24 and Au in Fig.25. If there were only one type of oxide formed at the noble metal surface and no rearrangement of the previously formed surface film were involved, then the cathodic reduction potential should

be independent of the anodic potential limit except for the total charge passed.

IV.A.1.2.b Anodic and Cathodic Peak Potential vs Sweep Rate

Fig.31 shows the effect of the rate of potential sweep on the anodic and cathodic peak potentials for Pt in $H_2SO_4$. Similar behaviour was also observed for Au in both $HClO_4$ and $H_2SO_4$ acids. It is seen that these plots are composed of two linear regions. The sweep rate at which the lines join and change slope is termed "$s_o$" as mentioned in the Introduction (cf. ref.[29]). At sweep rates below $s_o$, the process is to be regarded as "reversible" and above $s_o$, the process becomes kinetically irreversible. Thus, for the sake of discussion, the linear region below $s_o$ is referred to as the "reversible region" while the one above $s_o$ is called the "irreversible region". These kinds of plots are sometimes called "kinetic plots" as kinetic parameters such as $s_o$ and corresponding Tafel slopes can easily be evaluated. It is evident that the kinetic plots obtained for Pt in $H_2SO_4$ are quite similar to those for Au in $HClO_4$ and Au in $H_2SO_4$. That is, the potential of the anodic and cathodic peaks *do* depend on sweep-rate; however, there are some significant apparent effects at sweep-rates that are lower than $s_o$. For instance, for the oxide formation process, it was found that the slopes of the "reversible" region of the kinetic plots are $-0.018$ V/decade of sweep rate for Pt in $H_2SO_4$ and 0.024 and 0.040 V/decade of sweep rate for Au in $HClO_4$ and $H_2SO_4$, respectively. This is a good indication therefore that these oxide formation processes are not as "reversible" as expected at R.T. but these anomalous effects may be associated with slow anion adsorption/desorption. These plots also suggest that the oxidation of Pt in $H_2SO_4$ is apparently a more reversible process than

that of Au not just because there is less sweep rate dependence of its anodic peak potentials but because a longer reversible region ( cf. Fig.28 ) is exhibited.

It was found that for Pt, the oxidation process did not become irreversible until a sweep rate of about 20 V/s was reached while for gold, the process showed onset of irreversibility already at a sweep rate as low as 0.2 V/s in $HClO_4$ and about 1 V/s in $H_2SO_4$. In other words, Pt exhibits a higher "$s_o$" value than does Au.

For the oxide reduction processes, behaviour similar to that of the oxide film formation was observed except that there seems to be a larger dependence of peak potentials on sweep rate and lower "$s_o$" values are recorded for both Pt and Au. Typically, the apparent slopes for the "reversible region" of the kinetic plots are 0.018 V/decade for Pt and 0.033 V/decade and 0.06 V/decade for Au in $HClO_4$ and $H_2SO_4$, respectively.

The "irreversible region" of these kinetic plots provides information about the kinetics of the oxide film formation and reduction processes since their slopes have the same significance and are equal to their Tafel slopes as mentioned in the Introduction. Unfortunately, the accessible range of $s$ values was not enough to provide sufficient data points to allow reliable estimation of the slopes to be made in most cases, particularly for those at higher temperatures as will be seen later. Roughly estimated, the Tafel slopes for the oxide film formation processes are 0.036 V/decade of sweep rate for Pt in $H_2SO_4$ and 0.12 and 0.08 V/decade of sweep rate for Au in $H_2SO_4$ and $HClO_4$, respectively.

It is interesting to note that some of the Tafel slopes reported above could be explained by a simple mechanism of oxide formation. For instance, a slope of 0.12

V/decade implies that the first discharge step (I) is rate-controlling in the following postulated mechanism [58] which is speculative in nature and formally analogous to the HER or OER discussed earlier in the Introduction section.

In acid solutions, where M represents noble metal surface sites:

$$\text{(I)} \quad M + H_2O \rightarrow M(OH) + H^+ + e^- \qquad (69)$$

followed by

$$\text{(II)} \quad M(OH) \rightarrow M(O) + H^+ + e^- \qquad (70)$$

or alternatively to (70)

$$\text{(II)} \quad M(OH) + M(OH) \rightarrow M(O) + H_2O \qquad (71)$$

Here the "OH" or "O" species represent chemisorbed species on the metal surface but later, as the film exceeds a monolayer, states on the already developed oxide film. (Eventually these species are intermediates in anodic $O_2$ evolution).

The oxide reduction processes at the noble metals at R.T. are quite similar to those of oxide formation as far as the magnitude of their Tafel slopes are concerned. Typically, a slope of 0.12 V/decade was obtained for Au in both acids and about 0.08 V/decade for Pt. Incidentally, the Tafel slopes for the oxide formation and reduction at Au in $H_2SO_4$ are both near 0.12 V/decade. It is reasoned therefore that both oxide formation and reduction processes at gold in $H_2SO_4$ follow a similar reaction mechanism at R.T. Since it was not the intention of the present work to provide extensive experimental work on the mechanistic aspects of the oxide film formation and reduction process, no further speculations will or need be made here, at least with regard to the rate-determining step.

The main concern of the present work was, however, to investigate if and how

these processes could be made more reversible at temperatures substantially above room as will be shown in the next section by using essentially the same data treatment techniques that are employed here for results obtained at R.T. as reference examples.

## IV.A.2. Cyclic Voltammograms for Pt and Au at Elevated Temperatures

### IV.A.2.1 General

In contrast to the cyclic voltammograms obtained at R.T., those obtained at elevated temperatures, especially at temperatures well above 373 K, exhibit current peaks that are relatively narrower in shape and, as might be expected, much higher in current density. Some typical examples are presented in Figs 20a, b and c, 21a, b and c and 22a, b and c for gold in $H_2SO_4$, $HClO_4$ and platinum in $H_2SO_4$, respectively.

It should be emphasised that in spite of the extremely corrosive high-temperature/high-pressure conditions under which these cyclic voltammograms were recorded, remarkably "clean" double-layer regions were observed, e.g., between 0.5 to 1.0 V at Au and 0.3 to 0.7 V at Pt in $H_2SO_4$ at 473 K. Thus, this is a good indication that a contaminant-free environment was achieved inside the elevated temperature bomb, i.e., without incidental impurity currents arising significantly. This is to be regarded as a substantial experimental achievement but one that did not materialize without lot of frustrating preliminary work.

One of the consequences of increasing the temperature is that the processes of oxygen and hydrogen evolution commenced earlier ( i.e., at potentials less negative in the case of the cathodic HER and at potentials less positive in the case of the anodic OER than

at R.T.).

Perhaps the best way to visualize this is by considering the following example of hydrogen adsorption and desorption at Pt in $H_2SO_4$.

The T dependence of the H adsorption and desorption processes at Pt in $H_2SO_4$ was presented in Fig.23. Both stages of the H adsorption/desorption process exhibited a negative temperature coefficient, i.e., the peak potentials shifted to lower values with increasing T's. Up to about 373 K (Fig.22b), the typical two peak "butterfly" feature of the i/V profiles is maintained, suggesting that the processes remained highly reversible. At 423 K and above, the peak for weakly adsorbed H which arises at potentials > 0.1 V (vs Pd/PdH ) at lower temperatures could hardly be identified as it merges with the current profile for $H_2$ evolution. However, the strongly adsorbed H which is found at higher potentials of about 0.2 V (vs Pd/PdH ) at lower T's, is still observable at T's as high as 478 K (Fig.22c). These observations could be explained by the fact that first, hydrogen evolves at a more positive potential as T increases and second, the H adsorption/desorption peaks have a negative temperature coefficient. In fact, at 529 K (Fig.22d), when the same cathodic potential limit of zero volt vs Pd/PdH was used as at R.T., the i/V profiles exhibited a huge anodic peak at about 0.5 V vs Pd/PdH corresponding to the re-oxidation of some of the molecular $H_2$ evolved during the sweep experiment, under these conditions of sweep range. The correlation between the cathodic limits of the sweep and the current amplitude of the peak strongly support this view. As to the effect of T on the anodic OER, it is demonstrated in Fig.20c that oxygen had already started to become evolved at 1.4 V vs Pd/PdH at Au in $H_2SO_4$ at 450 K as compared to > 1.7 V at R.T.

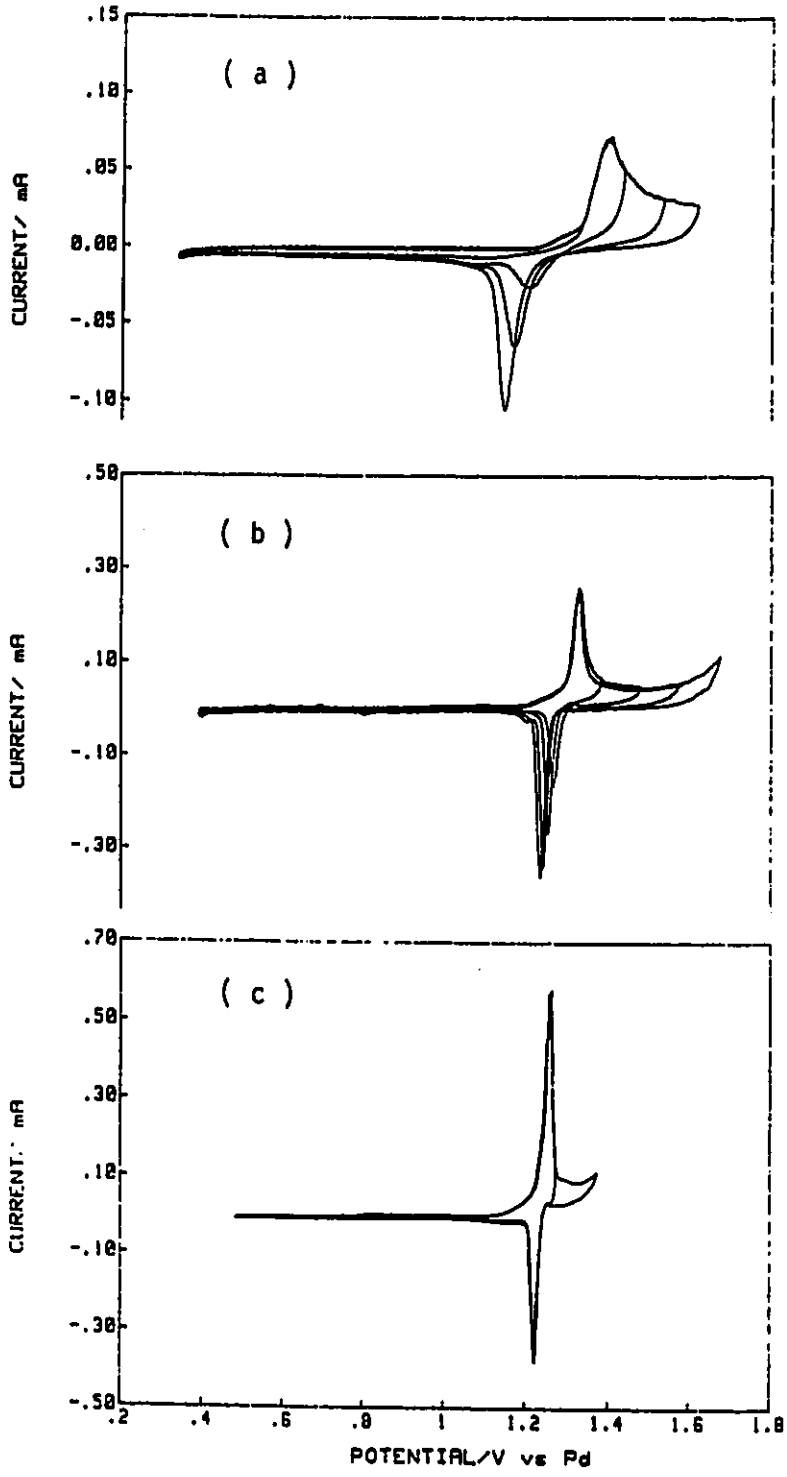


**Fig.20** Cyclic voltammograms for the oxide film formation and reduction processes at gold in 1 N $H_2SO_4$ solutions at three temperatures; a) 297 K, b) 377 K and c) 450 K.

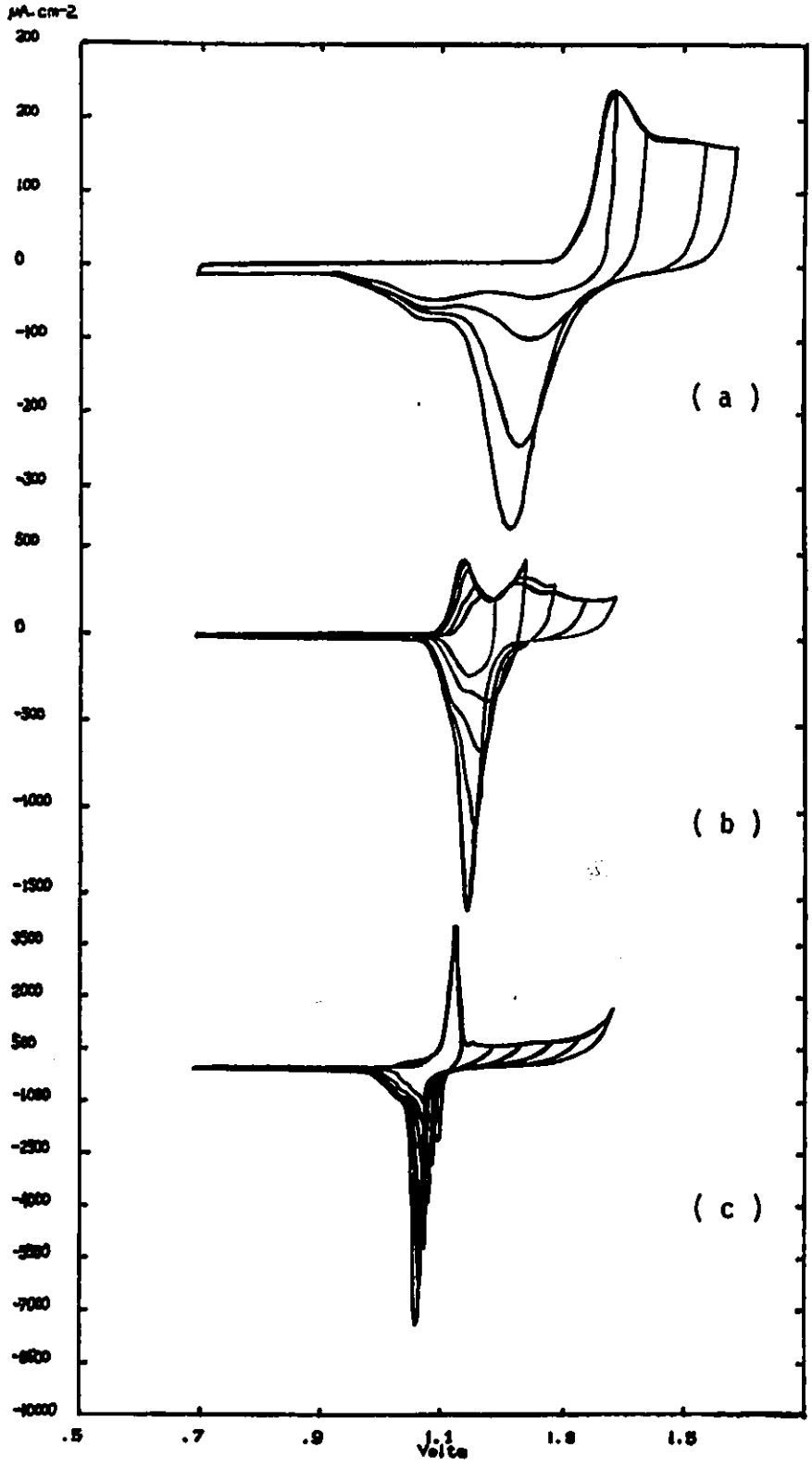


**Fig.21** Cyclic voltammograms for the UPD process at gold in 1 N $HClO_4$ solutions at three temperatures; a) 296 K, b) 398 K and c) 473 K.

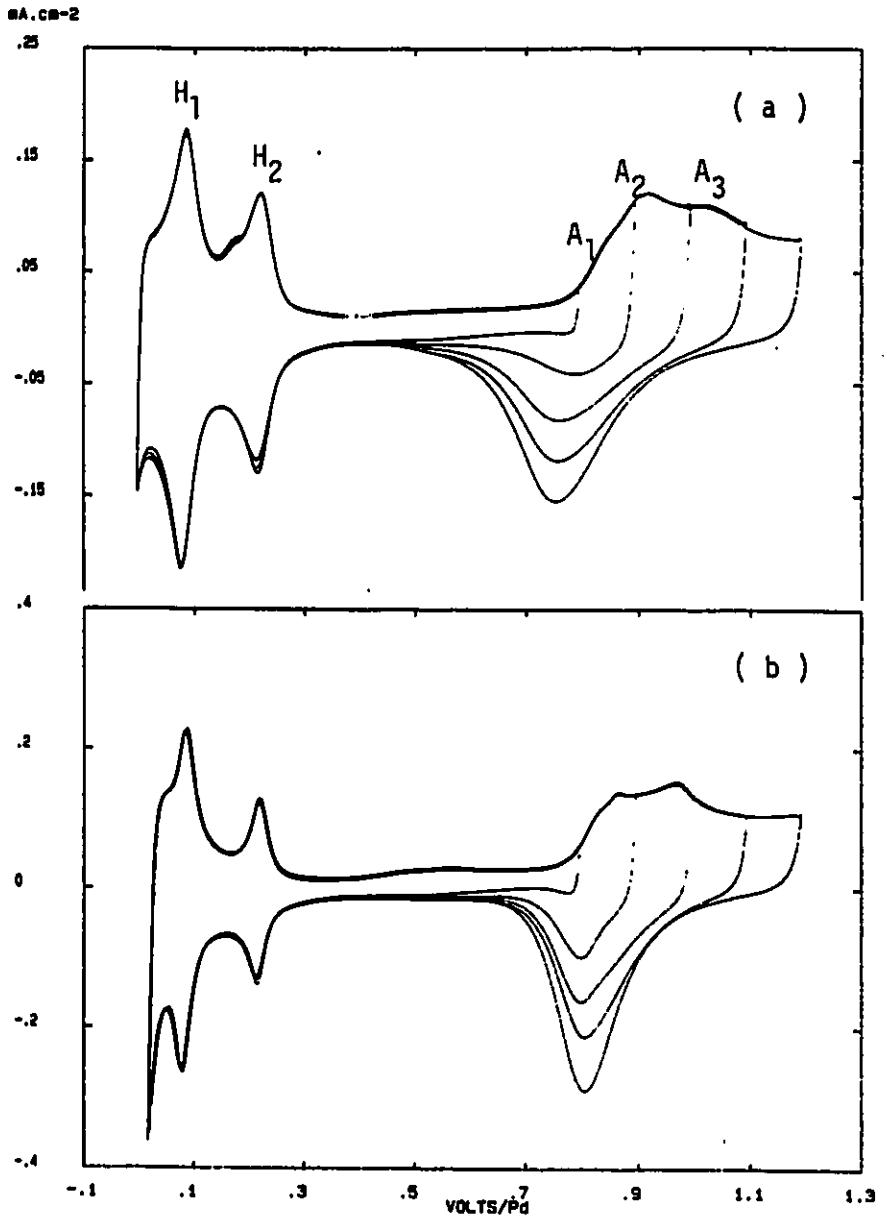


**Fig.22** Cyclic voltammograms for the oxide film formation and reduction processes at platinum in 1 N $H_2SO_4$ solutions at four temperatures; a) 295 K, b) 373 K c) 478 and d) 529 K.

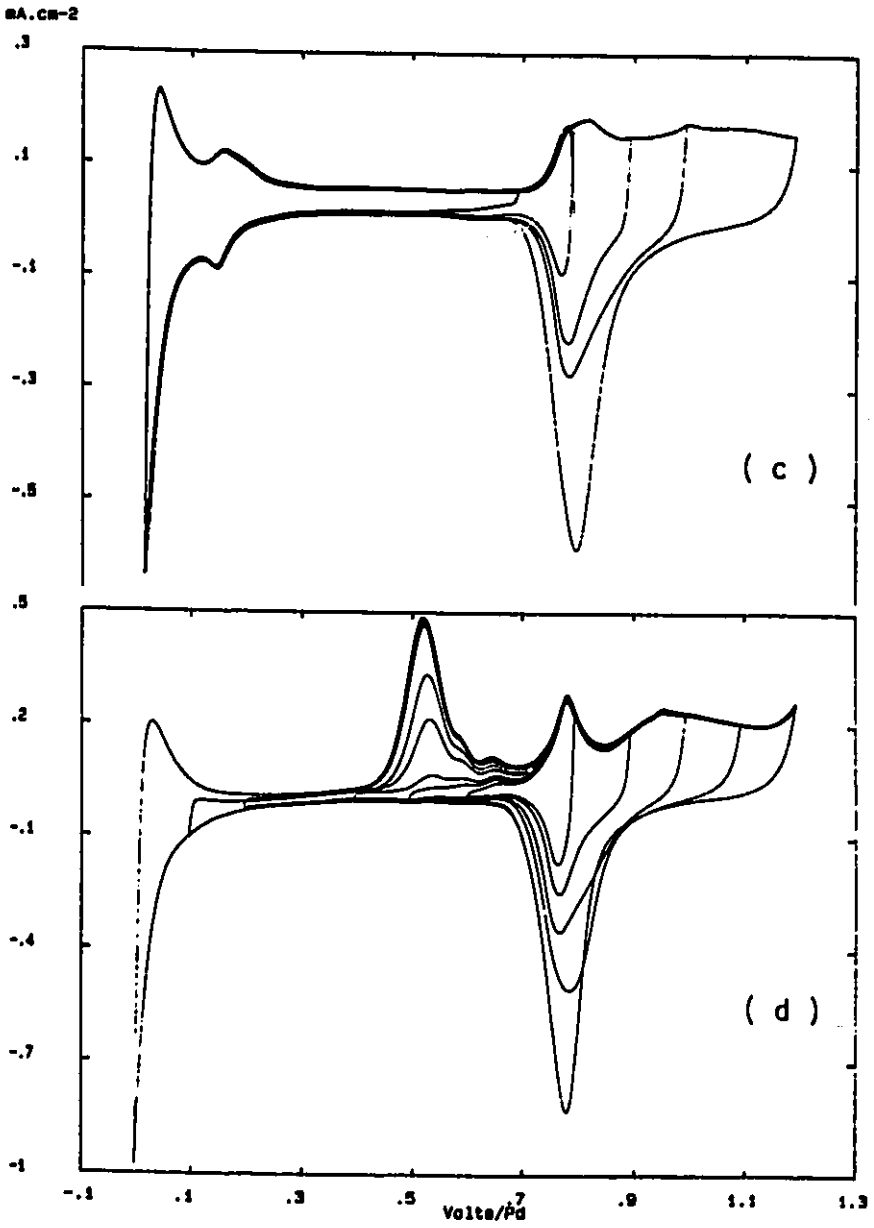


**Fig.22** Cyclic voltammograms for the UPD process at platinum in 1 N $H_2SO_4$ at four temperatures; a) 295 K, b) 373 K c) 478 and d) 529 K.

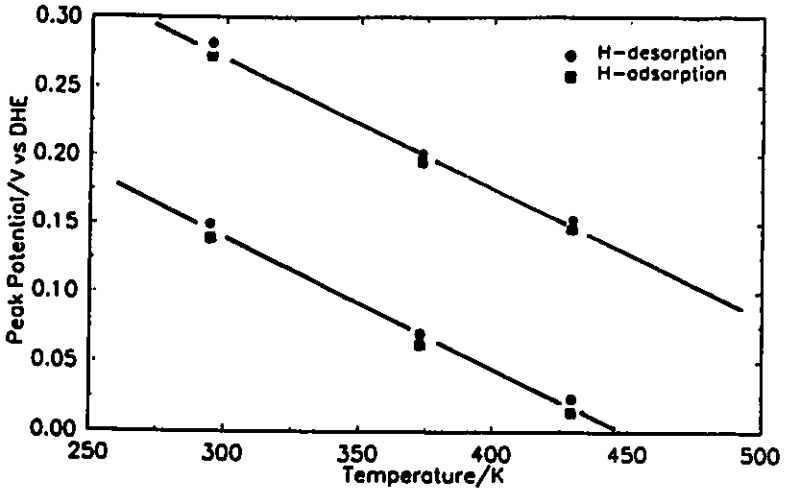


**Fig.23** Plot of the hydrogen adsorption/desorption peak potentials vs temperature for Pt in 1 N $H_2SO_4$.

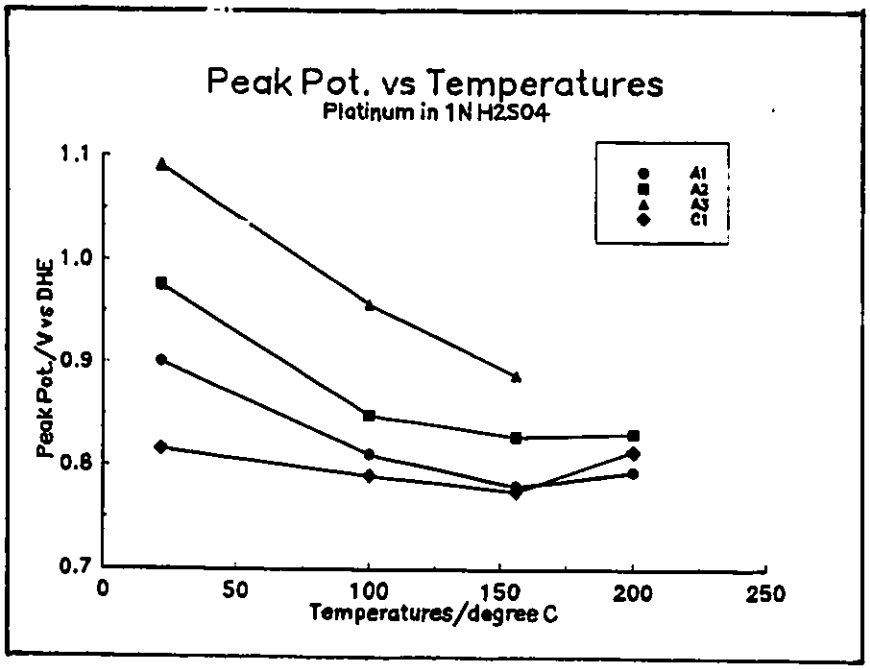


**Fig.23a** Plot of anodic/cathodic peak potential difference, $V_a$-$V_c$, vs temperature for platinum in 1 N $H_2SO_4$.

For the effect of T on the oxide film formation and reduction processes, it was found that both Pt and Au behaved in a similar way, especially in regard to how T enhances the reversibility of the process, the main point of interest here. In general, other than sharper and larger peaks that are observed at higher temperatures as mentioned earlier, the anodic i/V profiles are also simpler, or more symmetrical as can be seen, for example, in Fig.20c.

One feature that is not observed at R.T. but becomes rather important at elevated temperatures is that oxide film and/or anodic metal dissolution commences significantly. As expected, dissolution is a problem far more important at Au than at Pt, particularly in alkaline solutions as will be discussed later but first, the relation between T and reversibility of the oxide formation and reduction process will be discussed in the following paragraphs (Section IV.A.2.2 etc.).

For Pt in $H_2SO_4$, three states of oxide film formation and one reduction peak could be observed throughout most of the temperature range studied, up to 478 K; their relative intensities (currents) and peak potentials varied with T as illustrated for four temperatures in Figs 22a, b, c, and d. Above 478 K, however, the number of distinguishable peaks became reduced, probably due to overlapping of nearby ( on the V scale ) peaks.

### IV.A.2.2 Relationship between Temperature and Reversibility

#### IV.A.2.2.1 Cathodic Peak Potential vs Anodic Potential Limits

##### IV.A.2.2.1a Platinum

At Pt the cathodic peak potential was a function of anodic potential limits even at

elevated temperatures, as can be seen in Fig.24, but did not seem to be affected by increasing T, at least in the T range 373 to 529 K. In other words, the oxide film formation is probably still a stepwise process at higher temperatures involving several stages of formation and rearrangement of the previously formed oxide film. As a result, hysteresis remains. Nevertheless, the overall oxide formation process is seen to be more reversible as demonstrated by the i/V profiles at 529 K ( see i/V profile in Fig.22d when the anodic limit = 0.8 or 0.9 V vs Pd/PdH ) when the anodic potential limit was made not too positive relative to the onset oxide potential; then a completely reversible oxide formation/reduction peaks was obtained. i.e., mirror image profiles were observed (Fig.22d).

IV.A.2.2.1b Gold

In the case of gold, especially in $H_2SO_4$ solutions, extremely narrow and sharp oxide film formation and reduction peaks were observed at elevated temperatures, as exemplified in Fig.20c. It was noted earlier that the dependence of the cathodic peak potential on the anodic potential limits is particularly important for gold in $H_2SO_4$ at R.T. However, it can be seen in Fig.25 that with increasing T, the degree of this dependency gradually diminished until at a T of about 425 K, above which, cathodic peak potential became independent of anodic potential limit. This observation is a good indication of approach to complete kinetic reversibility. Further, this could be linked to the fact that at temperatures higher than 425 K, the shape of the i/V profiles became so much simpler that probably only *one* single stage of formation of the oxide was involved. In fact, the

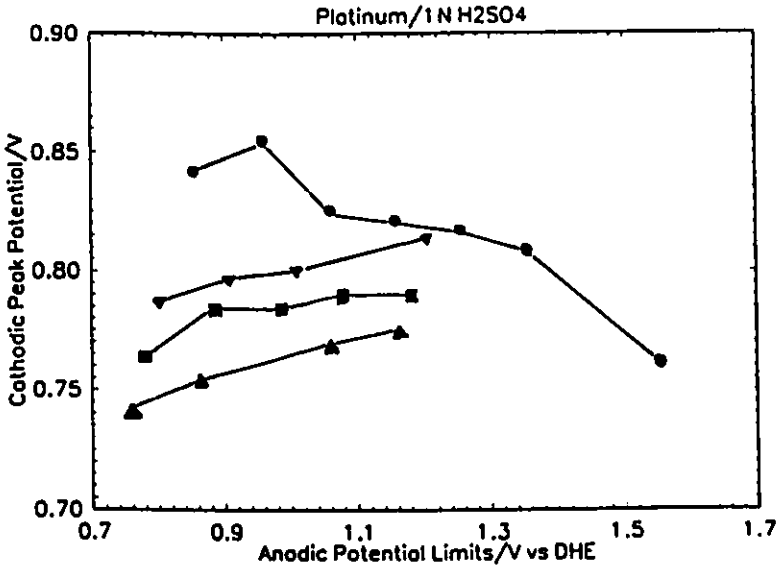


**Fig.24** Plot of cathodic peak potential vs anodic potential limits for the oxide formation and reduction processes at platinum in 1 N $H_2SO_4$ at 4 temperatures (●) 295 K, (▼) 373 K, (■) 429 K and (▲) 478 K.

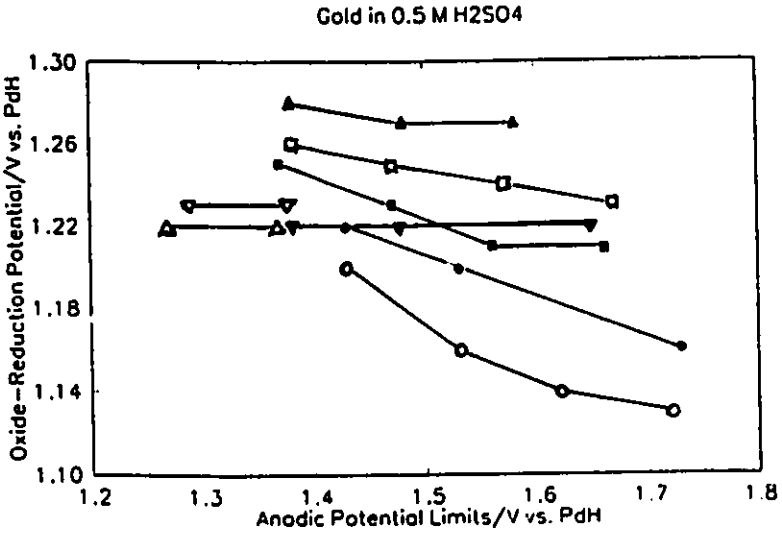


**Fig.25** Plot of cathodic peak potential vs anodic potential limits for the oxide formation and reduction processes at gold in 1 N $H_2SO_4$ at 8 Temperatures (○) 297 K, (●) 321 K, (■) 350 K, (□) 377 K, (▲) 402 K, (▼) 425 K, (△) 450 K, and (▽) 476 K.

anodic profile was almost a mirror image of the cathodic one ( see Fig.20c ). For Au in $HClO_4$, as for Pt in $H_2SO_4$ acid, T does not seem to have much influence on the way the reduction of oxide is dependent on the anodic potential limits.

IV.A.2.2.2 Anodic vs Cathodic Peak Potential Relations

IV.A.2.2.2a Gold

Perhaps a more direct way of treating the temperature dependence of the reversibility of the oxide formation and reduction process would be by plotting their anodic and cathodic peak potentials against T. Such a plot is shown in Fig.26 for Au in $H_2SO_4$. Clearly, the potential of the anodic peak ( when it is a principal one, easily resolvable ) becomes less positive while the cathodic one is shifted in the opposite direction with increasing T up to about 425 K. Then their potentials became constant independent of further change of T. Note that this result is also consistent with that obtained for the cathodic peak potential vs anodic potential limit plot above. Similar behaviour was also observed for Au in $HClO_4$. By taking the difference between the anodic and cathodic peak potentials, one can see clearly how the reversibility of the process is being improved by increasing T. This is demonstrated in Fig.27 for gold in $HClO_4$. Note that the anodic/cathodic peak potential difference, denoted as $V_a$-$V_c$, is actually approaching "0" above say 398 K, i.e., there is complete apparent reversibility between the anodic and cathodic processes.

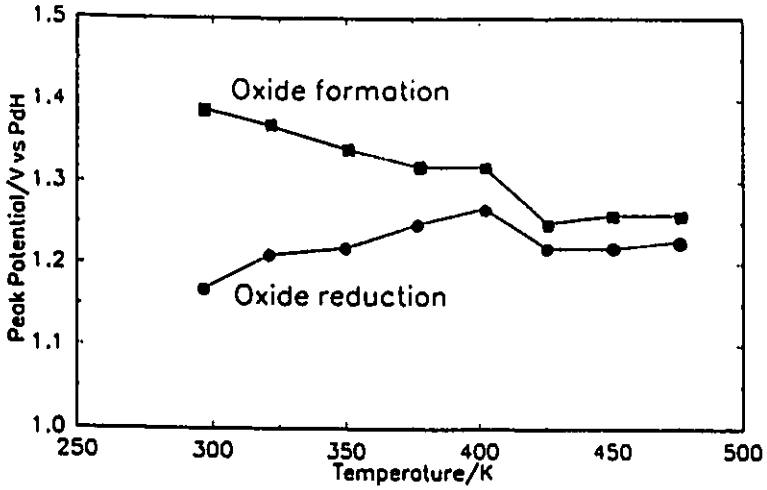


**Fig.26** Plot of oxide formation/reduction peak potentials vs temperature for gold in 1 N $H_2SO_4$.

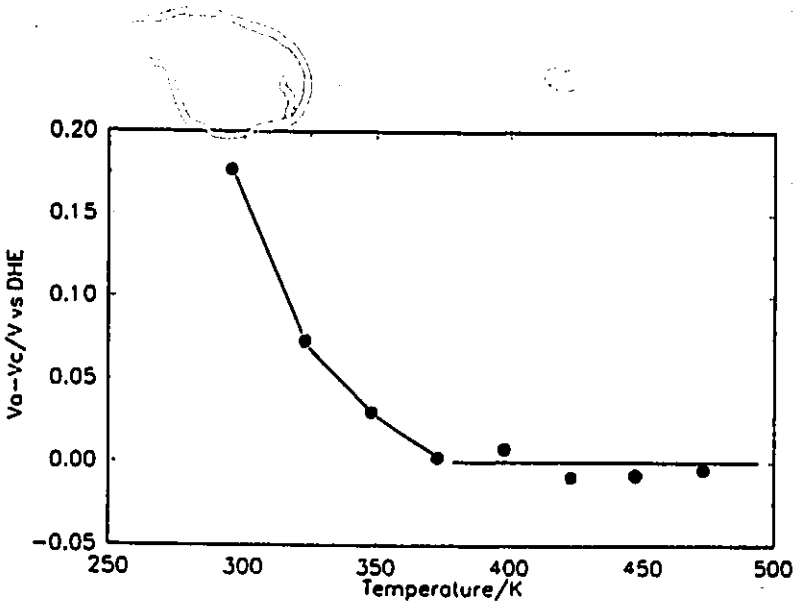


**Fig.27** Plot of anodic/cathodic peak potential difference, $V_a$-$V_c$, vs temperature for gold in 1 N $HClO_4$.

IV.2.2.2b Platinum

When the same was done for Pt in $H_2SO_4$, it was found that all the three major anodic peaks behaved in a way almost similar to those of gold. The cathodic peak, however, did not shift to a more positive potential as T increased as one have would expected. Nevertheless, the values of the $V_a$-$V_c$ potential difference did diminish gradually as T approached 473 K. (Fig.23a)

IV.A.2.2.3 Anodic and Cathodic Peak Potentials vs Sweep Rate

IV.A.2.2.3a Gold

i) Oxide Formation Processes

The kinetic plots ( peak potential vs sweep rate )for the oxide film formation and reduction process at elevated temperatures provided important complementary and unmistakable evidence of the fact that the process could be made observably more reversible by increasing T.

Fig.28 shows the kinetic plots for the oxide film formation process at Au in $HClO_4$ for a range of temperatures form 296 to 473 K. Evidently, there was lesser dependence of the peak potential on sweep rate for the "reversible region" of the kinetic plot at higher temperatures as would be expected in general kinetic principles. In fact, above 398 K, the peak potential became totally independent of sweep rate implying complete reversibility. Again, this is consistent with the conclusion drawn from the $V_a$-$V_c$ vs T plots discussed above. Further, the $s_o$ values seem to become larger with increasing T clearly suggesting that the oxide formation process is more kinetically reversible at higher temperatures. For

instance, the $s_o$ value was about 0.2 V/s at R.T. but increased to as high as 2.0 V/s at 473 K.

It is interesting to note that the Tafel slope derived from the "irreversible region" of the kinetic plots actually stays constant throughout the whole T range studied and had a value equal to that at R.T.( approximately 0.08 V/decade of sweep rate). It is likely therefore that the process of oxide film formation follows the same mechanism despite the large T change. Similar plots were obtained for Au in $H_2SO_4$ except that the Tafel slope found was ca. 0.12 V/decade. Thus, it is quite evident that the symmetry factor, $\beta$, when estimated from the classical representation of $b$ as $RT/\beta F$ would not be a constant, 0.5 $\pm$ 0.05, but a function of T. This is also observed for the corresponding oxide reduction process to be described in the next paragraphs.

ii) Oxide Reduction Processes

For the process of oxide reduction, T did influence the reversibility of the process but to a much smaller extent. For Au in $H_2SO_4$, the slope of the apparent "reversible region" of the kinetic plots changed from approximately 0.06 V/decade at R.T. to about 0.035 V/decade at 473 K. Again, the $s_o$ value increased with increasing T. The fact that T increase did not make the reduction become completely reversible is of interest. Thus, the results suggest that even at these high temperatures, relatively slow processes such as oxide rearrangement or ageing are still significant.

The Tafel slope obtained from the "irreversible region" of the kinetic plots was about 0.12 V/decade for all temperatures at Au in both $H_2SO_4$ and $HClO_4$.

IV.A.2.2.3b Platinum

For Pt in $H_2SO_4$, the $s_o$ value did not seem to be affected very much by the T change. For most temperatures, $s_o$ was estimated to be about 20 V/s. Perhaps the Pt oxide formation processes are already quite reversible at R.T. as suggested by the relatively large $s_o$ value ( cf. ref. [29] ) so that further increase in T does not make such a process much more reversible. Unlike the behaviour of Au in the acids, the Tafel slopes for Pt in acid derived from the "irreversible region" of the kinetic plots did not seem to be constant or following any kind of pattern with increasing T ( typically between 0.030 to 0.060 V/decade ). The smaller Tafel slopes indicate that a more complex multi-step mechanism of oxide formation at Pt is involved.

IV.A.2.3 Metal Oxide Dissolution at Elevated Temperatures

Fig.29 represents the plots of $Q_c/Q_a$ vs sweep rate for Au in $HClO_4$ for a range of T up to 473 K. It is evident that the anodic and cathodic charges are not balanced except at R.T. The higher the T, the larger the deviation is from unity in $Q_c/Q_a$. This observation could be attributed to a chemical and/or anodic dissolution of the metal oxide or metal which is expected to be more important at elevated temperatures. Such behaviour is well demonstrated and understood with baser metals, e.g., anodization of Zn in alkaline solution [119]. For a given sweep rate, the charge ratio decreases significantly with T, e.g., at 0.010 V/s, $Q_c/Q_a$ = 1.0 at 296 but is 0.2 at 398 K. If the "excess" anodic charge or the "missing" cathodic charge at elevated temperatures were connected to the process of dissolution of the oxide film, then the charge ratio should be improved by

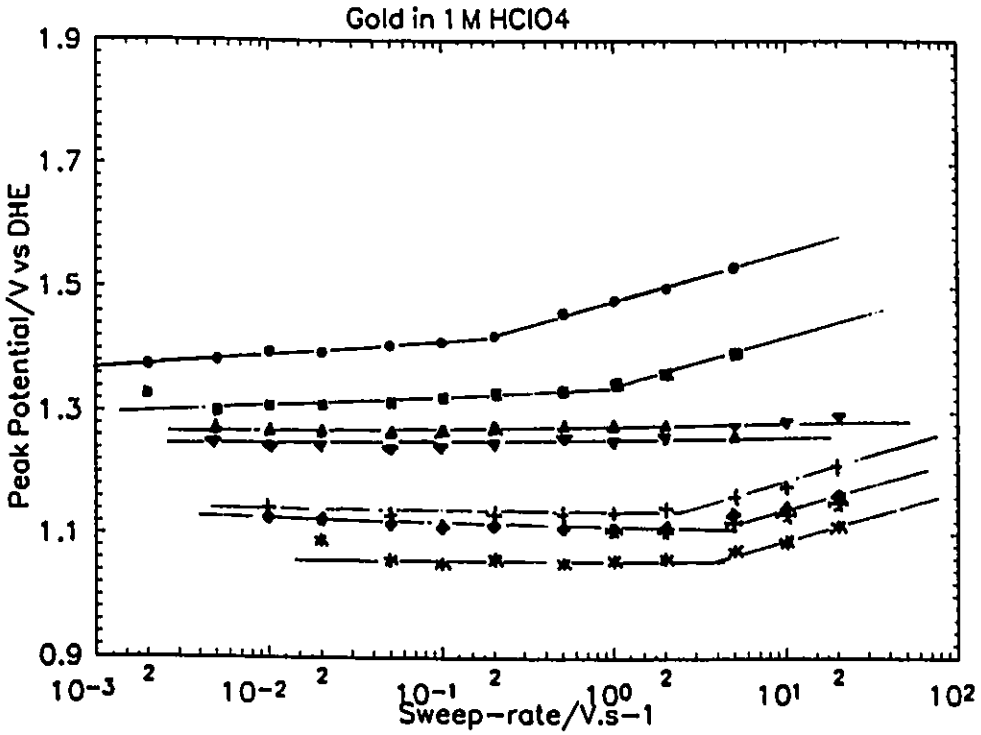


**Fig.28** Plots of anodic peak potential vs sweep-rate for gold in 1 N $HClO_4$ solutions at 8 temperatures (●) 296 K, (■) 323 K, (▲) 348 K, (▼) 373 K, (◆) 398 K, (+) 423 K, (✱) 448 K, and (✱) 473 K.

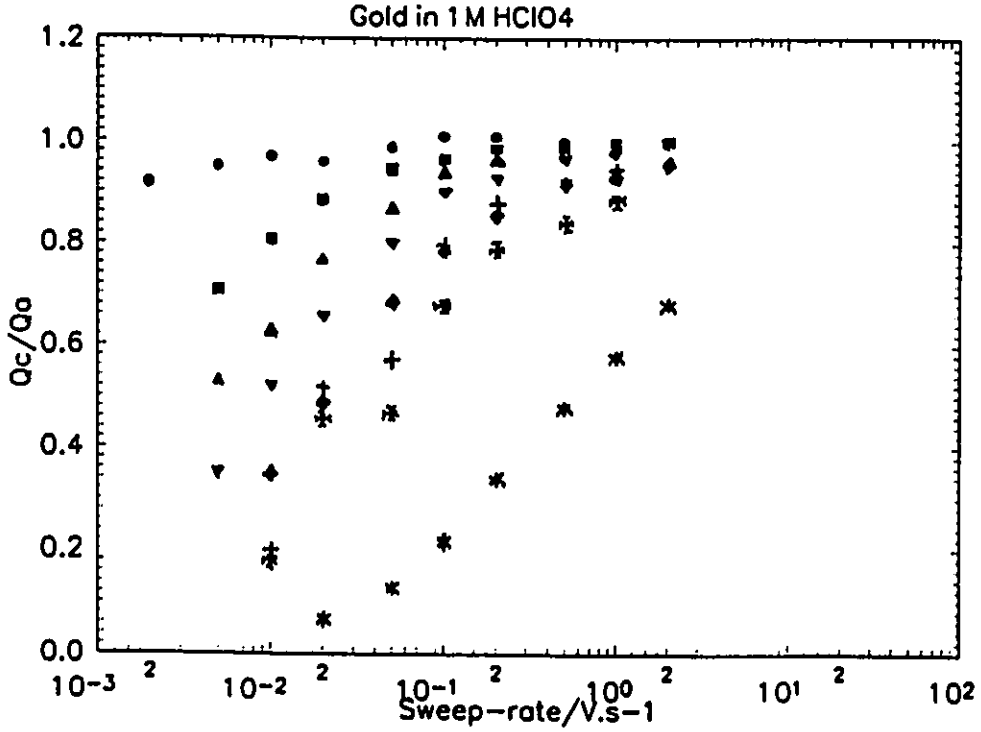


**Fig.29** Charge balance, $Q_c/Q_a$, vs sweep-rates plots for gold in 1 N $HClO_4$ solutions at 8 temperatures (●) 296 K, (■) 323 K, (▲) 348 K, (▼) 373 K, (◆) 398 K, (+) 423 K, (✱) 448 K, and (✱) 473 K.

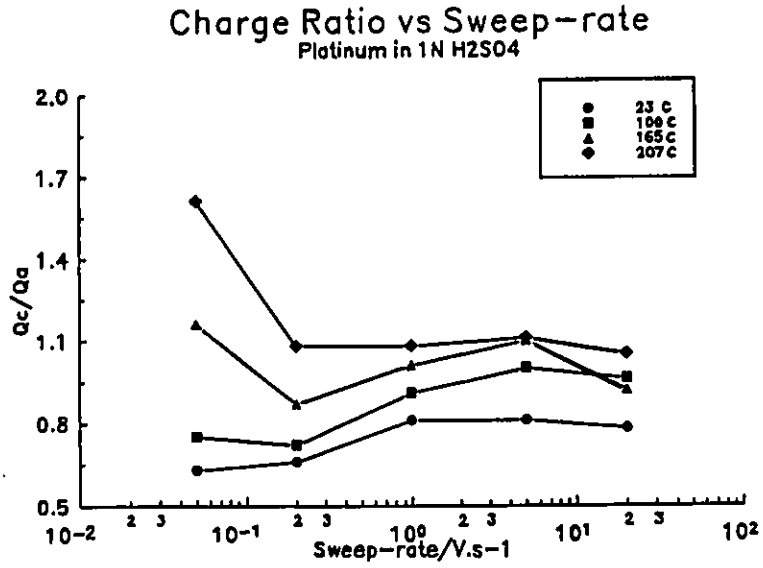


**Fig.29a** Charge balance, $Q_c/Q_a$, vs sweep-rate plots for platinum in 1 N $H_2SO_4$ solutions at 4 temperatures: 296 K, 373 K, 438 K, 480 K.

merely increasing the sweep rate. This is because the anodically formed oxide film will have a better chance to be reduced on the returning sweep before it became dissolved and diffused away from the electrode surface during the time-scale of the anodic sweep. This was indeed found to be the case as can be seen in Fig.29. Similar behaviour was observed for Au in $H_2SO_4$. Contrary to the behaviour at gold, for Pt in $H_2SO_4$, a $Q_c/Q_a$ charge ratio of about 1 could be observed for just about all temperatures and sweep rates. This strongly suggests that platinum oxides formed anodically do not undergo any significant or severe dissolution as does gold.

Among the systems studied, gold in NaOH showed most indications of dissolution. This is supported by the somewhat strange looking i/V profiles at temperatures well above 298 K as illustrated in Figs 30a, b, and c for three temperatures. At 425 K, in Fig.30b, along with the usual features of i/V profiles obtained at elevated temperatures, an "inverted" cathodic peak was observed. As T is increased, the amplitude of this inverted cathodic-sweep peak increases in the anodic direction as can be seen in Fig.30c for gold at 473 K. This unexpected inverted peak, however, could be made more "normal" again by applying a higher sweep rate as illustrated in Fig.30d. This phenomenon is probably connected to the anodic dissolution of the gold oxide film of the kind discussed above for gold in $HClO_4$ plus probably some direct anodic metal dissolution as well.

Abnormal behaviour for gold in NaOH can also be seen from the kinetic plots at different temperatures. For instance, the (apparent) $s_o$ value actually became smaller with increasing T. All of the above evidence strongly suggests that the process of oxide

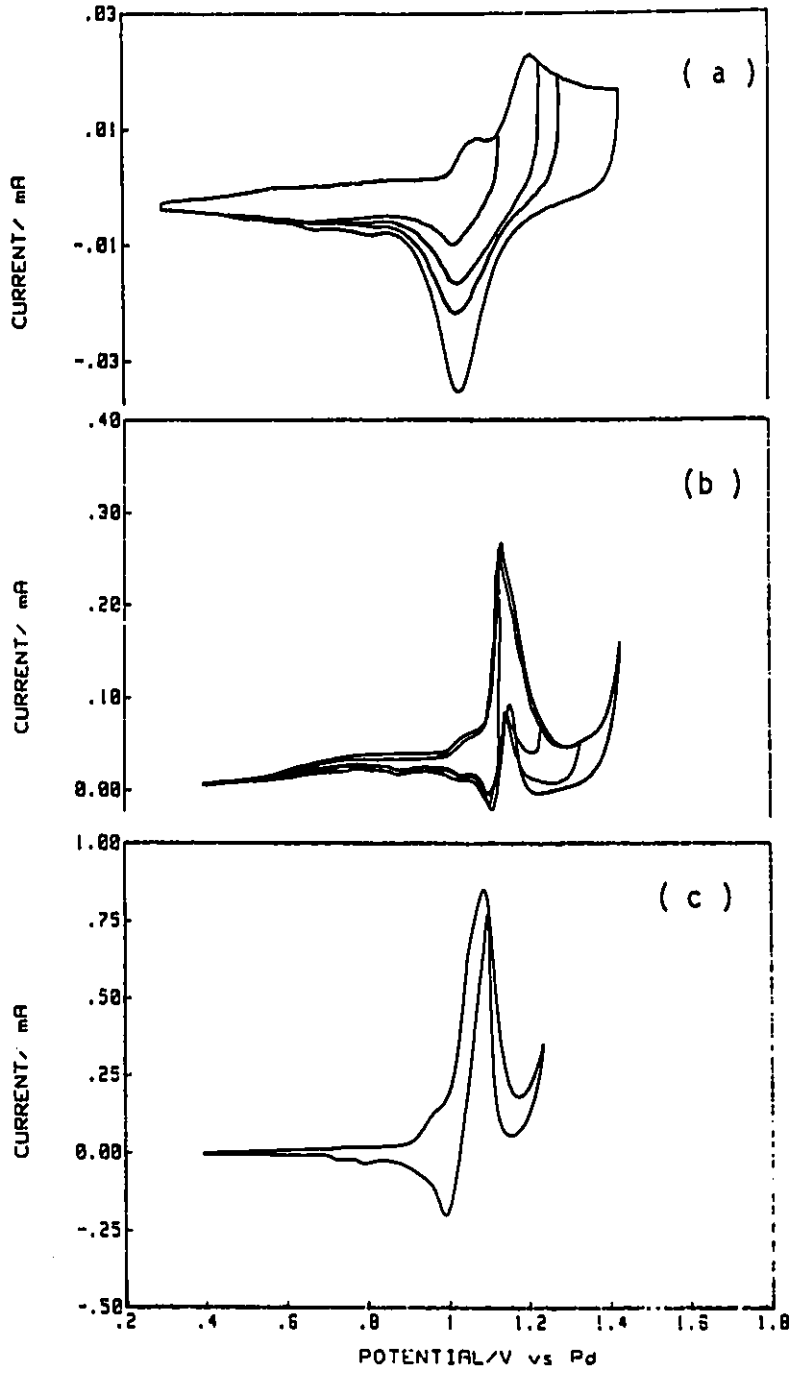


**Fig.30** Cyclic voltammograms for the oxide film formation and reduction processes at gold in 0.2 N NaOH for 3 temperatures; a) 298, b) 425 and c) 473 K at a sweep rate = 0.02 V/s.

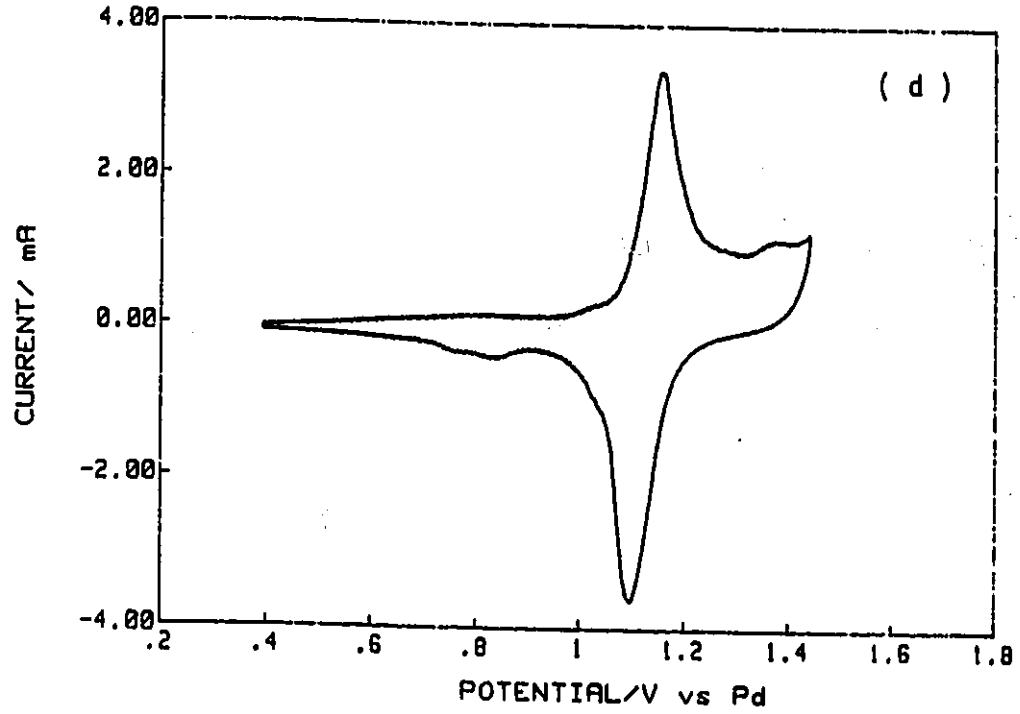


**Fig.30d** Cyclic voltammogram for the oxide film formation and reduction processes at gold in 0.2 N NaOH at 425 K and at a sweep rate = 1.0 V/s.

formation at gold in NaOH is complicated by the fact that both gold and its oxide film are soluble at substantially elevated temperatures.

## IV. A.3 Conclusions on the Oxide Film Formation and Reduction at Pt and Au at Elevated Temperatures

The oxide formation and reduction processes at Pt and Au were studied in 0.2 N aq. NaOH, 1 N aq. $H_2SO_4$ and 1 N aq. $HClO_4$ aqueous solutions at temperatures up to 538 K. It has been demonstrated that good cyclic voltammograms with "clean" double-layer regions could be obtained (e.g. Fig.21) in spite of the adverse high-temperature/high-pressure aqueous environment inside the bomb.

In general, cyclic voltammograms obtained at elevated temperatures exhibit current peaks that are relatively narrower in shape and much higher in current density, and obviously more reversible than that obtained at R.T. Further, the processes of $O_2$ and $H_2$ evolution commence earlier at higher temperatures.

The effect of T on the oxide film formation and reduction processes, at both Pt and Au, was found to behave in a similar way with respect to how T enhances the reversibility of these processes. That is, the cyclic voltammograms observed at elevated temperatures are sharper, simpler or more symmetrical. Also, the hysteresis between the oxide film formation and the corresponding reduction process becomes substantially reduced at sufficiently high temperatures, especially at Au where nearly mirror image profiles were observed. At Pt, however, the oxide film formation is possibly still a stepwise process at higher temperatures (at least up to 529 K) involving several stages of formation and

rearrangement of the previously formed oxide film. Thus, significant hysteresis between the oxide film formation and reduction processes is still observed at higher temperatures.

Tafel slopes derived from the "kinetic plots" of either the oxide formation or the reduction process seem to be constant in spite of the large temperature change, especially at Au in acids. Therefore, it is seen that the oxide film formation and reduction processes at Au do not follow the conventional behaviour of the Tafel slope, $b$, on temperature as is also the case for the studies of the HER and OER at several metals in 0.2 N aq. NaOH solutions.

The observed metal oxide and/or metal dissolution at elevated temperatures, as indicated by the substantial deviation from unity of the anodic and cathodic charge ratio, $Q_c/Q_a$, is more important and significant at Au, especially in alkaline solutions, than at Pt.

## IV.B. Hydrogen Evolution Reaction

This section describes results and gives discussion on the behaviour of the cathodic hydrogen evolution reaction at gold, platinum and nickel in 0.2 M NaOH obtained for several temperatures, from about 293 to 473 K. In most cases, *un*conventional temperature dependence of the Tafel slope $b$ was observed for the HER at metals where linear Tafel relations were obtained. Since only two metals exhibited some sort of linear Tafel regions at these elevated temperatures, there is not enough experimental information to justify the writer giving a detailed discussion on this matter. Nevertheless, these results represented yet another example of the unconventional behaviour of the dependence of $b$ on T referred to in Section I.A.2 of the Introduction. The quantitative discussion will

therefore be focused more on the double-layer capacitance and the determination of the potential dependence of coverage by the adsorbed intermediate, in this case H, at elevated temperatures. It was gratifying that information provided by the potential relaxation method ( see section III.A.4.5 ) was quite consistent with that of the a.c. impedance method for all three metals investigated in this part of the work.

## IV.B.1 Tafel Relations

### IV.B.1.1 Tafel Relations for the HER at Gold

Fig.32 shows the Tafel relations for the HER at gold in 0.2 M NaOH solutions at several temperatures ranging from 293 to 450 K. From the appearance of these Tafel lines, it is evident that their slopes do depend on T. Table I summarises the values of these Tafel slopes recorded at each temperature together with corresponding exchange current densities, $i_o$, obtained by extrapolation of the linear portions of the Tafel lines back to the reversible potential in the usually way.

Apparently, above 343 K, Tafel lines with two easily distinguishable linear regions arise. It is interesting to note that these two Tafel regions have somewhat opposite dependences of their slopes on T. That is, the lower Tafel slope decreases with increasing T while the upper slope increases simultaneously. The origin of these observed changes on Tafel slopes with potential at a given temperature could be due to a change of rate controlling step or conditions of chemisorption of H. What is clear, however, is that this rather uncommon appearance of the Tafel lines is not due to some incidental effect of impurities as demonstrated by the "clean" double-layer region of the i/V profile obtained

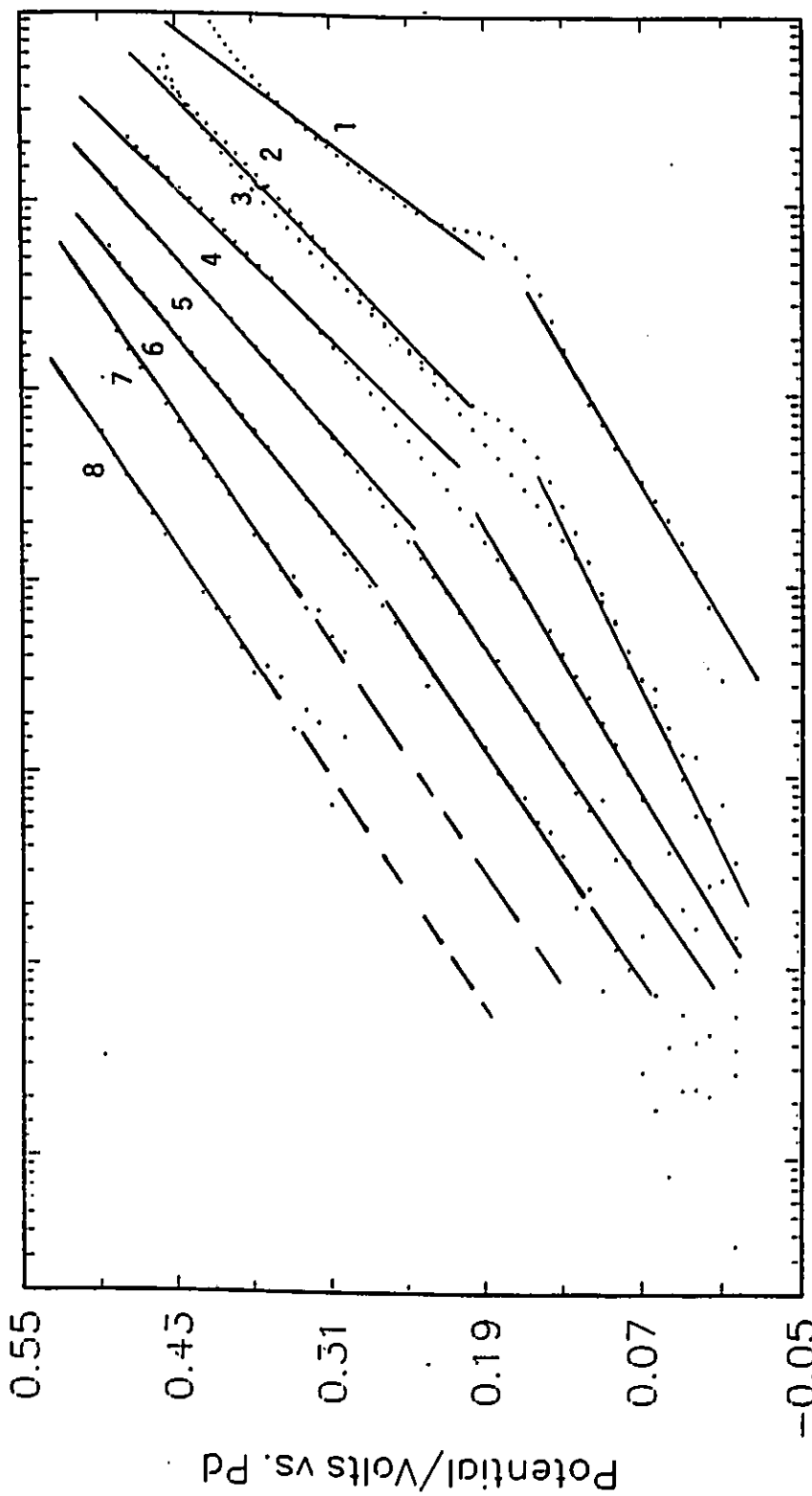


**Fig.32** Tafel relations for the HER at 8 temperatures 1) 450 K, 2) 432 K, 3) 405 K, 4) 382 K, 5) 361 K, 6) 343 K, 7) 318 K, 8) 293 K at gold in 0.2 N NaOH solutions.

**Table I.** Tafel slopes and exchange current densities recorded for various temperatures between 293 and 450 K for the HER at gold in 0.2 N NaOH solution

| Temp (K) | Lower Tafel slope, V/dec | $i_o$ low A cm$^{-2}$ | Upper Tafel slope, V/dec | $i_o$ high A cm$^{-2}$ |
|---|---|---|---|---|
| 450 | 0.045 | 5.0E-5 | 0.160 | 3.0E-4 |
| 432 | 0.059 | 3.0E-6 | 0.157 | 3.0E-5 |
| 405 | 0.073 | 3.0E-6 | 0.141 | 3.0E-5 |
| 382 | 0.076 | 1.0E-6 | 0.149 | 2.0E-5 |
| 361 | 0.092 | 5.0E-7 | 0.130 | 2.0E-6 |
| 343 | 0.100 | 2.0E-7 | 0.116 | 5.0E-7 |
| 318 | (0.100) | 5.0E-8 | 0.100 | 5.0E-8 |
| 293 | (0.097) | 1.0E-8 | 0.097 | 1.0E-8 |

Tafel slopes in brackets are obtained by extrapolation.

at elevated temperatures as seen in Fig.30c. The potential at which the Tafel line changes slope decreases with increasing T suggesting that the mechanism of HER corresponding to the upper region becomes more important at higher temperatures.

As can be seen in Table I, the exchange current density $i_o$ for both the lower and upper regions of the Tafel relations become larger as T increases, as expected. In general, the $i_o$ values are higher for the upper slope region than for the lower one. In other words, the upper Tafel region corresponds to a process that is faster at all temperatures than the one corresponding to the lower slope.

Fig.33 shows the plots of $b$/T as a function of T for gold. If the conventionally assumed representation of the Tafel slope as a f(T), $b = RT/\alpha F$, is obeyed, then a horizontal line with a constant value of $(b/T) = R/\alpha F$ should be obtained. It is seen in this figure that the upper Tafel region apparently follows the conventional T dependence

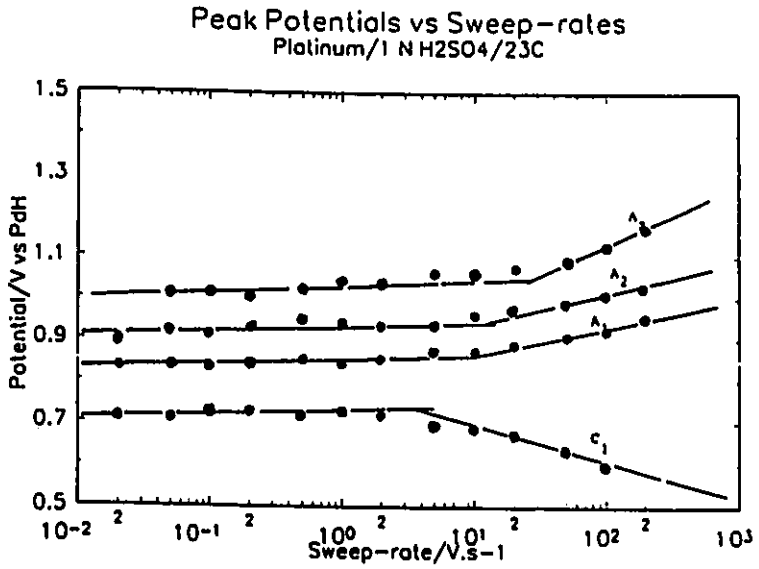


**Fig.31** Anodic and cathodic peak potentials vs sweep-rates plots for platinum at 296 K in 1 N $H_2SO_4$; $A_1$, $A_2$, $A_3$, and $C_1$ correspond to the 3 oxide formation states and 1 oxide reduction state observed in Fig.22a.

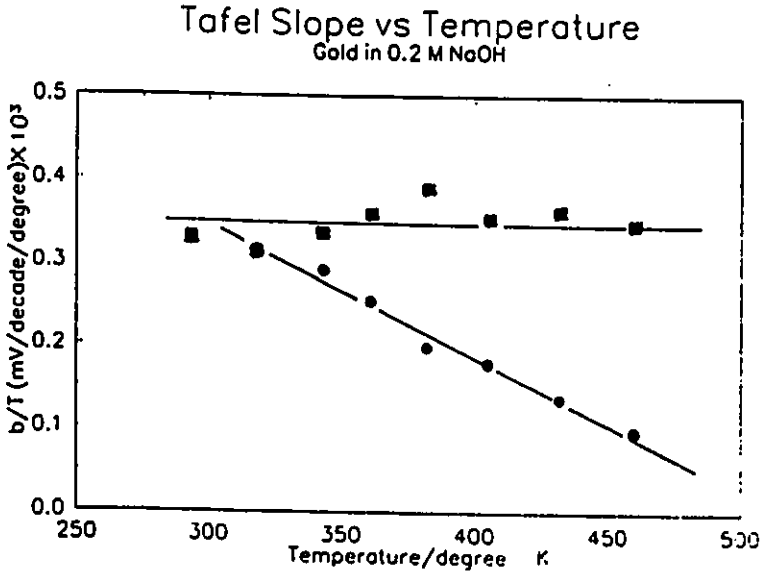


**Fig.33** *b*/T vs T plot for the upper (■) and lower (●) linear segments of the Tafel relations in Fig.32 for the HER at gold.

of $b$ with an estimated $\alpha$ value of about 0.6. The lower slopes, however, *do not* at all follow the conventionally assumed dependence of $b$ on T, i.e., $\alpha$ is dependent on T.

Despite the uncertainty due to the experimentally inaccessible change of the reference electrode potential with T, the apparent heat of activation for the HER at gold may be estimated through the use of Arrhenius plot as discussed in the Introduction section. When such an estimation was carried out, a value of approximately 40 and 53 kJ/mol was obtained for the two respective distinguishable Tafel regions at -0.5 and -0.1 V vs Pd/PdH. The smaller value obtained for the apparent activation energy in the high c.d. Tafel region implies that the process is kinetically more facile than that over the lower c.d. Tafel region. This is consistent with their exchange current density values referred to earlier.

**IV.B.1.2 Tafel Relations for the HER at Nickel**

Results similar to that for Au were obtained for nickel in 0.2 N NaOH solution as demonstrated in Fig.34 but for a smaller temperature range of 346 to 450 K. Although not as clearly shown as for gold above, Tafel lines were all made up of two linear segments at all temperature studied. The results are summarised in Table II in a way similar to that for gold in Table I, the major difference being that the extent of the dependence of $b$ on T is not as large. This is especially true for the lower Tafel region where the Tafel slope was almost constant with T. Also, the exchange current densities obtained for nickel are much higher than for gold, as can be seen in Table II. It should also be noted that similar behaviour was also observed for the HER at nickel in earlier

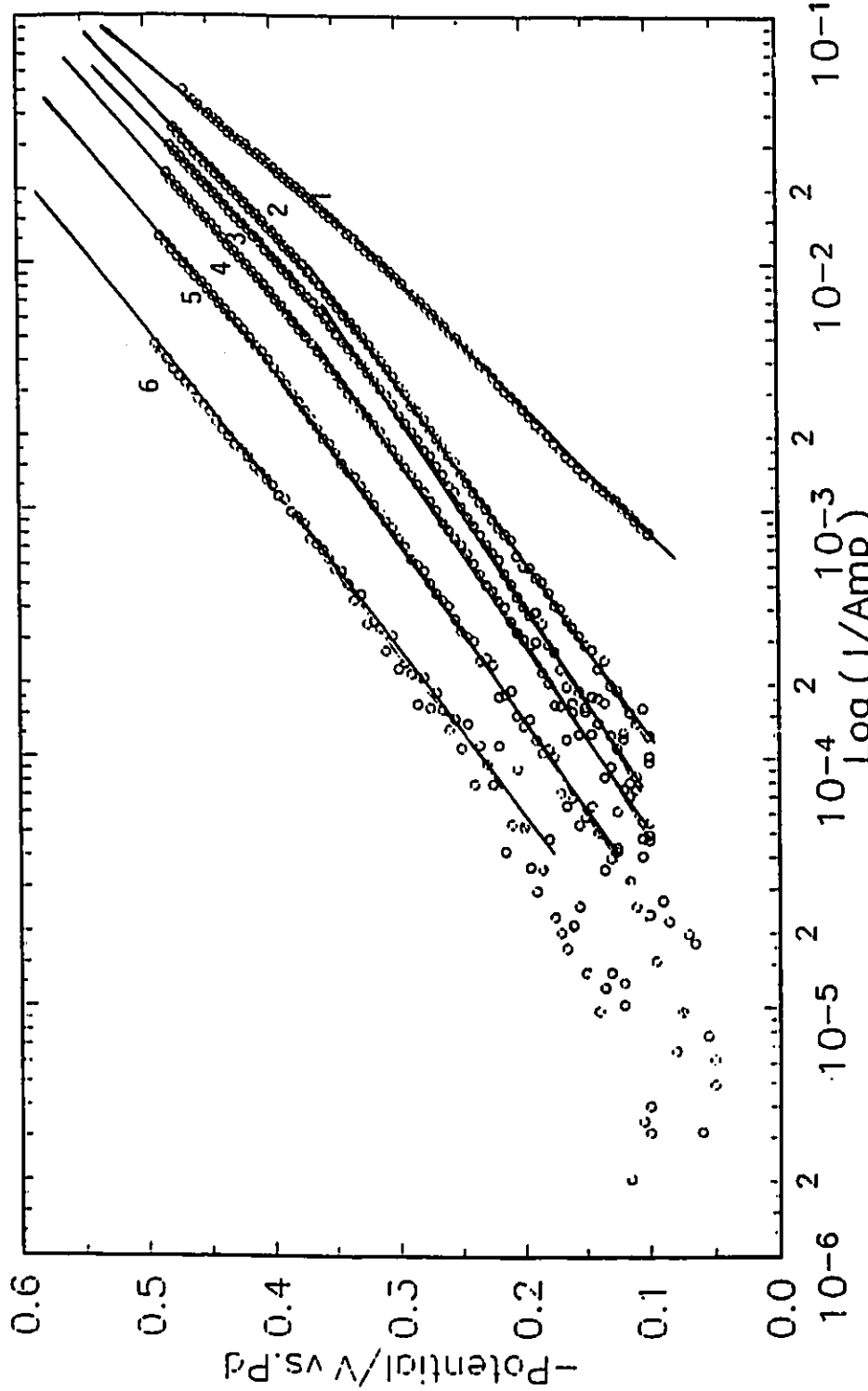


**Fig.34** Tafel relations for the HER at 6 temperatures 1) 450 K, 2) 432 K, 3) 408 K, 4) 384 K, 5) 360 K, 6) 347 K at nickel in 0.2 N NaOH solutions.

work in methanolic HCl at low temperatures [2] as mentioned in the Introduction section.

When the *b*/T vs T plots were constructed and their slopes measured, it was found once again that the upper Tafel region seems to be following the conventional T dependence of *b* on T but not the lower one. However, the estimated charge transfer coefficient, $\alpha$, was only 0.4, a value significantly displaced from the more commonly found value of 0.5 $\pm$ 0.05.

**Table II.** Tafel slopes and exchange current densities recorded for various temperatures between 346 and 450 K for the HER at nickel in 0.2 N NaOH solution

| Temp (K) | Lower Tafel slope,V/dec | $i_o$ low A cm$^{-2}$ | Upper Tafel slope,V/dec | $i_o$ high A cm$^{-2}$ |
|---|---|---|---|---|
| 450 | 0.189 | 2.0E-4 | 0.230 | 5.0E-4 |
| 432 | 0.135 | 2.5E-5 | 0.189 | 1.0E-4 |
| 408 | 0.130 | 1.3E-5 | 0.200 | 6.0E-5 |
| 384 | 0.124 | 8.0E-6 | 0.180 | 3.0E-5 |
| 360 | 0.135 | 5.0E-6 | 0.162 | 1.5E-5 |
| 346 | 0.146 | 5.0E-6 | 0.157 | 5.0E-6 |

Attempts were made to evaluate the apparent heat of activation energy, as in gold. Unfortunately, the experimental data were not well fitted by the Arrhenius equation in the sense that no linear log *i* vs 1/T relation was obtained either for the high or the low overpotential regions.

### IV.B.1.3 Tafel Relations for the HER at Platinum

Fig.35 represents the Tafel relations for Pt in 0.2 N NaOH over a range of temperatures from 294 to 473 K. It is clearly seen in this figure that a curved Tafel

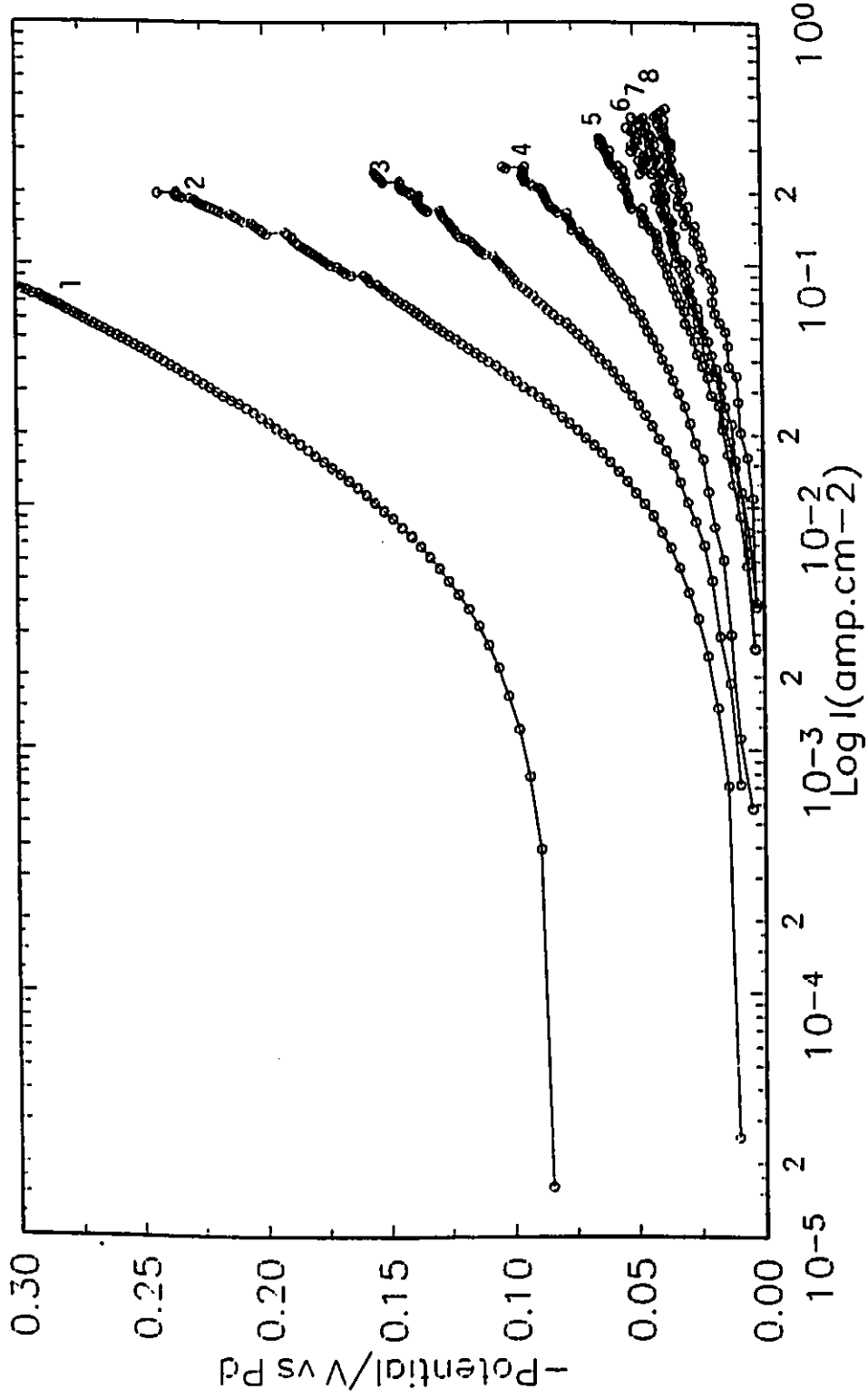


**Fig.35** Tafel relations for the HER at 8 temperatures 1) 294 K, 2) 320 K, 3) 347 K, 4) 371 K, 5) 398 K, 6) 423 K, 7) 449 K, 8) 473 K at platinum in 0.2 N NaOH solutions.

relation was observed at all temperatures. This is believed to be due to the fact that the kinetics of the HER at Pt in alkaline solutions are chemical H-recombination controlled (for the theoretical treatment of the recombination controlled mechanism, see the section on the HER in the Introduction ) and thus give rise to a Tafel slope varying continuously from RT/2F to $\infty$. Therefore, Pt under the present conditions, is not a candidate suitable for testing the conventional behaviour of $b$ on T. Nevertheless, with regard to the $i_o$ values, the general trend is that the higher is the T the larger is the $i_o$ is observed here as at gold or nickel. For instance, the $i_o$ values recorded for 294 and 371 K were $5.0 \times 10^{-3}$ and $1.5 \times 10^{-2}$ A $cm^{-2}$, respectively. For a given T, it was found that the magnitude of $i_o$ for the HER is the largest at Pt, followed by Ni and Au. Thus, in terms of the electrocatalytic effect in the HER, Pt > Ni > Au. Also, above 398 K, $i_o$ does not seem to be enhanced further by increasing T.

Up to now, we have not been able to provide even one single piece of experimental evidence for the conventional dependence of $b$ on T. For those cases vhere the expression $b \doteqdot 2.3\ RT/\alpha F$ does seem to be followed, the values of $\alpha$ were not anywhere near 0.5. Therefore it is concluded that the conventional behaviour of $b$ on T is not observed in the present work.

## IV.B.2 Potential Decay Transients and Analysis of Pseudocapacitance Behaviour

While the data processing procedure and theoretical aspects of the treatment of the potential decay transient procedure has been well documented in several earlier papers [48,60,61,62], particularly from this laboratory, it will be helpful to summarise briefly the

procedure employed here for the analysis of results reported below.

The potential relaxation or so-called decay transients, V(t), following interruption of a prior steady-state polarization current, are recorded digitally from various initial V values and corresponding polarization current densities, *i*. The Tafel relation, V vs log *i*, is determined in the usual way by means of a computer-controlled polarization system, under the same experimental conditions ( see III.A.4.5) as those obtaining in the potential relaxation measurement.

The potential-relaxation behaviour of a reaction, following interruption of a polarizing current, is represented by the following equation,

$$-C(V).dV/dt = i(t,V) = i_o \exp [V(t)/b] \qquad (72)$$

where $i(t,V)$ is the potential and time dependent internal self-discharge current passing across the interface upon current interruption and C(V), which is normally a function of V, is the total interfacial capacitance which determines the behaviour of the potential decay. C(V) is composed a) of the interfacial double-layer capacitance ($C_{dl}$) which is usually approximately a constant and thus not substantially a function of potential and b) a reaction pseudocapacitance ($C_\phi$) which represents the potential-dependence of the charge associated with changes of coverage, $\Theta$, by the adsorbed electroactive intermediate(s) in the reaction [63,64], H in the present case, *viz.* $C(V) = C_{dl} + C_\phi$. $C_\phi$ is usually a f(V) and is usually only significant at low overpotentials [68].

The Tafel relation, in exponential form, is related to the right-hand side of Eq. (72) as $i_o \exp (V/b)$ where *b* is the slope dV/d log *i* of the Tafel relation. The assumption implicit in this equation is that, upon interruption of a polarizing current, the same electron

transfer process is maintained across the interface as that in the steady-state through an internal self-discharge current $i(t,V)$ which has the same potential-dependence as the steady-state current density that is measured experimentally in a polarization experiment.

At high potentials, when the coverage by the electroactive intermediate becomes less potential dependent so that $C_\phi \rightarrow 0$ and $C(V) \simeq C_{dl}$, then Eq.(72) can be rewritten as

$$-C_{dl}.dV/dt = i_o.\exp[V(t)/b] \tag{73}$$

or

$$-C_{dl}.\exp[-V(t)/b].dV = i_o.dt \tag{74}$$

Integration of Eq.(74) gives

$$C_{dl}.b.\exp[-V(t)/b] = i_o.t + K \tag{75}$$

$$= i_o(t + K/i_o) \tag{76}$$

$$= i_o(t + \tau) \tag{77}$$

where $\tau = K/i_o$, an integration constant,

Then $$\ln[C_{dl}.b/i_o] - V(t)/b = \ln(t + \tau) \tag{78}$$

Hence,

$$V(t) = -\ln[i_o/C_{dl}.b].b - b.\ln(t + \tau) \tag{79}$$

Therefore it is seen from Eq.(79) that V is a function of ln $(t + \tau)$ in time t plus an integration constant, $\tau$, with a characteristic slope dV/d ln $(t + \tau)$ equal to $-b$ when $C_\phi = 0$. When C is a function of V, i.e., C(V), then the slope is determined by the Tafel slope, $b$, together with any potential-dependence of C(V). When $t < \tau$, the relation between V and log (t) will depend on the initial current, $i_{in}$ ($\tau = bC_{dl}/i_{in}$). Therefore, by

choosing the right $\tau$ arbitrarily, the $C_{dl}$ can be evaluated according to the relationship $\tau = bC_{dl}/i_{in}$ when a linear relation of the resulting ln $(t + \tau)$ plot in V with a slope equal to $-b$ is obtained. It should be mentioned that the double-layer capacitance can also be deduced by fitting the initial potential-transient decay at high potentials to an empirical mathematical extrapolation equation [122] thereby enabling the unequivocal evaluation of the integration constant, $\tau$.

It is useful to plot also V as a function of log ( -dV/dt ) arising from Eq. (72), *viz.*

$$\ln C(V) + \ln(-dV/dt) = \ln i_o + V/b \qquad (80)$$

i.e., ln(-dV/dt) would follow a linear relation in V except for possible potential-dependence of C, written as C(V). By processing the V(t) data this way, any dependence of the behaviour of V(t) vs log(t) on the initial current is avoided. Further, the pseudocapacitance, $C_\phi$, behaviour of the adsorbed intermediates can be evaluated directly from $C = i(V)/(-dV/dt)$ using the current-potential relationship together with the differentiated potential decay curves, Eq. (80).

In this thesis, the digitally acquired V(t) data are processed in the following ways:

(i) as plots of V(t) vs log (t);

(ii) as plots of V(t) vs log (-dV/dt) which should have slopes equal in numerical value as dV/d log (t) but opposite in sign [65]; and

(iii) by evaluation of C(V) as a function of V from Eq.(72)
as $C(V) = -i(V)/(dV/dt)$.

It must be mentioned that the V(t) transients can also be treated in terms of equivalent circuits for various electrode processes as discussed in several papers by Tilak

et al [63,67] and more recently in terms of the "rate constants" method of analysis described by Harrington and Conway [66] for processes involving chemisorbed intermediates. The latter procedure has the advantage over the former one that representation of the electrode process in terms of an arbitrary equivalent circuit is avoided.

The principal aim of this part of the work is the evaluation of the double-layer capacitance and the behaviour of the adsorbed intermediate species for several elevated temperatures up to 473 K at gold, nickel and platinum in 0.2 M NaOH solutions.

### IV.B.2.1 Potential-Decay Transients for the HER at Gold

Fig.36a represents a series of digitally acquired, potential decay transients for seven temperatures between 293 and 450 K. All transients were obtained using a polarization potential of -0.5 V vs PdH prior to current interruption. It should be emphasised that these transients were recorded under the same conditions and at about the same time as that of the Tafel relations as described in section III.B.1.1. It is to be noted, in respect to this figure, that the higher the temperature, the shorter is the time required for the decay curve to relax back to the reversible potential, in this case "zero" on the Pd/PdH scale. For instance, at 450 K, the potential decay in the transient reaches near completion in just about one second. This is, of course, the consequence of smaller faradaic resistance, hence higher discharge rates at higher temperatures, and is a general result of the applicability of the Arrhenius equation.

In Figs 37a and 37b, the effect of different polarization potentials, -0.5, -0.4,

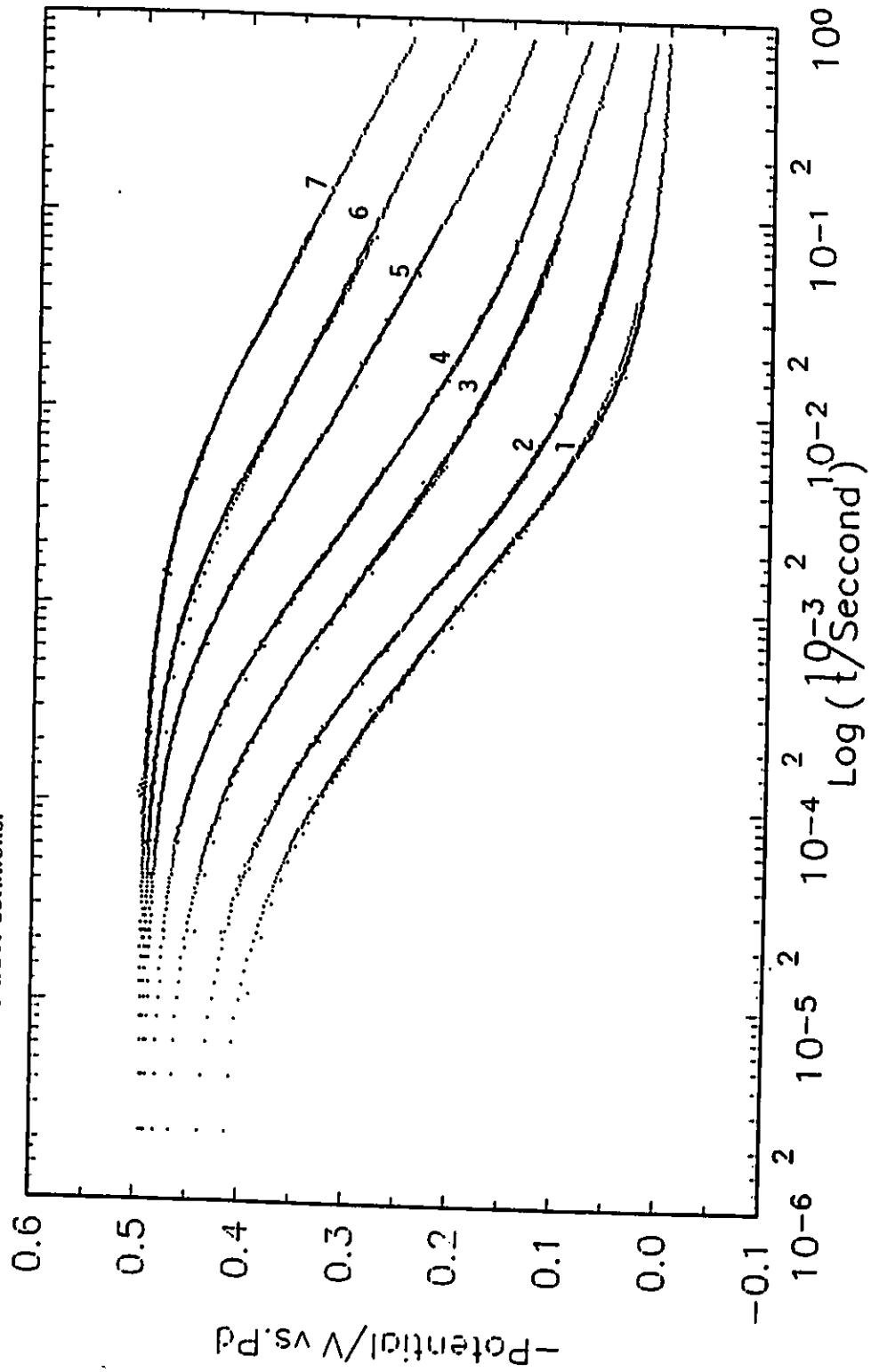


**Fig.36a** Potential-relaxation transients taken from -0.5 V (vs Pd/PdH) initial overpotential and corresponding prior steady-state current densities of the HER at gold at 7 temperatures: 1) 450 K, 2) 432 K, 3) 382 K, 4) 361 K, 5) 343 K, 6) 318 K, 7) 293 K in 0.2 N NaOH solutions.

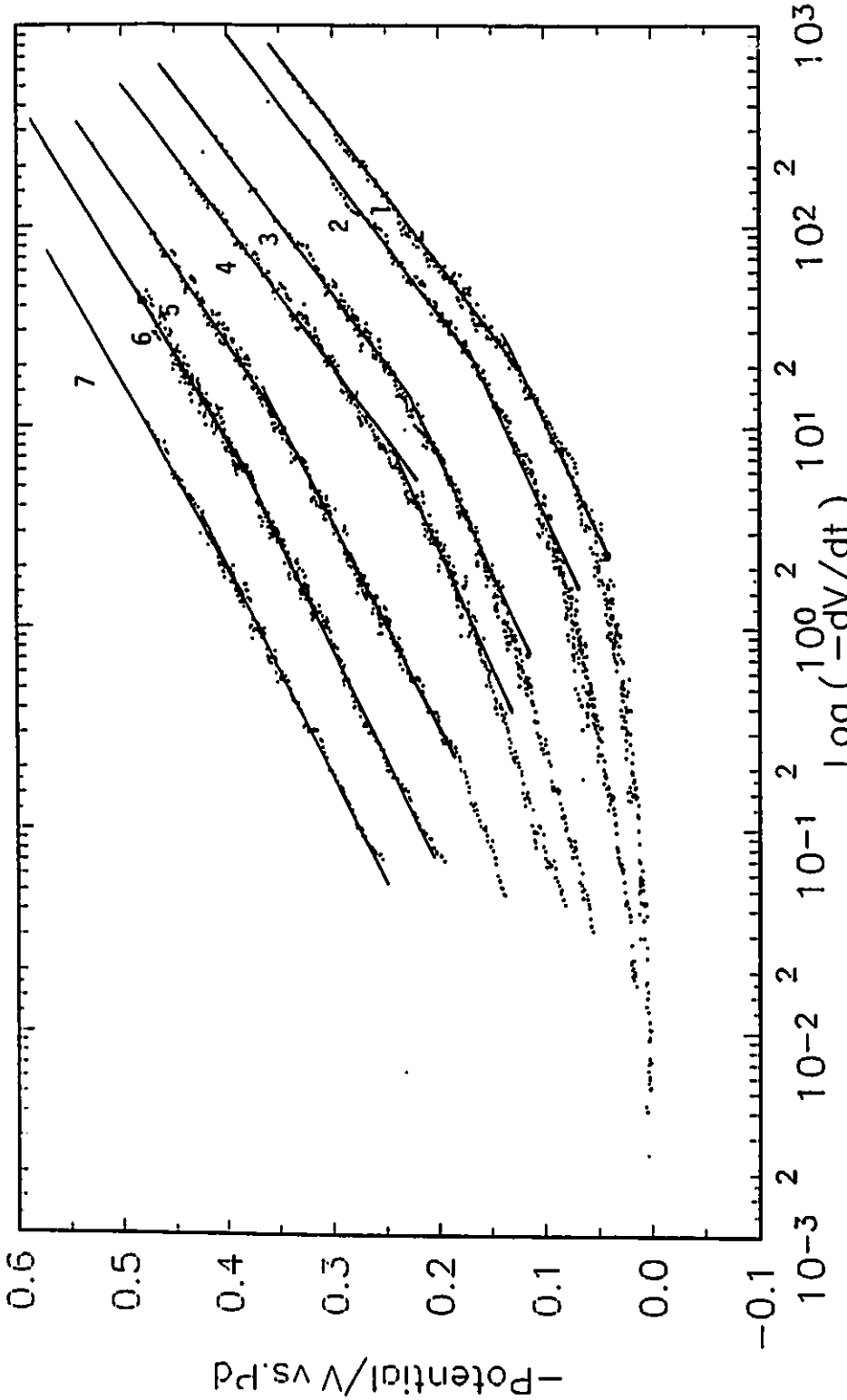


**Fig.36b** Plots of log[-dV/dt] vs overpotential in the HER at gold at 7 temperatures 1) 450 K, 2) 432 K, 3) 382 K, 4) 361 K, 5) 343 K, 6) 318 K, 7) 293 K in 0.2 N NaOH solutions.

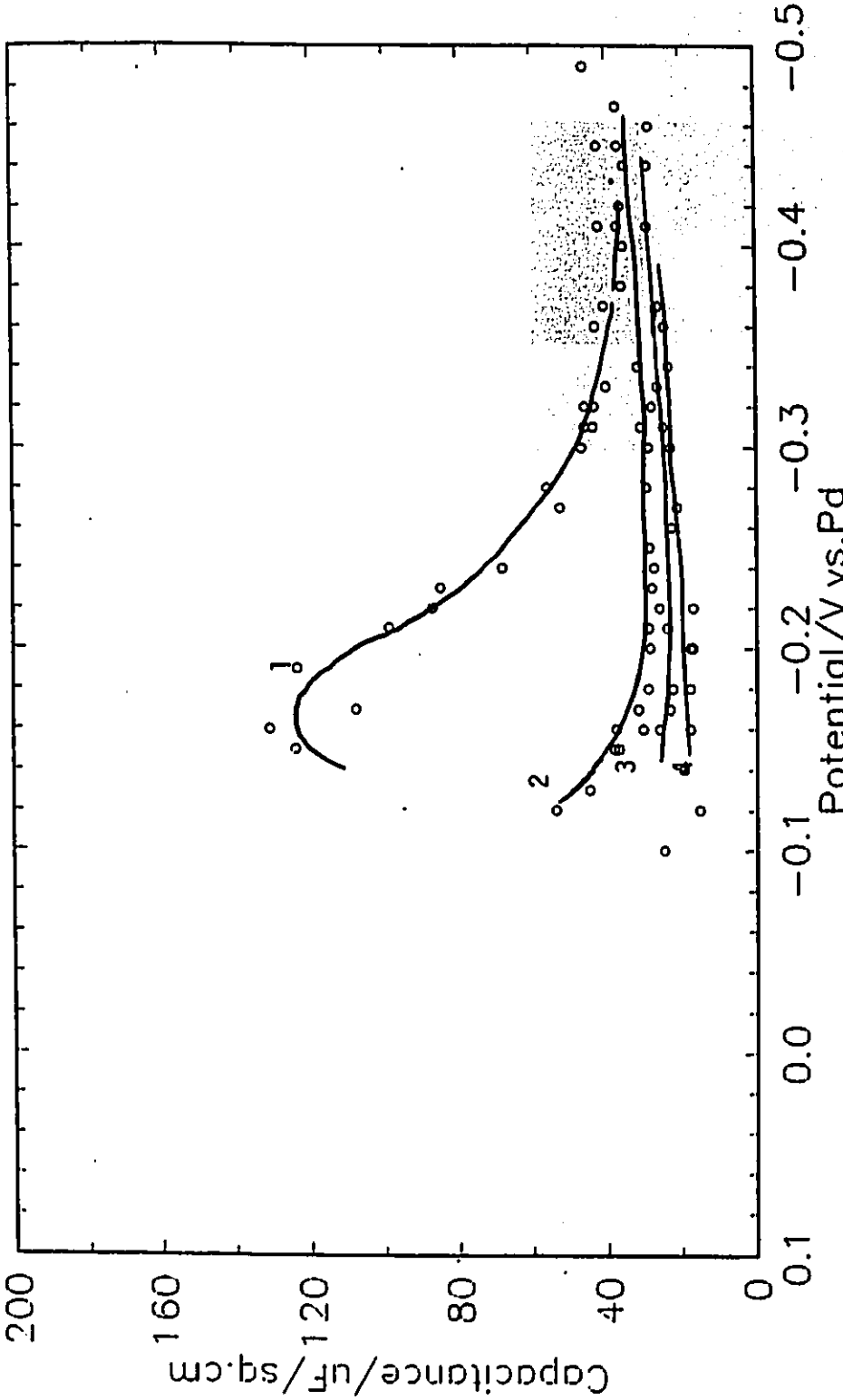


**Fig.36c** Interfacial capacitance vs potential plots derived from analysis of the potential-relaxation transients (with the respective Tafel relations in Fig.32) at gold in 0.2 N NaOH at 7 temperatures 1) 450 K, 2) 432 K, 3) 382 K, 4) 361 K, 5) 343 K, 6) 318 K, 7) 293 K.

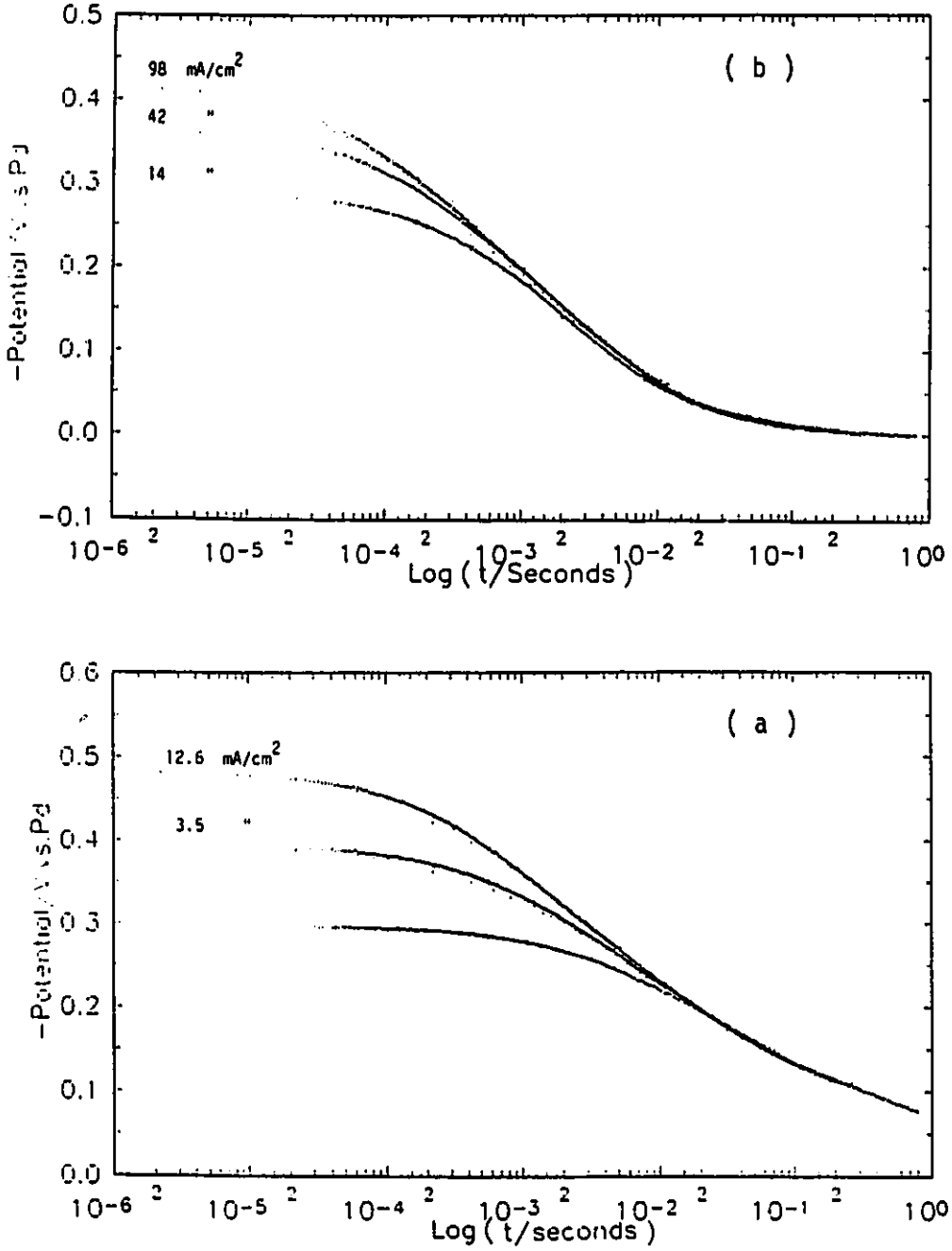


**Fig.37** Potential-relaxation transients, as in Fig.36a, but for 3 initial overpotentials and corresponding prior steady-state current densities of the HER at gold at (a) 361 K, and (b) 450 K.

-0.3 V ( or corresponding current densities) prior to circuit interruption is shown for two temperatures, 361 and 450 K. It is evident that at both temperatures, despite the different prior polarization conditions, the decay curves are all well coincident, especially after longer times when $t >> \tau$. This is a clear indication that i) the self-discharge reaction that takes place at an inert electrode surface is not modified by a change of potential and ii) the same mechanism of self-discharge is maintained.

When the decay transients in Fig.36a were plotted in the V vs log(-dV/dt) fashion, as illustrated in Fig.36b, the curves resemble the Tafel relations with similar slopes being observed; that is, Tafel regions made up of two linear segments are found. Therefore, one would expect that little adsorption of the intermediate H is involved.

When the differentiated potential decay curves in Fig.36b are treated, together with the corresponding Tafel relation in Fig.32 of section IV.B.1.1, the total capacitance of the system can be evaluated as a function of potential. These results are presented in Fig.36c. Indeed, the capacitance vs V plots reveal that especially at higher potentials, with the exception of the behaviour at 450 K, an almost constant capacitance value of the double layer was obtained. i.e., very little pseudocapacitance corresponding to the adsorption or desorption of the H intermediate is involved. Table III summarises the estimated values of the double layer and pseudocapacitances, $C_{dl}$ and $C_{\phi}$, as a function of T.

Thus, the experimental capacitance data suggest that the double layer capacitance is fairly constant with a value of about 40 $\mu$F cm$^{-2}$ for most temperatures. The extremely low $C_{\phi}$ value at just about all temperatures reveals the fact that the extent of H adsorption, in terms of coverage $\theta_H$ is not at all significant at the gold electrode. This is also in good

agreement with the observed lack of hydrogen adsorption and desorption UPD process on gold as revealed by their cyclic voltammograms and also with the poor "adsorbability" of H at Au known in surface chemistry and catalysis ( poor hydrogenation ) at Au. It must be emphasised, however, that the H intermediate involved in the HER process, or "OPD" H as it has been called, may or may not be in the same state as that involved in UPD processes, e.g. at Pt.

Table III. Estimated values of the double layer and pseudocapacitance derived from the potential decay data for gold in 0.2 M NaOH solutions between 293 and 450 K

| Temp (K) | $C_{dl}$ ($\mu$F cm$^{-2}$) | $C_{\phi}$ ($\mu$F cm$^{-2}$) |
|---|---|---|
| 450 | 36 | 130 |
| 432 | 16 | 40 |
| 405 | 20 | 44 |
| 382 | 28 | 57 |
| 361 | 23 | 30 |
| 343 | 40 | 90 |
| 318 | 44 | n.a. |
| 293 | 36 | n.a. |

$C_{\phi}$ values were estimated at -0.15 V vs PdH.
n.a. = not available.

## IV.B.2.2 Potential-Decay Transients for the HER at Nickel

Similar behaviour of the dependence of decay curves on T was also observed for nickel in the same electrolyte of 0.2 M NaOH. That is, the potential decay process became completed in shorter times at elevated temperatures as illustrated in Figs 38a, 38b for two temperatures, 360 and 450 K. Unlike gold, however, it can be seen from this figure that at lower temperatures such as 360 K, the decay transients taken from different

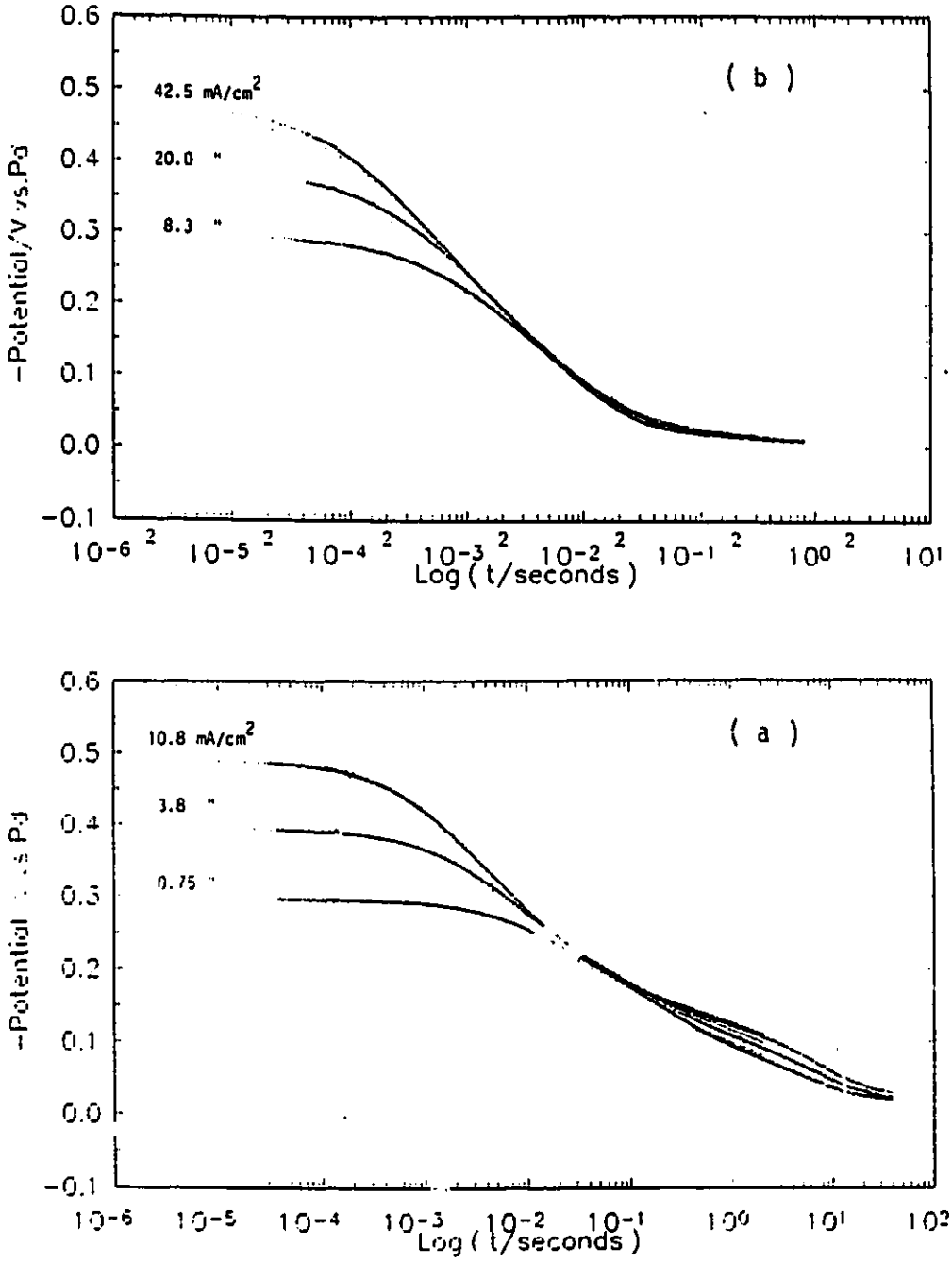


**Fig.38a,b** Potentia-relaxation transients for 3 initial overpotentials and corresponding prior steady-state current-densities of the HER at nickel in 0.2 N NaOH at 2 temperatures (a) 360 K and (b) 450 K.

initial polarization potentials ( -0.5, -0.4, -0.3 V vs PdH) are not coincident. The deviation is due to the potential arrest that arises at a potential ( -0.1 V ) fairly close to the reversible potential of the HER ( 0 V ). The extent of the potential arrest ( in time or log time ) seems to be larger the lower the initial polarization potential. However, with increasing T, the degree of deviation is reduced so that at 450 K, behaviour resembling that at gold is observed.

The above evidence indicates the possibility that nickel, being a transition metal, does not act just as an inert surface for the HER process, especially at lower temperatures, i.e., significant H chemisorption arises. In other words, as the potential difference at the nickel/electrolyte interface varies from one value to another, the chemical nature of the nickel interface is modified. It is believed that over the potential range studied, the most likely form of nickel compound responsible for the observed change of surface properties is chemisorbed H, "NiH" and to some extent nickel hydride. The formation of this nickel hydride is presumably related to the population of the adsorbed H on the surface of the electrode. Therefore, it is expected that nickel hydride could most likely be formed at potentials near that of the reversible potential of the HER. Indeed, this seems to be the case observed experimentally (cf. ref [33,70,120] ). It should be noted that the above observation is not due to any kind of electrode reaction with "impurities" in the electrolyte or, e.g., an electrode that is covered by a layer of nickel oxide since, on current interruption, all transients relaxed with time to the supposed reversible potential of "zero" on the ($\beta$)Pd scale which was close to the potential of the RHE.

Treating the decay curves in the same way as for gold, the total capacitance of the

electrode system could be evaluated and plotted as a function of potential. Such results are presented in Figs 38c, 38d for T = 360 and 450 K. It is seen that both capacitance plots are composed of two distinguishable regions, i) a constant capacitance region extending from the highest overpotential of -0.5 V down to about -0.2 V and ii) an exponential region where capacitance increases exponentially as potential decreases, beginning at about -0.2 V.

According to the theory of potential decay as outlined briefly in section IV.B.2, the the decay rate, at a given potential, is related to the double layer capacitance which is relatively less dependent on potential and arises at all metal/solution interfaces while the latter is due to the pseudocapacitance which arises as a result of the change of coverage, $d\Theta$, by the electroactive intermediate H, via the adsorption or desorption process when the potential is changed by dV, i.e., $C_\phi = q_1 \times d\Theta/dV$ where $q_1$ is a constant corresponding to the charge required for the formation of a hypothetical monolayer of H. Thus, essential information regarding the behaviour of the adsorbed intermediate H can be obtained through the evaluation of $C_\phi$ as a function of potential V. In other words, the coverage $\Theta$ could be estimated, when $q_1$ is known by integration of $C_\phi$ over a range of potential, i.e., the area under the determined $C_\phi$ vs V curve. It must be understood that the estimated coverage $\Theta$ really represents the "change" of H coverage relative to that at zero overpotential. Since not enough information is available on the value of $q_1$ at elevated temperatures, no rigorous attempt was made to evaluate the H coverage of the electrode at each T. However, $q_1$ is usually defined for full coverage by H on the surface. By assuming $q_1 = 210\ \mu C\ cm^{-2}$ ( as in platinum ) for all temperatures, a rather coarse

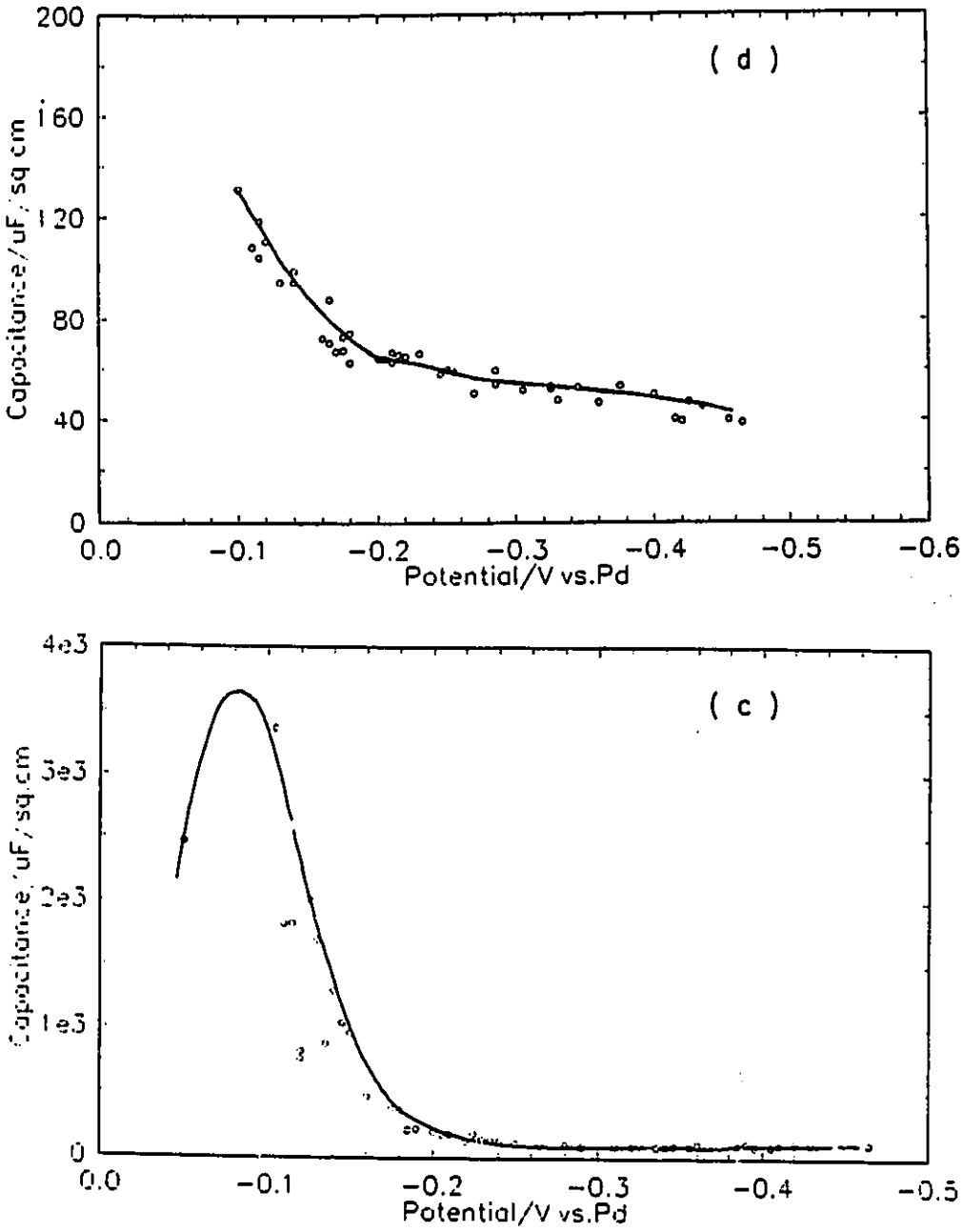


**Fig.38c,d** Interfacial capacitance vs potential plots derived from analysis of the potential-relaxation transients (with the respective Tafel relations in Fig.34) at nickel in 0.2 N NaOH at same 2 temperatures as in Fig.38a,b (c)360 K and (d) 450 K.

estimation of the H coverage was carried out for the potential range 0 to -0.2 V at three temperatures. Table IV summarises these coverage values as well as the capacitance values estimated by this potential decay method, for nickel.

**Table IV.** Estimated values of the double-layer capacitance and pseudocapacitance derived from the potential decay data for Ni in 0.2 M NaOH solutions between 346 and 450 K

| Temp (K) | $C_{dl}$ ($\mu$F cm$^{-2}$) | $C_{\phi}$ ($\mu$F cm$^{-2}$) | $\Theta_H$ |
|---|---|---|---|
| 450 | 51 | 130 | 0.03 |
| 432 | 58 | 200 | |
| 408 | 50 | >1.0E+3 | 0.30 |
| 384 | 80 | 3.0E+3 | |
| 360 | 87 | >3.0E+3 | 1.13 (apparent) |
| 346 | n.a. | >5.0E+4 | |

$C_{\phi}$ values were estimated at -0.1 V vs Pd/PdH.
n.a. = not available.
Note: results are presented in the same order as the order of change of T during the experiment.

It is clear from Table IV that the effect of temperature on $C_{\phi}$ is quite large; however, it is found that the value of $C_{\phi}$ decreases with increasing temperature. It varied from as high as mF per sq.cm of electrode area at -0.1 V for temperatures say below 408 K to a value that is negligible at higher temperatures. It follows therefore from the argument above that the charge due to the adsorbed intermediate H at 360 K is relatively high when compared with that of say 450 K. Knowing the relative amount of charge involved at the two temperatures, it is not difficult to understand that the potential arrest observed previously is substantially greater at 360 than at 450 K, i.e., the higher is the charge or

surface population of H involved at lower T, the bigger is the tendency for hydride formation. This is also reflected in the coarsely estimated H coverage for 450 K, at which T the electrode is hardly covered ( only 3% ) but at 360 K, a nominal apparent coverage of "1.13" was derived.

Contrarily, the estimated $C_{dl}$ is basically less variable with T with values ranging from 51 $\mu$F cm$^{-2}$ at 450 K to 87 $\mu$F cm$^{-2}$ at 360 K. Roughly speaking, the estimated value of the double layer capacitance is, within experimental error, comparable to that at gold in the same electrolyte as it should be. However, as will be shown later in section IV.B.3.2, the small but significant increase in the double-layer capacitance may be due to a change in surface area through the formation of surface-region nickel hydride as a result of prolonged heating over the course of the series of "temperature" experiments.

### IV.B.2.3 Potential-Decay Transients for the HER at Platinum

A series of digitally acquired, potential decay curves for Pt in 0.2 M NaOH solution for temperatures between 294 and 473 K are shown in Fig. 39a. The corresponding V vs log (-dV/dt) plots are given in Fig.39b. Unlike gold and nickel, where relatively simple V(t) behaviour was observed, an interesting dependence of V(t) on log (t) or log (-dV/dt) arises at Pt. Principally, three regions can be distinguished on the V vs log (t) decay curves. The first region arising when V > approx. 0.05 V, i.e., for times in the range 1 $\mu$s to approx. 0.4 ms depending on T, corresponds to discharge of the double-layer capacitance through the non-linear faradaic reaction resistance $R_t$ [63]. The third region arising when V < 0.03 V, for times between 80-800 ms, again depending on T,

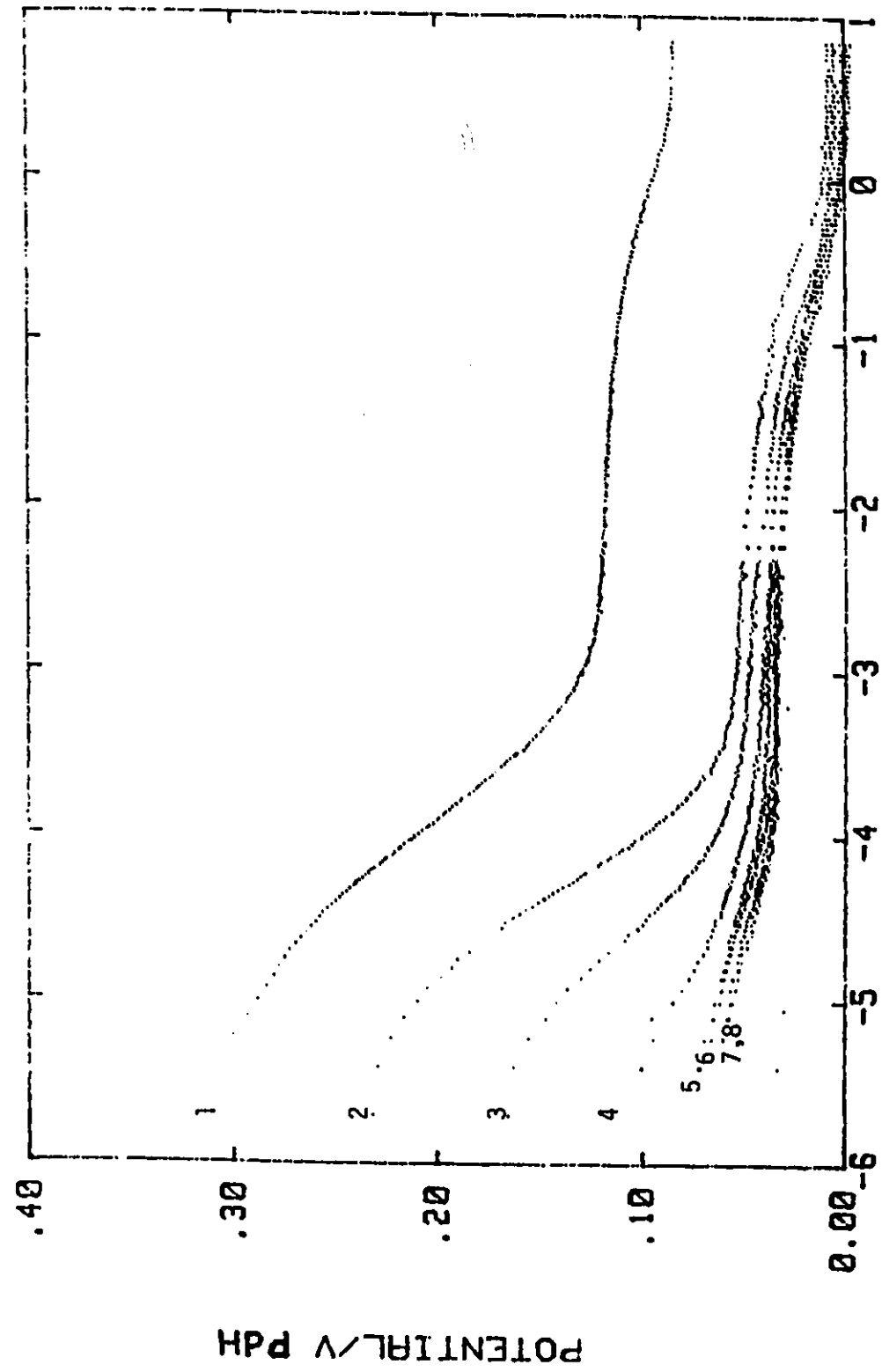


**Fig.39a** Potential-relaxation transients from various initial overpotentials and corresponding prior steady-state current densities of the HER at platinum at 8 temperatures 1) 294 K, 2) 320 K, 3) 347 K, 4) 371 K, 5) 398 K, 6) 423 K, 7) 449 K, 8) 473 K at platinum in 0.2 N NaOH solutions.

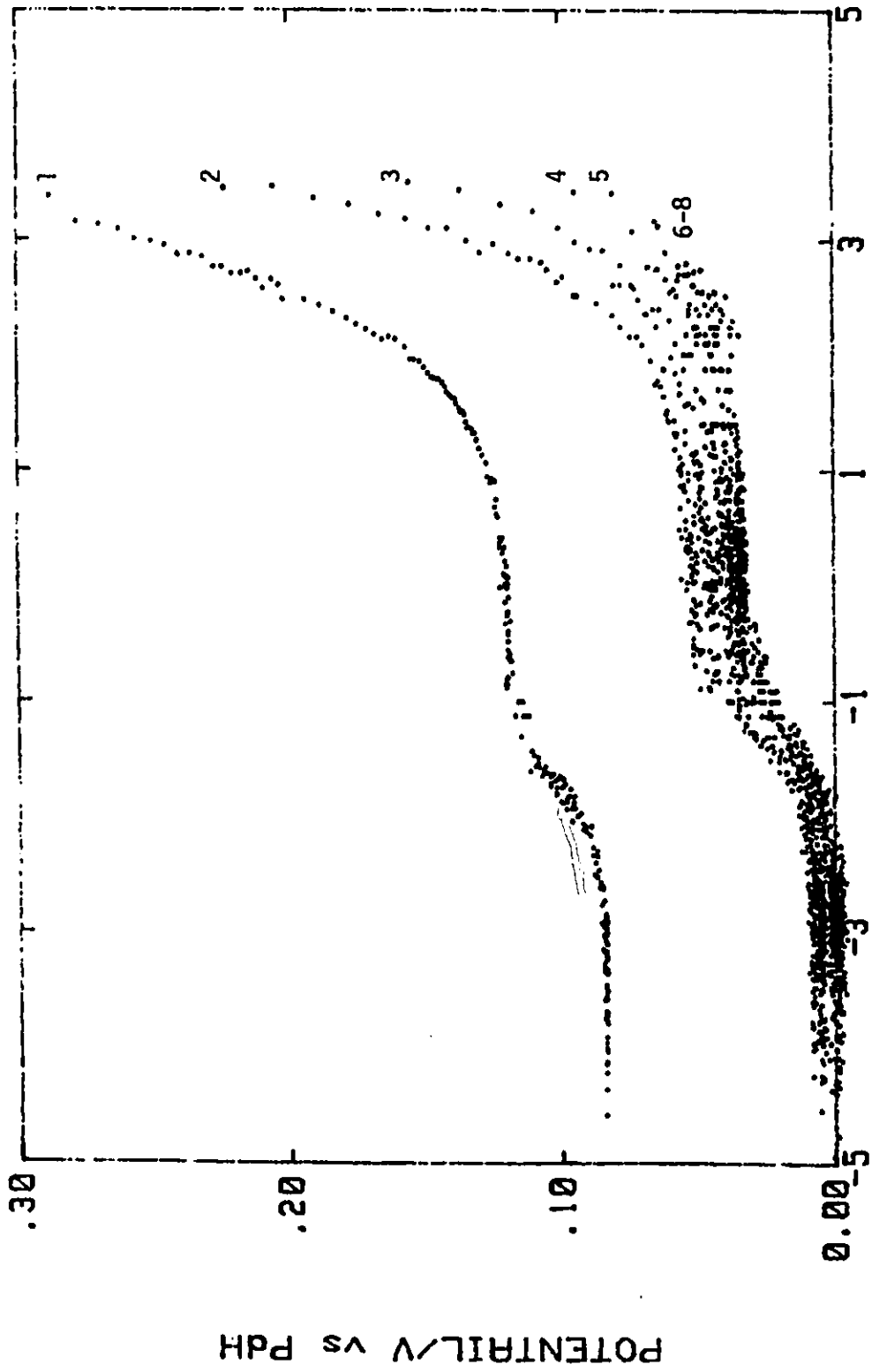


**Fig.39b** Plots of log[-dV/dt] vs overpotential in the HER at platinum at 8 temperatures 1) 294 K, 2) 320 K, 3) 347 K, 4) 371 K, 5) 398 K, 6) 423 K, 7) 449 K, 8) 473 K in 0.2 N NaOH solutions as in Fig.39b.

corresponds principally to the discharge of the OPD H pseudocapacitance. The second region is a relatively flat potential arrest and arises between the first and third regions over the time range approximately 0.4-80 ms.

It is seen from the decay curves that because the faradaic reaction resistance is relatively small in the case of the HER at Pt, especially for the results at the higher T, that the discharge of the double-layer capacitance is near completion after a very short time. The discharge of the H pseudocapacitance is, however, a relatively slow process and is only observed at lower potentials, that is, manifested on the potential decay curves as the relatively flat region; it is more explicitly manifested in the derivative plots in Fig.39b.

The shape of the second region of the potential decay curves is quite similar to the potential arrest that arises during potential decay for the HER on a thin layer of palladium electrodeposited on a platinum rotating disc electrode in 1 M KOH [69] except that it is shorter. It is well known that H can be absorbed "into" the palladium lattice. By analogy, it is likely, therefore, that in this case, H is absorbed significantly into the bulk of the platinum electrode in its "near surface" region, as well as being adsorbed on its surface.

When the Tafel lines referred to in section IV.B.1.3 and the corresponding V vs log (-dV/dt) plots in Fig.39b are treated together, as for gold and nickel, according to the basic equation, Eq.(72), of the potential decay method, i.e., $-dV/dt = i(V)/(C_{dl} + C_{\phi})$, information on the $C_{dl}$ and $C_{\phi}$ could be obtained. The results of the above treatment are presented in Fig.39c in the form of capacitance versus potential plots. It is seen from these that in addition to the constant double-layer regions which characterize the behaviour at higher potentials and at short times, a large

pseudocapacitance peak is also observed at lower potentials at each temperature, the values of which increase with temperature from about 80 mF $cm^{-2}$ at R.T. to as high as 600 mF $cm^{-2}$ at 473 K. The charges involved, estimated by integration over the potential range of the pseudocapacitance peaks, i.e., areas under the peaks, are unexpectedly high. By assuming again that the H deposition charge for a monolayer on platinum at R.T is $q_1$ = 0.21 mC $cm^{-2}$, it was found that the apparent coverage of H on platinum is rather high at ca. 9 equivalent monolayers at 294 K ( 1.9 mC $cm^{-2}$ ).

**Table V.** Estimated values of the double-layer and pseudocapacitance derived from the potential decay data for Pt in 0.2 M NaOH solutions between 294 and 473 K

| Temp (K) | $C_{dl}$ ($\mu$F $cm^{-2}$) | $C_\phi$ (mF $cm^{-2}$) | $\Theta_H$ (apparent) |
|---|---|---|---|
| 294 | 43 | 80 | 9 |
| 320 | 54 | 90 | |
| 347 | 64 | 90 | |
| 371 | n.a. | 150 | 17 |
| 398 | n.a. | 300 | |
| 423 | n.a. | 300 | |
| 449 | n.a. | 600 | |
| 473 | n.a. | 600 | 118 |

$C_\phi$ are estimated for the maxima of the pseudocapacitance curves.
n.a. = not available.

Since it is difficult to cover the electrode with more than a monolayer or two of H, it is reasoned therefore that the electrochemically generated H can also be absorbed by diffusion into the platinum lattice as discussed above, especially at higher temperatures. Further, the potential at which the large capacitance peak arises corresponds very well to that of the potential arrest, providing yet more support for the above possibility. Table

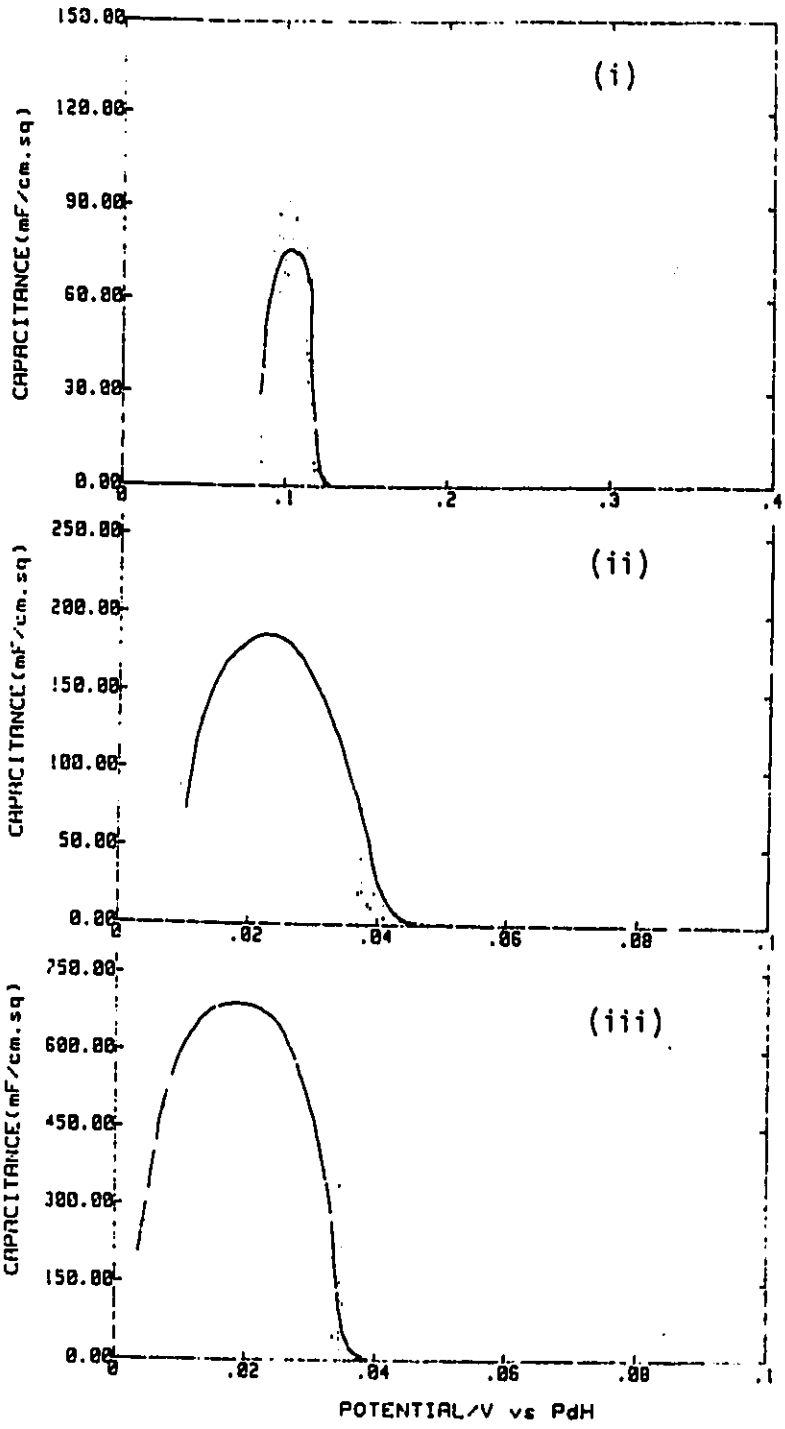


**Fig.39c** Interfacial capacitance vs potential plots derived from analysis of the potential-relaxation transients (with the respective Tafel relations in Fig.35) at platinum in 0.2 N NaOH at same 3 temperatures (i) 294 K, (ii) 371 K, and (iii) 473 K.

V summarises the estimated $C_{dl}$ and $C_{\phi}$ values at each temperature. It can be seen from this Table that the extent of this apparent "H absorption" into the platinum electrode increases almost linearly with T; the process is presumably diffusion controlled.

## IV.B.3 A.C. Impedance Behaviour

Important complementary information can be provided by impedance spectroscopy [103,104] conducted not only as a function of frequency but also of potentiostated "d.c."-level potential (cf. ref.[105] ). The results are conveniently represented in terms of complex-plane and Bode-type plots of phase-angle or of the modulus $|Z|$ vs $\log(\omega)$, the frequency. The phase-angle $\phi$ is $\tan^{-1}(-Z''/Z')$ and $|Z|^2 = (Z'')^2 + (Z')^2$ where Z'and Z" correspond to the real and imaginary component of the impedance, respectively. Both the complex-plane and the phase plots provide a frequency response spectrum of the kinetic or dynamic electrochemical behaviour of the system characterized by the relaxation time(s) of the C/R combinations of the equivalent circuit that may represent the frequency response of the overall electrode process in relation to charge and discharge processes across the double-layer and to charge and discharge of $C_{dl}$ itself, always a significant and unavoidable process.

There are two principal and now well known ways in which the frequency response behaviour of an electrochemical reaction can be simulated:one, based on an intuitive but rationally chosen equivalent circuit, such as that in Fig.41b; the second, by means of fitting the observed frequency-response behaviour to a series of reaction steps and respective rate constants for them. The latter procedure was initiated by Armstrong and

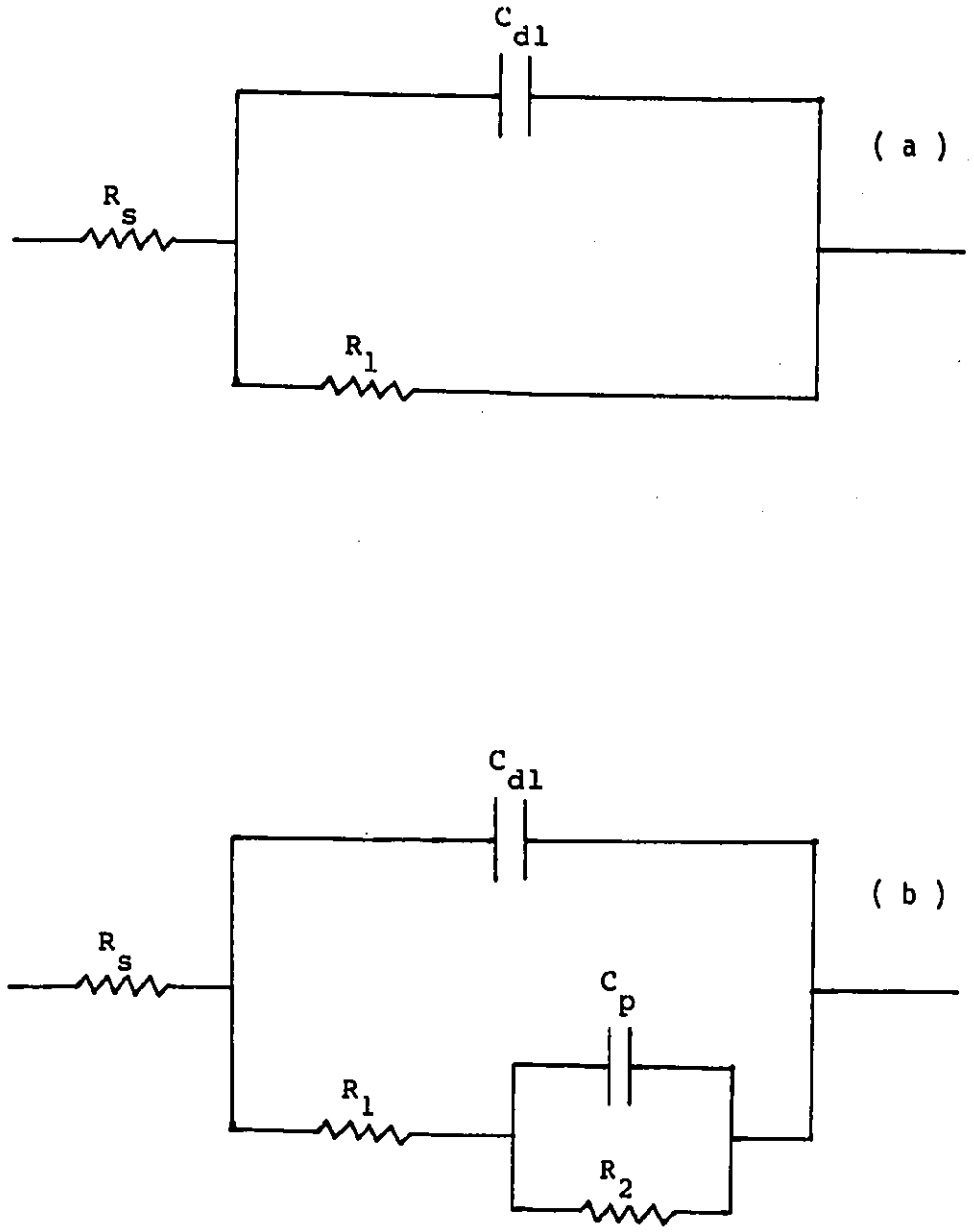


**Fig.41** Simplest equivalent circuit for surface reactions: (a) simple charge-transfer across the double-layer capacitance involving a potential-dependent Faradaic resistance $R_1$; (b) charge-transfer reaction across the double layer capacitance leading to potential dependence of coverage by a chemisorbed intermediate characterized by an adsorption capacitance, $C_\phi$ or $C_p$. $R_s$ represents the solution resistance between the working and the reference electrode.

Henderson [103] and the former, in various ways, by Randles [100] and by (J.)Sluyters and (M.)Sluyters [108].

The experimental a.c.impedance data obtained for the HER at gold, nickel and platinum in 0.2 M NaOH solutions reported below were analyzed by the equivalent circuit procedure. Although there is no equivalent circuit which can represent precisely the actual mechanistic details of an electrode process (except for a simple-discharge redox reaction ), in so far as the experimental data can be represented in terms of a single type of equivalent circuit over a wide range of d.c. potentials and frequencies, the simulation and physical significance of the behaviour often is very significant although the simulation procedure is empirical. However, the simulation is relatively demanding as fits of semi-circle curves at various potentials and of the phase-plots are to be achieved by means of a single assigned equivalent circuit.

**IV.B.3.1 A.C. Impedance Behaviour of the HER at Gold**

Fig.40a shows the complex-plane plots of the frequency response of the HER at gold at -0.5 V ( vs PdH ) where an appreciable steady-state rate of $H_2$ evolution is occurring; the behaviour is over the same range of temperatures as in the Tafel relation experiments in Fig.32. The corresponding Bode type plots of the dependence of phase angle and $|Z|$ on log ($\omega$) are shown, respectively, in Figs 40b and 40c.

It is clear that the phase-angle plots in Fig.40b exhibit only one component at all temperatures. At such a high polarization potential of -0.5 V, this phase-angle profile is determined mainly by the double-layer capacitance, $C_{dl}$, coupled with the Faradaic

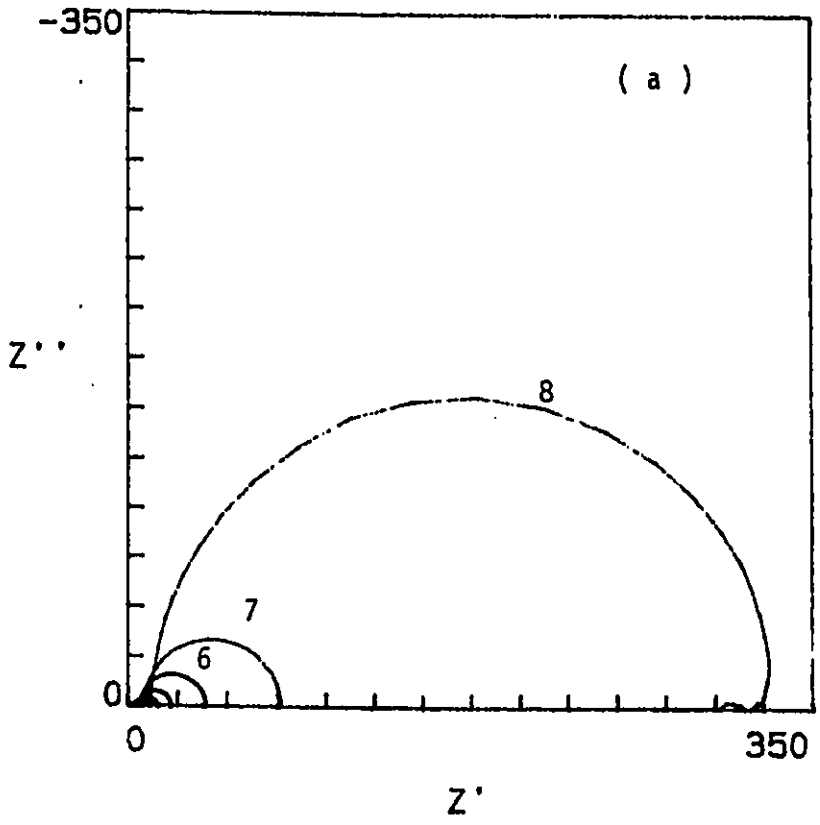


**Fig.40a** Complex-plane plots for the frequency response of impedance of the HER at gold for the HER overpotential of -0.5 V vs PdH at 8 temperatures 1) 450 K, 2) 432 K, 3) 405 K, 4) 382 K, 5) 361 K, 6) 343 K, 7) 318 K, 8) 293 K in 0.2 N NaOH solutions.

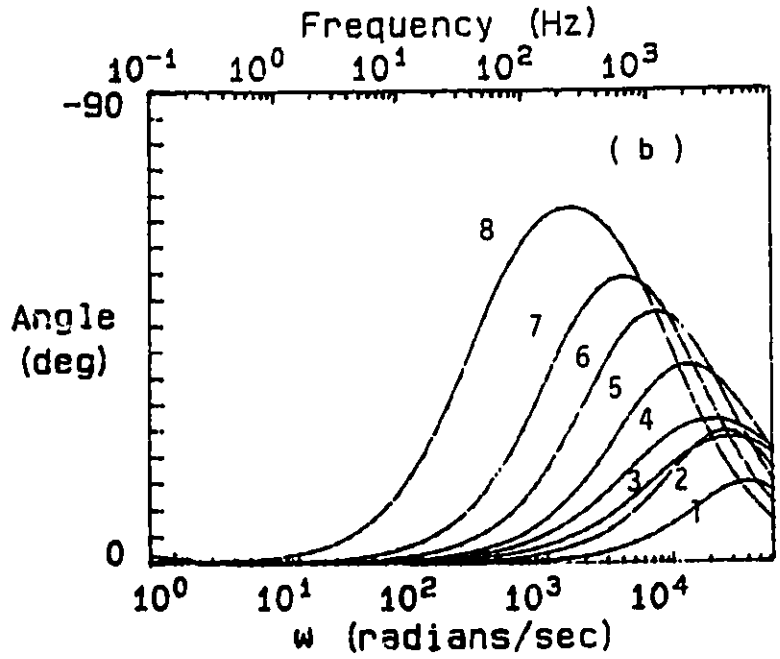


**Fig.40b** Phase-angle Bode-type plots as a function of log ω for the HER overpotential of -0.5 V vs PdH at the same 8 temperatures as in Fig.40a at gold.

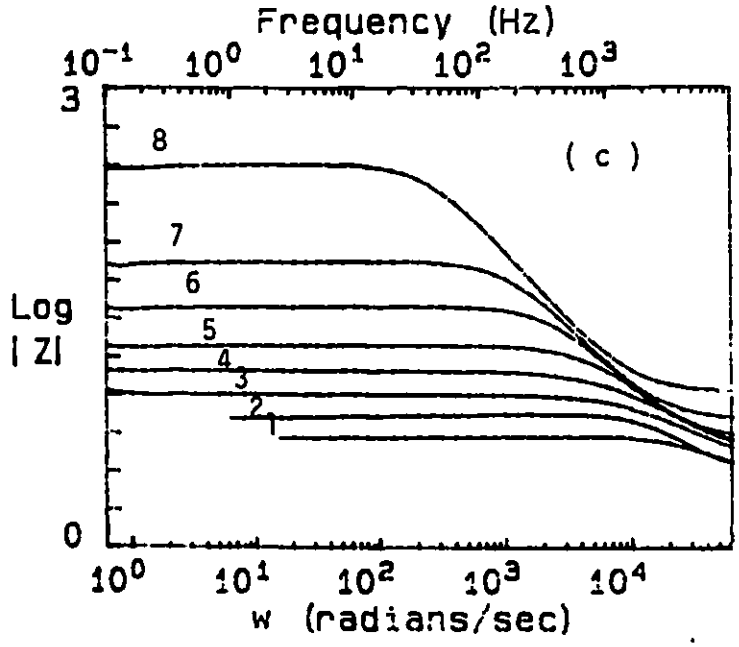


**Fig.40c** Log | Z | vs log ω plots for the same HER overpotential and temperatures as in Fig.40a at gold.

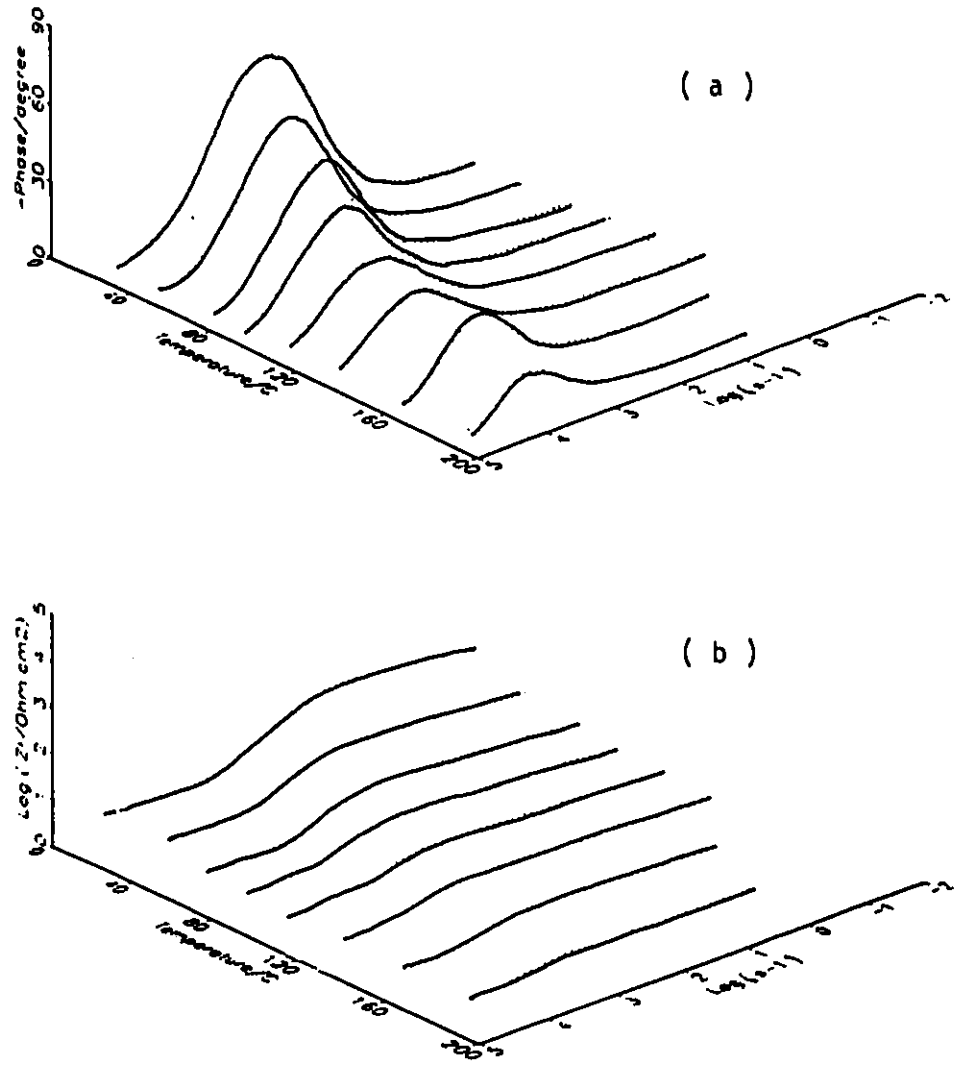


**Fig.42** 3-dimensional Bode-type plots for the HER at gold: (a) phase-angle vs log $\omega$ corresponds to the 2-dimensional plots in Fig.40b, and (b) Log $|Z|$ vs log $\omega$ corresponds to the 2-D plots in Fig.40c.

impedance, $R_1$, as the pseudocapacitance $C_\phi$ is only significant at substantially lower potentials, near the reversible potential of the HER.

It is also seen in Fig.40a that, at all temperatures, the complex-plane plots are in the form of nearly perfect semi-circles and can be represented adequately by a simple equivalent circuit of the kind shown in Fig.41a. Again, this is a good indication that there is only one component involved, probably that involving simple charging and discharging of the $C_{dl}$. When ideal semi-circle(s) complex-plane plots are obtained, information about the individual components of the C/R circuit, in this case, $C_{dl}$ and the corresponding $R_1$, can be estimated relatively easily without going to the simulation procedure mentioned above, according to the following basic relationship of the frequency response of a simple (parallel) C/R circuit:

$$C = 1/(R \times \omega) \tag{81}$$

where $\omega$ is the angular frequency (or $2\pi f$) at the top of the semi-circle and R can be read directly from the diameter (Z') of the semi-circle. The estimated $C_{dl}$ values are presented in Table VI for all temperatures, along with those derived from the potential decay method in section IV.B.2.1 for comparison.

From Fig.40c, it is evident that the total impedance of the system decreases with increasing T. In other words, the rate of charging and discharging of the double-layer capacitance is higher at higher T. This is also observed in the potential decay experiments (section IV.B.2.1) that the time required for the completion of potential decay (i.e., the discharge time for $C_{dl}$) decreases as temperature increases. These effects are as expected for general kinetic reasons, for a process having an activation energy.

Table VI. Comparison between estimated values of the $C_{dl}$ for the HER at Gold in 0.2 M NaOH derived from impedance spectroscopy and the potential decay method for several temperatures

| Temp (K) | $C_{dl}$ A.C. ($\mu F\ cm^{-2}$) | $C_{dl}$ Potl.Decay ($\mu F\ cm^{-2}$) |
|---|---|---|
| 450 | 49 | 36 |
| 432 | 38 | 16 |
| 405 | 35 | 20 |
| 382 | n.a. | 28 |
| 361 | 42 | 23 |
| 343 | 42 | 40 |
| 318 | 42 | 44 |
| 293 | 45 | 36 |

A.C. = a.c. impedance method and Potl.Decay = Potential Decay method

The effect of temperature on the HER can be seen more explicitly in the form of 3-dimensional Bode-type plots as illustrated in Figs. 42a and 42b, corresponding to the 2-D plots in Figs. 40b and 40c. Seemingly, apart from the change of the solution resistance, $R_s$, the effect of V is mainly on the reaction resistance $R_t$ of the system as similar behaviour can be simulated by the use of a simple $C_{dl}/R_t$ equivalent circuit ( Fig.41a) with constant $C_{dl}$ but various $R_t$ values dependent on potential and temperature. The results of the simulation are demonstrated in Fig.43.

The effect of d.c. level potential, V, on the a.c. behaviour is illustrated in Fig.44 again in a form of 3-D Bode-type plots for the 450 K temperature. The observed dependence of $R_t$ on V is, however, as expected as the reaction resistance is always an exponential function of V ( Tafel type relation ).

For the low d.c. polarization potential of -0.1 V vs PdH ( Figs 45a, 45b, and 45c),

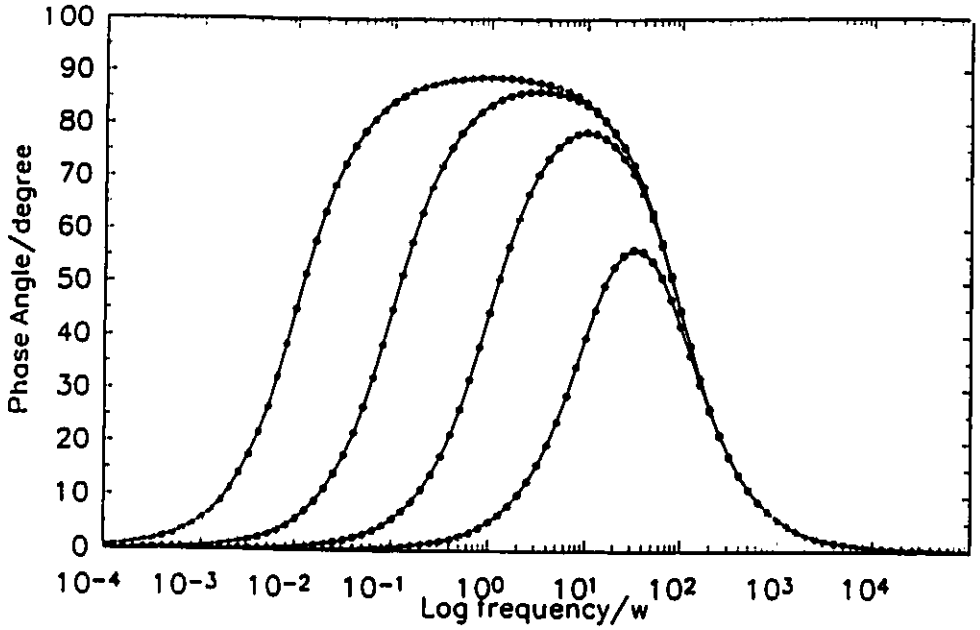


**Fig.43** Simulated phase-angle plots using an equivalent circuit of the type illustrated in Fig.41a for $C_{dl} = 10^{-2}$ F, $R_s = 1\ \Omega$, and four $R_p$'s 1) $10^1\ \Omega$, $10^2\ \Omega$, $10^3\ \Omega$, and $10^4\ \Omega$. Note the characteristic width at the peaks' half-height.

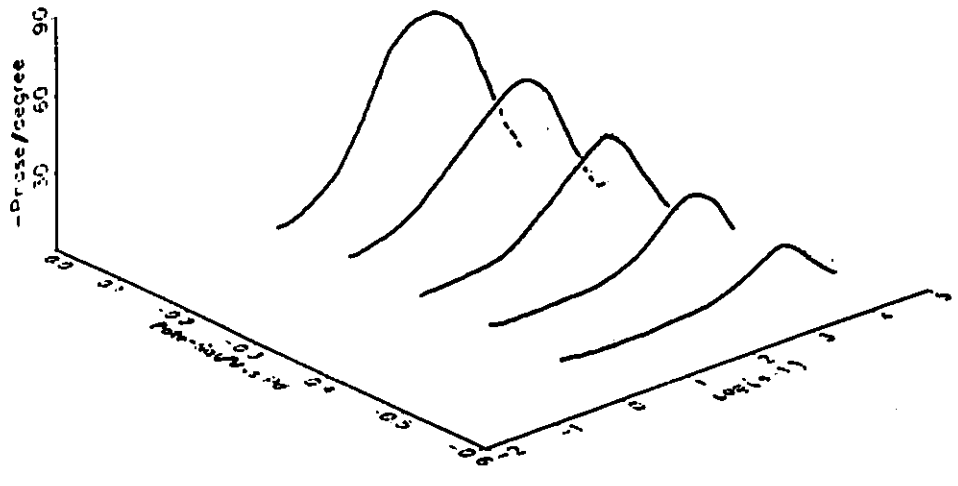

**Fig.44** 3-dimensional Bode-type phase-angle plots for a series of overpotentials in the HER for gold at 450 K.

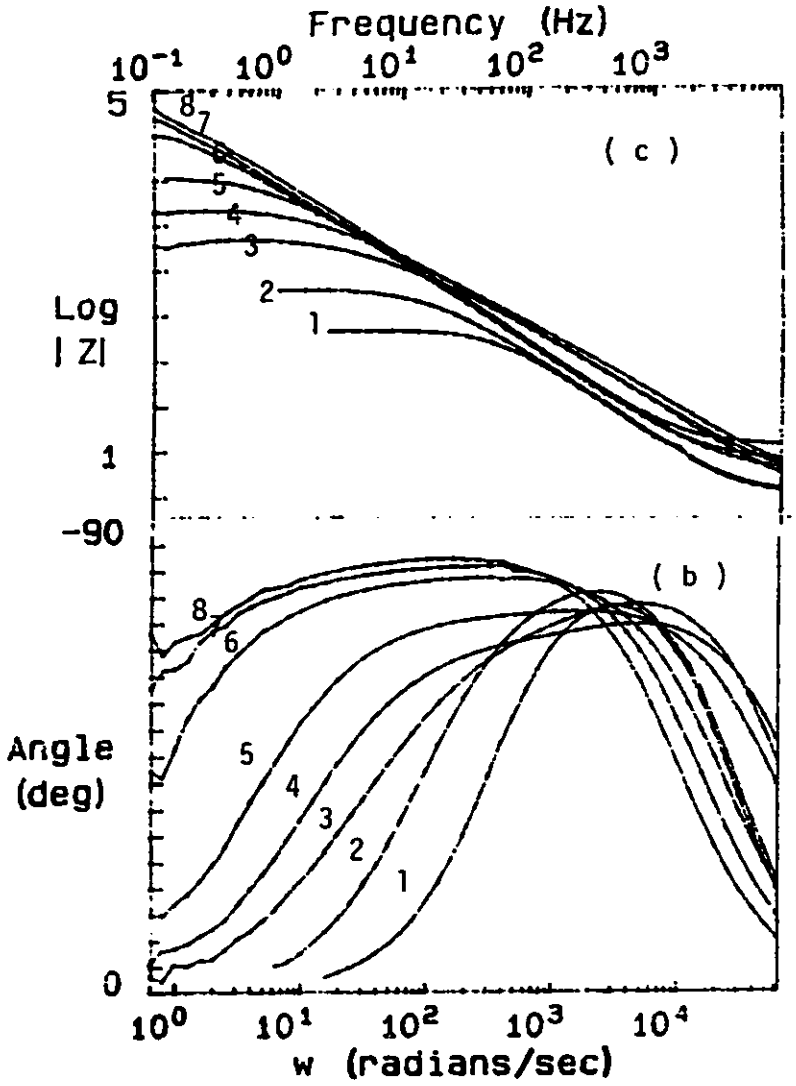


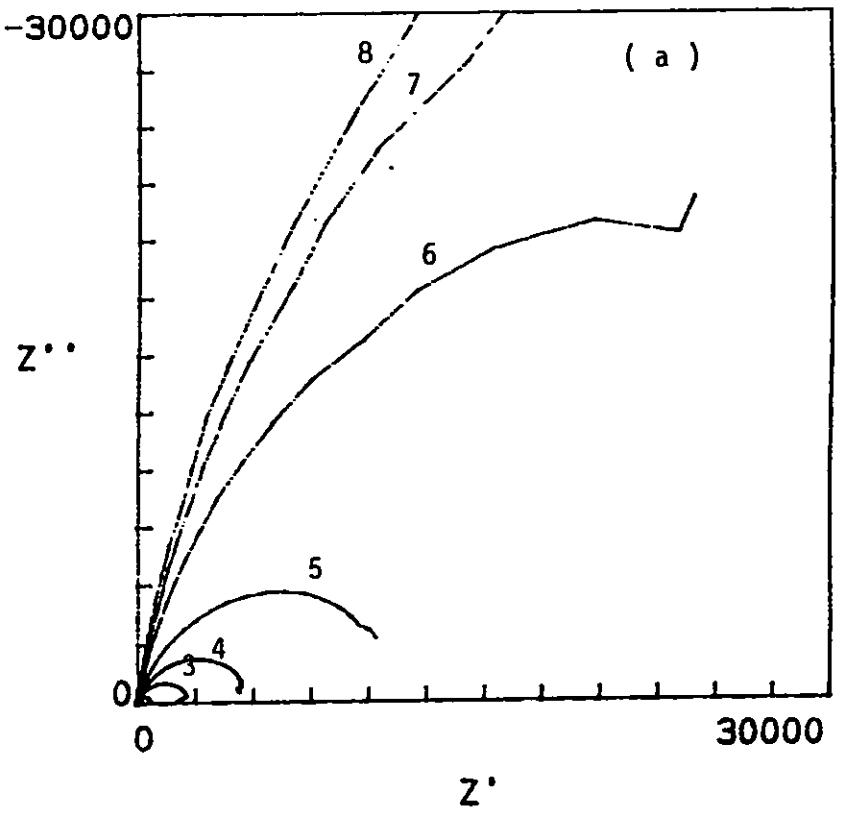


**Fig.45** A.c.impedance plots for gold as in Fig.40a-c but at -0.1 V vs PdH: (a) complex-plane plots; (b) phase-angle vs log ω plots; and (c) log | Z | vs log ω plots.

slightly distorted complex-plane plots (Fig.45a) were obtained for the same T range. It is likely, therefore, that the observed frequency-response is composed of *two components* which closely overlap. The contribution from the second component, which appears at lower frequencies and temperatures, did not, however, seem to be that significant since the same simple $R_t/C_{dl}$ equivalent circuit could be used to simulate similar behaviour but with larger reaction resistance values.

It is seen in Table VI that the values of the double-layer capacitance derived from the complex-plane plots in Fig.40a, show very little dependence on T and are about 40 $\mu$F cm$^{-2}$. These values are also quite similar to those derived from the potential decay method especially at temperatures below 361 K. Therefore, it is reasonable to assume that for the HER at gold in 0.2 M NaOH, no or very little adsorption of the intermediate H is involved even at temperatures as high as 450 K. This confirms the conclusion reached from interpretation of the potential relaxation results at Au.

In the light of all the evidence above, it can be concluded that the initial discharge step (I), not the subsequent electrochemical desorption step (II) or the alternative chemical recombination step (III) of the HER mechanism ( see section I.C.1a ), is rate-determining, otherwise the excess surface concentration of H would be manifested as a measurable pseudocapacitance. In fact, the values of upper Tafel slopes observed ( which are in the range 100 to 160 mV decade$^{-1}$, see section IV.B.1.1 ) are consistent with this proposition.

### IV.B.3.2 A.C.Impedance Behaviour of the HER at Nickel

As with the study of Ni in 0.2 M NaOH by the potential-transient decay method, a

range of T from 293 to 450 K was employed but for the sake of clarity, only the data for 360 and 450 K are shown below. The a.c.impedance behaviour at nickel examined as a function of frequency and d.c.-level potentials is shown in Figs 46a, 46b and 46c and Figs 47a, 47b and 47c, corresponding to the two respective temperatures. For the a.c. response at 360 K ( Fig.46b ), it is clear that the phase-plot exhibits *two components* ( unlike the behaviour at Au ) which become more separated as a function of $\omega$ as the electrode potential is decreased. The potential at which the second component becomes significant corresponds very well to the potential ( approximately -0.4 V vs Pd/PdH ) where the Tafel lines change their slopes ( Fig.34 ). Therefore, it is likely that the behaviour of the Tafel line is related to the two components of the phase plots. A similar kind of behaviour was also observed, as will be shown later, for the OER at $\beta$-$PbO_2$ at R.T. except that the respective Tafel lines have more distinguishable slopes and the two components of their phase plots are better resolved. The complex-plane plots at 360 K ( Fig.46a ) also reveal multi-component behaviour as imperfect or "depressed" semi-circles were observed, especially at lower d.c. potentials.

At 450 K (Fig.47c), the phase-angle profiles at various d.c.-level potentials exhibit principally one maximium which moves to lower frequencies as potential decreases. These profiles matched, closely in terms of shape and the frequencies of the maxima, with the first component of the bimodal phase plots at 360 K. That is, the main contribution of the a.c.impedance is most likely that of $C_{dl}$ and the contribution from the second component in the phase plots is minimal at such a high temperature ( 450 K ). However, the contribution from this second component, $C_\phi$, coupled with its reaction resistance $R_2$,

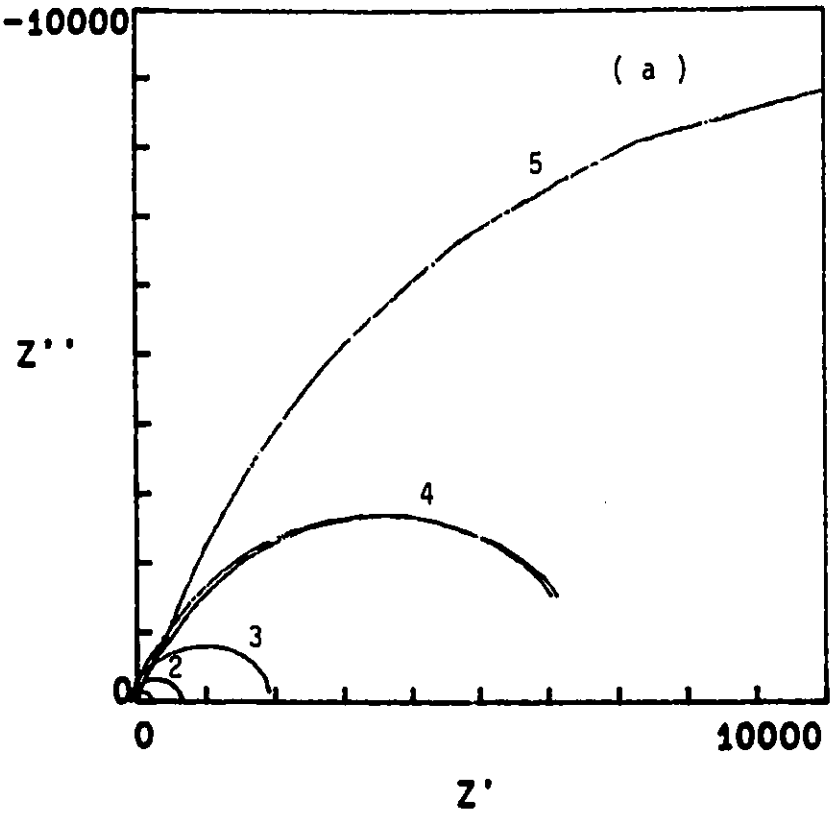


**Fig.46a** Complex-plane plots for the frequency response of impedance of the HER at nickel at 360 K for 5 HER overpotentials of 1) -0.5 V, 2) -0.4 V, 3) -0.3 V, 4) -0.2 V, and 5) -0.12 V vs PdH.

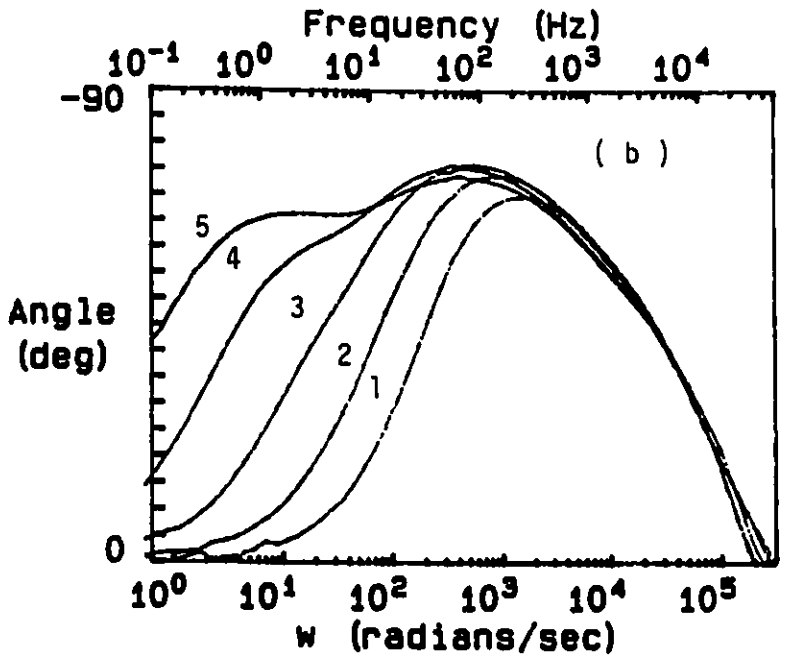


**Fig.46b** Phase-angle Bode-type plots as a function of log ω for the same series of HER overpotentials and temperature as in Fig.46a for nickel.

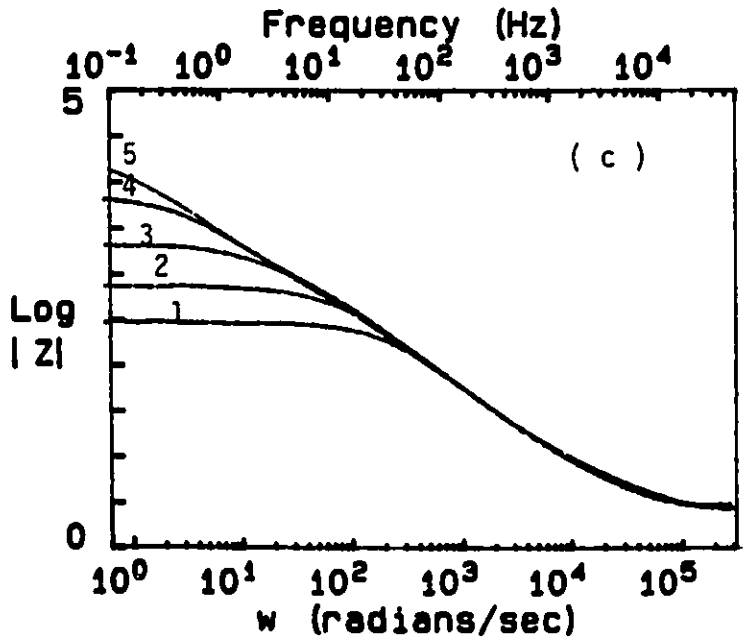


**Fig.46c** Log | Z | vs log ω plots for the same HER overpotentials and temperature as in Fig.46a at nickel.

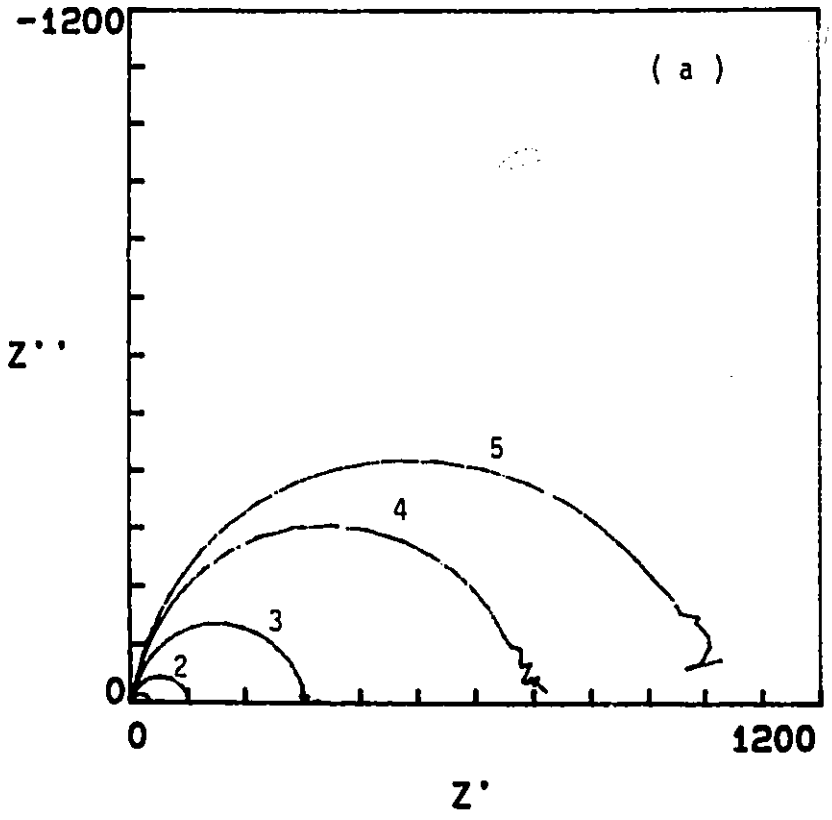


**Fig.47a** Complex-plane plots for the frequency response of impedance of the HER at nickel at 450 K for 5 HER overpotentials of 1) -0.5 V, 2) -0.4 V, 3) -0.3 V, 4) -0.2 V, and 5) -0.12 V vs PdH.

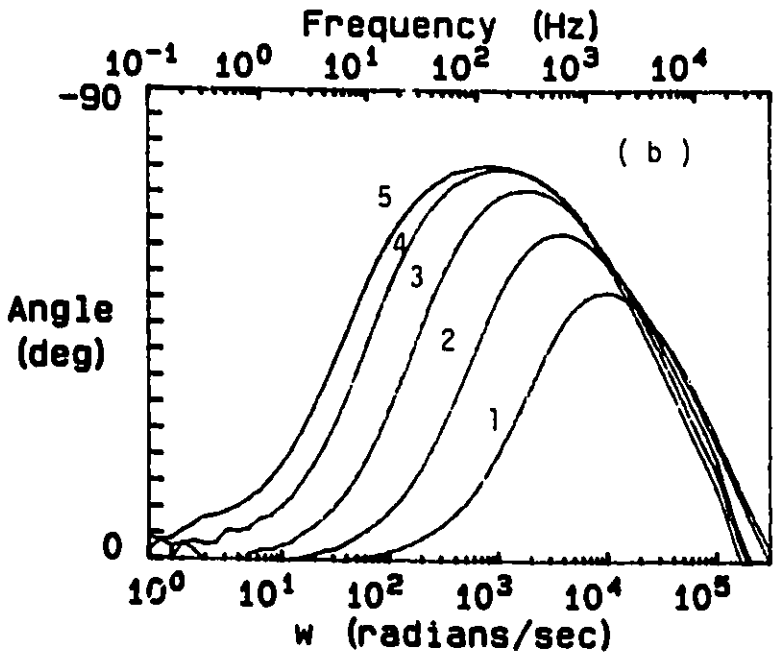


**Fig.47b** Phase-angle Bode-type plots as a function of log ω for the same series of HER overpotentials and temperature as in Fig.47a for nickel.

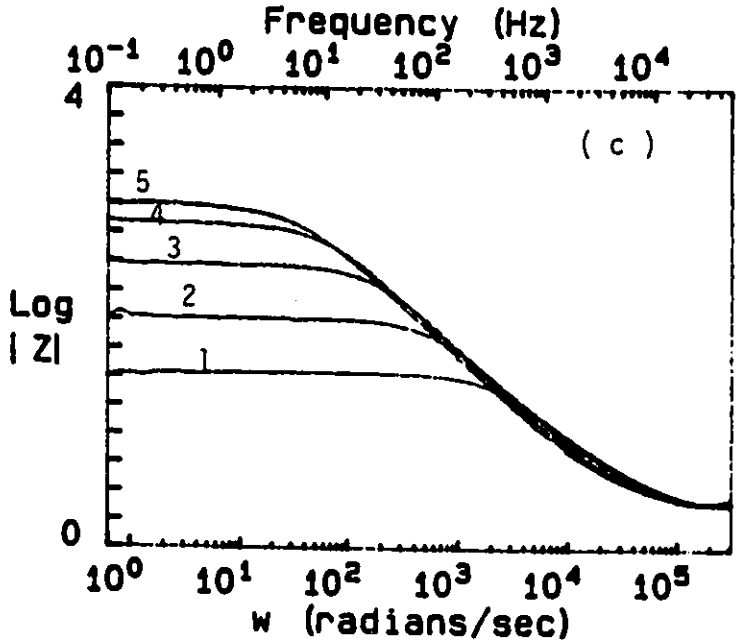


**Fig.47c** Log | Z | vs log ω plots for the same HER overpotentials and temperature as in Fig.47a at nickel.

becomes more important at lower potentials as revealed by the "depressions" of the respective complex-plane plots.

Operating in the same way as for the results at gold, the $C_{dl}$ at Ni was evaluated for a series of temperatures and its values are presented in Table VII below, together with the corresponding values obtain by the potential decay method for comparison.

Despite the fact that similar values were obtained for the entire T range by the two methods, the direction of change of the double-layer capacitance values does not seem to be following that of the temperatures. That is, from 450-346 K, there seems to be a gradual increase in the value of the $C_{dl}$ with decreasing T, implying that at 294 K, if the experiment were not stopped at 346 K, the value of $C_{dl}$ will be even higher than that of at 346 K. However, as can be seen in Table VII, the $C_{dl}$ obtained at 294 K before the system was heated up to the highest T of 450 K was about 40 $\mu$F cm$^{-2}$ which is the lowest value recorded in this experiment and is comparable with that at gold or at platinum.

**Table VII.** Estimated $C_{dl}$ for Nickel in 0.2 M NaOH solutions between 294 and 450 K

| Temp (K) | $C_{dl}$/a.c ($\mu$F cm$^{-2}$) | Time Lapse (days) | $C_{dl}$/pot.decay ($\mu$F cm$^{-2}$) |
|---|---|---|---|
| 294 | 40 | 0 | n.a. |
| 450 | 58 | 1 | 51 |
| 432 | 67 | 2 | 58 |
| 408 | 62 | 3 | 50 |
| 384 | 74 | 4 | 80 |
| 360 | 81 | 5 | 87 |
| 346 | 118 | 6 | n.a. |

Note: results are presented in the same order as experiments were conducted.

Careful re-examination of the results presented in Table VII indicated that the

observed change in $C_{dl}$ at Ni is possibly not the sole effect of T but of time as well. Since the values of $C_{dl}$ seems to follow a linear relation in time lapse, it is therefore resonable to assume that the electrode was becoming modified gradually by the increasing T over the course of the experiment. By assuming the $C_{dl}$ for 1 $cm^2$ of nickel is 40 $\mu$F, as found in the present work, the above behaviour implies that the surface area of the electrode had been expanded approximately thrice after only six days of heating at various temperatures. Thus, the interpretation of the a.c. impedance behaviour of nickel is rather more complicated than that of gold which did not suffer from surface modification under the same experimental conditions.

**IV.B.3.3 A.C.Impedance Behaviour for the HER at Platinum**

Interesting but unexpected a.c.impedance behaviour was observed for Pt in 0.2 M NaOH. Basically, distorted complex-plane plots were obtained for temperatures from 294 up to 371 K. Again, the extent of distortion became reduced with increasing d.c. polarization potential ( Fig.48a ). The corresponding phase-angle plots exhibit a single-peaked profile which moves progressively to lower frequencies as potential is made lower presumably due to increasing contribution from a second component ( Fig.48b ). The reaction resistances are relatively small in comparison to those of Au and Ni, consistent with the short self-discharge times observed in section VI.B.2.3 by the potential-transient decay method.

For some unknown reasons, the a.c.impedance behaviour at T above 371 K showed very little reaction impedance, real or imaginary, apart from the solution resistance which

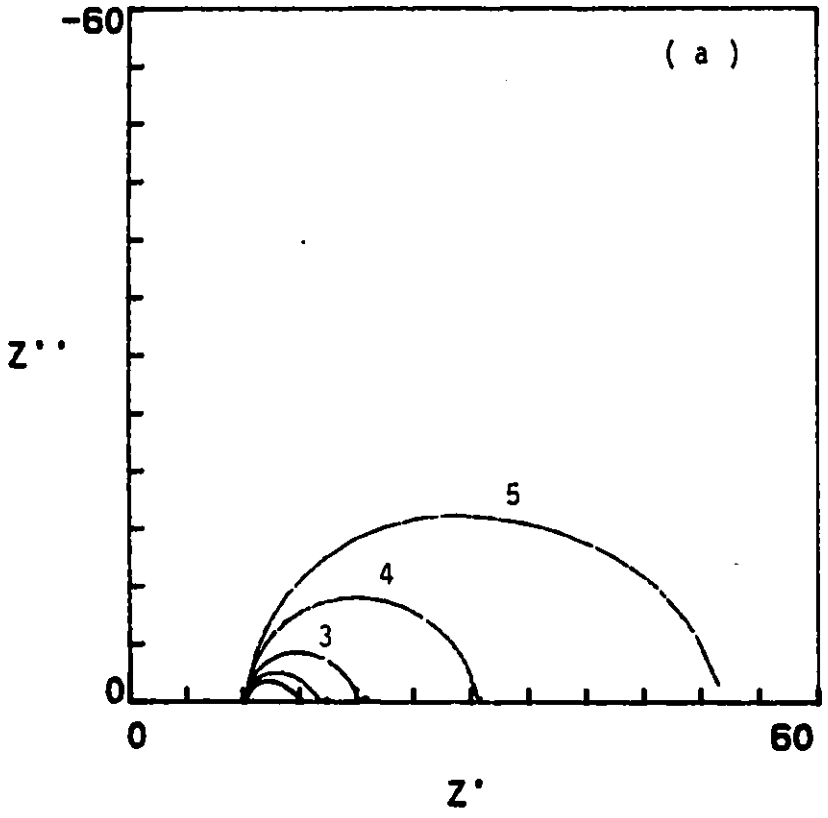


**Fig.48a** Complex-plane plots for the frequency response of impedance of the HER at platinum at 294 K for 5 HER overpotentials of 1) -0.5 V, 2) -0.4 V, 3) -0.3 V, 4) -0.2 V, and 5) -0.10 V vs PdH.

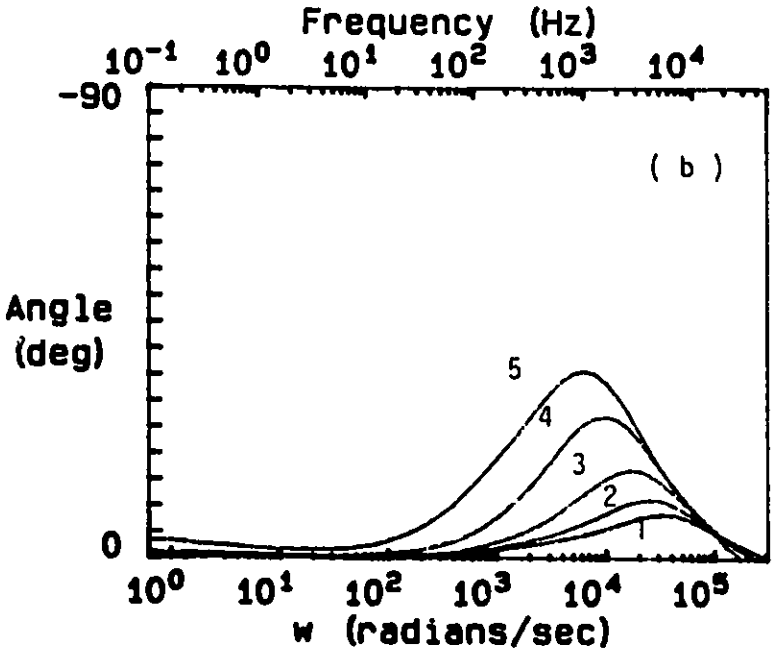


**Fig.48b** Phase-angle Bode-type plots as a function of log ω for the same series of HER overpotentials and temperature as in Fig.48a for platinum.

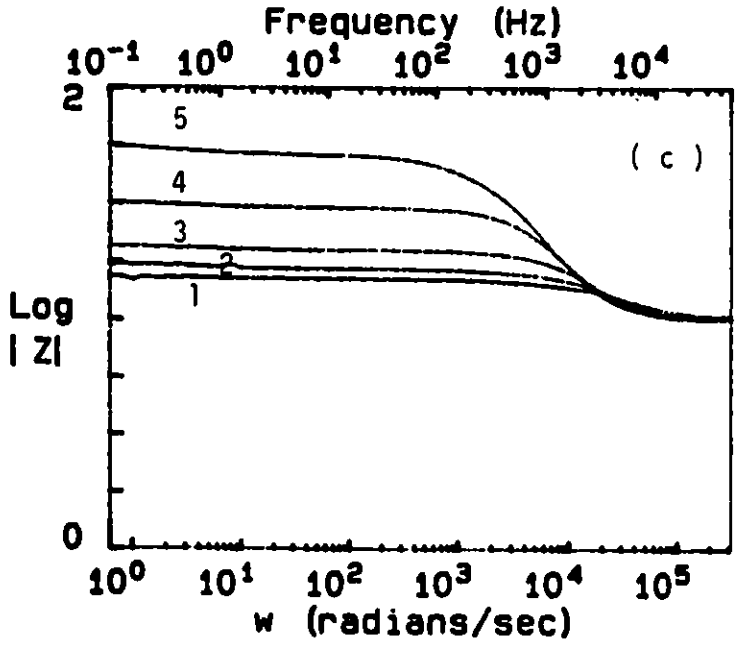


**Fig.48c** Log | Z | vs log ω plots for the same HER overpotentials and temperature as in Fig.48a at platinum.

was observed throughout the entire temperature range. Therefore, it is possible that the a.c.impedance technique is not capable of providing the necessary information about the electrode system when excessive absorption of H into the metal is involved and where reaction rates are high. Nevertheless, the double-layer capacitance values deduced from both the a.c. impedance and the potential decay methods at the lower temperatures are in quite good agreement with each other as recorded in Table VIII.

**Table VIII.** Comparison of the estimated $C_{dl}$ values obtained by the a.c. impedance and the potential decay methods

| Temp (K) | $C_{dl}$/a.c. $\mu F\ cm^{-2}$ | $C_{dl}$/Pot.decay $\mu F\ cm^{-2}$ |
|---|---|---|
| 294 | 43 | 43 |
| 320 | 46 | 54 |
| 347 | 65 | 64 |

## IV.B.4 Conclusions on the HER at Au, Ni and Pt at Elevated Temperatures

The behaviour of the cathodic $H_2$ evolution reaction at Au, Ni and Pt in 0.2 N NaOH solution was studied at temperatures from 293 to 473 K. Both Au and Ni electrodes exhibited similar Tafel relations in which Tafel lines were all made of two linear segments while Pt gave rise to curved Tafel relations at all temperatures studied. It was found that in most cases, the conventional temperature dependence of the Tafel slope, $b$, expressed as $b = 2.3\ RT/\alpha F$ was not followed. For those cases ( e.g. the high c.d. Tafel regions for Au and Ni ) where the conventional expression of $b$ does seem to be followed, the values of $\alpha$ or $\beta$ were not anywhere near 0.5.

With regard to the rate of the HER, expressed in terms of the $i_o$ values, the general

trend is that the higher is the T the larger is the $i_o$, a result expected in terms of the Arrhenius equation. For a given T, it was found that the magnitude of $i_o$ for such reaction is the largest at Pt, followed by Ni and Au, as is well known from other literature data.

Amongst the three metals studied, the extent of the electrode coverage by the electroactive intermediate, H, at a given T seems to follow the same order as for the $i_o$ values, i.e., Pt > Ni > Au. In the case for Pt, apparent coverage of more than 100 monolayers of H at elevated temperatures ( e.g., 473 K ) appears to be related to the extensive " H absorption " into the Pt electrode. On the other hand, the gold electrode does not seem to be covered significantly by adsorbed H, and the capacitance which arises at the interphases of the gold electrodes is primarily that of the double-layer.

The double-layer capacitances, measured by means of either the potential-relaxation transient or a.c. impedance technique for the three metals studied here are in good agreement with each other and have values of about 40 $\mu$F cm$^2$ at R.T. Interestingly, an almost constant $C_{dl}$ value was observed at Au at all T while at Pt and Ni, a gradual increase in values of the $C_{dl}$ was observed. The interpretation of the changes in the $C_{dl}$ values at Ni and Pt, however, is complicated by the probable formation of "NiH" at the Ni electrode interphase, thereby increasing its "real" surface area on prolonged experiments, and the possible involvement of "H absorption" into the Pt electrode.

## IV.C Oxygen Evolution Reaction

### IV.C.1 Oxygen Evolution Reaction at Platinum

In the present work it was found that reproducible experimental results were

generally harder to obtain for the OER than for its counter reaction, the HER, under the high-temperature/high-pressure conditions. One of the possible reasons is that the chemical and/or physical nature of the surface metal oxide film can be adversely affected by temperature. For instance, there is always the possibility that, during the polarization experiments under high T conditions, additional layers of metal oxide may be formed depending on the duration and potential of the experiment.

It has been reported [110-114] that the rate of the OER in acid solutions depends, at Pt, on the thickness of the Pt oxide film on which the $O_2$ evolution takes place. In alkaline solutions, conflicting Tafel relations have been reported. For instance, in earlier papers, Hoar [115] reported a linear Tafel relation with a slope of ca. 60 mV/decade while others [116] reported a slope of ca. 120 mV/decade. Also, Tafel relations with *two* linear regions, 60 and 120 mV/decade for the low and high current density regions, respectively, have been reported [117,118]. All of these ambiguities probably stem from the different electrode pre-treatment procedures leading to various kinds of poorly characterized platinum oxide surfaces. In the present work, a Tafel relation of yet another form is reported. Moreover, the evaluation of the behaviour of the adsorbed intermediate species could be more complicated than in the case of the HER due to the possible involvement of two adsorbed species, O and OH, and correspondingly different oxidation states of Pt in the oxide film. The double-layer capacitance and the potential dependence of the adsorption behaviour of the O or OH intermediates in the OER at Pt was investigated here only by the method of a.c.impedance as it was shown in the previous sections that it is capable of providing adequate and useful information.

**IV.C.1.1 Tafel Relations for the OER at Pt**

Fig.49 represents a series of potential vs log (current density) Tafel relations for the OER at platinum in 0.2 M NaOH solutions corresponding to a T range of 476 to 301 K. It is seen from these Tafel lines that three regions can be distinguished. For the Tafel line recorded at 301 K: first, a linear low current density region arises when $V < 0.2$ V vs PtO; second, a limiting current ( or potential jump ) region arises between 0 and 0.8 V over less than a decade of current; third, a linear high current density region arises when $V > 0.8$ V over a current range of two to three decades. The low and high Tafel regions have slopes of approximately 0.055 and 0.15 V/decade, respectively. As temperature is increased, there is a corresponding increase in current density at a given potential, as expected, while the height of the potential jump decreased presumably due to the fact that the high current density Tafel region commenced at lower potentials at higher temperatures. While the general shapes of the first and second Tafel regions did not change much with temperature, the slope of the third Tafel region did. Table IX summarises the change of this slope as a function of temperature.

When the test for constancy of the transfer coefficient was carried out by plotting $b/T$ vs T assuming $b/T = 2.303(R/\alpha F)$, as in section IV.B.1.1, no uniform value was obtained, especially at lower T as can be seen in Table IX. This is another example of the frequently observed unconventional behaviour of $b$ with respect to its dependence on T.

The presence of the potential jump near the reversible potential was of concern since a very effective membrane separator was employed between the working and the counter

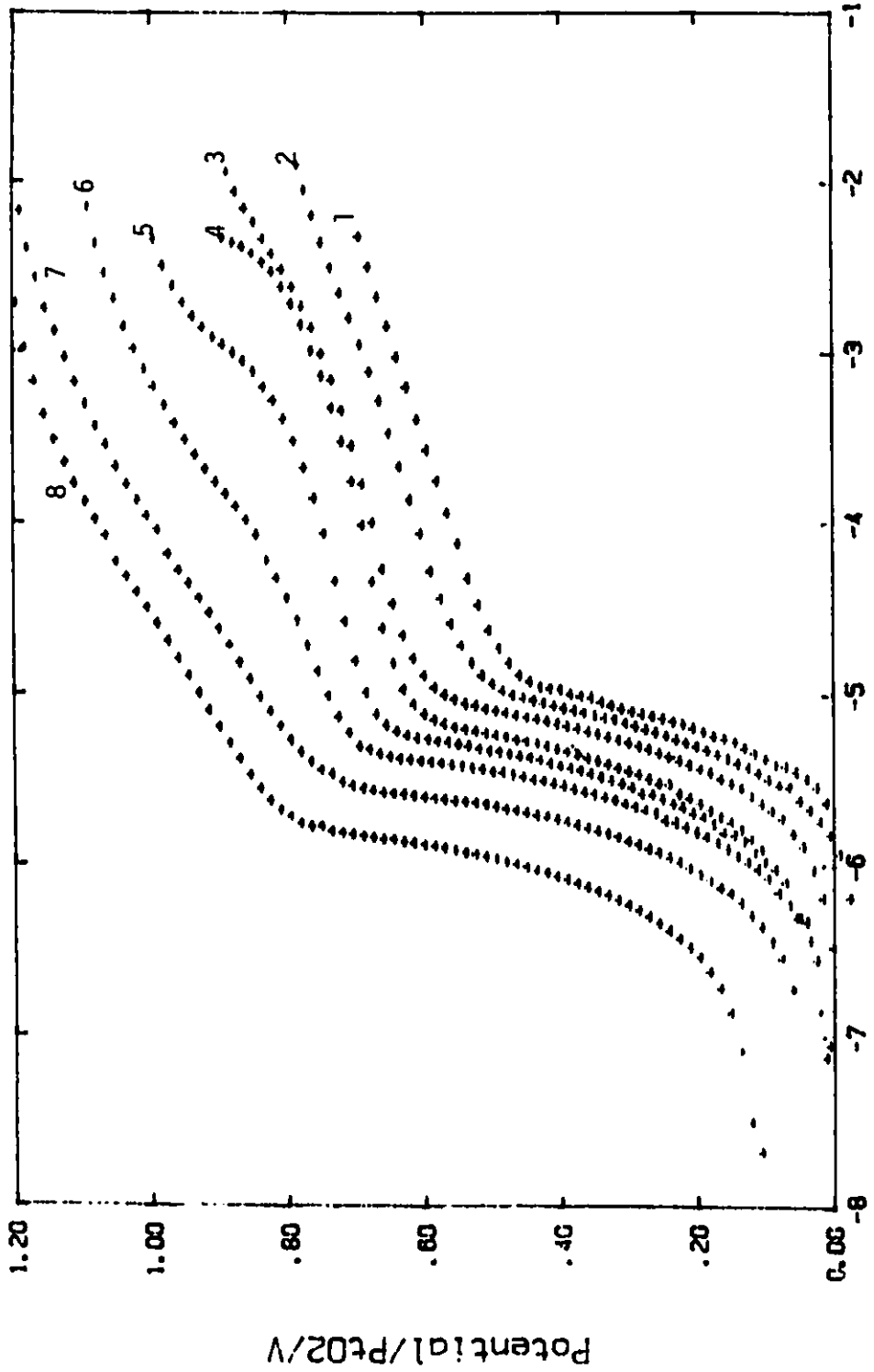


**Fig.49** Tafel relations for the OER at 8 temperatures 1) 476 K, 2) 449 K, 3) 423 K, 4) 399 K, 5) 370 K, 6) 349 K, 7) 325 K, and 8) 301 K at platinum in 0.2 N NaOH aq. solutions.

electrode compartments so that anodic oxidation of molecular hydrogen generated in the counter compartment is unlikely. In fact, at most temperatures, the reversible region of the Tafel lines at about 0 V vs PtO could be seen clearly, thus, precluding the above possibility. A similar sort of "break" in the Tafel relations were also observed for the OER at Pd and Au in $H_2SO_4$ as reported in some earlier papers [94,109]. It was thought that the origin of this break might be due to a change of oxidation-state of Pt as the potential is made more positive or negative. In other words, the behaviour of the Tafel lines immediately before and after the potential jump was connected to two different kinds of metal oxide surfaces. The possibility of oxidation-state change is, however, not very likely in the present case as the platinum atoms in the $PtO_2$ lattice should already be in their highest possible oxidation-state of +4 ( the same situation arises for the lead dioxide electrodes also examined in this work, as will be shown later).

Formally, this change of Tafel behaviour could be accounted for as a change of reaction mechanism. The first curved Tafel regions could be attributed to a mechanism involving recombination control while the third Tafel region, at higher potentials, is most likely that of control by the electrochemical desorption step.

The two chemical-type recombination processes possible at Pt-oxide in alkaline solutions are;

$$(1) \qquad 2\ Pt.Ox(OH) \rightarrow Pt.Ox(O) + Pt.Ox + H_2O \qquad (67)$$

and

$$(2) \qquad 2\ Pt.Ox(O) \rightarrow Pt.Ox + O_2 \qquad (68)$$

and the desorption step is:

$$Pt.Ox(OH) + OH^- \rightarrow Pt.Ox(O) + H_2O + e^- \qquad (69)$$

**Table IX.** Tafel slopes observed for the OER at Pt in 0.2 M NaOH at several temperatures

| Temp (K) | b,dV/dlogi (V/dec i) | *b*/T (V K/dec i) |
|---|---|---|
| 476 | 0.080 | 1.7E-4 |
| 449 | 0.075 | 1.7E-4 |
| 423 | 0.060 | 1.4E-4 |
| 399 | 0.060 | 1.5E-4 |
| 370 | 0.060 | 1.6E-4 |
| 349 | 0.105 | 3.0E-4 |
| 325 | 0.160 | 4.9E-4 |
| 301 | 0.150 | 5.0E-4 |

## VI.C.1.2 A.C Impedance Behaviour of the OER at Pt

Figs 50a, 50b and 50c represent, for the respective T's of 476, 399 and 301 K, the dependence of phase-angle on frequency for the OER at Pt in 0.2 M NaOH at various d.c.-level potentials corresponding to the linear high current-density or potential regions and the limiting-current regions of the Tafel relations ( Fig.49 ). It is to be emphasised that distinguishable phase-angle profiles are observed for these two different Tafel regions, as can be seen clearly in Fig.50b for 399 K.

For the high current-density region, the single-peaked profile which corresponds mainly to relaxation involving the double-layer capacitance, seems to have similar potential-dependence to that for nickel, i.e., the peak maxima move progressively to lower frequencies as the overpotential is decreased. Again this is probably due to the increasing contribution of a second component in the lower frequency range and arises as a result of

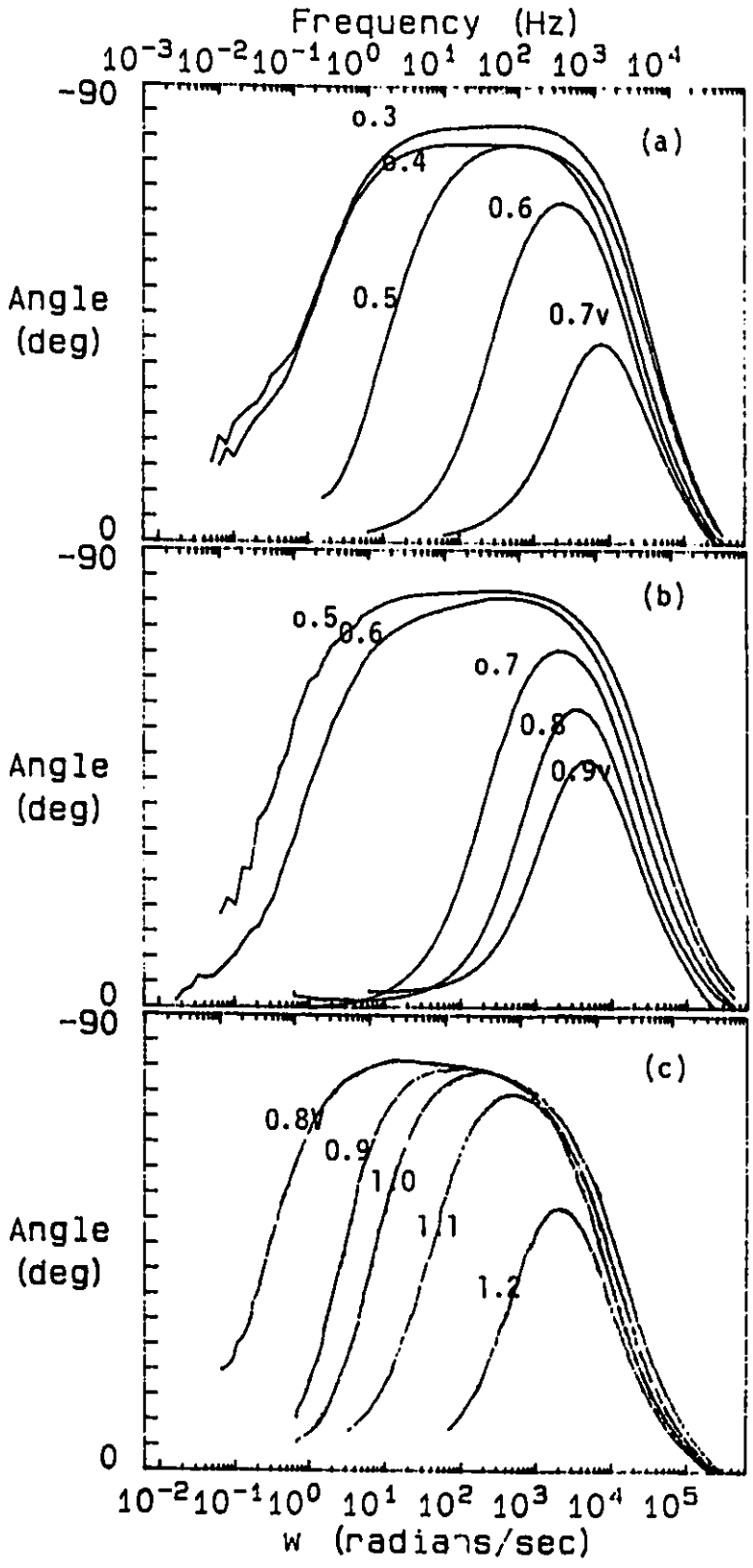


**Fig.50** Phase-angle Bode-type plots as a function of log ω for a series of OER low and high overpotentials at 3 temperatures: (a) 476 K, (b) 399 K, and (c) 301 K for platinum in 0.2 N NaOH solutions.

adsorption/desorption of the electroactive intermediates, in this case, O and/or OH. This is consistent with a mechanism with an electro-desorption rate-controlling step.

For the limiting-current region of the Tafel relations, the phase-angle profiles do not seem to be influenced very much by the potential change. Therefore, it is reasonable to assume that in the "potential jump" region of the Tafel lines, there is no further pseudocapacitance contribution to the phase-angle profile, i.e., $C_\phi = 0$. This would be the case when the relevant $\theta$ is approximately equal to 1. The above evidence implies that the potential jump region is, in fact, the result of an OER mechanism that becomes recombination controlled rather than being related to a possible change of oxidation-states of Pt in the oxide film.

## IV.C.2 Conclusions on the Oxygen Evolution Reaction at Pt at Elevated Temperatures

A new form of Tafel relation is reported here in this thesis for the OER at Pt in aq. 0.2 N NaOH solutions, that is, Tafel relations with two linear segments corresponding to the low and high c.d. regions of the Tafel lines, together with a limiting current or "potential jump" region in between, were observed. The linear low c.d. region and the limiting current region are believed to be related to the OH and/or O recombination controlled mechanism of the OER process while the linear high c.d. region of the Tafel line is most likely that of control by an electrochemical desorption step. Further, the Tafel slope, $b$, behaved unconventionally as observed for the HER at various metals studied and as reported in the last section of this thesis.

## IV.D Electocatalysis and Adsorption in the Anodic Oxygen Evolution Reaction at Lead Dioxide in its Dimorphic States, $\alpha$ and ß-$PbO_2$

In this section of the thesis, the study of the OER described in Section IV.C.1 for Pt is extended to $PbO_2$ in its two principal allomorphic forms, $\alpha$- and $\beta$-$PbO_2$. These two materials provide the opportunity of examining differences of electrocatalysis and adsorption behaviour in the OER at two structurally different oxides that are chemically identical, except perhaps for very slight differences of perfection of stoichiometry. Also, behaviour at several temperatures enabled a further opportunity for the variation of $b$ with T to be examined.

The mechanism and other factors involved in the OER process were discussed already in Sections I.C.1b and Section IV.C.1. In the case of $PbO_2$, the OER takes place at the surface of a bulk, electronically-conducting oxide rather than on a very thin oxide film, as for the case of the reaction at Au and Pt. On account of the difference of bulk structures of $\alpha$- and $\beta$-$PbO_2$, the surfaces of exposed planes of the oxide, on which the OER proceeds, will also be different.

It is important [33,68,70] to characterize the electrochemical adsorption behaviour of the chemisorbed intermediates that are involved in the electrocatalytic multi-step reaction mechanisms of processes [71,72] such as evolution of $H_2$, $Cl_2$, $F_2$, $N_2$ (from $N_3^-$) and $O_2$. Such studies provide an essential complement to works on surface structure, surface composition, electronic band-structure and direct examination of reaction kinetics that provide the conventional basis of research on electrocatalysis.

There are several aspects of significance of the present work in relation to earlier

works done in this laboratory on anodic $O_2$ evolution on transition metal oxides or oxide films: a) the examination of the adsorption behaviour of OH and O intermediates on a non-transition-metal oxide surface, of $PbO_2$; b) the existence of the $PbO_2$ in dimorphic states, $\alpha$ and ß, on which $O_2$ evolution behaviour and adsorption effects can be compared in relation to the structures of these "allotropic" forms of $PbO_2$ and, in particular, their surfaces and c) the practical involvement of $O_2$ evolution on overcharge at lead-acid battery positive plates.

The existence of two structurally different forms of a conducting metal oxide on which $O_2$ evolution can be studied and which is also a process of practical significance in lead acid battery operation, provides almost a unique opportunity of examining the structural effect in electrocatalysis of the OER on an oxide material.

## IV.D.1 Review of Relevant Previous Work

Before the discovery of $\alpha$-$PbO_2$ by Kameyanm and Fukumoto [73] in 1946 and its subsequent identification by Zaslavsky et al.[74], only ß-$PbO_2$ was known. The two modifications differ only in their crystal structure with the former being orthorhombic and the later tetragonal. These different 3-D structures will give rise to different 2-D surface oxide geometries, depending on the orientation of the crystal plane exposed. The major structural differences between the two lead dioxides are illustrated in Fig. 62a,b extracted from a recent paper of Rüetschi [76]. Both modifications of lead dioxide have been found to coexist in the positive electrode of the lead-acid battery as revealed by microscopic studies of lead-acid battery electrodes [75]. Under carefully controlled conditions, pure

dioxide free from the other form can be prepared by electrodeposition from electrolytes [35,77]. In general, $\alpha$-$PbO_2$ is formed under alkaline conditions while the ß-$PbO_2$ from arises under acidic conditions. Unlike many other metal oxides which are usually only semiconducting, the lead dioxides are good conductors of electricity. The resistivity [78] of electrodeposited ß-$PbO_2$ at 298 K was found to be $0.95 \times 10^{-4}$ ohm cm and the principal charge carriers in the lead dioxides are electrons [79]. It is the metal-like property of lead dioxides that enables their direct study to be made by means of conventional electrochemical techniques of the kind that have been successfully applied to many other metal/electrolyte systems.

Since $PbO_2$ is an important material of the lead-acid battery, its electrochemical properties have been the subject of active research over many years. Most of this work has however, been related to practical aspects of battery behaviour such as anodic corrosion of the lead or lead-alloy electrodes. The principal reason why lead-acid batteries wear out in service is the anodic corrosion of the grid of the positive plate with $\alpha$-$PbO_2$ as the major corrosion product [80,81] and "sulphation", the irreversible accumulation of un-rechargeble $PbSO_4$. In the industrial evaluation of this corrosion, an overcharge test is often applied which involves anodizing the electrode at a constant current or potential in the region of oxygen evolution. Therefore the study of the accompanying $O_2$ evolution reaction ( OER ) is also important for understanding this aspect of lead-acid battery behaviour as also for overcharge behaviour in general.

Several studies of the OER on lead dioxides have been reported previously: Jones et al.[82] determined the $O_2$ overvoltage on lead dioxide electrodes in aq. $H_2SO_4$ under

---

* While the two forms of $PbO_2$ have high conductivities,comparable with those of some metals,it is not altogether clear if the former materials are to be regarded as metals or degenerate semiconductors.The distinction depends on the signs of the temperature coefficients of their electrical conductivities, metallic conductivity having a characteristic negative coefficient.

(a)

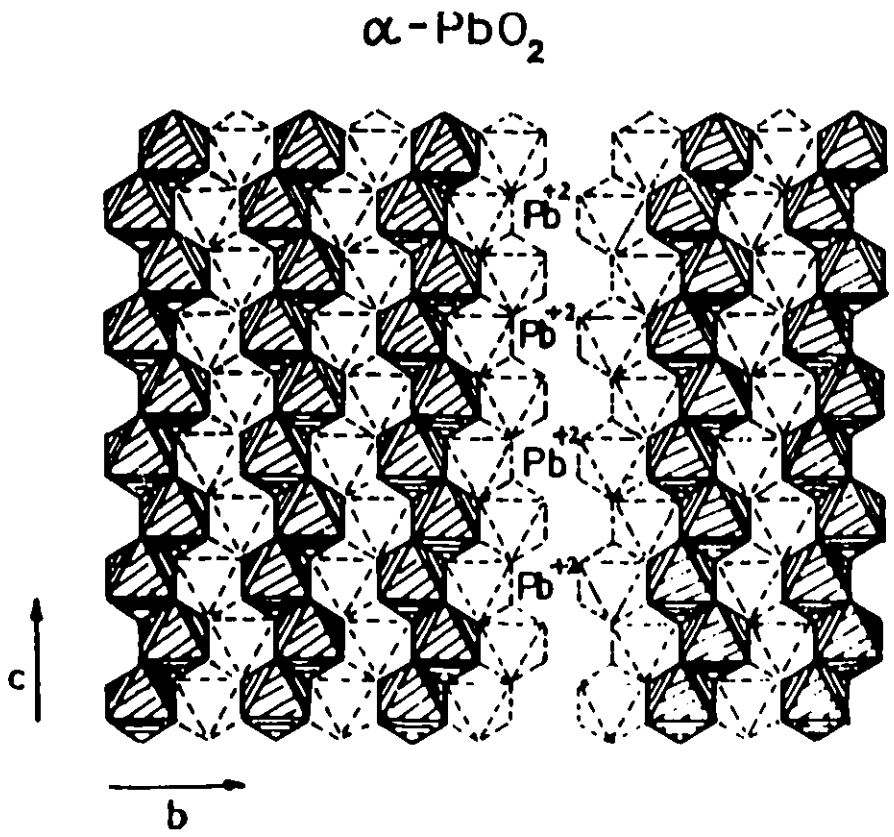


**Fig.62** The structural differences between (a) α- and (b) β-$PbO_2$ arise principally from the different arrangement of "$PbO_2$" hexa-coordinate units. (From Ref.76).

(b)

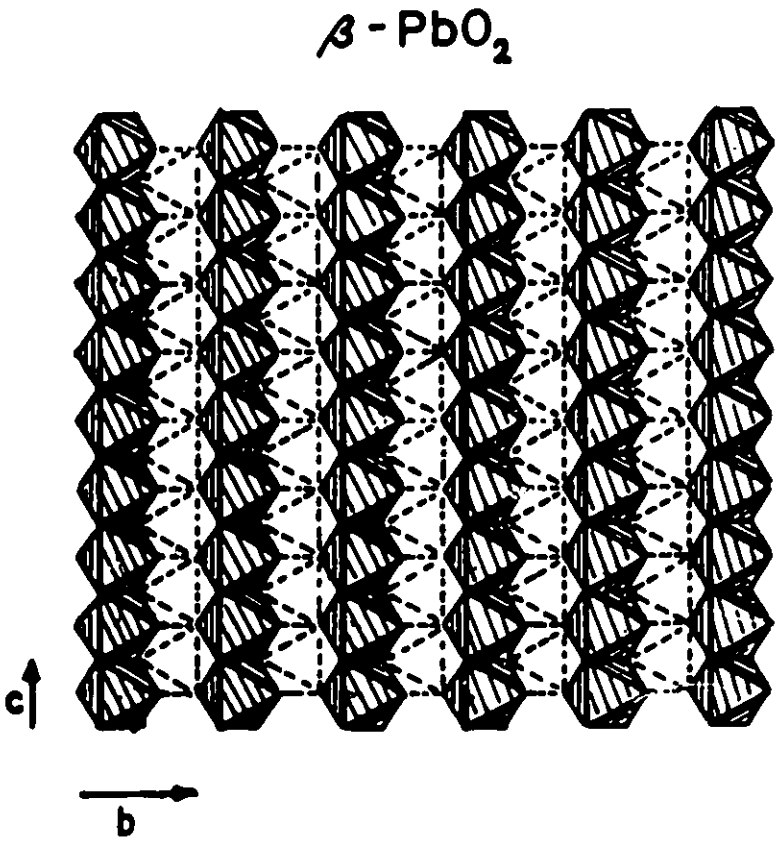


**Fig.62** The structural differences between (a) $\alpha$- and (b) $\beta$-$PbO_2$ arise principally from the different arrangement of "$PbO_2$" hexa-coordinate units. (From Ref.76).

constant current steady-state polarization conditions, the electrodes being prepared both by electrolytic oxidation of Pb in $H_2SO_4$ and by electrodeposition of $PbO_2$ onto platinum. Linear Tafel polarization relations were found. The first comparative studies of the OER on the two $PbO_2$ modifications were made by Rüetschi et al.[80] by means of anodic open-circuit decay experiments. They reported Tafel slopes of 0.07 V and 0.14V for $\alpha$ and ß-$PbO_2$, respectively.

Although most studies on the OER at $PbO_2$ have been performed in aq.$H_2SO_4$, as in the lead-acid battery, various other electrolytes have also been investigated, including KOH, NaOH, $HClO_4$, amongst which aq.$HClO_4$ is the most attractive since complications due to formation of an insoluble non-conducting $PbSO_4$ or to anion adsorption are minimal, although the latter has been detected [83,84]. $HBF_4$ has also been investigated as the battery acid.

In most of the OER studies on lead dioxides [35,82,85-93] a generalized theory for the mechanism was formulated in which the first step of the reaction sequence usually involves adsorption of an OH intermediate from discharge of $H_2O$ in acid or $OH^-$ in alkaline solution, followed by the rate-controlling step of electrochemical oxidation of OH to form a second intermediate O which undergoes chemical recombination giving rise to the evolution of $O_2$ ( cf.ref.[34] ).

Rüetschi and Delahay [94] in their theoretical studies of the kinetics of the OER on various metals showed that there is a correlation between the oxygen overvoltage on metals and the respective M-OH bond energies, assuming that the first step of formation of OH in the mechanism above, was the rate-controlling step. Three methods were employed in

estimating the metal-OH bond energies and the values were plotted against the oxygen overvoltage on different metals at 1 A $cm^{-2}$ in 1 N KOH. Their results, however, were not conclusive as the correlation depends very much on how the M-OH bond energies were calculated. Also, the validity of their approach is questionable as it must be recognized that the OER proceeds not on the bare metal surface but on one already covered with a layer of metal oxide.

Search of the recent literature reveals a substantial activity in Soviet research on the OER at $PbO_2$ and related behaviour, and several selected significant papers are referenced as [83,84,89,90,92,95,96].

In studies of the mechanism of the OER on $PbO_2$, or that of other complex, heterogeneously catalysed Faradaic reactions such as the $H_2$ evolution reaction, it is important to take into account the potential dependence of the coverage by the adsorbed intermediates that are kinetically involved in the major steps of the reactions, as has been emphasised earlier in this thesis. In the case of anodic gas evolution reactions, the processes are fundamentally different from that of $H_2$ evolution since they proceed on a metal oxide or a metal oxide film instead of on the bare metal surface, as mentioned earlier. Therefore, in addition to OH or O, the intermediate species on the surface of the electrode can be some higher oxidation states of the metal in the oxide at its surface, acting as mediators for charge transfer. It is the potential-dependence of the intermediate(s) that determines, in part, the Tafel slope,b, in the polarization behaviour of the electrode. Along with the exchange current density, $i_o$, this is one of the bases for characterizing the electrocatalytic performance of an electrode process.

In the case of the OER on base metals (e.g.Ni,Co) and, to some extent, on noble metals (e.g.Au,Pt), the oxidation state of the metal ion in the metal oxide lattice at the surface of electrode can be a function of potential,i.e. more than one oxidation state of the metal can be involved in the process as the electrode potential changes from low to high values. These surface metal ions of higher oxidation states can act as charge-transfer mediators in the OER as, for example, at Ni as proposed by Conway and Bourgault [99]. Recently, Rasiyah and Tseung [87] investigated the practical"minimum potential" for onset of the OER on several metal oxides, including $PbO_2$ in 5N KOH, by steady-state polarization and galvanostatic charging experiments. They found a good correlation between the redox potentials of the higher oxide/lower oxide couple and their minimum potentials for onset of the OER on almost all the oxides studied except "$PtO_2$" and $PbO_2$. It should be noted that the Pb cation in the $PbO_2$ lattice is already in its highest possible oxidation state of 4+ and no higher oxidation state of lead has been reported in the literature so no higher oxidation-state mediator could be involved. They therefore suggested a mechanism for the OER on $PbO_2$ that involves formation of the $OH^{\cdot}/HO_2^{\cdot}$ peroxide intermediate physisorbed on the oxide surface. The $PbO_2$ surface according to these authors, therefore merely acts as an inert surface in the process. The authors, however, did not specify which modification of the $PbO_2$ was examined. Although much work has been done on, and various mechanisms have been proposed for, the OER on $PbO_2$, the behaviour of the adsorbed intermediates, kinetically involved in the process, has not previously been investigated.

In this part of the thesis, the behaviours of the kinetically significant adsorbed

intermediates that are involved in the OER at the surface of both the $\alpha$- and $\beta$-$PbO_2$ comparatively studied by means of the potential-transient decay and a.c. impedance frequency response of the processes in relation to the steady-state polarization behaviour, will be reported and discussed. The objective is to compare the adsorption behaviour of the intermediates in relation to the OER kinetics on the $\alpha$ and ß forms of $PbO_2$ electrodes.

## IV,D,2 Choice of Experimental Approaches

As with other studies in electrocatalysis and related electrode kinetics of such processes [35,70,71,101], the kinetics of oxygen evolution at $\alpha$ and ß-$PbO_2$ were first evaluated comparatively by determination of the exchange current densities ( $i_o$ ) and Tafel slopes ( $b$ ) of log [current-density($i$)] vs potential plots. However, as has been stressed in previous works [70,102], the $b$ value is as important in characterizing electrocatalysis as the value $i_o$, especially with regard to electrode performance at elevated current-densities (c.d's) and particularly also in relation to the potential-dependence of coverage by electro-active adsorbed intermediates [63,67].

In this thesis, the important complementary evaluation of the behaviour of the adsorbed intermediate species, OH and O, in the OER has been made at a series of anode potentials. Such determinations require non-steady state procedures: here the methods of potential relaxation [33,60,66,70] following current interruption, and impedance spectroscopy [103,104] have been employed as for the the HER at elevated temperatures described and discussed in section IV.B.2. and IV.B.3. These approaches give information on the potential-dependence of coverage by the kinetically-significant adsorbed

intermediates through evaluation of the pseudocapacitance which is a component of the Faradaic impedance of the process ( Fig.41b ), coupled with the interfacial double-layer capacitance and kinetics of the discharge processes. Here the faradaic impedance may be more complex than that [104] in the $H_2$ evolution reaction due to the probable involvement of the two intermediates,OH and O ( cf.ref.[105] ).

The comparative evaluation of the impedance behaviour of the OER at the two "allotropic" forms of $PbO_2$ is an important part of the new work presented in this thesis.

## IV.D.3 The Primary Current vs Potential Relations at Several Temperatures

These are shown for five temperatures, T, comparatively, in Figs 51a and 51b. The $\alpha$-$PbO_2$ gives rise principally to more or less single-lined Tafel relations with some bend-off below ca.1.80 V vs RHE, having *b* values of ca. 140 mV per decade of *i* at each of the five T values. At ß-$PbO_2$ the OER Tafel relations exhibit two slopes of ca. 125 and 167 mV per decade over low and high c.d. ranges, respectively, again with little dependence of *b* values on T especially in the high c.d. range.

These results for the OER on Pb provide, incidentally a further fairly convincing example of the frequently observed [20,26] ( but see also ref.[16] ) non-conventional temperature dependence of the Tafel slope, *viz.* that is almost independent of, rather than proportional to, T implying that the transfer coefficient $\alpha$, or the electrochemical Bronsted coefficient, ß, for electron charge-transfer [2,26] is itself, or contains a component, linearly dependent on T.

The c.d.'s for the OER on the $\alpha$-$PbO_2$ over much of the experimental c.d. range are

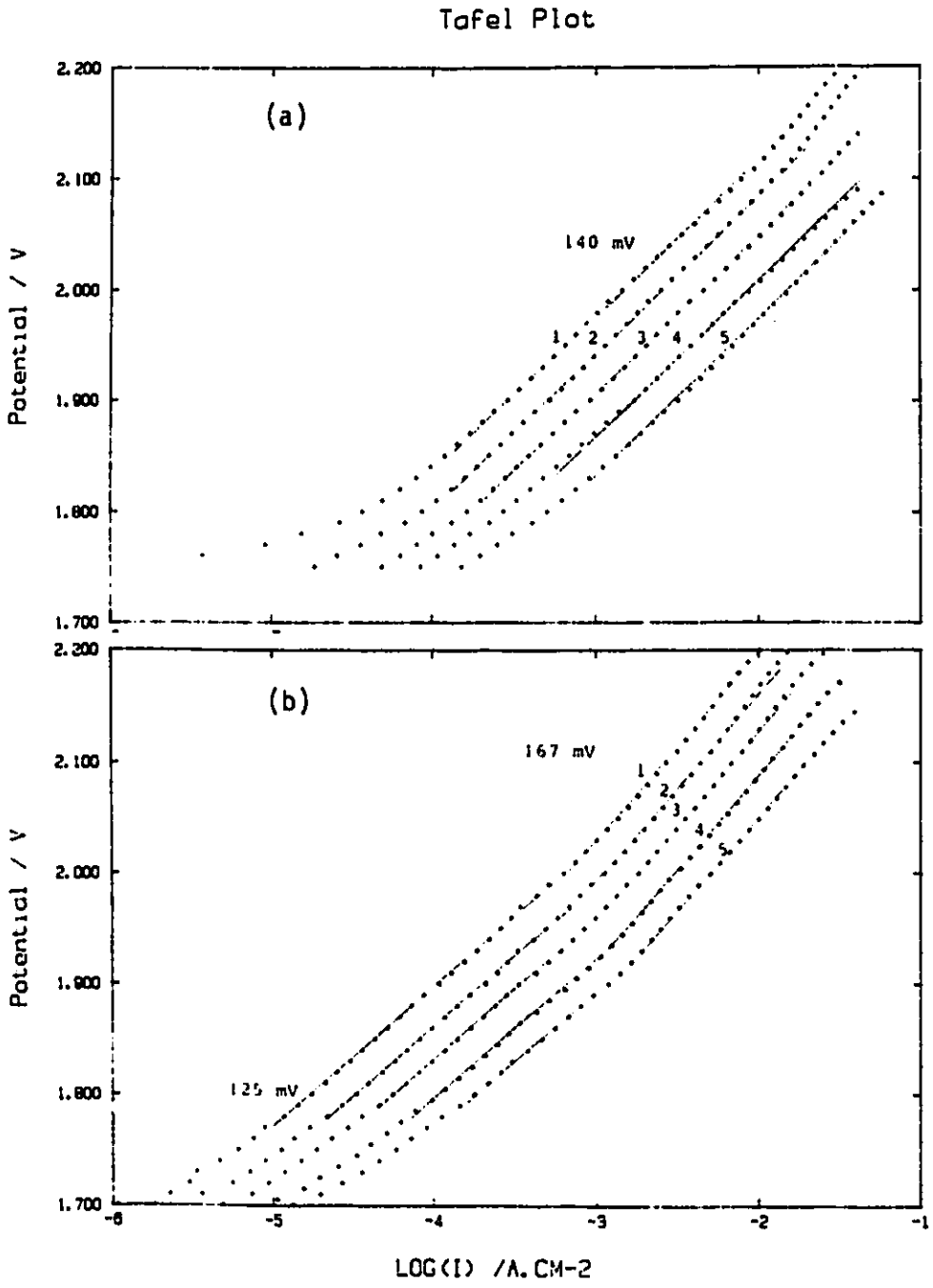


**Fig.51** Tafel relations for the OER at 5 temperatures 1) 299 K, 2) 309 K, 3) 319 K, 4) 329 K, 5) 339 K at (a) $\alpha$-$PbO_2$ and (b) $\beta$-$PbO_2$.

approximately 3 times greater than on the ß-$PbO_2$, this ratio being little dependent on T due to the only weak dependence of *b* values on T for these anode materials. Part of the above difference could be due to the difference of real area per apparent sq.cm, on account of the different morphologies of the macroscopic surfaces of the two preparations as seen in the scanning electron micrograph of Fig.52.

The transition in slope of the Tafel relations in Fig.51b for ß-$PbO_2$ from $b$ = 125 to 167 mV per decade arises at all five T values at a c.d. around 1 mA $cm^{-2}$. Formally, this direction of transition with increasing overpotential corresponds to a change of rate-determining step with potential in a consecutive multi-step reaction and/or change of adsorption conditions for the intermediate(s) involved. It is not clear here, however, if the former possibility could be the reason since the lower-slope region already has a *b* value of 125 mV, i.e. near 2.3 RT/0.5F. Clearly, this behaviour cannot be due to parallel contributions from some α-component in the ß-$PbO_2$ which would give the opposite direction of change of apparent Tafel slope. In the early work of Rüetschi el al.[35], *b* for ß-$PbO_2$ was found to be about twice that for the α form.

Operating in the conventional way to obtain apparent heats of activation, ( $\Delta H^{\ddagger}$ ) from the current vs potential plots of the five temperatures gave the following ( $\Delta H^{\ddagger}$ ) values (sometimes referred to confusingly as the "real" heat of activation):

$$\alpha\text{-}PbO_2 \qquad (\Delta H^{\ddagger}) \simeq 49 \pm 2 \text{ kJ mol}^{-1}$$

$$\beta\text{-}PbO_2 \qquad (\Delta H^{\ddagger}) \simeq 50 \pm 2 \text{ kJ mol}^{-1}$$

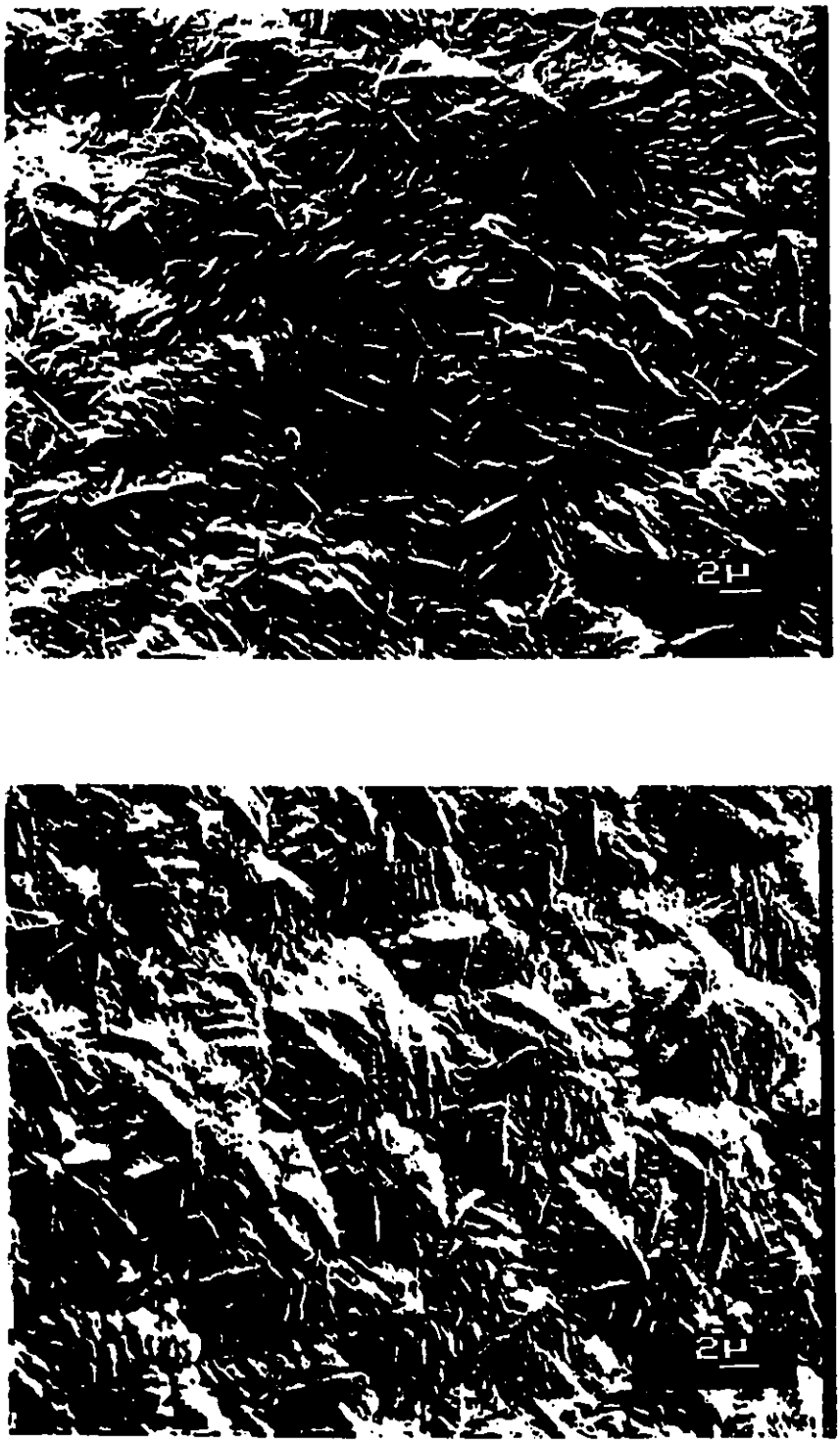


**Fig.52a,b** Scanning electron micrographs of (a) $\alpha$-$PbO_2$ prior to polarization measurements, (b) after such experiments.


(c)


(d)

**Fig.52c,d** Scanning electron micrographs of (c) $\beta$-$PbO_2$ prior to polarization measurements, (d) after such experiments.

Complications arise in the evaluation and significance of $\Delta H^{\ddagger}$ for processes that involve a T-dependent transfer coefficient, as for the present results. Readers are referred to the full analysis of this situation given in the review of Conway [26] and the papers of Conway and MacKinnon [2]. In particular, if $\alpha(T)$ has the form $\alpha(T) = \alpha_o T$, there is no potential-dependence of $\Delta H^{\ddagger}$ since the potential-dependence of ln $i$ is then $-\alpha_o T$ VF/RT.

## IV.D.4 Potential-Relaxation Transients and Analysis of Adsorption Pseudocapacitance Behaviour of the OER at $PbO_2$ Surfaces

The digitally acquired potential-relaxation transients at $\alpha$- and ß-$PbO_2$ ( see Experimental Section ) are shown typically in Figs 53a and 53b for several initial (iR-corrected) polarization potentials (V) at T = 299 K and in Figs 54a and 54b for three T values, 299, 319 and 339 K. Elsewhere [70] and in section IV.B.2. it has been shown that it is useful to plot also the electrode potential as a function of log(-dV/dt) arising from the basic potential-relaxation equation, Eq. (72), i.e., $-C(V)dV/dt = i(t,V) = \exp[\alpha\ V(t)F/RT]$ where $i(t,V)$ is the time and V-dependent self-discharge current passing at the interphase during the potential decay transient, as mentioned earlier. For short times, it has been shown [66] that the relaxation transient V(t) is determined by $C = C_{dl}$, the interfacial double-layer capacitance. When a chemisorbed intermediate, I, is involved whose coverage is V-dependent, C additionally involves the adsorption pseudocapacitance $C_\phi = q_I(d\Theta_I/dV)$ ( as discussed earlier ) where $q_I$ is the charge for adsorption or desorption of an hypothetical monolayer of I as mentioned in the Introduction section. $C_\phi$ dominates the potential decay behaviour at lower V's and sufficiently long t's when

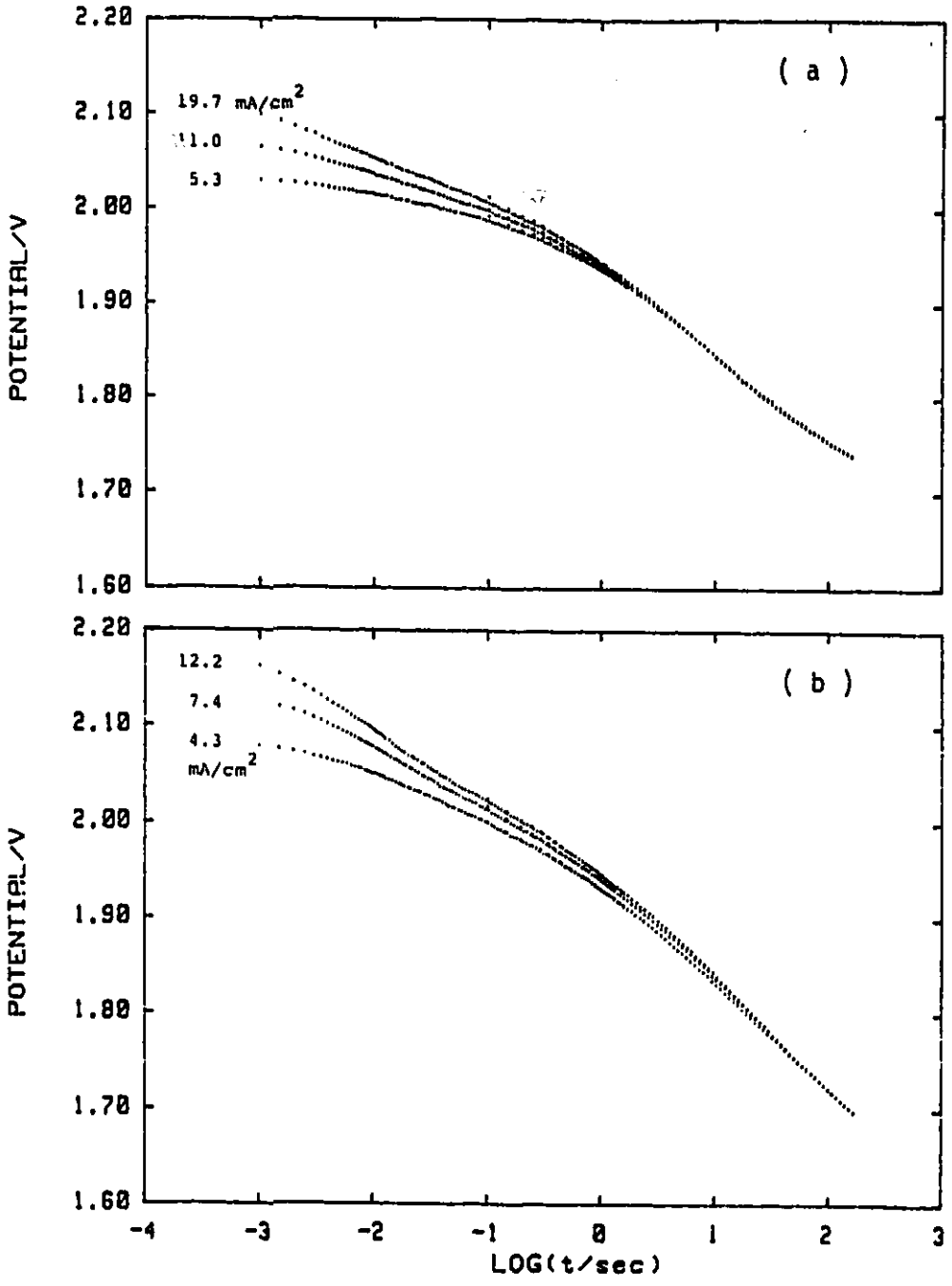


**Fig.53** Potential-relaxation transients for 3 initial overpotentials and corresponding prior steady-state current-densities of the OER at (a) $\alpha$-$PbO_2$ and (b) $\beta$-$PbO_2$ at 299 K.

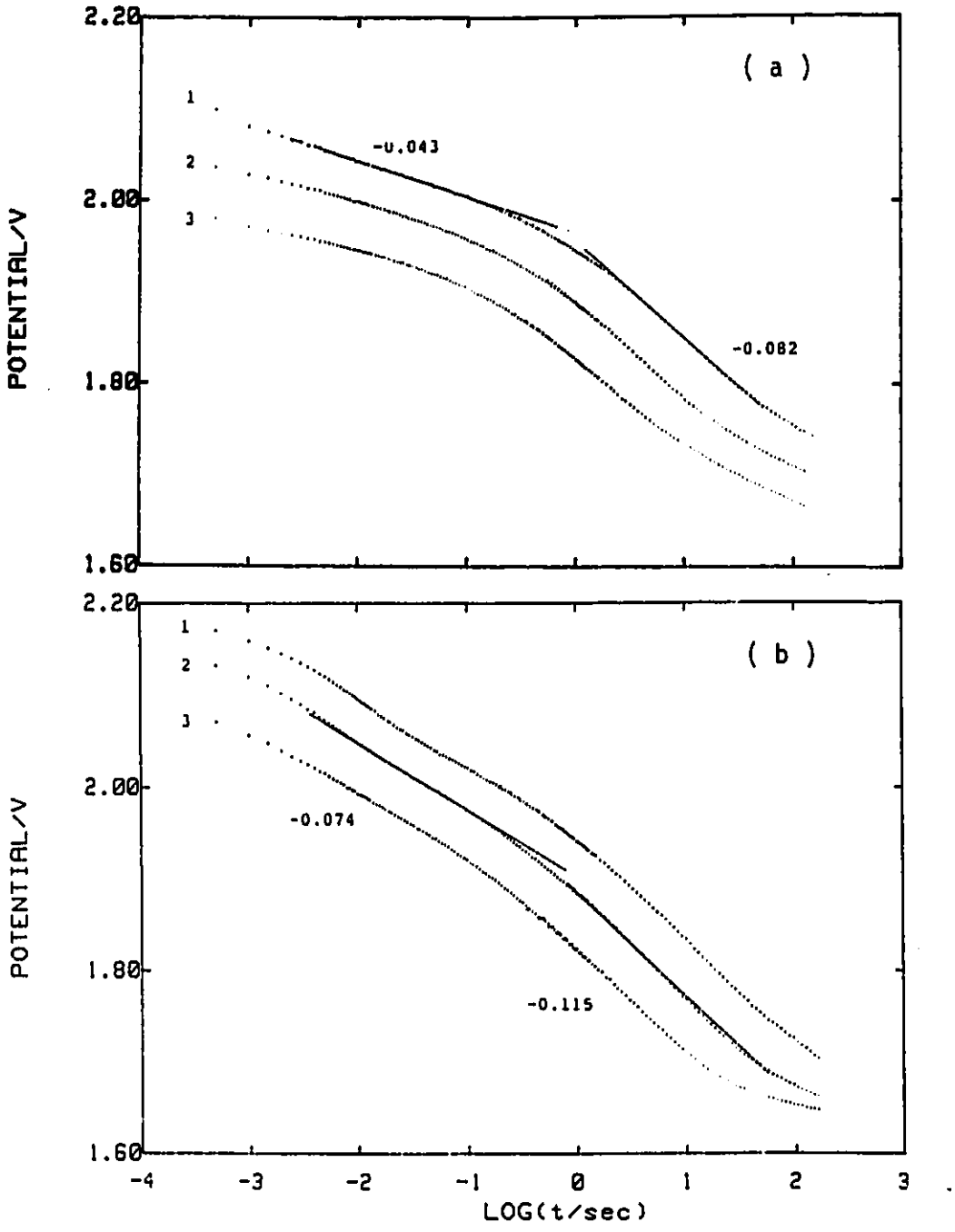


**Fig.54** Potential-relaxation transients, as in Fig.53, but at 3 temperatures (1) 299, (2) 319 and (3) 339 K for (a) $\alpha$-$PbO_2$ and (b) $\beta$-$PbO_2$.

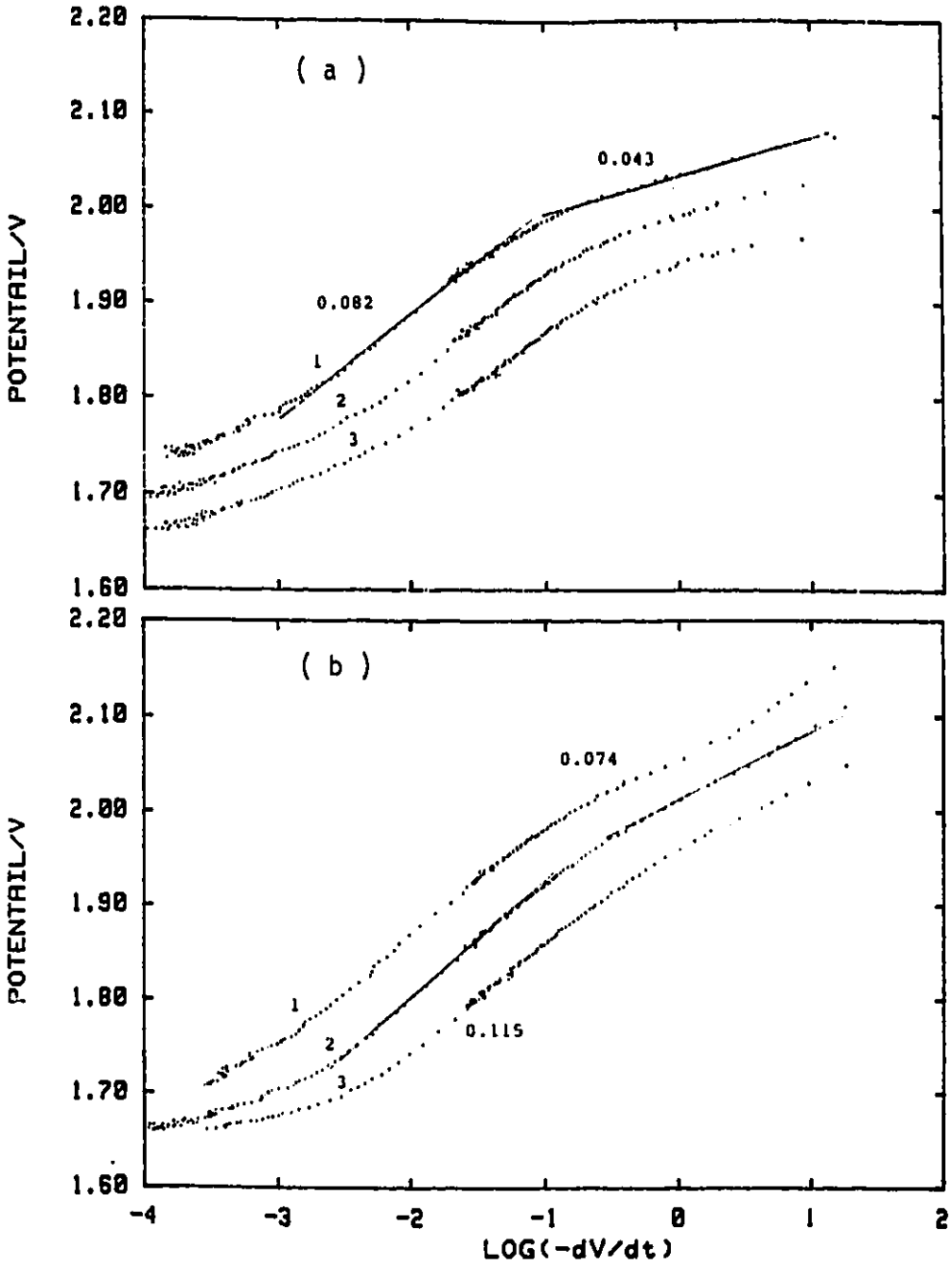


Fig.55 Plots of Log[-dV/dt] vs overpotential in the OER at (a) $\alpha$-$PbO_2$ and (b) $\beta$-$PbO_2$ at (1) 299, (2) 319 and (3) 339 K.

$C_\phi >> C_{dl}$, as discussed in refs [70] and [66].

It is seen from Eq.(80) in section IV.B.2. i.e., ln C(V) + ln(-dV/dt) = ln $i_o$ + $\alpha$ VF/RT that ln(-dV/dt) would follow a linear relation in V except for possible potential-dependence of C, written as C(V). Figs 55a and 55b show the V(t) vs log(-dV/dt) plots for potential-relaxation in the OER at $\alpha$ and ß-$PbO_2$, respectively. These relations for the two states of $PbO_2$ are similar but not identical and are certainly not linear. Hence the C in Eq.(72) is not constant with V.

An estimate of $C_\phi$ behaviour can be made from Eq.(80) for longer times (lower V's) in the potential-relaxation transients as has been shown for the HER [33,48,70] and also the OER on other materials [65,72,99]. V(t) transients can also be treated by the "rate-constants" methods of analysis described by Harrington and Conway [66] as mentioned earlier, by fitting the V(t) curves by a series of rate constants for the steps in some relevant two or three-stage mechanism; then $\Theta_i(V)$ and $d\Theta_i(V)/dV$ can be evaluated from the series of rate constants that fit the steady and non-steady-state behaviour of the reaction.

Treating the potential-relaxation transients by the first, more empirical approach leads to the capacitance vs potential relations of Figs 56a and 56b, for the three temperatures in the case of ß-$PbO_2$. It is seen that a broad maximum arises with (maximum) capacitance values around 6 to 10 mF $cm^{-2}$(apparent), possibly exhibiting two overlapping component curves. At high V's [initial regions of the V(t) transients], the C declines towards the double-layer capacitance value as it should according to the analysis in an earlier paper [66].

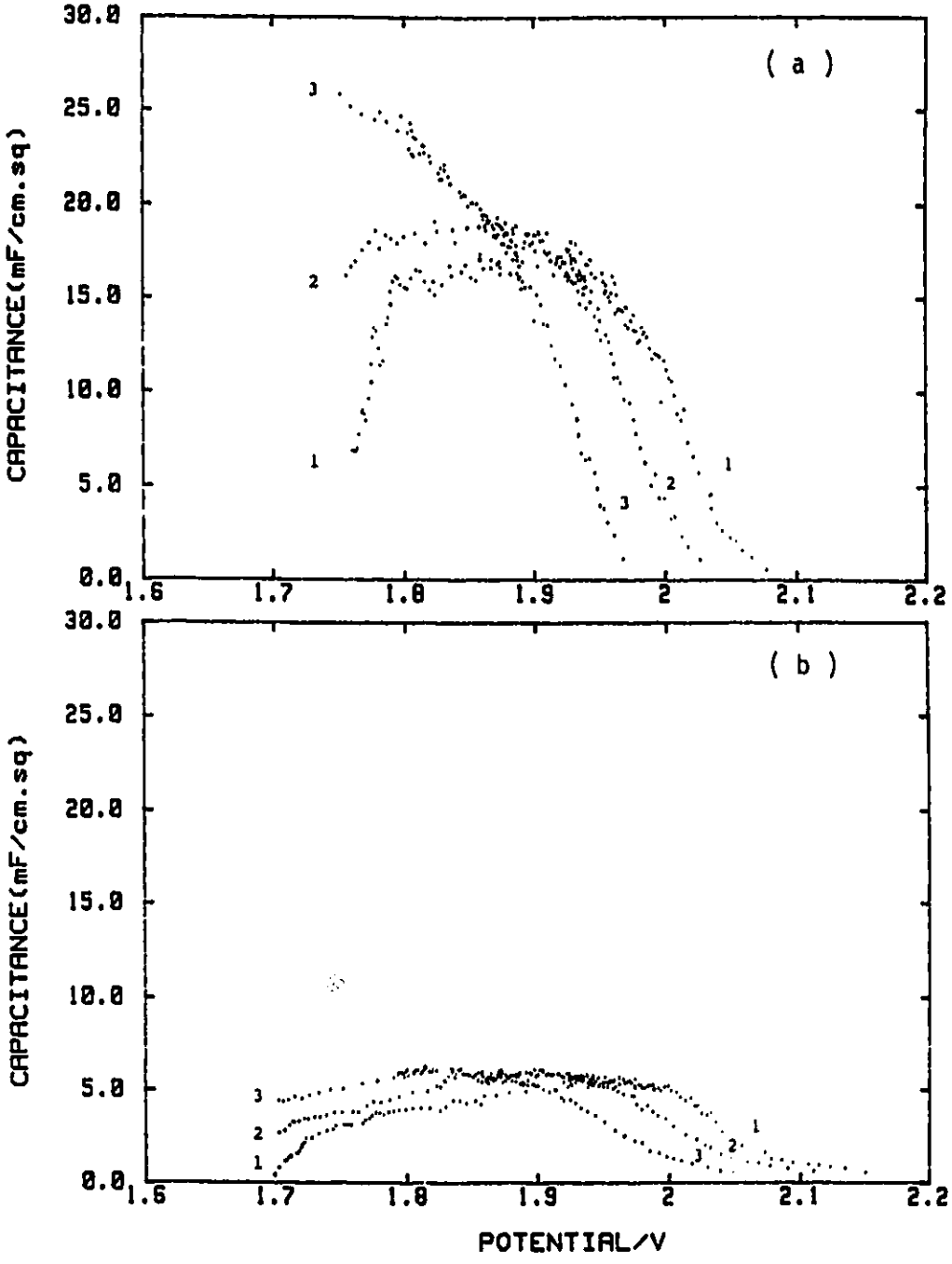


**Fig.56** Interfacial capacitance vs potential plots derived from analysis of the potential-relaxation transients (with the respective Tafel relations) at (a) $\alpha$-$PbO_2$ and (b) $\beta$-$PbO_2$ at (1) 299, (2) 319 and (3) 339 K.

For the $\alpha$-$PbO_2$ material, the C(V) results are somewhat similar but a larger maximum capacitance, up to 20 mF $cm^{-2}$ (apparent) arises. The values of maximum C are substantially larger than those expected ( cf.ref.[106] ) for development of a monolayer of intermediates on a smooth surface and probably therefore indicate substantial microscopic roughness of the surfaces of the $PbO_2$ preparation, as indeed is shown by inspection of the electron micrographs ( Figs 52a-d ). Since these photos indicate the exposure of many crystal-plane orientations, it is not surprising that the C(V) profiles of Figs 56a and b are bi- or multi-modal with respect to V.

## IV.D.5 A.C.Impedance Behaviour at R.T.

Shown in Figs. 57a, 57b and Figs. 57c, 57d are the complex-plane plots of the frequency response of the OER at $\alpha$ and ß-$PbO_2$ at several potentials in the range where appreciable steady-state rates of $O_2$ evolution are occurring, corresponding to the Tafel relations of Figs 51a and 51b derived from room temperature experiments.

In Figs 58a and 58b are shown comparatively, on the same scales, the dependence of phase angle on log($\omega$) for seven d.c. level potentials from 1.75 to 2.3 V. It is not possible to go much below 1.7 V (RHE) in these and the Tafel kinetic plots owing to reduction of the $PbO_2$ ( to $Pb^{2+}$ ions, in acidic medium; cf.ref.[107] )

For the ß-$PbO_2$, it is clear that the phase plot exhibits two components which become more separated as a function of $\omega$ as the electrode potential is decreased; at the most positive polarization potentials the phase-angle profile is simply that of the $C_{dl}$ coupled with the Faradaic impedance, as is also the situation that obtains for the initial, short-time

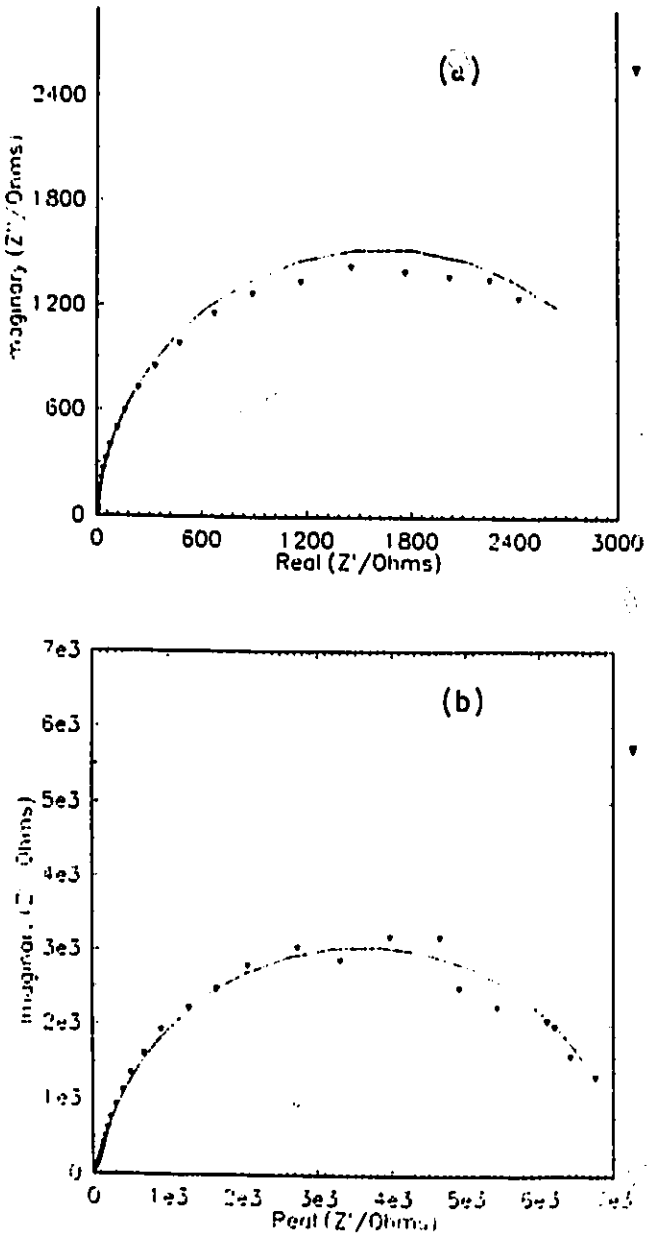


**Fig.57a,b** Complex-plane plots for the frequency response of impedance of the OER at (a) $\alpha$-$PbO_2$ and (b) $\beta$-$PbO_2$ at 299 K for OER overpotentials of 1.80 V vs RHE.

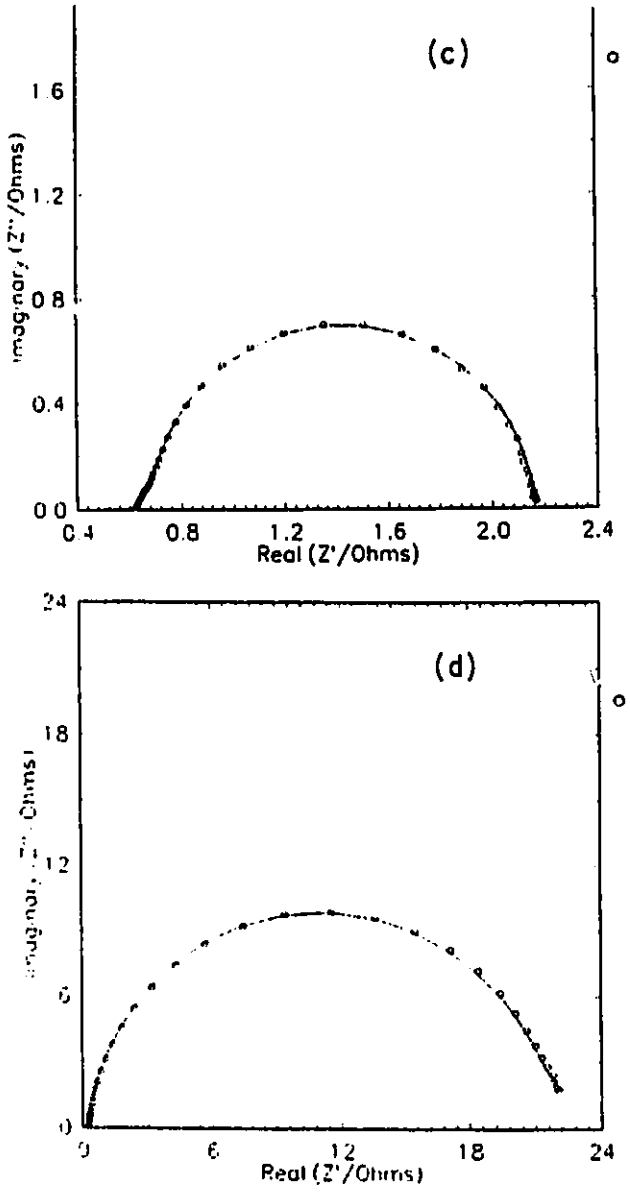


**Fig.57c,d** Complex-plane plots for the frequency response of impedance of the OER at (c) $\alpha$-$PbO_2$ and (d) $\beta$-$PbO_2$ at 299 K for OER overpotentials of 2.20 V vs RHE.

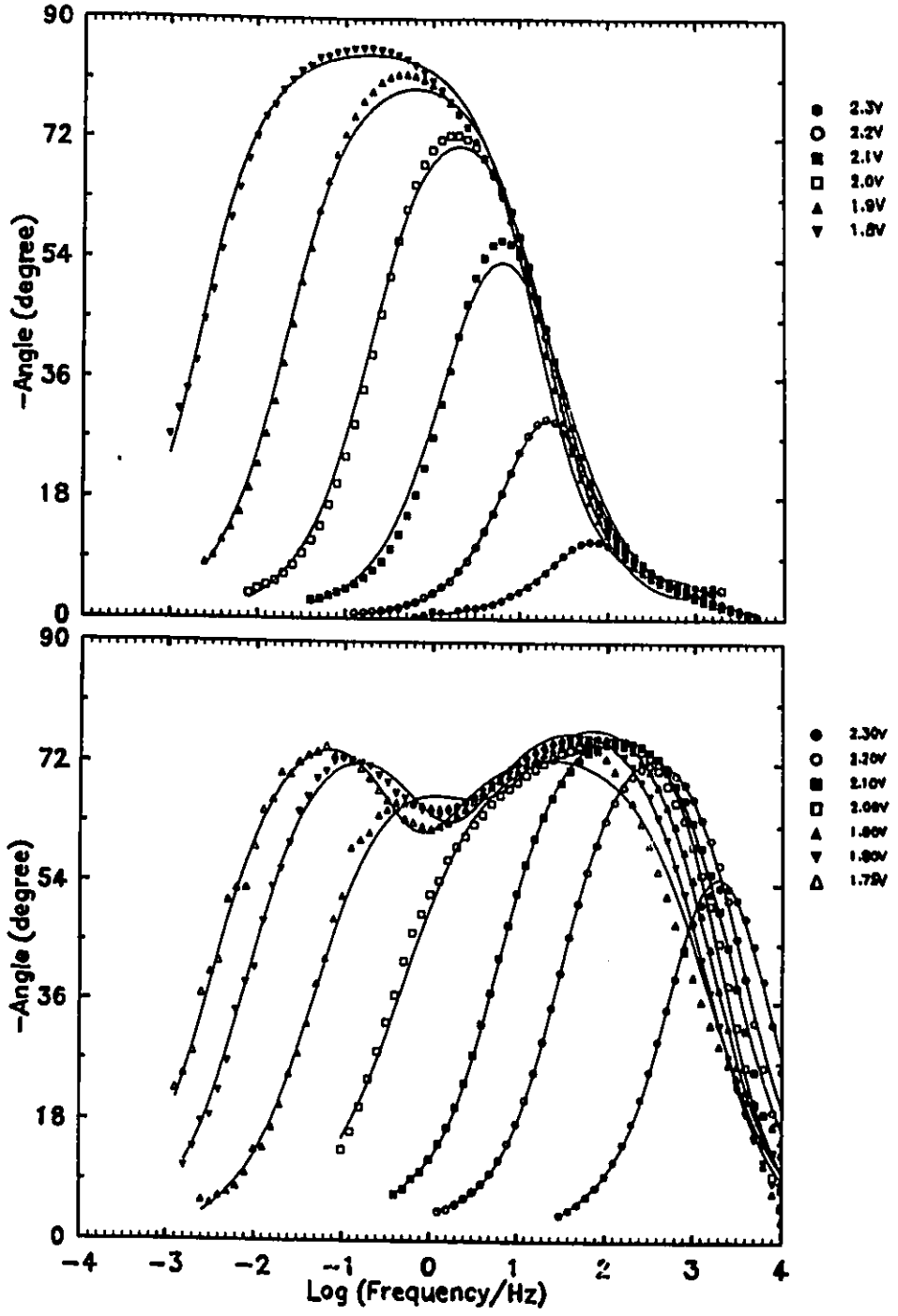


Fig.58 Phase-angle Bode-type plots as a function of log $\omega$ for a series of overpotentials in the OER: (a) for $\alpha$-$PbO_2$; (b) for $\beta$-$PbO_2$, both at 299 K.

region of the potential-relaxation transients as demonstrated in ref.[66].

With decreasing anodic potential ( for the ß-$PbO_2$ ), it is clear that a second peak develops in the phase plots of Fig.58b, i.e. as the Faradaic impedance increases with decreasing d.c. level potential. This extended second peak that develops and appears over the lower frequency range ( log[frequency] from ca $10^{-3}$ to 10 Hz, allowing for the overlap of the curves ) corresponds to the relaxation process(es) associated with the pseudocapacitance represented as $C_\phi$ in the probably oversimplified but commonly used equivalent circuit of Fig.41b and derived in the analysis of the potential-relaxation transients that give the C(V) results shown in Figs 56a and 56b.

For the $\alpha$-$PbO_2$ (Fig.58a), a single peak is observed in the phase plots for various potentials but the maxima in these phase angle plots depend substantially on V and there is a systematic movement of the maxima to lower log $\omega$ values as the potential is again made less positive. The phase-angle profiles become progressively wider ( e.g. width at half-heights on the log $\omega$ axis ) as the potential is decreased and this seems to be due to an increasing contribution of another component at lower frequencies as in Fig.58a but without the actual resolution of a separate low-frequency component of the kind that is clearly seen in Fig.58b for ß-$PbO_2$. For a simple combination of $C_{dl}$ with a Faradaic resistance $R_f$, a single peak of characteristic width at half-height (like the shapes of the profiles in Figs 58a and 58b for the highest positive potentials) would arise and the characteristic frequency for its maximum would decrease with diminishing potential, i.e. exponentially decreasing $R_f$ (Fig.41b).

It is then seen, especially from Figs.58a and 58b, that the frequency-response

behaviours of the OER processes at $\alpha$ and ß-$PbO_2$ are quite recognizably different in their dependence on polarization potential, probably corresponding to the different Tafel lines in Figs 51a and 51b. Since Fig 51b for the $\beta$-$PbO_2$ shows distinctive sections of the Tafel lines, having easily distinguishable slopes, it is tempting to suggest that this behaviour is related in the kinetic relaxation response over two distinguishable frequency ranges manifested in the bimodal phase plots where the second, low-frequency profile emerges as anodic potential is decreased. At ß-$PbO_2$, the inflection in the Tafel lines arises at ca. 2.0 V (RHE) at 299 K which is near the potential in Fig.58b where the second (low-frequency) peak begins to emerge from the first peak. Comparison of the shapes of the profiles of Figs 58a and 58b suggests that the profile in Fig.58a might tend to become split if the potential range at $\alpha$-$PbO_2$ could be extended below 1.8 V which is found to be experimentally difficult.

## IV.D.6 Simulation of the Frequency Response Behaviour

Based on the equivalent circuit approach (cf. Fig.41b), the observed frequency-response behaviour of the OER, shown in Figs. 57a and 57b, can be rather well simulated, including the curves exhibiting the two maxima in Figs 58a,b. In these two figures, the simulated behaviour is represented by the solid lines and the experimental data by the indicated points, for various anode potentials and over a rather wide ($10^4$ to $10^{-3}$ Hz) frequency range. Evidently, excellent simulation can be achieved with the single equivalent circuit of Fig.41b.

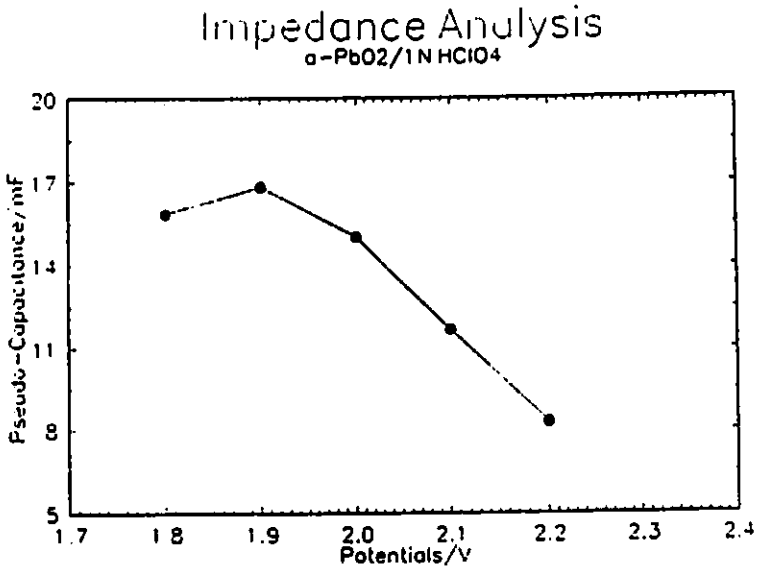


**Fig.59** Evaluation of the pseudocapacitance arising in the OER at $\alpha$-$PbO_2$ (299 K) fro the impedance analysis as a function of overpotential in the OER.

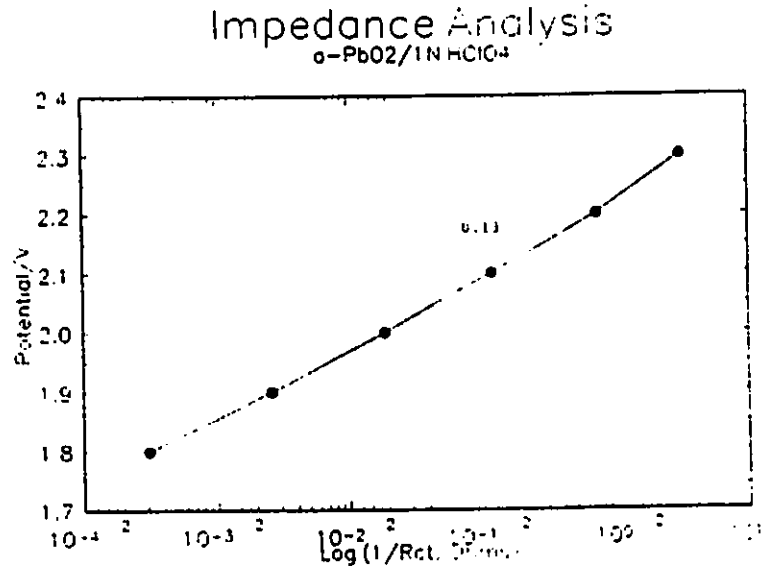


**Fig.60** Evaluation of the charge-transfer resistance, $R_{ct}$, arising in the OER at $\alpha$-$PbO_2$ (299 K) as a function of overpotential, derived from the analysis of the impedance behaviour. (Note equivalence of the $R_{ct}^{-1}$ plot to Tafel polarization behaviour, as expected.)

From the impedance analysis, the pseudocapacitance component can be evaluated as a function of potential (Fig.59) and also the charge-transfer resistance, $R_{ct}$ as shown in Fig.60. For the example of the $\alpha$-$PbO_2$, the pseudocapacitance as a function of potential is similar to the curve found from analysis of the potential-relaxation data (Fig.56), with a maximum around 17 mF $cm^{-2}$ (apparent). Correspondingly, the reaction resistance, $R_{ct}$, derived from the simulation calculations, plots out (see Fig.60) on a log scale like the Tafel relation in Fig.51a, so the simulation results are self-consistent, and also consistent with the d.c. and the transient relaxation behaviour.

## IV.D.7 Conclusion on the OER Behaviour at $\alpha$- and $\beta$-$PbO_2$ Surfaces

Tafel or steady-state polarization relations for the OER at the two $PbO_2$ surfaces obtained at several elevated temperatures exhibit significant differences, as would be expected from the striking differences in the morphology of the two structures. Principally, the $\alpha$-$PbO_2$ gives rise to single-lined Tafel relations i.e., with a single Tafel slope, $b$, while the $\beta$-$PbO_2$ exhibits Tafel relations with two linear regions and thus two $b$'s. However, at least over the temperature range studied, none of these Tafel slopes exhibits significant temperature dependence. Thus, these results provide another convincing example of the non-conventional temperature dependence of the Tafel slope that is frequently observed in the work of this thesis and by others.

Similar behaviour for the adsorbed, kinetically important reaction intermediate(s), O and OH, for the OER is observed at the two "allotropic" forms of $PbO_2$, that is, at both surfaces, a broad maximum arises in the capacitance vs. potential relations, C(V), possibly

due to overlapping of two component curves corresponding to the two intermediates O and OH involved in the process. Apparently, the amount of charge derived from the C(V) relations is larger at $\alpha$-$PbO_2$ than at $\beta$-$PbO_2$ and is consistent with the higher current densities observed on $\alpha$-$PbO_2$. However, the fact that these observed charges are substantially higher than those expected for a monolayer of intermediates on a smooth surface indicates rather substantial microscopic roughness of the $PbO_2$ surfaces.

Significant qualitative differences, however, are observed between the impedance behaviour of the OER obtained at the two forms of $PbO_2$. The differences are more easily observed when the experimental frequency-response behaviour of the OER at the two surfaces is plotted in a form of Bode-type phase angle vs log (frequency) plot. That is, a single-peaked phase angle plot that is d.c.-level potential dependent was observed at the $\alpha$ surface while that for the $\beta$ surface is basically composed of two-components. It seems likely therefore that the a.c. behaviour is related closely to the single-lined and two-sloped Tafel relations observed for the two "allotropic" forms of the $PbO_2$, $\alpha$ and $\beta$.

Further, the experimental frequency-response behaviour of the OER at either form of $PbO_2$ could be rather well simulated using a single type of equivalent-circuit (cf. Fig.41b).

## V. CLAIMS TO ORIGINAL RESEARCH

1) The reversibility of oxide film formation and reduction processes at Pt and Au in various aqueous solutions up to 538 K is examined. It is seen that cyclic voltammograms obtained at elevated temperatures, especially at temperatures well above 273 K, exhibit current peaks that are relatively narrower and much higher in current density. It is shown that the reversibility of the processes is enhanced significantly at elevated temperatures, particularly at the Au electrode. This is discussed in terms of i) cathodic peak potential vs anodic potential limits, ii) anodic vs cathodic peak potential relations and iii) anodic and cathodic peak potential vs sweep rate relations.

2) The remarkably "clean" double-layer regions of the cyclic voltammograms recorded at elevated temperatures indicate that the highly specialized home-made high-temperature/high-pressure apparatus developed for the work described in this thesis functioned properly and is suitable for the investigation of various electrochemical processes at elevated temperatures under aqueous conditions up to 538 K.

3) The kinetic behaviour in the HER and OER at elevated temperatures at Pt, Au and Ni in various aqueous solutions is evaluated. It is shown that, in general, the rate of reaction is higher at elevated temperatures, as would be expected. This is discussed in terms of the $i_o$ values. Interesting Tafel relations are observed for the HER at Au and Ni in that the Tafel lines exhibit two easily distinguishable linear regions and these two Tafel regions have somewhat opposite dependences of their slopes on temperature.

4) The problem of temperature dependence of the Tafel slope for various processes including i) the HER at Pt, Au and Ni, ii) the OER at Pt and to a smaller extent, iii) the oxide film formation and reduction processes at Pt and Au is examined at elevated temperatures in aqueous solutions. It is shown that the classical relationship representing the Tafel slope $b$ as $b = 2.3\ RT/\beta F$ with $\beta$, the symmetry factor, equals to $0.5 \pm 0.05$, is <u>not</u> actually followed, at least for those electrochemical systems studied in this thesis work.

5) The adsorption behaviour of the kinetically important adsorbed intermediate(s), H in the case of the HER and O or OH in the case of the OER, in aqueous solutions at elevated temperatures, is evaluated by means of the potential-relaxation and the a.c. impedance methods. It is shown that up to the relatively high temperature of 450 K, the double-layer capacitance, $C_{dl}$, is fairly constant for all three metals investigated. The adsorption behaviour of the intermediate(s) is discussed in terms of the coverage, $\theta_H$ derived from the log C(V) vs V relations derived from the results of potential-relaxation experiments. In the case of Au, the extent of H-adsorption is not at all significant as revealed by the extremely low pseudocapacitance, $C_\phi$, values at most temperatures. In the case of Ni, the effect of temperature on $C_\phi$ is quite large. It is shown that the estimated $\theta_H$ for higher T can be negligible but at lower T, a nominal apparent coverage of close to unity is derived. In the case of Pt, unexpectedly high apparent $\theta_H$ is recorded experimentally at most temperatures, especially at elevated ones. This is discussed in terms of the possibility that in addition to H-adsorption, H is also absorbed significantly into the "near surface"

region of the electrode.

6) The kinetics of the OER at Pt is examined at elevated temperatures. The Tafel relations observed exhibit principally two Tafel regions. The low current-density curved Tafel region is attributed to a mechanism involving recombination control while the linear high current-density region is most likely that of control by the electrochemical desorption step.

7) The existence of two structurally different forms of a conducting metal oxide, $\alpha$- and $\beta$-$PbO_2$, on which the OER can be studied, provides an almost unique opportunity of investigating how electrocatalysis in this reaction depends on structure of these otherwise chemically identical materials, having otherwise identical composition.

8) The kinetics of the OER at the two "allotropic" forms of $PbO_2$ is examined. Significant differences of the Tafel relations are observed. This is discussed in terms of the Tafel slope, $b$ and the exchange current-density, $i_o$.

9) The adsorption behaviour of the kinetically involved intermediates, OH and O, at the $\alpha$- and $\beta$- forms of $PbO_2$ is examined comparatively by means of potential-relaxation transients, following anodic current interruptions, and a.c. frequency response measurements. Significant differences in the behaviour of the adsorbed species in the OER are found. This is discussed in terms of the C(V) vs V relations derived from the results of potential-relaxation transient experiments as well as the simulated a.c. frequency response based on the equivalent circuit approach.

## VI. LIST OF REFERENCES:


1. B. E. Conway and D. J. MacKinnon, *J. Electrochem. Soc.*,**116**, 1665 (1969).

2. B. E. Conway, D. J. MacKinnon, and B. V. Tilak, *Trans. Faraday Soc.*,**66**, 1203 (1970).

3. B. E. Conway and M. Salomon, *J. Chem. Phys.* **41**, 3169 (1964).

4. B. E. Conway and M. Salomon, *Disccuss. Faraday Soc.* **39**, 223 (1965).

5. B. E. Conway and D. F. Wilkinson, *J. Electroanal. Chem.*, **214**, 633 (1986).

6. A. J. Appleby, *J. Electrochem. Soc*, **117**, 1158 (1970) and **117**, 641 (1970).

7. E. Yeager, D. Scherson and B. Simić-Glavaski, Extended Abstracts of the Spring Meeting of The Electrochemical Society, San Francisco, Calif. p. 1043 (1983).

8. U. Stimming and W. Schmickler, *J. Electroanal. Chem.*, **150**, 12 (1983).

9. R. M. Crooks and A. J. Bard, *J. Phys. Chem.* **91**, 1274 (1987).

10. R. M. Crooks, F. F. Fan, and A. J. Bard, *J. Am. Chem. Soc.*, **106**, 6851 (1984).

11. T. Erdey-Gruz and E. Volmer, *Z. Physik. Chem.*, **150A**, 203 (1930); **162**, 53 (1932).

12. J. A. V. Butler, *Trans. Faraday Soc.*, **19**, 729 (1924); **28**, 379 (1932).

13. S. Glasstone, K. J. Laidler, and H. Eyring, *J. Chem. Phys.*, **7**, 1053 (1939).

14. J. N. Agar, *Discuss. Faraday Soc.*, **1**, 84 (1947).

15. B. E. Conway, D. P. Wilkinson, and D. F. Tessier, *Ber. Bunsenges. Phys. Chem.*, **91**, 484 (1987).

16. E. Gileadi, *J. Electrochem. Soc.*, **137**, 3870 (1990).

17. M. J. Weaver, *J. Phys. Chem.*, **83**, 1748 (1979).

18. M. J. Weaver, *J. Phys. Chem.*, **80**, 2645 (1976).

19. E. Kirowa-Eisner, M. Schwarz, and E. Gileadi, *Electrochimica Acta.*, **34**, 1103 (1989).

20. H. P. Stout, *Trans. Faraday Soc.*, **41**, 64 (1945).

21. B. E. Conway and T. C. Liu, *Langmuir*, **6**, 268 (1990).

22. B. E. Conway, D. F. Tessier, and D. F. Wilkinson, *Chemical Phys. Letters*, **125**, 589 (1986).

23. J.O'M. Bockris and A. Gochev, *J. Electroanal. Chem.*, **214**, 655 (1986).

24. V. M. Tsionskii, L. I. Krishtalik, and L. B. Kriksunov, *Electrochimica Acta.*, **33A**, 623 (1988).

25. R. M. Crooks and A. J. Bard, *J. Phys. Chem.*, **91**, 1274 (1987).

26. B. E. Conway, in "Modern Aspects of Electrochemisty",Vol.16, B. E. Conway, J.O'M. Bockris, and R. White, Editors, Chap.2, Plenum Press, New York (1985).

27. B. E. Conway and H. Angerstien-Kozlowska, *Acc. Chem. Res.*,**14**, 49 (1981).

28. F. G. Will, *J. Electrochem. Soc.*, **112**, 481 (1966)

29. H. Angerstien-Kozlowska and B. E. Conway, *J. Electroanal. Chem.*, **95**, 1 (1979).

30. A. J. Calandra, N. R. De Tacconi and A. J. Arvía, *J. Electroanal. Chem.* **49**, 145 (1974).

31. N. R. De Tacconi, A. J. Calandra and A. J. Arvía, *J. Electro*anal. Chem. & Interfacial Electrochem., **51**, 25 (1974).

32. B. E. Conway, H. Angerstein-Kozlowska, F. C. Ho, J. Klinger, B. MacDougall and S. Gottesfeld, *Discuss. Faraday Soc.*, **56**, 210 (1973).

33. B. E. Conway, L. Bai, and D.F. Tessier, *J. E.ectroanal. Chem.*, **161**, 39 (1984).

34. J. O'M. Bockris, *J. of Chem. Phy.* **24**, 817 (1956).

35. P. Ruetschi, R. T. Angstadt, and B. D. Cahan, *J. Electrochem. Soc.*, **106**, 547 (1959).

36. M. Nicolas, L. Dumoulin and J. P. Burger, *J. Electroanal. Chem.*, **172**, 389 (1984).

37. S. J. Clouser, J. C. Huang and E. Yeager, National Meeting, The Electrochem. Soc., Montreal, May, 1982, Ext. Abstr., 82-1, no. 348.

38. C. M. Ferro, A. J. Calandra and A. J. Arvía, *J. Electroanal. Chem.*, **50**, 403 (1974).

39. C. M. Ferro, A. J. Calandra and A. J. Arvía, *J. Electroanal. Chem.*, **55**, 291 (1974).

40. J. D. Bernal and R. H. Fowler, *J. Chem. Phys.* **1**, 515, (1933).

41. R. P. Bell, *Proc. Soc. London, Ser.* **A 139**, 466 (1933).

42. C. E. H. Bawn and G. Ogden, *Trans. Faraday Soc.*, **30**, 432, (1934).

43. B. E. Conway, *Can. J. Chem.* **37**, 178 (1959).

44. St. G. Christov, *Electrochim. Acta* **4**, 194 (1961); **4**, 306 (1961);**9**, 575 (1964).

45. B. E. Conway and D. M. Novak, *J. Chem. Soc., Faraday Trans 1*, **75**, 2454 (1979).

46. J. J. Lander, *Surf. Sci.*, **1**, 125 (1964).

47. A. U. MacRae, *Surf. Sci.*, **1**, 319 (1964).

48. B. E. Conway and L. Bai, *J. Electroanal. Chem.*, **198**, 149 (1986).

49. D. de G. Jones and H. G. Masterson, in *Advances in Corrosion Science and Technology*; M. G. Fontana, R. W. Staehle, Eds.; Plenum: New York, 1970. Vol.1, pp 1-49.

50. J. N. Gaur and G. M. Schmid, *J. Electroanal. Chem.*, **24**, 279 (1970).

51. A. J. Monack, *Electrical Manufacturing*( now *Electro-Technology* ), February, (1947).

52. J. Giner, *J. Electrochem. Soc.*, March, 376 (1964).

53. J. V. Dobson, P. R. Snodin and H. R. Thirsk, *Electrochimica Acta*, **21**, 527 (1976).

54. M. W. Connell, U.S. Patent 2,625,573 (1953).

55. H. Angerstein-Kozlowska, B. E. Conway, and W. B. A. Sharp, *J. Electroanal. Chem.*, **43**, 1 (1973).

56. B. V. Tilak, B. E. Conway, and H. Angerstein-Kozlowska, *J. Electroanal. Chem.*, **48**, 1 (1973).

57. K. J. Vetter and J. W. Schultze, *J. Electroanal. Chem.*, **34**, 131 (1972).

58. M. D. Goldshtein, T. I. Zaĭkind, and V. I. Veselovskii, *Electrokhim.*, **9**, 699 (1973).

59. B.E. Conway, H. Angerstein-Kozlowska and W. B. A. Sharp, *J. Chem. Soc., Faraday Trans.* I, **74**, 1373 (1978).

60. J. A. V. Butler and J. F. Armstrong, *Trans. Faraday Soc.*, **29**, 1261 (1933).

61. H.B. Morley and F. E. W. Wetmore, *Can. J. Chem.*, **34**, 359 (1956).

62. B. E. Conway and L. Bai in T. N. Veziroglu and Taylor (Eds.), Proceedings of the 5th world Hydrogen Energy Conference, Toronto, Canada, 1984, Pergamon Press, New York, 1985.

63. B. V. Tilak and B. E. Conway, *Electrochim. Acta*, **21**, 745 (1976).

64. E. Gileadi and B. E. Conway, in 'Modern Aspects of Electrochemistry', Vol. III, (edited by J.O'M Bockris and B. E. Conway), Butterworths, London (1964) Chap.5.

65. B. E. Conway and T. C. Liu, *J. Chem. Soc., Faraday Trans.* I, **83**, 1063 (1987).

66. D. A. Harrington and B. E. Conway, *J. Electroanal. Chem.*, **221**, 1 (1987).

67. B. V. Tilak, C. G. Rader and B. E. Conway, *Electrochim. Acta*, **22**, 1167 (1977).

68. B. E. Conway and L. Bai, *J. Electroanal. Chem.*, **82**, 149 (1986).

69. M. Elam and B. E. Conway, *J. Electrochem. Soc.*, in press.

70. B. E. Conway and L. Bai, *J. Chem. Soc., Faraday Trans.* 1, **81**, 1841 (1985).

71. P. Gu and B. E. Conway, *J. Chem. Soc., Faraday Trans.*, in press.

72. B. E. Conway and T. C. Liu, *Proc. Roy. Soc.*, London, **A429**, 375 (1990).

73. N. Kameyama and T. Fukumoto, *J. Soc. Chem. Ind. Japan*, **46**, 1022 (1943).

74. A. J. Zaslavski and S. S. Tolkachev, *Zh. Fiz. Khim.*, **26**, 743 (1952).

75. N. E. Bagshaw and K. P. Wilson, *Electrochimica Acta*, **10**, 867 (1965).

76. P. Rüetschi, *J. Electrochem. Soc.*, **139**, 1347 (1992).

77. N. E. Bagshaw, R. L. Clarke and B. Halliwell, *J. Appl. Chem.*, **16**, 180 (1966).

78. K. H. Palmer, *Z. Elektrochem.*, **29**, 415 (1923).

79. U. B. Thomas, *J. Electrochem. Soc.*, **94**, 42 (1948).

80. H. Bode and E. Voss, *Z. Elektrochem.*, **60**, 1053 (1956).

81. P. Rüetschi and B. D. Cahan, *J. Electrochem. Soc.*, **104**, 406 (1957).

82. P. Johes, R. Lind and W. F. K. Wynne-Jones, *Trans. Faraday Soc.*, **50**, 972 (1954).

83. B. N. Kabanov, I. B. Kiseleva and D. I. Leikis, *Dokl. Akad. Nauk SSSR*, **99** 805 (1954).

84. G. A. Kokarev, N. G. Bakhchisaraits'Yan and V. V. Panteleeva, *Trans. Mosk. Tekhnol. Inst.*, **54**, 167 (1967).

85. M. Dimitrov, *J. Power Sources*, **41(1-4)**, 121 (1990).

86. X. Gao, Y. Shi, H. Zhang, S. Wang, Z. Zhang, *Yingyong Huaxue*, **1(1)**, 87 (1983).

87. P. Rasiyah, A. C. C. Tseung, *J. Electrochem. Soc.*, **131(4)**, 803 (1984).

88. P. Rasiyah, A. C. C. Tseung, *Adv. Hydrogen Energy* 1982, **3** ( Hydrogen Energy Prog. 4, vol.1 ) 383.

89. F. K. Andryushenko, A. K. Gorbachev, *Vestn. Kharkov. Politekun. In-ta* **147**, 33 (1987).

90. G. N. Kokhanov, N. G. Baranova, *Eletrokhimiya*, **8(6)**, 864 (1972).

91. S. H. Chin, Y. C. Chu, C. W. Chin and K. T. Yuan, *Chung Kuo K'o Hsueh Yuan, Ying Yung Hua Hsueh Yen Chiu Chi K'an*, **16**, 34 (1966).

92. A. I. Krasil'shchikov, *Zh. Fiz. Khim.*, **37**, 531 (1963).

93. D. F. A. Koch, *Australian J. Chem.*, **12**, 127 (1959).

94. P. Rüetschi, P. Delahay, *J. Chem. Phys.*, **23**, 556 (1955).

95. Yu. V. Fedorov and F. I. Kukoz, *Primenenie Ul'traakustiki k Issled. Veshchestra* **12**, 159 (1960).

96. S. S. Popova, L. N. Cjernova, Yu. B. Radkevich, Yu. N. Chernykh, *Issled. V Obl. Khim. Istochnikov Toka, Saratov*, **7**, 55 (1980).

97. A. T. Kuhn, *Chem. Ind. (London)* **20**, 867 (1976).

98. B. E. Conway and T. C. Liu, *Ber, Bunsenges. Phys. Chem.* **91**, 461 (1987).

99. B. E. Conway and P. L. Bourgault, *Can. J. Chem.*, **38**, 1557 (1960); **40**, 1690 (1962).

100. J. E. B. Randles, *Disc. Faraday Soc.*, **1**, 11 (1947).

101. R. Parsons, *Trans. Faraday Soc.*, **54**, 1053 (1958).

102. B. E. Conway, L. Bai, M. A. Scattar, *Int. J. Hydrogen Energy*, **12**, 607 (1987).

103. R. D. Armstrong and M. Henderson, *J. Electroanal. Chem.* **39**, 81 (1972).

104. L. Bai, D. A. Harrington and B. E. Conway, *Electrochim. Acta*, **32**, 1713 (1987).

105. L. Bai and B. E. Conway, *J. Electrochem. Soc.*, **137**, 3737 (1990).

106. E. Gileadi and B. E. Conway, *J. Chem. Phys.*, **39**, 3420 (1963).

107. M. Pourbaix, "Atlas of Electrochemical Equilibrium," Gauthiers-Villar, Paris, 1963.

108. M. Sluyters-Rehbach and J. H. Sluyters, *Electroanalytical Chemistry* ( A. J. Bard (Ed)), vol.4, Ch.1, Marcel Dekker (1970).

109. A. Hickling and S. Hill, *Discussions Faraday Soc.*, ,**1**, 236 (1974).

110. A. Damjanovic and B. Jovanovic, *J. Electrochem. Soc.*, **123**, 374 (1976).

112. V. I. Birss and A. Damjanovic, *J. Electrochem. Soc.*, **130**, 1694 (1983).

113. J. W. Schultze and K. J. Vetter, *Electrochim. Acta*, **18**, 889 (1973).

114. A. T. Ward, A. Damjanovic, E. Gray, and M. O'Jea, *J. Electrochem. Soc.*, **123**, **1599** (1976).

115. T. P. Hoar, *Proc. R. Soc. London, Ser. A* **142**, 628 (1933).

116. R. I. Kaganovich and M. Lich, *Zh. Fiz. Khim.*, **38**, 1656 (1964).

117. A. Damjanovic, A. Dey, and J. O'M. Bockris, *Electrochim. Acta*, **11**, 791 (1966).

118. C. Iwakura, K. Fukuda, and H. Tamura, *Electrochim. Acta*, **21**, 501 (1976).

119. D. C. W. Kannangara and B. E. Conway, *J. Electrochem. Soc.*, **134**, 894 (1987).

120. B. E. Conway, H. Angerstein-Kozlowska, M. A. Sattar and B. V. Tilak, *J. Electrochem. Soc.*, **130**, 1825 (1983).

121. B. E. Conway, H.Angerstein-Kozlowska and W. B. A.Sharp, in *Proc. Symposium on Electrocatalysis*, ed. M. Breiter ( The Electrochemical Society, 1974 ), P. 94.

122. L. J. Bai, L. J. Gao, and B. E. Conway, *J. Chem. Soc. Faraday Trans.*, **89**, (1993). In press.

123. G. Gouy, *J. Chim. Phys. (Paris)*, **29**, 145 (1903).

124. D. L. Chapman, *Phil. Mag.*, **25**, 475 (1913).

125. A. Sevčik, *Collection Czech. Chem. Commun.*, **13**, 349 (1948).